



Masters Thesis

OUT-OF-PLANE STRENGTHENING OF UNREINFORCED MASONRY WALLS
USING FRP TECHNIQUES

BY

QI YANG

B.E., Civil/Structural

School of Civil and Environmental Engineering
The University of Adelaide

May 2007

DECLARATION

This work contains no material which has been accepted for the award of any other degree or diploma in any university or other tertiary institution and, to the best of my knowledge and belief, contains no material previously published or written by another person, except where due reference has been made in the text. I give consent to this copy of my thesis, when deposited in the University Library, being available for loan and photocopying.

Q. Yang

17 May 2007

ACKNOWLEDGEMENTS

The author wishes to express his sincere gratitude to his supervisors, Associate Professor M. Griffith, Dr. R. Seracino and Dr. S.H. Xia, for their guidance and advice throughout the course of this work. The author would also like to express the full thanks and appreciation to Dr. Craig Willis, the postdoctoral fellow of this school, for his valuable advice and suggestions that definitely enhanced the quality of this study.

Recognition must go to the laboratory and technical staff whose contributions made the experimental component of this project possible and the author is particularly grateful to G. Atkins, I. Cates, S. Huskinson and D. Hale.

Most importantly, the author thanks his family and friends for their ongoing support.

ABSTRACT

Unreinforced masonry (URM) structures comprise a significant proportion of the building stock in many countries worldwide, however they do not behave well under out-of-plane loading, such as that experienced during seismic events. Consequently, many existing masonry structures require some form of retrofit to comply with existing codes. Moreover, retrofit solutions of historical structures must also consider the impact on aesthetics. Hence, research is being directed to developing quick and efficient retrofitting techniques with negligible aesthetic impact.

As part of ongoing research at The University of Adelaide on the out-of-plane behaviour of URM walls, this study was carried out to develop and test innovative fibre reinforced polymer (FRP) strengthening techniques for retrofitting of masonry walls in order to sustain out-of-plane bending. Both externally bonded (EB) and near-surface mounted (NSM) techniques were applied. Twenty-seven push-pull tests were conducted to study the FRP-to-masonry bond behaviour with the variables including: masonry surface preparation; bonding agent of masonry bed joints; location of FRP strips; FRP materials; and, geometric properties. An FRP-to-masonry bond model was developed by modifying an existing FRP-to-concrete bond strength model. Four severely damaged URM full-scale walls (with window openings), previously tested under reversed-cyclic loading, were repaired with either glass FRP (GFRP) or carbon FRP (CFRP) EB vertical strips (3 walls) and CFRP NSM vertical strips (1 wall) and tested under two-way monotonic out-of-plane bending to quantify the increase in strength and ductility relative to the original and residual capacities of the URM walls. Air bags were used to apply lateral pressure onto the FRP strengthened URM wall specimens to simulate out-of-plane load induced by earthquakes. Based on these tests, a lower bound mechanics based analysis approach was developed to predict the failure mode and out-of-plane capacity of URM walls repaired with

adhesively bonded vertical strips.

It is anticipated that the results of this study will lead to the development of FRP strengthening techniques for URM structures in practical use, upgrading existing masonry buildings for seismic loading and also to extend their service life. The implementation of this innovative technique could have a significant economic impact in addition to the cultural and social impacts on conservation of the architectural heritage.

CONTENTS

DECLARATION	I
ACKNOWLEDGEMENTS	II
ABSTRACT	III
LIST OF FIGURES.....	VIII
LIST OF TABLES.....	XI
1. INTRODUCTION.....	1
1.1. BACKGOURND	1
1.2. SCOPE AND OBJECTIVES	2
1.3. THESIS OUTLINE.....	3
2. LITERATURE REVIEW.....	5
2.1. INTRODUCTION	5
2.2. BACKGROUND OF URM STRUCTURES.....	5
2.3. CONVENTIONAL METHODS FOR URM STRENGTHENING.....	7
2.4. FIBRE REINFORCED POLYMER (FRP).....	8
2.5. APPLICATION OF FRP.....	9
2.5.1. <i>FRP strengthening RC Beams</i>	9
2.5.2. <i>Application of FRP to URM Walls</i>	12
2.6. SUMMARY	17
3. EXPERIMENTAL PROGRAM – BOND TESTS.....	19
3.1. INTRODUCTION	19
3.2. BOND TEST PROGRAM	20
3.2.1. <i>Test Method</i>	20
3.2.2. <i>Material Properties</i>	21
3.2.3. <i>Specimen Design, Fabrication and Instrumentation</i>	28
3.2.4. <i>Test Set-up and Loading Procedure</i>	36
3.3. TEST RESULTS – EB GFRP	38

3.3.1.	<i>Test Summary</i>	38
3.3.2.	<i>Test Observation and Failure Modes</i>	39
3.3.3.	<i>Effects on Bond Strength</i>	43
3.4.	TEST RESULTS –NSM CFRP	46
3.4.1.	<i>Summary of NSM Test</i>	46
3.4.2.	<i>Test Observations and Failure Modes</i>	48
3.4.3.	<i>Effects on NSM Bond Strength</i>	51
3.5.	PUSH-PULL TEST RESULTS ANALYSIS	55
3.5.1.	<i>Push-pull Test Data Processing</i>	55
3.5.2.	<i>Load Transfer Mechanism</i>	58
3.6.	SUMMARY	65
4.	THEORETICAL MODELLING: BOND TESTS	67
4.1.	INTRODUCTION	67
4.2.	THEORETICAL MODELLING	67
4.2.1.	<i>Chen and Teng’s Bond Strength Model</i>	68
4.2.2.	<i>Seracino et al’s Generic Model</i>	70
4.2.3.	<i>Prediction and Comparison of Theoretical Models</i>	72
4.2.4.	<i>Modification of GFRP EB Masonry Model</i>	78
4.4.	CONCLUSIONS	79
5.	EXPERIMENTAL PROGRAM – FULL-SCALE WALLS	81
5.1.	INTRODUCTION	81
5.2.	FULL-SCALE WALL TEST PROGRAM	82
5.2.1.	<i>Masonry Wall Specimens</i>	82
5.2.2.	<i>Design for FRP Strengthening Schemes for Damaged Masonry Walls</i>	86
5.2.3.	<i>FRP Retrofitted Masonry Wall Test Set-up</i>	90
5.2.3.	<i>Instrumentations</i>	99
5.3.	EXPERIMENTAL RESULTS OF FULL-SCALE WALL TESTS	103
5.3.1.	<i>Overall Behaviour of FRP Retrofitted Masonry Wall</i>	103
5.3.2.	<i>Individual Behaviour of FRP Retrofitted Masonry Wall</i>	105

5.4.	CONCLUSIONS.....	121
6.	THEORETICAL MODELLING: RETROFITTED WALLS	124
6.1.	INTRODUCTION	124
6.2.	LATERAL RESISTANCE OF THE WALL UNDER BIAIXAL BEDNING.....	124
6.3.	ONE-WAY VERTICAL BENDING CAPACITY.....	125
6.4.	RIGID BODY DEFLECTION ANALYSIS.....	129
6.4.1.	<i>Observed Rigid Body Behaviour.....</i>	<i>129</i>
6.4.2.	<i>Wall Displacement at the FRP-Diagonal Crack Intersections</i>	<i>130</i>
6.4.3.	<i>Modelling of Wall Displacements.....</i>	<i>133</i>
6.4.4.	<i>Prediction for FRP Slip Crossing Crack Openings</i>	<i>137</i>
6.4.5.	<i>Prediction and Comparison for Wall Displacements.....</i>	<i>139</i>
6.5.	CONCLUSIONS.....	142
7.	CONCLUSIONS AND RECOMMENDATIONS	144
7.1.	SUMMARY AND CONCLUSIONS	144
7.2.	RECOMMENDATIONS FOR FURTHER RESEARCH.....	146
	NOTATIONS.....	148
	REFERENCES.....	151
	APPENDIX A: FRP RETROFITTED URM WALL TESTS DATABASE.....	157
	APPENDIX B: GFRP MATERIAL TEST RESULTS.....	163
	APPENDIX C: FRP TO MASONRY BOND TEST RESULTS.....	165
	APPENDIX D: DESIGN FOR FRP RETROFITTED WALL TESTS.....	192
	APPENDIX E: FRP RETROFITTED WALL TEST RESULTS	194

LIST OF FIGURES

FIGURE 2.1 DEBONDING FAILURE MODES OF FRP EB RC BEAMS.....	10
FIGURE 3.1 SCHEMATIC OF PUSH-PULL TEST SIMULATING IC DEBONDING.....	20
FIGURE 3.2 PUSH-PULL TEST SPECIMENS	21
FIGURE 3.3 MASONRY UNIT	22
FIGURE 3.4 MASONRY UNIT DIMENSIONS (NOMINAL, MM).....	22
FIGURE 3.5 GLASS FIBRE SHEET.....	24
FIGURE 3.6 MANUFACTURE OF GFRP STRIP.....	25
FIGURE 3.7 FAILURE MODE OF GFRP STRIPS IN TENSILE TESTS	26
FIGURE 3.8 ARRANGEMENT OF STRAIN GAUGES FOR EB PUSH-PULL TEST	31
FIGURE 3.9 CFRP NSM BOND TEST SPECIMENS.....	33
FIGURE 3.10 NSM CFRP POSITION (PLAN VIEW).....	33
FIGURE 3.11 PUSH-PULL TEST SPECIMEN SETUP	37
FIGURE 3.12 GFRP FULLY DEBONDING FAILURE (SPECIMEN GP-5-NE-Q-2).....	40
FIGURE 3.13 COMPARISON OF FULLY DEBONDING FAILURE.....	41
FIGURE 3.14 GFRP PARTIAL DEBONDING AND RUPTURE FAILURE.....	42
FIGURE 3.15 BRICK WEDGE AND CRACKING IN BRICK.....	43
FIGURE 3.16 COMPARISON OF MASONRY SURFACE PREPARATION METHODS.....	44
FIGURE 3.17 COMPARISON OF MORTAR AND QUICK DRYING PASTE	45
FIGURE 3.18 CRACKING OF NSM PUSH-PULL TEST	48
FIGURE 3.19 SLIDING FAILURE MODE (ST1.0-2-10-1/2).....	49
FIGURE 3.20 DEBONDING FAILURE OF CFRP NSM SPECIMEN (HO1.0-4-15-0-NSG).....	50
FIGURE 3.21 RUPTURE FAILURE OF NSM PUSH-PULL TEST SPECIMEN	50
FIGURE 3.22 EFFECT OF d_p ON NSM BOND STRENGTH	52
FIGURE 3.23 EFFECT OF FRP POSITION RELATIVE TO PERPEND JOINTS	53
FIGURE 3.24 SYMBOLS USED IN BOND ANALYSIS.....	56
FIGURE 3.25 SHEAR STRESS ANALYSIS FREE BODY DIAGRAM.....	57
FIGURE 3.26 STRAIN DISTRIBUTION IN FRP STRIP (GP-5-GR-Q).....	59

FIGURE 3.27 SHEAR STRESS DISTRIBUTION ALONG FRP STRIP (GP-5-GR-Q)	60
FIGURE 3.28 LOAD-DISPLACEMENT RESPONSE AT LOADED END (GP-5-GR-Q)	61
FIGURE 3.29 LOCAL SHEAR-SLIP RESPONSE AT VARIOUS POSITIONS (GP-5-GR-Q).....	62
FIGURE 3.30 IDEALISED BI-LINEAR BOND-SLIP MODEL.....	63
FIGURE 3.31 COMPARISON OF LOCAL BOND-SLIP MODELS	64
FIGURE 4.1 DEFINITION OF IC DEBONDING FAILURE PLANE (CROSS SECTION)	71
FIGURE 4.2 VALIDATION OF PREDICTION FOR GFRP/CFRP-EB MASONRY	74
FIGURE 4.3 VALIDATION OF PREDICTION FOR CFRP-NSM.....	78
FIGURE 5.1 MASONRY WALL SPECIMENS.....	82
FIGURE 5.2 LOAD-DISPLACEMENT BEHAVIOUR OF CONTROL WALLS.....	85
FIGURE 5.3 FRP STRIP DESIGN	87
FIGURE 5.4 DEFINITION OF WALL SUB-PANELS	89
FIGURE 5.5 SURFACE PREPARATION OF FRP EB WALL (WALL 1).....	91
FIGURE 5.6 GROOVES CUT IN MASONRY WALL (WALL 4).....	91
FIGURE 5.7 FRP EB ONTO THE MASONRY WALL.....	92
FIGURE 5.8 DAMAGED CONNECTION BETWEEN MAIN WALL AND RETURN WALL	94
FIGURE 5.9 WALL SUPPORT DETAILS	95
FIGURE 5.10 DETAILS OF PRECOMPRESSION ARRANGEMENT.....	97
FIGURE 5.11 OVERALL TEST ARRANGEMENT	98
FIGURE 5.12 LOAD CELL CONNECTIONS	99
FIGURE 5.13 LOAD CELL POSITIONING (VIEW FROM WALL OUTSIDE FACE)	100
FIGURE 5.14 ARRANGEMENT OF STRAIN GAUGES AND LVDTs	101
FIGURE 5.15 COMPARISON OF LOAD-DISPLACEMENT BEHAVIOUR FOR WALLS.....	104
FIGURE 5.16 LATERAL LOAD-DISPLACEMENT BEHAVIOUR FOR WALL 1	106
FIGURE 5.17 SCHEMATIC OF CRACKING PATTERN AND FRP DEBONDING OF WALL 1	107
FIGURE 5.18 SCHEMATIC OF THE PEELING DEBONDING FAILURE MODE FOR WALL 1	108
FIGURE 5.19 STRAIN DISTRIBUTION IN CARBON FRP STRIP V3 OF WALL 1.....	109
FIGURE 5.20 LATERAL LOAD-DISPLACEMENT BEHAVIOUR FOR WALL 2	110
FIGURE 5.21 SCHEMATIC OF CRACKING PATTERN AND WALL FAILURE OF WALL 2	111
FIGURE 5.22 PHOTO FOR CRACKING AND FAILURE PATTERNS OF WALL 2.....	112

FIGURE 5.23 STRAIN DISTRIBUTIONS IN GLASS FRP STRIP V3 AND V4 OF WALL 2.....	112
FIGURE 5.24 LATERAL LOAD-DISPLACEMENT BEHAVIOUR FOR WALL 3 (PHASE 3 EXCLUDED)	113
FIGURE 5.25 SCHEMATIC OF CRACKING PATTERN AND FRP DEBONDING OF WALL 3	114
FIGURE 5.26 PHOTOS FOR CRACKING AND FAILURE PATTERNS OF WALL 3.....	116
FIGURE 5.27 STRAIN DISTRIBUTIONS IN ALL FIVE GLASS FRP STRIPS OF WALL 3	117
FIGURE 5.28 HORIZONTAL DEFLECTION PROFILE OF WALL 3	117
FIGURE 5.29 LATERAL LOAD-DISPLACEMENT BEHAVIOUR FOR WALL 4	118
FIGURE 5.30 SCHEMATIC OF CRACKING PATTERN AND FRP DEBONDING OF WALL 4	119
FIGURE 5.31 PHOTOS FOR CRACKING AND FAILURE PATTERNS OF WALL 4.....	119
FIGURE 5.32 STRAIN DISTRIBUTIONS IN CARBON FRP STRIPS OF WALL 4	120
FIGURE 6.1 IC DEBONDING FAILURE OF FRP UNDER-REINFORCED URM WALL.....	127
FIGURE 6.2 ROTATION OF SUB-PANELS OF FRP STRENGTHENED URM WALL	130
FIGURE 6.3 CRACK LINES AND DEFLECTIONS OF FRP STRENGTHENED URM WALL	131
FIGURE 6.4 RIGID BODY REPRESENTATION OF A MEMBER WITH A SINGLE MIDSPAN CRACK ..	134
FIGURE 6.5 RIGID BODY REPRESENTATION OF A MEMBER WITH TWO CRACKS	134

LIST OF TABLES

TABLE 3.1 MASONRY MATERIAL PROPERTIES	23
TABLE 3.2 CARBON FRP MATERIAL PROPERTIES	23
TABLE 3.3 GFRP MATERIAL PROPERTIES	26
TABLE 3.4 ADHESIVE MATERIAL PROPERTIES.....	27
TABLE 3.5 GLASS FRP EB BOND TEST SPECIMEN DETAILS.....	30
TABLE 3.6 CFRP NSM BOND TEST SPECIMEN DETAILS	35
TABLE 3.7 SUMMARY OF EXPERIMENTAL RESULTS FOR GLASS FRP EB TESTS	39
TABLE 3.8 EFFECT OF MORTAR JOINTS ON BOND STRENGTH.....	45
TABLE 3.9 SUMMARY OF EXPERIMENTAL RESULTS FOR NSM TEST.....	47
TABLE 3.10 THE EFFECT OF STRIP POSITION RELATIVE TO BRICK CORES	54
TABLE 3.11 AVERAGE OF SHEAR-SLIP PARAMETERS FOR PUSH-PULL TEST SPECIMENS	64
TABLE 4.1 SUMMARY OF IC DEBONDING RESISTANCE PREDICTION FOR GFRP/CFRP-EB	75
TABLE 4.2 SUMMARY OF THEORETICAL PREDICTION FOR CFRP NSM IC DEBONDING RESISTANCE	77
TABLE 4.3 SUMMARY OF PREDICTION FOR GFRP-EB WITH MODIFIED MODELS	80
TABLE 5.1 MASONRY WALL CONFIGURATIONS IN PREVIOUS EXPERIMENTAL STUDY.....	83
TABLE 5.2 STRENGTHENING SCHEMES OF FRP RETROFITTING MASONRY WALL TEST.....	88
TABLE 5.3 RESULTS OF THE FRP RETROFITTED FULL-SCALE WALL TEST	103
TABLE 6.1 SUMMARY OF ONE-WAY VERTICAL BENDING CAPACITY PREDICTION	128
TABLE 6.2 WALL DISPLACEMENT AT FRP-DIAGONAL CRACK INTERSECTION	132
TABLE 6.3 UPPER BOUND PREDICTION FOR THE CRITICAL DISPLACEMENTS OF THE WALL....	140

1. INTRODUCTION

1.1. BACKGOURND

Unreinforced masonry (here after simply called masonry) walls are prone to failure when subjected to out-of-plane and in-plane loads induced by earthquakes, as masonry buildings have historically been designed with little or no regard for the effects of seismic loadings (Hendry et al.,1981). Many of these structures fail in out-of-plane bending due to the lack of reinforcement. Moreover, unreinforced masonry buildings have been identified as the main cause of loss of life in recent earthquakes (Ehsani et al., 1999). The upgrading of such structures has become a priority in the field of earthquake engineering (Gilstrap & Dolan, 1998).

Current methods of retrofitting masonry structures have proven to be effective, but have many drawbacks. These methods usually include the addition of framing elements such as steel columns, pilasters, beams, or surface treatments to increase the strength and ductility of the walls. Such procedures are often time consuming, costly, and add significant mass to the structure. Added to this is the possibility of corrosion which could adversely affect the bond strength, leading to failure of the strengthening system (Hollaway & Leeming, 1999).

To overcome some of the shortcomings of traditional retrofitting, it was proposed in the mid-1980s that fibre reinforced polymer (FRP) plates could prove advantageous over steel plates in strengthening applications (Meier, 1987a&b; Kaiser, 1989; Meier and Kaiser, 1991). Most of the existing research and development in the use of FRP for reinforcement, repair, strengthening and retrofitting was conducted for reinforced concrete applications, whereas the use of FRP for retrofitting of masonry walls is still

in a primary state. The existing investigations have not clearly considered the influence of certain factors affecting the shear strength at the FRP-to-masonry interface. Furthermore, there is no theoretical model developed to quantify the behaviour of the FRP-to-masonry bond interface. Most of the current FRP retrofitted masonry wall tests were carried out under one-way vertical bending. The major failure modes under one-way bending have been identified, for which simple theoretical modes were developed based on the cross section analysis method of beam theory. However, less research has been reported for strengthening of masonry walls that are subjected to biaxial bending, and there are currently no comprehensive design guidelines for FRP strengthening of masonry walls. Hence, there is an urgency to develop cost-effective, reliable and efficient retrofitting solutions for masonry walls that may be subjected to two-way bending.

1.2. SCOPE AND OBJECTIVES

The purpose of the proposed study was to investigate methods of enhancing the out-of-plane seismic resistance of masonry walls using FRP reinforcement. Although out-of-plane strengthening techniques may also enhance in-plane performance of masonry walls, the in-plane behaviour of strengthened walls is beyond the scope of this study. This investigation was expected to have a significant economic impact in addition to the cultural and social impact of conservation of masonry heritage buildings or seismic strengthening for post disaster infrastructure. This research program was intended to develop and test innovative rehabilitation techniques for existing masonry structures.

The overall aim of this research project was to firstly investigate and characterise the bond behaviour for FRP bonded to masonry, and secondly assess this technique for

enhancing out-of-plane strength of masonry walls through a series of experimental wall tests and analytical modelling.

The investigation considered both carbon FRP (CFRP) and glass FRP (GFRP) materials. Other specific objectives of the proposed research included:

- 1) experimental investigations of externally bonded (EB) and near surface mounted (NSM) FRP-masonry bond behaviour and the effectiveness of these two techniques to enhance the out-of-plane performance of existing masonry walls;
- 2) development of FRP-to-masonry bond strength models capable of predicting the ultimate bond strength and maximum strain in the FRP at the onset of debonding for both externally bonded and near surface mounted applications; and
- 3) development of a theoretical model capable of predicting the strength of retrofitted walls to be used as a basis for a design method.

It should be noted that while this research used FRP to “repair” previously tested walls, the technique is also considered to be applicable for the retrofit of existing undamaged masonry walls.

1.3. THESIS OUTLINE

In this introductory chapter, the background, scope of the research, and the specific objectives of this investigation are presented. The content of the following chapters are briefly described below:

Chapter 2 presents a review of the literature relevant to this thesis, the general background of the features of masonry structures, conventional masonry

strengthening methods and the advantages of FRP materials. A brief overview of findings from both experimental and analytical studies of FRP strengthened concrete beams, and the current status of the application to masonry walls were also provided.

Chapter 3 describes the experimental program of bond tests for externally bonded glass FRP and near surface mounted carbon FRP strips.

Chapter 4 presents a quantitative analysis of the FRP-to-masonry bond test results.

Chapter 5 describes the experimental program on four full-scale walls repaired with FRP strips.

Chapter 6 presents the theoretical modelling for FRP retrofitted masonry wall subjected to two-way bending. Based on the experimental observation from the full-scale wall tests, a lower bound mechanics based analysis approach was developed to predict the out-of-plane capacity of masonry walls retrofitted with adhesively bonded FRP vertical strips.

The thesis concludes in Chapter 7 with a summary of the findings of this research and recommendations for further research.

An FRP retrofitted masonry wall test database including the published tests subjected to one-way bending is reported in Appendix A. Appendix B and C summarise GFRP material test results and FRP to masonry bond test results, respectively. The design process of FRP reinforcement for damaged walls in this study and the test results of FRP repaired masonry full-scale wall are summarised in Appendix D and E, respectively.

2. LITERATURE REVIEW

2.1. INTRODUCTION

The literature reviewed here presents background related to masonry structures, the conventional methods of masonry strengthening, fundamental aspects of FRP, and the achievements of existing studies relating to this research. Since the scope of this research is limited to enhancing the out-of-plane flexural resistance of masonry walls, a review of the applications of FRP composites to masonry walls and their behaviour under out-of-plane loads has been provided.

2.2. BACKGROUND OF URM STRUCTURES

Masonry is one of the oldest construction materials, and for thousands of years it was the predominant building material. Masonry is not only one of the main structure components of existing buildings, but it may also be widely used in the future since masonry is a well proven building material possessing excellent properties in terms of appearance, durability, fire resistance and cost in comparison with alternatives. Masonry is commonly used in buildings for load bearing walls, for veneers attached to backup frames, for infill panels in framed construction, for piers and columns and even for freestanding walls in the form of parapets and fences. However, masonry structures are vulnerable to lateral loads such as those caused by earthquakes and high-speed winds (Griffith and Klopp, 1998). Under reversing cycles of seismic loading, the ductility of the masonry walls is also a critical problem. In order to restore the structural function of deficient masonry members and to increase the

resistance to earthquake loading, a retrofitting technique with low-impact on function and appearance of the building is of particular importance.

Generally, masonry is considered to have no tension strength, and for this reason the structural design concepts of old masonry buildings have taken into account this specific nature, often utilizing appropriate structural shapes and systems. As a consequence, a majority of heritage buildings are vulnerable to the forces induced by earthquakes. On the other hand, the degradation of materials, the variation of service loads involved in many cases and different cracking phenomena observed represent a high risk for the total stability of some masonry structures.

In Australia, masonry is one of the predominant building materials for residential apartment and small commercial buildings. For many years, a significant number of masonry buildings were designed without considering the earthquake loading, because earthquakes were seldom recorded in Australia (Griffith & Klopp, 1998). However, the damage caused by the 1989 Newcastle earthquake highlighted the potential vulnerability of URM to earthquake loading. A new Australian Standard for the determination of Earthquake Loading (AS1170.4, 1993) was introduced in 1993, making it mandatory for the first time in Australia to consider earthquake design and detailing for all structures. This provided an impetus for research in this area. Research on the earthquake capacity of existing masonry buildings in Australia was undertaken by Griffith and Klopp (1998). This research found that the most critical failure mechanism of the two to five storey masonry buildings investigated was a potential out-of-plane failure of the wall, particularly in the upper walls, in which the vertical compression stress due to gravity loads is the lowest and the horizontal acceleration due to the earthquake is the greatest. This also suggested that out-of-plane wall failure is likely induced by earthquake and severe wind load for veneer and infill masonry in framed construction higher than four to five storeys. In addition, masonry walls are frequently detailed to act as shear walls to transfer to ground lateral in-plane forces generated from earthquakes and wind.

In summary, the shortcomings of masonry buildings have led to a surge of interest in recent years in developing techniques for improving seismic behaviour of these structures. Strengthening of the masonry walls is urgent to those existing buildings, which do not meet the current earthquake design standards.

2.3. CONVENTIONAL METHODS FOR URM STRENGTHENING

Conventional retrofitting techniques can be classified according to the problem to be addressed: damage repair or structure upgrading (Deslauriers et al., 1997). For damage repair in the form of cracks, the following methods can be used: filling of cracks and voids by injecting epoxy or grout; stitching of large cracks and weak areas with metallic or brick elements. For strengthening or upgrading, the following procedures are available: grout injection of hollow masonry units with non-shrink Portland cement grout or epoxy grout to strengthen or stiffen the wall; construction of an additional wythe to increase the axial and flexural strength; post-tensioning of an existing construction; external reinforcement with steel plates; surface coating with reinforced cement paste or shotcrete, such as a welded mesh. Most of these methods have proven to be impractical, time and labour intensive, costly, add considerable mass which may modify the dynamic response characteristics (which means the earthquake-induced inertia forces may be increased), irreversibly affect the aesthetics and function of the structure, and cause significant impact on the occupants (Spyrakos & Vlassis, 2003). These problems may be overcome by using fibre reinforced polymer (FRP) reinforcement instead of the conventional methods. Recent field applications have demonstrated the feasibility of this procedure (Ehsani & Saadatmanesh, 1997).

2.4. FIBRE REINFORCED POLYMER (FRP)

The production of Fibre reinforced polymer (FRP) started in the 1940s, and it has been used in a variety of industries such as aerospace, automotive, shipbuilding, chemical processing, etc., for many years. Its application in civil engineering was very limited. However, their excellent properties make them an attractive material for structural applications. FRP is a composite material composed of matrix of polymeric material reinforced by unidirectional or multi-directional fibres, usually 3 to 5 microns in diameter, placed in a resin matrix, polymer, and hence stems the name “Fibre Reinforced Polymers”. For the special class of matrix materials utilized in structural engineering applications (i.e. the thermosetting polymers), the continuous fibre will usually be stiffer and stronger than the matrix. The resin matrix binds the fibres together, allows load transfer between fibres and it also protects the fibres from the environment. FRP is mechanically different from steel in a sense that it is anisotropic, linear-elastic and it is usually of higher strength with a lower modulus of elasticity than steel. FRP has desirable physical properties over steel, such as corrosion resistance, high strength-to-weight ratio, high fatigue resistance, and dimensional stability. FRP also has the disadvantages of susceptibility to moisture and chemicals, the loss of properties at high temperatures, as in the case of fire, and damage from Ultra-Violet light.

There has been a rapid growth in the application of advanced fibre-reinforced polymer (FRP) composites in construction around the world in terms of both research activity and practical implementation since the late 1990s (Shrive, 2006). Indeed, many have hailed FRP composites as a new generation of construction materials, following steel and concrete (Hamoush et al., 2002). The satisfactory performance of FRP materials experienced in different fields of civil engineering suggests the opportunity to also employ composites for the repair and/or strengthening of masonry structures. Presently, several types of FRP materials have been considered for repair and retrofit

of concrete and masonry structures, among them glass fibre-reinforced polymers “GFRP”, carbon fibre-reinforced polymers “CFRP”, and aramid fibre-reinforced polymers “AFRP”. The use of FRP, in the form of sheets, strips and rebars, presents several advantages with respect to traditional steel reinforcement:

- 1) the tailor-ability of composite materials allows reinforcement to be designed as a function of specific requirements, which leads to greater ease in site handling, thus reducing labour cost and interruptions to existing services;
- 2) the low weight of composites with respect to steel reduces the transport and installation costs, avoiding at the same time any increase of structural mass;
- 3) the durability of FRPs with regard to electrochemical corrosion reduces the maintenance costs.

On the other hand the lack of long experience and reliable design rules limits the wider use of these materials. Further experimental and theoretical investigations are needed and some key aspects (i.e. the bond between FRP-to-masonry and the stress transfer mechanism along the bond joint) are important to be studied. And the effectiveness of the technique both under service and ultimate load conditions also needs to be estimated.

2.5. APPLICATION OF FRP

2.5.1. FRP Strengthening of RC Beams

Over the last decade, external bonding of FRP plates has emerged as a popular method for strengthening existing reinforced concrete (RC). Past studies have shown that, for FRP plates externally bonded (EB) to RC structural members, there is a risk that plates will debond before their tensile capacity is reached. Debonding means that a plate is detached from the concrete surface along the FRP-to-concrete interface

(normally a few millimetres beneath the concrete) and no longer contributes to the strength of the member (Teng et al., 2002). It is also found that debonding is caused by the formation of stress concentrations in the plate ends and in the vicinity of shear and flexural cracks that intercept the plate. Three main mechanisms of debonding have been identified for plated RC beams: intermediate flexural crack induced (IC) interfacial debonding, critical diagonal crack (CDC) debonding, and plate end (PE) debonding, as shown in Figure 2.1.

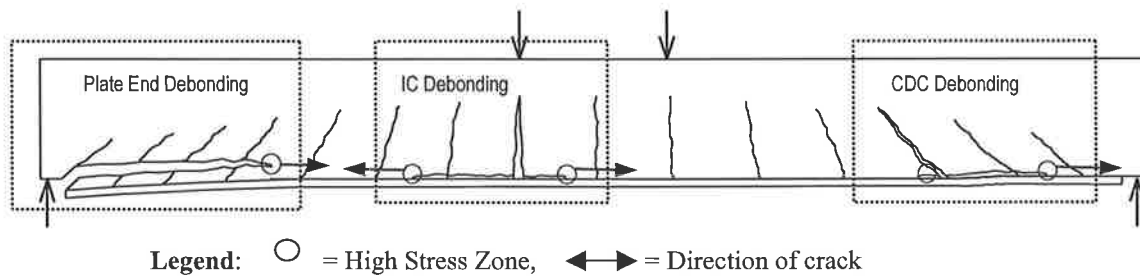


Figure 2.1 Debonding failure modes of FRP EB RC beams

The debonding failure mechanisms of retrofitted RC are generally well understood and research on this technique has reached a stage where a number of design guides (e.g. ACI 440.2R-02 2002, and Concrete Society TR No.55 2004) and books (e.g. Teng et al., 2002 and Oehlers & Seracino 2004) have been published.

Of the major forms of debonding recognised in RC structures retrofitted with adhesively bonded plates or sheets, IC debonding is considered to be the most important (Oehlers & Seracino, 2004) and it occurs when a crack in the RC section intercepts the plate, usually in the maximum moment region. The plate strain, or force P_{IC} , at which IC debonding occurs controls the increase in moment capacity and sectional ductility. The IC debonding strain is also required in the analysis of critical diagonal crack (CDC) debonding, which is considered to be the most common form of debonding (Oehlers & Seracino, 2004) in flexural members with longitudinal plates. In lieu of undertaking beam tests to quantify the IC debonding mechanism, it is well established that simple push-pull tests provide a lower bound to the IC debonding

plate strain in a flexural member (Teng et al., 2002 and Yuan et al., 2004). From push-pull tests, it is also possible to determine the fundamental property of such adhesively bonded joints, that is the interface shear stress – slip relationship (often referred to as the bond-slip model), which is analogous to a material's constitutive model. Teng et al. (2002) also developed a bond strength model based on fracture mechanics theory, which has been recently identified as the most accurate one to predict the IC debonding resistance of FRP externally bonded to reinforced concrete by Lu et al. (2005).

Although externally bonded reinforcement is effective in increasing the strength of concrete members (Oehlers & Seracino, 2004), there are a number of limitations associated with its use, including: low plate strains at debonding leading to inefficient use of reinforcement material and reduced sectional ductility such that moment redistribution is typically precluded (Oehlers et al., 2004); issues associated with adhering the reinforcement in negative moment regions due to floor finishes; exposure of large areas to the environment (in particular, UV and fire); susceptibility to damage and vandalism; and significant surface preparation of the concrete. These limitations with EB reinforcement restrict its use in many applications, particularly when moment redistribution is required. Therefore, a new retrofitting technique, near surface mounted (NSM), has emerged in recent year. It was found by Hassan & Rizkalla (2003) that the advantages of NSM strips over EB plates include: significantly higher axial plate strain at debonding, resulting in larger increases in moment capacity with less material and significantly less impact on sectional ductility; a very small exposed surface area; and typically reduced construction time as the groove suitable to accommodate the NSM strip and adhesive may be made with a single saw cut.

Recently, a generic analytical model was derived by Seracino et al. (2006) to determine the debonding resistance of any adhesively bonded plate-to-concrete joint using an idealized linear-softening local interface bond-slip relationship. The model is

derived using a unique definition of the debonding failure plane and confinement ratio such that it is suitable for both the external bonding and near surface mounting techniques. The model was also validated by comparison with existing bond test data as well as 14 new bond tests with varying FRP plate cross-section aspect ratios.

2.5.2. Application of FRP to URM Walls

Strengthening of RC and other structures using FRP composites has become very popular in the last few years. This has been due both to the needs for maintaining and upgrading essential infrastructure in all parts of the world, and many studies have been done in this subject area. In contrast, research on FRP retrofitted masonry walls is still in its infancy and not yet at the same level as that for reinforced concrete, which might hamper the application of FRP for strengthening masonry structures. However, the existing studies (Velazquez-Dimas & Ehsani, 2000; Gilstrap & Dolan, 1998) have confirmed, experimentally, the potential of adhesively bonded FRP in increasing the strength and reducing the overall structural deformation of masonry walls. An FRP retrofitted masonry wall test database including the published tests subjected to one-way bending is reported in Appendix A. A brief description of reviewed FRP retrofitted masonry tests are discussed in this section.

One-way flexural study of FRP retrofitted URM walls

Triantafillou (1998) conducted an experimental program including testing 12 small wall specimens strengthened with externally bonded FRP strips under one-way monotonic out-of-plane bending, in-plane bending and in-plane shear. It was found that when out-of-plane bending response dominates, which is typically in the case of upper levels of masonry structures (where axial loads are low), the increase in the

bending capacity is quite high. A systematic numerical analysis procedure was also presented for predicting short-term strength of masonry walls strengthened with externally bonded FRP strips.

Ehsani et al. (1999) presented a series of experimental results from three half-scale unreinforced brick walls retrofitted with vertical glass FRP composite strips. The specimens were subjected to cyclic out-of-plane loading. They investigated five reinforcement ratios and two different glass fabric composite densities. The mode of failure was found to be controlled by FRP rupture when wider and lighter FRP strips were used and by debonding when stronger ones were used. It was found that the tested specimens were capable of supporting a lateral load up to 32 times the weight of the wall. A deflection of as much as 2% of the wall height was measured. Although it was found that both URM walls and FRP strips behaved in a brittle manner, the combination resulted in a system capable of dissipating some energy. It was concluded that retrofitting URM walls with composite strips proved to be a good and reliable strengthening alternative.

Recent experimental studies have focused on making FRP retrofitting a viable alternative to conventional retrofitting techniques, and on the derivation of semi-empirical formulae to predict the response of FRP retrofitted masonry walls. The effect of varying FRP material and layout on the load carrying capacity and ductility of URM walls were investigated under one-way out-of-plane bending.

Velazquez-Dimas and Ehsani (2000) carried out a series of tests, including the testing of seven half-scale brick masonry walls externally strengthened with vertical glass-fabric composite strips, and subjected to static cyclic out-of-plane loading using air bags. The flexural behaviour of the tested specimens was characterized by three main stages corresponding to the first visible bed-joint crack, the first debonding, and the ultimate load. The main parameters investigated in this study were the amount of composite reinforcement, the height-to-thickness ratio h/t of the masonry wall, the tensile strain in FRP, and the mode of failure. The observed experimental results were

compared with the predicted values using the ultimate strength method and the linear elastic approach. Based on the trends observed in the experimental phase, it was concluded that the behaviour of the walls is best predicted with a linear elastic approach. The use of the ultimate strength approach was not recommended for estimating the flexural capacity of masonry walls retrofitted with composite materials because the ultimate strength method overestimated the flexural capacity and the ultimate deflection of the wall. Preliminary design recommendations were also proposed for tensile strain in the composite, maximum deflection, and maximum reinforcement ratio.

Hamoush et al. (2001) investigated the effectiveness of using FRP composite overlays to strengthen existing URM walls under one-way out-of-plane bending. A total of fifteen 1200 x 1800 x 200 mm concrete masonry wall specimens were tested. The first reinforcement configuration consisted of two layers of fibre-reinforced plastic webbing and the second consisted of vertical and horizontal bands of unidirectional fibre composites. Two methods of surface preparation were also evaluated: sand blasting, and wire brushing. A uniform pressure was applied to the wall specimens using an airbag. Failure loads, strains in the FRP, out-of-plane deformations and failure modes were recorded. It was found that the shear strength of the masonry wall had a major influence on the failure load of the system. Most of the tested wall specimens failed prematurely by shear debonding at the end connection between FRP overlay and masonry. Another source of premature debonding failure was entrapped air and faulty fabric that created stress concentrations. Not much difference in strength gain was observed between retrofitting by a continuous overlay on the entire wall specimen area and retrofitting by the unidirectional strips applied orthogonally. This suggests that covering the whole surface area does not necessarily yield the highest gain. Both sand blasting and manual steel brushing produced sufficient bond at the interface between the FRP overlay and the masonry. Cross section analysis method based on the beam theory was used to predict the flexural capacity of the strengthened wall under one-way vertical bending and the depth of neutral axis was suggested to be less than the masonry unit shell thickness.

Hamilton and Dolan (2001) performed a series of tests on unreinforced concrete masonry walls strengthened with vertical externally bonded glass FRP strips under one-way bending. The objective of their research work was to develop a general approach to provide design guidelines to strengthen concrete masonry walls with FRP. In their study, retrofitted masonry wall systems were tested for flexure under out-of-plane static loading. Debonding failure mode was observed in the tests, which was similar to the IC debonding observed in FRP strengthened RC beam tests. General flexural strength design equations derived from the cross section analysis method were presented and compared with the results of the testing conducted. It was found that the equations over-predicted the actual capacity of the test specimens by no more than 20%. The test results also indicated that the flexural strength of FRP retrofitted masonry systems is controlled by either the fracture of the FRP, shear or tension in the masonry, or by FRP debonding. They also mentioned that the predictions given only account for the flexural strength limit state and do not address other possible failure modes.

Kuzik et al. (2003) carried out a full-scale test program consisting of eight masonry walls retrofitted with vertical externally bonded glass FRP strips subjected to cyclic loading to investigate the out-of-plane flexural behaviour of retrofitted concrete block masonry walls under one-way bending. It was found that the amount of glass FRP sheets, along with compression strength of the masonry, significantly affected the flexural behaviour of the retrofitted URM walls, and walls with small cracks under successive out-of-plane loading cycles could still maintain their integrity. A simple method to predict the overall moment-deflection response of FRP retrofitted walls was presented. However, the ultimate FRP strain was derived from regression analysis of test data with the only variable being the amount of FRP.

Tan and Patoary (2004) summarised the simple theoretical models derived from beam theory corresponding to four failure modes including: punching shear through the

bricks, crushing of brick in compression, tensile rupture of the FRP reinforcement, and debonding of FRP reinforcement at the interface. The moment capacity for the retrofitted masonry wall was derived based on strain compatibility. The parabolic stress-strain relation for masonry brick was assumed for flexural compression failure or FRP rupture failure modes. For FRP debonding failure mode, elastic behaviour was assumed for masonry brick and it was found that a triangular stress block could be applied for stress distribution in masonry. FRP debonding failure mode was also recommended for design purpose, because of its ductile failure behaviour compared with the brittle behaviour of other failure modes.

Two-way flexural study

There were no published studies for FRP retrofitted masonry wall under two-way bending until recently a series of tests have been carried out in McMaster University by Ghobarah and Galal (2004) to investigate the out-of-plane behaviour of reinforced walls under biaxial bending. More recently, FRP NSM technique for retrofitting masonry wall also emerged. And a theoretical model was also developed by Korany et al. (2005) based on virtual work to predict the behaviour of FRP NSM masonry walls subjected to biaxial bending.

Ghobarah and Galal (2004) conducted an experimental program on FRP strengthening of cracked walls under two-way bending to investigate the performance of enhancement when strengthening walls with openings under four-side simply supported condition. Five full-scale masonry block walls with different opening configurations, which had been previously tested to failure, were strengthened by 50 mm carbon FRP strips spacing at 1.2 m with anchorage at both ends. These walls were tested under cyclic out-of-plane loading using an airbag. Failures were found to be along the mortar joints and in concrete blocks near the carbon strips. The lateral

load carrying capacity of the strengthened walls was found to be significantly higher than that of the unstrengthened walls. Based on the test results, it was concluded that the proposed strengthening system increased the ductility of the walls by approximately 10-fold compared to the unstrengthened walls and proper anchoring of the ends of the carbon FRP strips was found to be important in preventing debonding of the carbon FRP strips from the concrete blocks. Moreover, anchored carbon FRP strips restrained the broken blocks from collapse at failure of the wall.

Korany et al. (2005) conducted a series of test on near surface mounted carbon FRP cable retrofitted masonry walls under two-way bending. Using this innovative FRP retrofitting technique, unbonded and intermittently bonded FRP cables were used to produce higher rotations and, consequently, large displacements for increasing their ability to absorb seismic energy. Both vertical and horizontal carbon FRP cables were used and the test variables included masonry wall support conditions (three-side and four-side simply supported), spacing of carbon FRP cables and openings. The test results showed that a significant increase in flexural capacity and ductility was achieved. Carbon FRP debonding and rupture failure were observed. It was also found that the crack lines of retrofitted wall were similar to the typical cracking patterns of original wall. An analytical model was developed based on the virtual work theory by equating the internal work done by resisting moments to the external work done by the applied pressure. The model was also validated by the experimental results. And a simplified design methodology for calculating the capacity of this type of FRP retrofitted masonry wall panel under out-of-plane pressure was also presented.

2.6. SUMMARY

It was shown that FRP-strengthening techniques appear to provide a simple, efficient and effective method for masonry walls. These published studies have been

invaluable in establishing the direction for further research on FRP retrofitting masonry walls.

The literature reviewed in this chapter suggested that although the more conventional failure modes, including masonry crushing or FRP rupture, may control the flexural strength/ductility of FRP retrofitted masonry walls, the debonding mechanisms of externally bonded FRP often governs failure. The challenge is to better understand the potential failure modes, which are generally directly related to the interfacial behaviour between the FRP composite and the masonry in masonry walls. It is crucial to identify and quantify the debonding mechanisms for both external bonding and near surface mounting techniques as debonding typically occurs prior to obtaining the theoretical ultimate flexural or shear capacity of the wall.

The cross section analysis method based on beam theory has been demonstrated to be valid to predict the capacity of FRP retrofitted masonry walls under one-way bending corresponding to the failure modes. However, the strain parameter of FRP at debonding failure used to predict the retrofitted wall bending capacity was derived from the experimental data or an empirical value. There is no published bond model to quantify the externally bonded or near surface mounted FRP to masonry bond behaviour.

Most of the FRP retrofitted wall tests were conducted under one-way bending. As the two-way bending condition is very common in practice, more tests need to be carried out to study the two-way flexural behaviour of retrofitted masonry walls. Theoretical models also need to be developed and validated.

3. EXPERIMENTAL PROGRAM – BOND TESTS

3.1. INTRODUCTION

As mentioned in the literature review, the FRP-to-concrete bond behaviour has been widely studied in recent decades, whereas there has been less research on FRP-to-masonry bond behaviour. This experimental program was focused on the bond behaviour of glass FRP strips externally bonded (EB) to brick masonry and carbon FRP strips near surface mounted (NSM) to brick masonry. The bond tests in this program were only used to simulate the behaviour of intermediate crack induced debonding (IC debonding) as shown in Figure 3.1.

Carbon FRP has been widely used in previous FRP externally bonded masonry wall tests due to its higher Young's Modulus and tensile strength compared to glass FRP. However, it was found that the usable strain of carbon FRP was quite low, compared with its rupture strain (Tran, 2004). Considering the efficient use of FRP material, glass FRP strips were used in the externally bonded tests in this research, while carbon FRP strips were used in the near surface mounted tests.

In addition to quantifying the bond-slip behaviour and IC debonding load P_{IC} (refer Figure 3.1 (b)), other parameters that were considered include:

- the effect of the masonry surface preparation method for the externally bonded strengthening technique;
- the different bond methods of glass FRP fibre;
- the effect of the masonry mortar joint on bond strength;
- the effect of NSM strip bond dimensions; and,
- the different bond positions for NSM FRP strip.

To achieve these aims, 12 externally bonded tests and 15 near surface mounted tests

were performed in the Chapman Laboratory of the School of Civil and Environmental Engineering, University of Adelaide.

3.2. BOND TEST PROGRAM

3.2.1. Test Method

Various experimental set-ups have been used for simulating IC debonding and exploring the FRP-to-concrete bond behaviour. Existing bond test set-ups have been classified into the following types (Chen et al., 2001): double shear pull tests, double shear push tests, single shear pull tests, single shear push tests, and beam (or bending) tests. Double shear pull tests and single shear push tests have been the most popular test methods due to their simplicity (Chen et al., 2001). In this research program, single shear push test, also normally termed push-pull test, was used to simulate IC debonding and to investigate the FRP-to-masonry bond behaviour. As shown in Figure 3.1 (a), a masonry wall panel in one-way vertical bending with FRP strips strengthened at the tension side can be expected to undergo debonding failure at an intermediate flexural crack between the mortar and masonry unit. Figure 3.1 (b) shows how the push-pull test method simulates the IC debonding mechanism. The ultimate debonding resistance is denoted by P_{IC} .

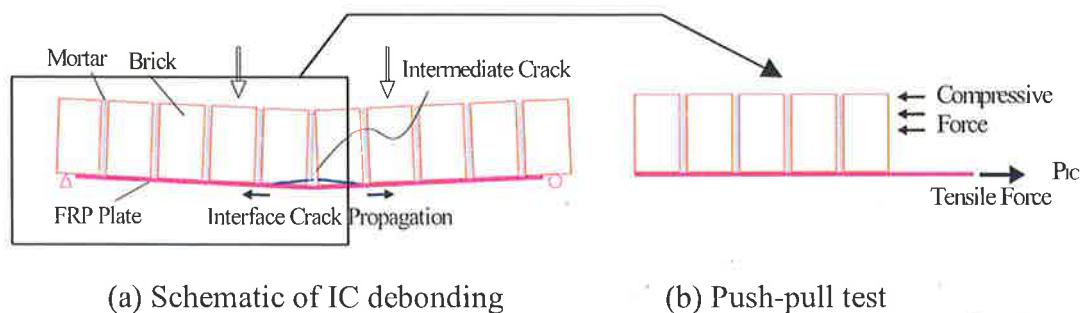


Figure 3.1 Schematic of push-pull test simulating IC debonding

A five brick high short-stack masonry prism was used for each push-pull test. After

the masonry surface preparation, an FRP strip was then mounted to the masonry prism with a series of strain gauges attached along its surface. The test specimen was subsequently placed on a test machine with a tensile force applied onto the loaded end of FRP strip and a compressive force applied by the reaction from a steel restraint plate onto the top surface of the masonry prism to simulate the situation of IC debonding (Figure 3.2). Load was applied to the FRP strip until it debonded from the masonry prism. The tensile force and strains along the FRP were recorded throughout each test.

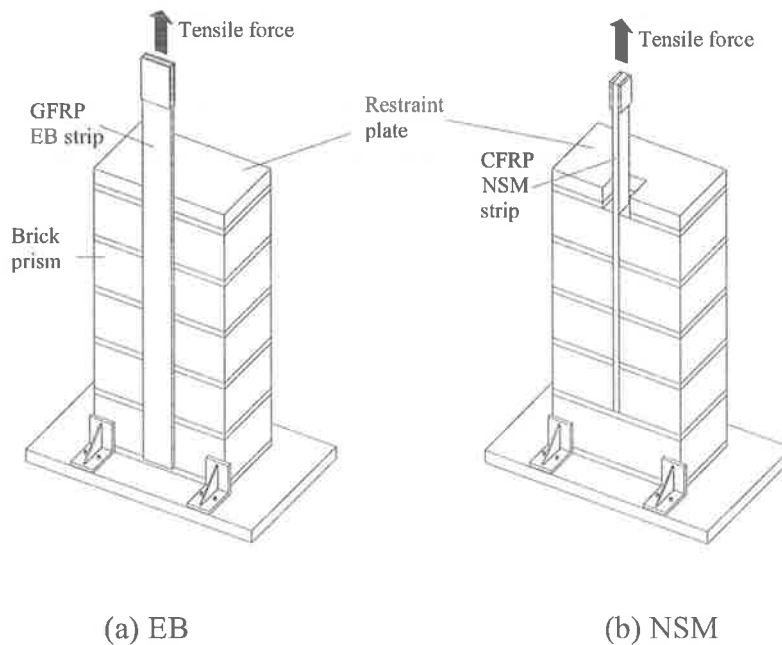


Figure 3.2 Push-pull test specimens

3.2.2. Material Properties

Masonry

As subsequent experiments in this research program utilised cracked masonry wall specimens leftover from previous research work (Griffith and Vaculik, 2005), the

push-pull test program employed the same brick units and mortar mix ratio as those of the wall specimens to ensure material consistency in the whole research project.

The masonry units used were standard clay brick units, manufactured by Hallet Brick Pty Ltd., with nominal dimensions of 230 x 110 x 76 mm. The specifications were 10-hole (two rows of five cores), exterior plain colonial red clay bricks as shown in Figure 3.3. The nominal dimensions of this masonry unit are shown in Figure 3.4.

The mortar used to bond the masonry units was made from a mix of air-dried sand with an 8.2% clay content, lime and Portland cement. These were mixed in the proportions of 1:2:9 for the cement, lime and sand respectively. All mortar joints were specified to a standard thickness of 10 mm (± 1 mm).



Figure 3.3 Masonry unit

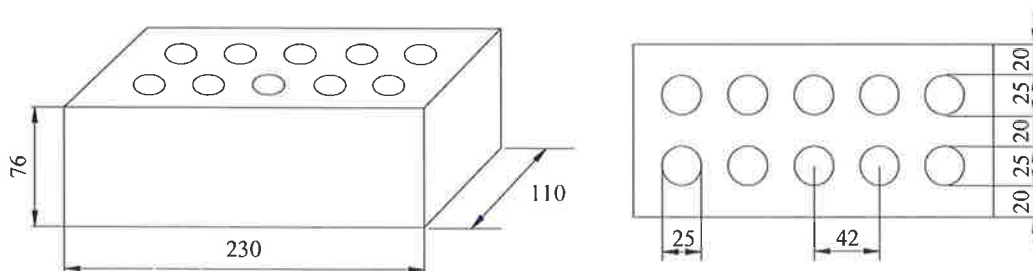


Figure 3.4 Masonry unit dimensions (nominal, mm)

As the masonry units and mortar used in this research were identical to the previous test (Griffith and Vaculik, 2005), the material properties of interest to this study are

quoted from the experimental data in the research work of Griffith and Vaculik as shown in Table 3.1.

Table 3.1 Masonry material properties

Compressive strength of masonry, f_{mc}	16 MPa
Young's modulus of masonry, E_m	3539 MPa
Lateral modulus of rupture of the brick unit, f_{ut}	3.55 MPa

Carbon FRP

The reinforcing strips used in all near surface mounted push-pull tests were a pultruded carbon fibre strip supplied by MBT (Australia) Pty Ltd. The carbon FRP came in sheets of 1.2 mm thickness and was carefully cut to the widths of 10 mm, 15 mm and 20 mm using a guillotine. Although typical performance data was supplied by the manufacturer, experimental data, produced by Ing et al. (2004) for the same carbon FRP sheets, was quoted for the material properties as shown in Table 3.2. Their material tests were carried out on strip of widths of 10 mm and 20 mm. The average value was found to be comparable with the manufacturer data.

Table 3.2 Carbon FRP material properties

Data Source	Nominal dimensions	Young's modulus	Rupture strain	Rupture stress
	$t_p \times b_p$	E_p	ϵ_{ult}	f_t
	(mm)	(GPa)	($\mu\epsilon$)	(MPa)
Manufacturer	1.2 x 50	160	14000	2700
Ing's test data (2004)	1.2 x 10	157.7	16300	2802
	1.2 x 20	165.2	17200	2796
	Average	161.5	16750	2799

Glass FRP

The MBrace unidirectional glass sheet (S&P G-sheet 90/10) and MBrace solvent free epoxy resin, supplied by MBT (Australia) Pty Limited, were used. Two types of glass sheet bonding method were applied in this bond test to compare the bond effect and ease of application. The first method, ‘dry lay-up’, involves applying a layer of primer on the masonry bonding surface, cutting a glass sheet into two 50 mm strips and bonding the dry glass strip directly onto the masonry surface layer by a layer coated with saturant. The second method, ‘plate bonding’, involves prefabricating a 50 mm wide glass FRP strip containing two layers of glass sheet and adhesively bonding to masonry in a similar manner to which a pultruded FRP strip is bonded. Full application guidelines may be obtained from FRP manufactures. The material properties provided by the manufacturer are summarised in Table 3.3. For the prefabricated glass FRP strips, a series of material tests were conducted to obtain the material properties.

To prefabricate a glass FRP strip, a glass fibre sheet was first cut into 50 mm strips as shown in Figure 3.5. The two glass FRP sheets were then constructed using epoxy resin to form a nominal 2 mm thick strip. This thickness was determined to ensure that rupture of the strip was avoided during tests, and that debonding failure would occur. However, this was also dependent on the strength of the adhesive and bond effect along the FRP-masonry bonding interface.



(a) A roll of glass fibre sheet

(b) 50 mm glass fibre sheet

Figure 3.5 Glass fibre sheet

The glass FRP strips were constructed in a mould composed of a plywood base covered with a plastic sheet and a pair of parallel 2 mm thick aluminium plates fixed on either side of the plywood base to create a channel of the required width. Figure 3.6 depicts the manufacturing process of the glass FRP composite. After laying-up the glass sheets, weight was applied on the aluminium plates covered with another plastic sheet to ensure an even strip thickness and smooth surfaces as well. The glass FRP strip was sufficiently cured and stripped off the mould after 24 hours. However, seven days of curing was allowed prior to testing.

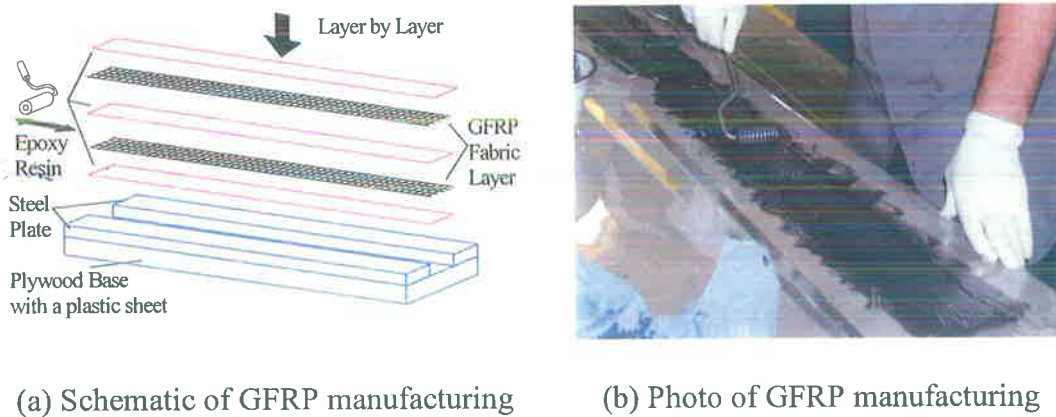


Figure 3.6 Manufacture of GFRP strip

Accurate material properties are essential to this study for use in analytical studies of the glass FRP bond behaviour. Glass FRP tensile tests were employed to determine the Young's modulus, rupture strain and stress. Three coupons of prefabricated glass FRP strips with dimensions of 50 mm x 350 mm were constructed for this tensile test. They were bonded with aluminium tabs, 50 mm x 50 mm, at both ends to ease the clamping and distribute the tensile force evenly through the glass FRP strips. Strain gauges were attached at the centre of the coupons on both sides of each strip. During the tensile tests, the first coupon failed in the aluminium tabs. This specimen was fixed by cutting the faulty end off and bonding a new pair of aluminium tabs, and then retested to glass FRP rupture failure. The rupture failure mode is shown in Figure 3.7. The tensile test results can be found in Appendix B.

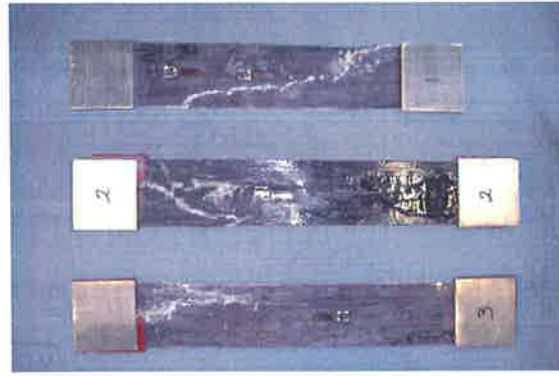


Figure 3.7 Failure mode of GFRP strips in tensile tests

The glass FRP prefabricated material properties were obtained based on the tensile test results and are summarised in Table 3.3. The average of rupture strain was found to be approximately 11500 microstrain. The experimental values for Young's modulus and strength of the GFPR strip are 19.3 MPa and 223 MPa, respectively.

Table 3.3 GFRP material properties

Data Source	Material	Nominal dimensions	Young's modulus	Axial rigidity	Rupture strain	Rupture stress
		$t_p \times b_p$	E	EA	ϵ_{ult}	f_t
		(mm ²)	(GPa)	(GPamm ²)	($\mu\epsilon$)	(MPa)
Manufacturer	Glass fibre only (two layers)	0.616 x 50	73	2248	45000	2700
Test data	Prefabricated glass strip	2.0 x 50	19.3	1930	11500	222

Note: the prefabricated glass strip includes two-layer glass fibre sheet.

If the properties of glass sheet are known, the Young's modulus of glass FRP strip can be estimated by the Eq. 3-1 (Gilstrap & Dolan 1998).

$$E_p = E_f V_f + E_m (1 - V_f) \quad \text{Eq. 3-1}$$

where: E_p , E_f and E_m represent the Young's modulus of FRP strip, fibre and epoxy resin, respectively, and; V_f is the volume fraction of fibre in the FRP strip.

In this case, E_f and E_m are equal to 73 MPa and 3.0 MPa, respectively. The thickness of two layers of glass fibre sheet is 0.616 mm. Thus, the volume fraction of fibre in the composite V_f is 30.8%. Therefore, the theoretical Young's modulus of this glass FRP strip calculated from Eq. 3-1 is 24.5 MPa. This theoretical Young's modulus is approximately 25% higher than the experimental result. However, it can be used as a rough estimate prior to design the nominal thickness of a prefabricated FRP strip.

FRP Bonding Adhesive

The adhesive is one of the key components in the FRP to masonry bond, as it is the interfacial medium through which stress transfers from the FRP strip to the masonry. An epoxy adhesive (MBrace Laminate Adhesive) was used for bonding the FRP to the masonry. The material properties of the adhesive are quoted from the experimental data in the research work of Lee et al. (2005) as shown in Table 3.4.

Table 3.4 Adhesive material properties

Property	MBrace Laminate Adhesive
Tensile strength	13.9 MPa
Young's modulus	6697 MPa
Poisson's ratio	0.312

3.2.3. Specimen Design, Fabrication and Instrumentation

GFRP EB Masonry Push-Pull Test

(1) Specimen Design

Twelve specimens were designed for externally bonded push-pull tests to consider three variables:

1) The glass FRP bonding techniques:

Two different glass FRP bonding techniques were discussed in Section 3.2.2. Ten specimens were attached with prefabricated glass FRP strips, while glass fibre sheets were attached using ‘dry lay-up’ method for the other two specimens.

2) Masonry surface preparation methods:

The consideration of varying the surface preparation in this program was to seek the most effective and practical preparation technique. Three different surface preparation methods (i.e. needle gun, sander and grinder) were compared. These were believed to be able to remove any oils/grease and glazing from the masonry surface layer and might well be adequate in providing a bondable surface and minimising the possibility of premature debonding. The most effective and efficient method was determined by evaluating the results of the push-pull test (i.e. bond behaviour, failure mode, ultimate load). Two specimens were designed as reference specimens without any masonry surface preparations. In order to reduce the impact of surface preparation onto the strength of masonry prism itself and prevent damaging the mortar joints by lateral forces when they were prepared using the three techniques, the masonry prisms were clamped in the direction normal to the bed joint.

3) Mortar substitutes:

Common mortar and quick drying paste were compared to determine the effect of the mortar joint on the FRP-to-masonry bond strength. The other concern was the

problem associated with constructing the stacks with mortar requiring at least 28 days curing time. If a quick drying agent could be shown to have little to no effect on the bond behaviour, this would significantly ease time constraints in future. Dental paste was used as quick drying paste.

Table 3.5 gives the details of 12 externally bonded push-pull test specimens. A five-part code, 'FB- L_b -SP-J-N' was used to identify the specimens. The first part of the code, 'FB', identifies the FRP material ('G' for glass FRP, and 'C' for carbon FRP) and bonding method ('P' for prefabricated strip bonding and 'D' for dry lay-up method). The next part ' L_b ' refers to the FRP bond length, which is denoted by the numbers of bricks, bonded with the FRP strip. The third part 'SP' identifies the masonry surface preparation methods, using 'NG' for needle gun, 'Sa' for sander, 'Gr' for grinder, and 'Re' for reference specimens without any surface preparations. The fourth part 'J' identifies the masonry bed joint material, 'M' for mortar and 'Q' for quick drying paste. The last part refers to the number of repetitions of the test with the same layout. For example, 'GD-5-Sa-Q-2' denotes the second specimen constructed using quick drying paste, prepared by sanding, bonded to length of five bricks, with glass FRP strip using dry lay-up method.

(2) Fabrication of Specimens

The fabrication of the specimen generally included the preparation of the masonry surface, the gluing of the glass FRP strip to the masonry prism and cleaning up the excess adhesive around the bonding area. Of the three-step procedure, the first consisted of the following process:

- 1) clamping the masonry prism in the direction perpendicular to the bed joints and lying the prism horizontally on a work table for surface preparation;
- 2) marking the bonding location on each specimen and preparing the surface with the designated preparation tool, particularly noting that the bonding area must be as even as possible, especially along the bond length, to prevent the development of peeling stresses between the interface during testing; and,

- 3) vacuuming the prepared surface and cleaning the bonding surface of both the masonry prism and glass FRP composite strip with acetone prior to bonding.

Table 3.5 Glass FRP EB bond test specimen details

Specimen	Masonry Prism Construction		Masonry Prism Dimensions		GFRP Bond length	GFRP Strip Dimensions	
	Bonding Agent	Surface Preparation	b_m (mm)	L_m (mm)		L_b (mm)	b_p (mm)
GP-5-Ne-M-1	Mortar	Needle Gun	230	420	420	50	2.0
GP-5-Ne-Q-1	QDP	Needle Gun	230	395	395	50	2.0
GP-5-Ne-M-2	Mortar	Needle Gun	230	419	419	50	2.0
GP-5-Ne-Q-2	QDP	Needle Gun	230	396	396	50	2.0
GP-5-Sa-M	Mortar	Sander	230	416	416	50	2.0
GP-5-Sa-Q	QDP	Sander	230	394	394	50	2.0
GP-5-Gr-M	Mortar	Grinder	230	423	423	50	2.0
GP-5-Gr-Q	QDP	Grinder	230	393	393	50	2.0
GP-5-Re-M	Mortar	No	230	410	410	50	2.0
GP-5-Re-Q	QDP	No	230	393	393	50	2.0
GD-5-Sa-Q-1	Mortar	Sander	230	386	386	50	2.0
GD-5-Sa-Q-2	QDP	Sander	230	386	386	50	2.0

The prism was then covered with plastic sticking tape at either edge of the bonding area to ease the clean up of the excess adhesive. The MBrace Laminate Adhesive was then applied to the marked area of masonry prism using a paintbrush.

The glass FRP strip was subsequently placed on the proper location, which was coated with the adhesive. The top surface was subsequently rolled using a metal roller in order to impregnate properly the glass FRP strip with adhesive and then a uniformly distributed load was exerted on the glass FRP strip using a plywood batten, clamped at both ends. The excess adhesive was cleaned up and the finished specimen was left at room temperature to cure for at least seven days before testing. The

specimen ‘GP-5-Re-M’ was found to contain only one layer of glass fabric due to an error during manufacture.

Finally, it is emphasised that the adhesive, which consisted of two components, should be mixed together properly as per the supplier’s instruction. If not, premature failure could occur by debonding along the adhesive-to-masonry or adhesive-to-FRP interface.

(3) Instrumentation

Strain gauges were used to measure strains along the centreline of the glass FRP strip. Eleven strain gauges of 10 mm gauge length were attached to the surface of glass FRP strip for each specimen. Among the eleven strain gauges, two gauges were attached on both sides of the glass FRP strip out of the bonded area, 90 mm away from the masonry prism top edge of the prism. This provided information on the alignment of the glass FRP strip during testing and allowed the elastic modulus of the glass FRP strip to be determined. The other nine gauges were glued 20 mm away from each brick edge within the bonded length as shown in Figure 3.8, to measure the strain profile along the glass FRP strip.

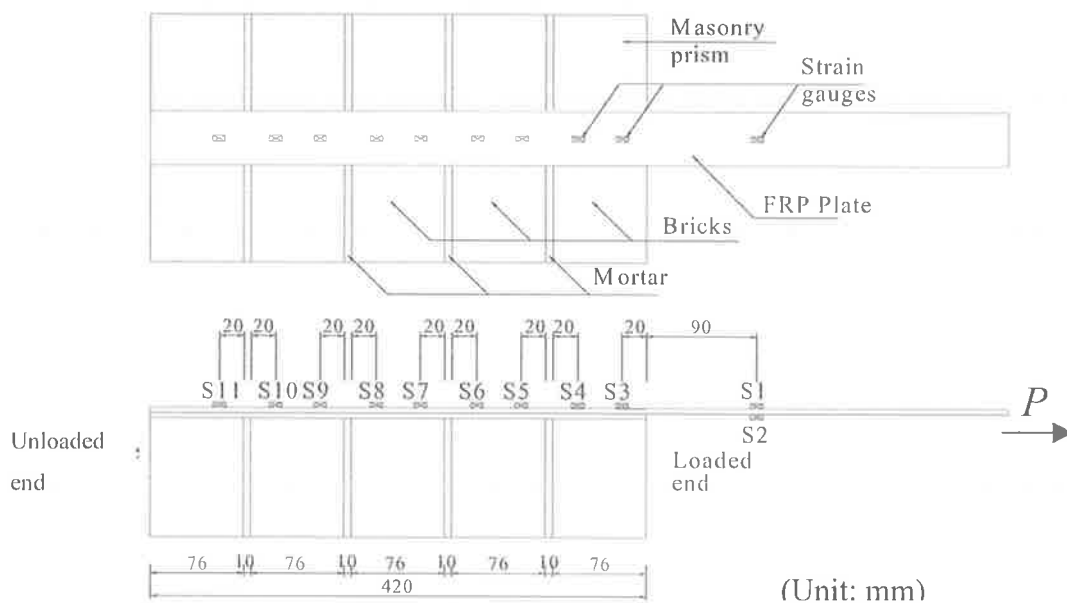


Figure 3.8 Arrangement of strain gauges for EB push-pull test

CFRP NSM Masonry Push-pull Test

(1) Specimen Design

NSM push-pull tests used fifteen specimens mounted with pultruded carbon FRP strips. Three variables were considered:

1) FRP strip bond dimensions:

The CFRP strip bond dimensions (i.e. embedment depth, b_p , and bond length, L_b , refer Figure 3.9) were varied to study the effect of bond dimensions on bond strength. The bond length L_b is denoted by the number of bricks bonded with a FRP strip, which varied from one to five. Three embedment depths, 10 mm, 15 mm and 20 mm were used, which was equivalent to the width of each FRP strip, as the edge of the strip was aligned with the brick prism edge.

2) Masonry prism types:

Three types of masonry prism were designed to vary the configuration of masonry as shown in Figure 3.9. The five rows high brick prism was designated to be sufficient for the required CFRP bond length and manageable for material handling. Considering the practical use of this technique, half overlap stretcher bonded masonry, which is commonly used in building construction, was employed. ‘HO1.5’ and ‘HO1.0’ denote half overlap stretcher bonded masonry prisms that were 1.5 and 1.0 brick long, respectively. Simple stacked brick prism was also used for comparison, represented by ‘St1.0’.

3) FRP strip location relative to both perpend joint and brick cores:

Various FRP strip positions were considered to investigate the impact of perpend joint and brick cores on the FRP-to-masonry bond strength. Firstly, the FRP strip position relative to the perpend joint was varied. Four different distances away from the perpend joint were considered including 0, 1/2, 1/4, and 1/6 brick length as shown in Figure 3.10 (a). ‘0’ represents the FRP strip in the perpend joint, used only in HO1.0 prism type (refer Figure 3.9 (b)). ‘1/2’ brick length away from perpend joint was applied only in St1.0 prism type (refer Figure 3.9 (c)). ‘1/4’ and ‘1/6’ brick length away from perpend joint was used in HO1.5 prism type and the

latter was specially designed to model the 1/3 overlap stretcher bonded masonry (refer Figure 3.9 (a)). Another factor that may influence the strip bond strength is the proximity of the strip end to the edge of the brick cores. This was investigated by applying a 20 mm d_p CFRP strip in two different positions relative to the cores: directly at the core, and between two adjacent cores (in the web) as shown in Figure 3.10 (b). The plan view clearly shows the difference of brick confinement to FRP strips. When the 20 mm strip is located at the core, the strip then reaches the edge of core and there is almost no brick confinement at the inner edge along the strip. In the case of strip between cores, the influence of cores is proposed to be smaller and the effect of brick confinement is greater than that of strip into core.

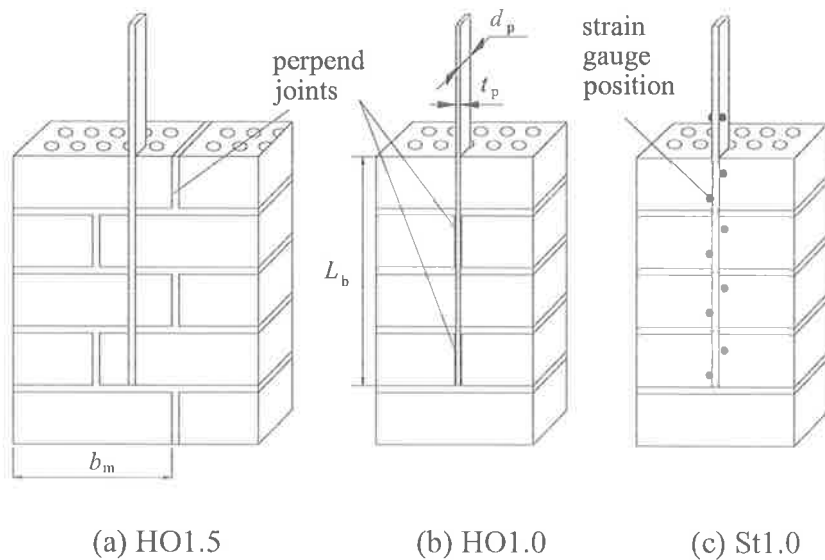


Figure 3.9 CFRP NSM bond test specimens

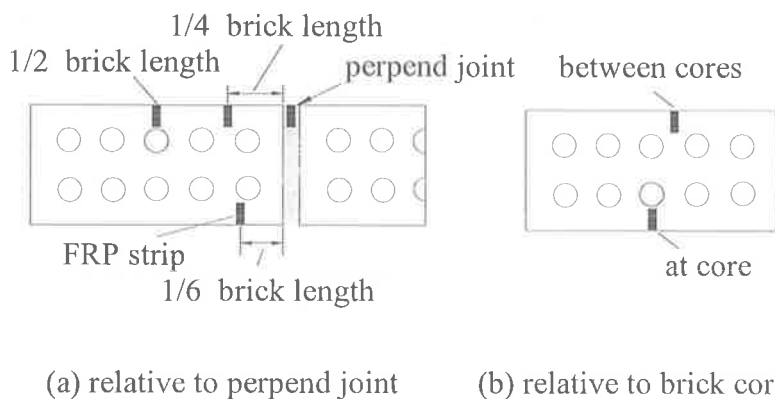


Figure 3.10 NSM CFRP position (Plan view)

4) Strain gauges in bond zone:

Due to the different orientation of the NSM strips compared to the EB strips, it was necessary to attach the strain gauges along the FRP strip prior to bonding to the masonry prisms. As the strain gauges reduce the bonded area, four specimens were prepared without any strain gauges to investigate the impact that the strain gauges had on the maximum load.

Table 3.6 gives the details of all fifteen FRP NSM bond test specimens. A five-part code, 'PT- L_b - d_p -D(C)-NSG', was used to identify the specimens. The first part 'PT' denotes the masonry prism type (HO1.0, HO1.5, or St1.0). The next part ' L_b ' refers to the FRP bond length, which is denoted by the numbers of bricks, bonded with the CFRP strip. The third part ' d_p ' identifies the depth of FRP strip embedment (10, 15 or 20 mm). The fourth part 'D' identifies the distance from the strip to the perpend joint (0, 1/6, 1/4 or 1/2 brick length) or 'C' identifies the strip location with respect to cores ('AC' for at core and 'BC' for between cores). The last part 'NSG' refers to no strain gauges attached in carbon FRP-to-masonry bond zone. For example, 'HO1.5-4-15-1/4-NSG' denotes a specimen of HO1.5 type prism near surface mounted with a carbon FRP strip 1/4 brick length away from the nearest perpend joint with 15 mm embedment depth and without strain gauges attached in the bond zone. In Table 3.6, the bond lengths, L_b , are measured before test, while the other dimensions of the carbon FRP are nominal values.

(2) Fabrication of Specimens and Instrumentation

The fabrication of the NSM push-pull test specimens was similar to that of the EB specimens with two differences. Firstly, there was no need to prepare the masonry surface; instead a groove was cut in the masonry prism. Secondly, the FRP strips needed to be strain gauged prior to placement into grooves.

Table 3.6 CFRP NSM bond test specimen details

Phase	Specimen	FRP Bond length		CFRP Strip Dimensions	
		Bond to brick No.	L_b	Width (d_p)	Thickness (t_p)
			(mm)	(mm)	(mm)
1	HO1.5-2-10-0	2	158	10	1.2
	St1.0-1-10-1/2	1	76	10	1.2
	St1.0-2-10-1/2	2	159	10	1.2
2	St1.0-3-10-1/2-NSG	3	244	10	1.2
	St1.0-3-15-1/2-NSG	3	241	15	1.2
3	HO1.5-4-15-1/4	4	328	15	1.2
	HO1.5-4-15-1/4-NSG	4	334	15	1.2
	HO1.0-4-15-0	4	328	15	1.2
	HO1.0-4-15-0-NSG	4	334	15	1.2
	St1.0-4-15-1/2	4	328	15	1.2
4	HO1.5-4-15-1/6	4	328	15	1.2
	HO1.5-4-15-1/4	4	328	15	1.2
	HO1.5-4-20-1/2	4	328	20	1.2
	St1.0-4-20-AC	4	328	20	1.2
	St1.0-4-20-BC	4	328	20	1.2

The brick prisms were constructed, with both bed and perpend joints approximately 10 mm in thickness. All the masonry prisms were left to cure for 28 days. A groove was then cut into the masonry specimen, according to designated locations and dimensions, using a diamond-coated blade on a circular saw. The groove was vacuumed and cleaned prior to bonding. Carbon FRP strips were cut to the required width and length. And the strip surface was cleaned with acetone to remove any foreign substances.

Strain gauges were glued to the strips on alternating sides at an initial spacing of 20 mm with the expectation that more strain data would be obtained allowing a more accurate analysis. However, the bond was compromised due to the strain gauges reducing the FRP-to-masonry bond area significantly. Subsequently, the gauge spacing was increased to 41 mm. Strain gauges were distributed on alternating sides

equally along the strip, with two gauges per brick, as shown in Figure 3.9 (c). Two strain gauges were attached 25 mm above the top surface of masonry prism on both sides of the strip. The reason for attaching gauges on alternating sides along the strip was to minimise the weakening effect on the bond in comparison to attaching all gauges on only one side of strip, so as not to affect the bond on one side only. After the strain gauges were glued to the strips, they were coated with a waterproofing layer to protect them during the insertion of the strips into the grooves cut in masonry prisms and filled with the adhesive.

The brick prism was then covered with plastic stick tapes at either edge of the groove. Adhesive was then applied evenly both into the groove and directly onto the carbon FRP strip. The strip was subsequently inserted into the groove and the excess adhesive was removed. This method of bonding ensured that the groove was completely filled with adhesive. A pair of aluminium plates was also adhered to either side of the FRP strip at loaded end for ease of clamping to the test machine grips and distributed the load evenly.

All the specimens were left at least seven days before testing to allow the adhesive to cure. The reinforced face of the masonry prism (i.e. the side containing the FRP strip) was painted with white paint to make it easier to observe the formation of cracks during testing.

3.2.4. Test Set-up and Loading Procedure

Test Setup

An Avery universal testing machine was employed for all the push-pull tests. The test setup was similar for both the externally bonded and near surface mounted push-pull tests. Figure 3.11 shows the test setup for an externally bonded specimen.

Each specimen was carefully placed into the testing device with the strip centred under the loading clamp. A layer of quick drying paste was applied to both the top and bottom surfaces of the masonry prism in order to ensure the load and reaction are transferred evenly. Four positioning angles were used to fix the specimen at the unloaded end and prevent any movement of masonry prism. A solid steel plate with a small gap for the reinforcing strip to pass through was placed onto the top surface of the specimen. This restraining plate was used to apply approximately 1 kN of precompression. This helped to settle the specimen, especially at the early stages of loading, and developed the compressive force, which reacted against the tensile load applied to the test FRP strip. After the specimen was secured in the test rig, the strain gauges were connected to a Kwoya Electronic Instruments Co. Ltd. Universal Digital Measuring System (U-CAM). The U-CAM recorded strain data from each of the gauges at constant time intervals throughout the testing procedure. The top end of FRP strip was then clamped into the grips of the test rig. The alignment of the strip was also checked to prevent the splitting of strips.

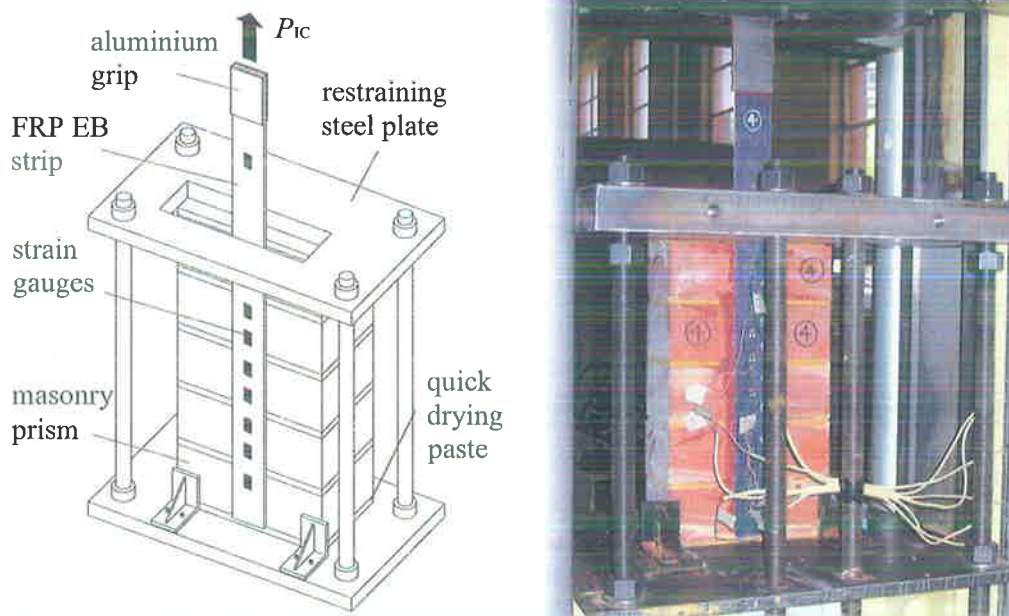


Figure 3.11 Push-pull test specimen setup

Loading Procedure

Loading was applied through a manually controlled hydraulic ram. The testing procedures were performed as described below:

- (a) an initial tensile load of 0.5 kN was applied to the glass FRP strip to verify that the mechanical and electrical equipment were working properly;
- (b) the load was then released and an initial reading of load and strain was carried out;
- (c) the load was reapplied to failure at a steady rate of approximately 1 kN/min.

The crack load P_{cr} was recorded when the first crack along the glass FRP-to-masonry interface was observed visually. Both externally bonded and near surface mounted push-pull test results are reported in the following section.

3.3. TEST RESULTS – EB GFRP

3.3.1. Test Summary

The glass FRP externally bonded test results are summarised in Table 3.7, where E_p is the Young's modulus of the FRP strip computed from the experimental data; P_{cr} and P_{IC} are the recorded loads at initial visible cracking and specimen failure, respectively; ε_{max} is the maximum strain recorded in the FRP strip prior to failure. The observed failure modes were either by full debonding or by partial debonding prior to rupture of the FRP strip. The glass FRP strip rigidity $E_p A_p$, calculated from the measured data is also included in Table 3.7.

Table 3.7 Summary of experimental results for glass FRP EB tests

Specimen	L_b	P_{cr}	P_{IC}	ϵ_{max}	$E_p A_p$	Failure mode
	(mm)	(kN)	(kN)	($\mu\epsilon$)	(GPa*mm ²)	
GP-5-Ne-M-1	420	14.5	22.1	12143	1820	FD
GP-5-Ne-Q-1	395	12.5	21.5	11257	1910	FD
GP-5-Ne-M-2	419	12.8	21.9	11433	1916	FD
GP-5-Ne-Q-2	396	13.2	18.1	9560	1893	FD
GP-5-Sa-M	416	12.8	23.0	12597	1826	PD+R
GP-5-Sa-Q	394	13.3	24.7	13529	1826	FD
GP-5-Gr-M	423	12.7	18.9	10710	1765	PD+R
GP-5-Gr-Q	393	15.0	24.3	12339	1969	FD
GP-5-Re-M	410	8.4	11.8	11885	993	FD
GP-5-Re-Q	393	8.8	14.3	7591	1884	FD
GD-5-Sa-Q-1	386	16.6	19.9	10522	1891	FD
GD-5-Sa-Q-2	386	15.4	18.6	8619	2158	FD

Notes: $b_m=230$ mm, $b_p=50$ mm, $t_p=0.2$ mm, $E_p A_p=P_{IC}/\epsilon_{max}$;

FD=Full debonding, PD+R=Partial debonding prior to rupture.

3.3.2. Test Observation and Failure Modes

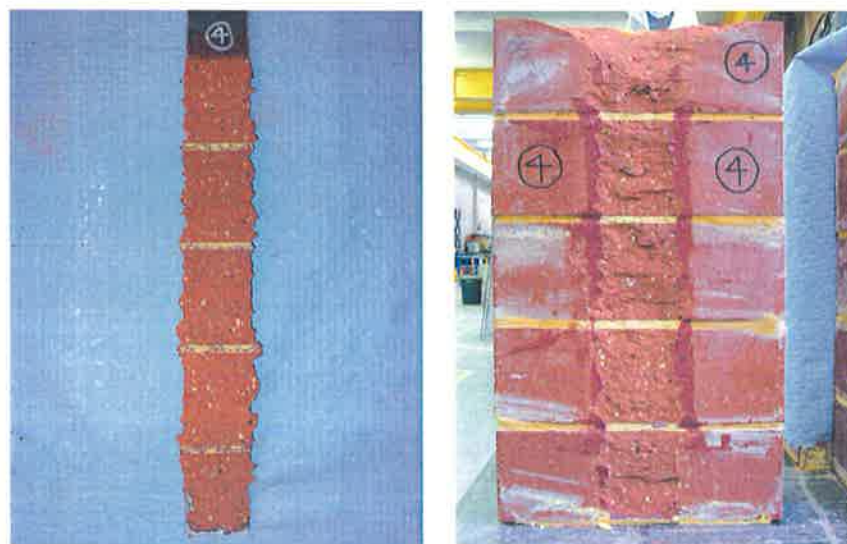
General Test Observation

As the specimens were loaded, the load increased until the initial vertical cracks formed at around 12.5 ~ 16.6 kN for the surface prepared specimens and about 8 kN for the two reference specimens with unprepared surfaces. The visible cracks formed along the edge of FRP strip close to the mid-height of the first brick and then developed at around 45 degree towards the top surface with increasing applied load. The initial vertical cracks subsequently propagated along the FRP strip edge downwards to the bottom unloaded end of the specimen with increasing load until the FRP fully debonded or ruptured.

Failure Modes

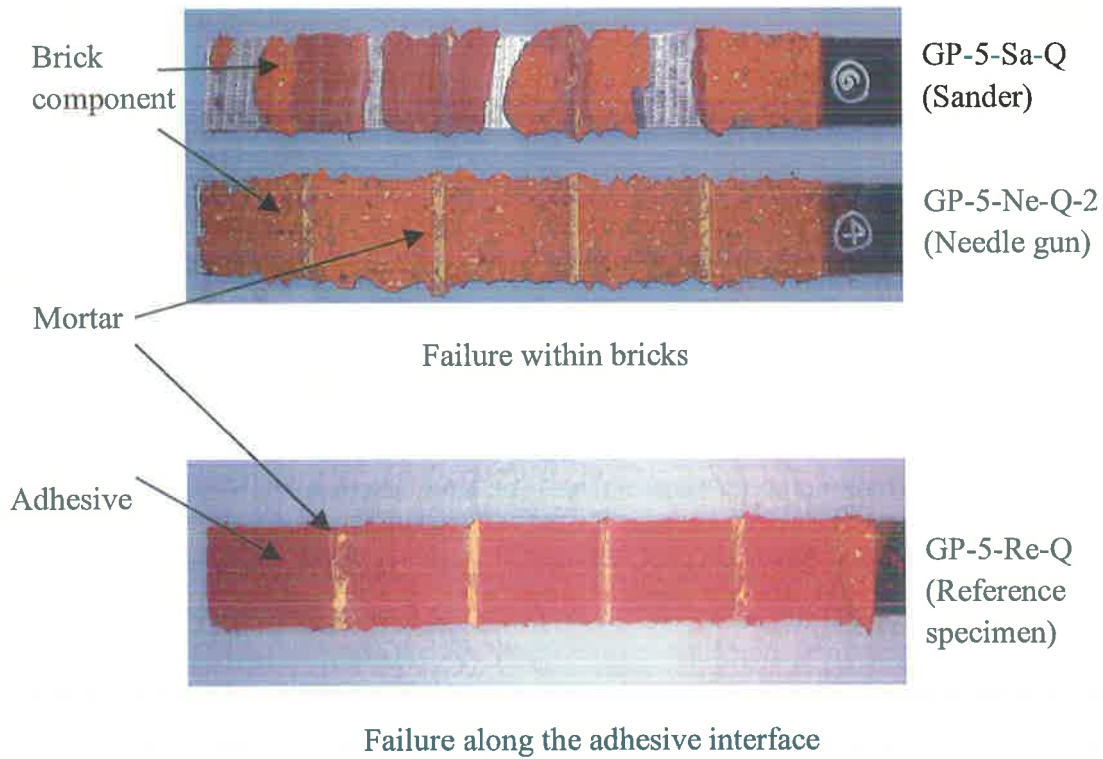
All the test specimens with prepared surfaces performed well and failed either by full debonding or FRP rupture after partial debonding. Glass FRP full debonding failure was observed as debonding propagated from the loaded end of the strip towards the unloaded end until the strip was completely detached from the masonry prism as shown in Figure 3.12. Ten glass FRP specimens failed by full debonding.

According to the different conditions of failed brick prism surface, the full debonding failure could be subclassified into two types. The first type can be defined as the debonding crack propagating either within masonry, a few millimeters beneath the adhesive-to-masonry interface which indicates good bond. Figure 3.13 shows the types of debonded surfaces for both detached glass FRP strips and brick prisms. The second type was only observed in the brick surface of the two unprepared reference specimens. As Figure 3.13 shows, the debonding failure in the reference specimens occurred along the adhesive interface between glass FRP strip and brick surface due to a weak bond. The brick surface was almost undamaged. The glass FRP strip was observed to detach directly from the brick surface, with only adhesive and a few pieces of mortar fixed to the detached strip.

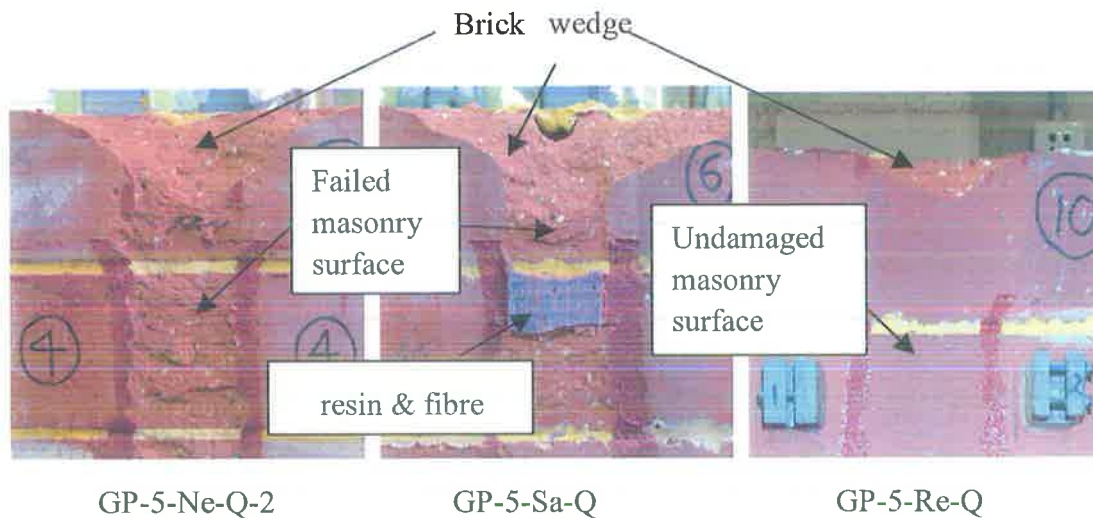


(a) detached glass FRP strip (b) failed surface of brick prism

Figure 3.12 GFRP fully debonding failure (specimen GP-5-Ne-Q-2)



(a) Different debonding surfaces of detached GFPR strips



(b) Different debonding surfaces at bond zone of brick prisms

Figure 3.13 Comparison of fully debonding failure

The second failure mode was regarded as glass FRP rupture with partial debonding. In this case the glass FRP started debonding from the loaded end, then propagated towards the unloaded end and eventually ruptured near the region of the aluminium

grips, while a short length of glass FRP strip was still attached to the prism at the unloaded end. This failure mode occurred in specimens GP-5-Sa-M and GP-5-Gr-M, as shown in Figure 3.14. Both glass FRP strips ruptured at the aluminium grip bonding zones. The maximum strain of these two specimens prior to failure was found to be 11579 and 9704 microstrain, respectively. The former one was quite close to the FRP rupture strain of 12000 microstrain, which indicated that this failure mode is reasonable. The latter maximum strain recorded was not so close to the rupture strain, which might mean there was a stress concentration in the glass FRP strip at the bonding end of aluminium grips.

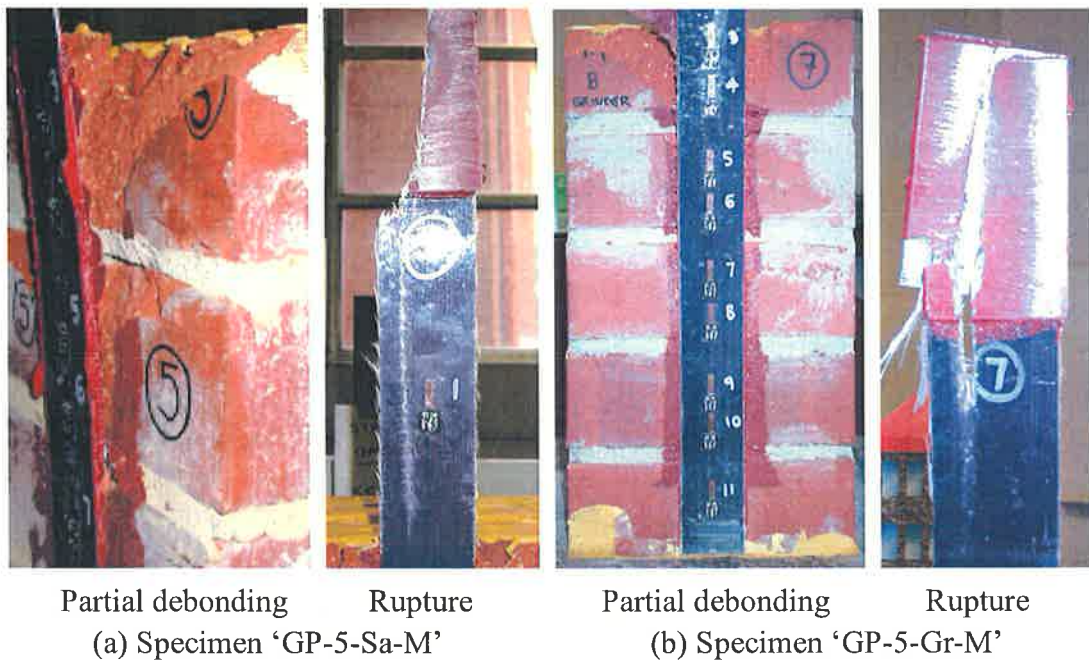
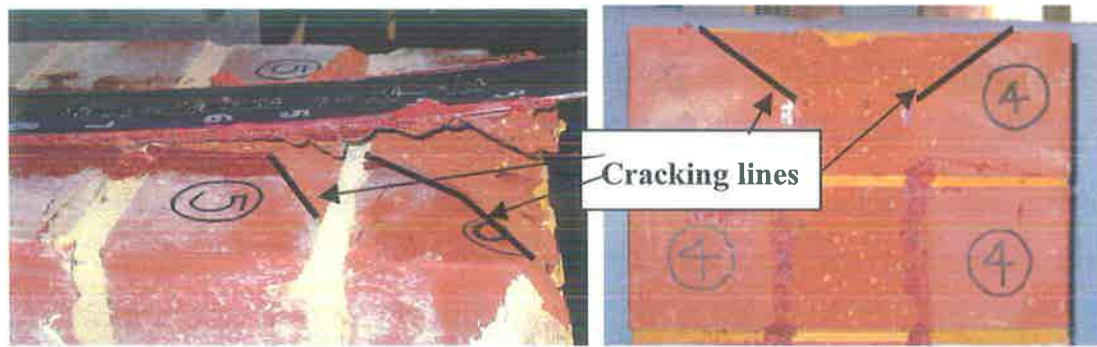


Figure 3.14 GFRP partial debonding and rupture failure

The failure of all specimens started from glass FRP debonding and the debonding process were almost identical. After the initial cracks formed, it propagated at around 45 to 60 degrees to the longitudinal axis of the glass FRP strip towards the first brick surface at the loaded end as shown in Figure 3.15. These cracks contributed to the formation of the brick wedge in the first brick, which was attached to the glass FRP strips and pulled out subsequently. The force when initiation of cracking in the first brick was observed, P_{cr} , was found to be within the range of 55% to 70% of the

ultimate load, P_{IC} , except for the two reference specimens. As the load increased, glass FRP debonding commenced at the location where these cracks occurred, and then propagated towards the unloaded end and eventually led to partial or complete detachment of the glass FRP strip from the brick prism.



(a) Brick wedge (GP-5-Sa-M)

(b) Cracking lines (GP-5-NG-Q-2)

Figure 3.15 Brick wedge and Cracking in brick

3.3.3. Effects on Bond Strength

Effect of masonry surface preparation

The needle gun was expected to be the most effective tool in terms of achieving a satisfactory bond. However, several drawbacks exist with this apparatus, including the inconvenience of application, labour intensive problem and inducing significant lateral force, which is undesirable in masonry. Additionally, over a large area of preparation, the needle gun is not a practical option. Figure 3.16 compares the P_{IC} of the ten externally bonded push-pull specimens and shows that the average bond strength of specimens prepared with a sander or grinder were slightly higher than that of the needle gun. This is probably due to the fact that the needle gun damaged and thus weakened the brick surface. The bond strength of surface unprepared specimens was significantly lower than the surface prepared ones. Due to the application ease and the higher bond strength, surface sanding is recommended to be the most

effective among the three methods investigated to prepare the masonry surface for external bonding of FRP.

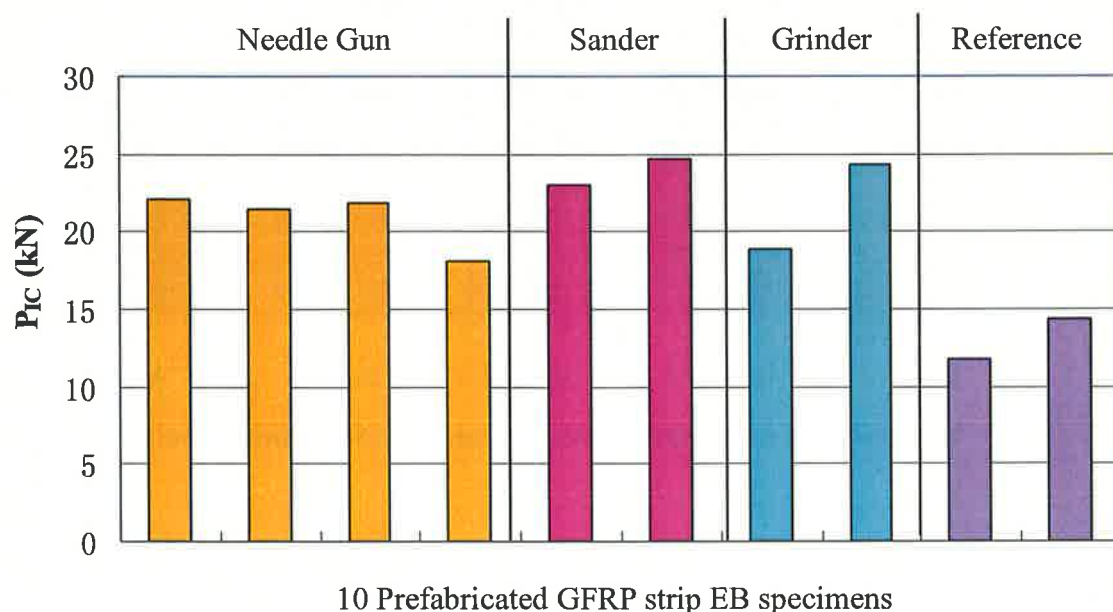


Figure 3.16 Comparison of masonry surface preparation methods

Effect of mortar substitutes on bond strength

The effect of mortar on bond strength was investigated by using the quick drying paste as a mortar substitute. Figure 3.17 compares the P_{IC} of corresponding counterpart specimens using mortar and quick drying paste. It is obvious that there is no clear trend and generally there is not much difference between using mortar and quick drying paste.

Table 3.8 gives the mean, standard deviation (S.D.) and coefficient of variation (COV) for mortar and quick drying paste individually. It shows that there is approximately 3% difference between the mortar and quick drying paste, which is insignificant. The COV for both of them are within 15% (8% for the mortar specimens and 14% the for QDP specimens), which is quite small and insignificant, as a 30% COV is typical for plain unreinforced masonry.

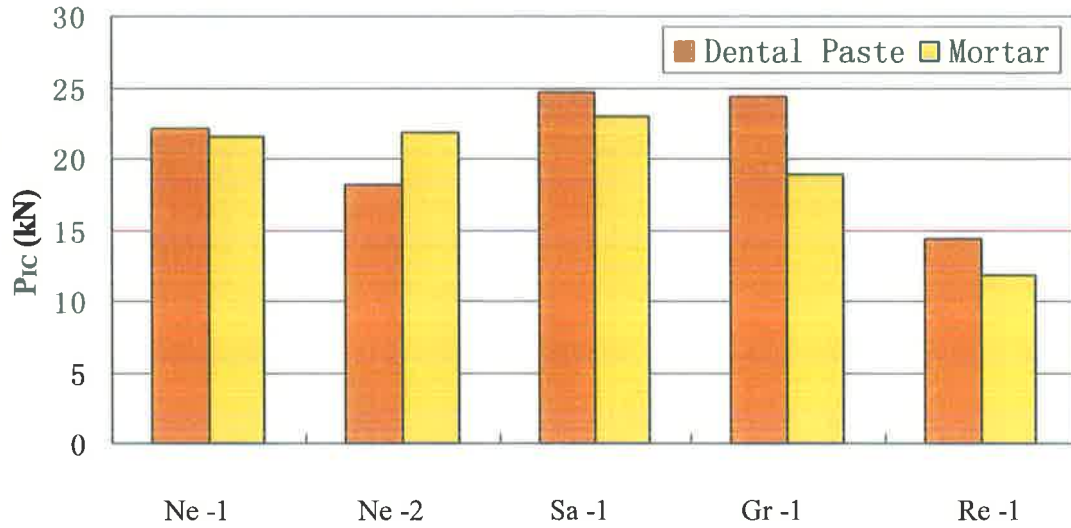


Figure 3.17 Comparison of mortar and quick drying paste

Table 3.8 Effect of mortar joints on bond strength

	P_{IC} (kN)				Mean	S.D.	COV
	Ne-1	Ne-2	Sa-1	Gr-1			
Mortar	22.1	21.9	23	18.9	21.5	1.78	0.08
QDP	21.5	18.1	24.7	24.3	22.2	3.05	0.14

Hence, it was concluded that mortar joints do not have a significant impact on the bond behaviour of such FRP-to-masonry interfaces. This may be attributed to the dominant surface area fraction of the bricks in masonry over the mortar joints. Therefore, common mortar may be replaced with other alternatives such as quick drying paste when preparing FRP-to-masonry bond test specimens.

Effect of glass FRP bonding methods on bond strength

According to the test summary (Table 3.7), the average P_{IC} of two glass sheet dry lay-up specimens (i.e GD-5-Sa-Q-1 and GD-5-Sa-Q-2) was 19.3 kN, while 24.7 kN was achieved for the specimen (GP-5-Sa-Q) with prefabricated glass FRP strip

bonding method. Therefore, approximately 28% increase can be obtained by using a prefabricated glass FRP strip bonding method. However, it takes extra time for prefabricating the glass FRP strip before bonding. Dry lay-up bonding method may be suitable for practical use, for it can significantly reduce the labour cost and solve time restraint problem.

3.4. TEST RESULTS –NSM CFRP

3.4.1. Summary of NSM Test

Four separate phases of testing were carried out over the whole test series. The first phase involved using a strip embedment depth d_p of 10 mm, a strain gauge spacing of 20 mm between adjacent gauges, and varying bond length L_b . It was found from the results of these preliminary tests that the specimens failed along the adhesive and FRP strip interface, which was due to the reduced bond area resulting from the large number of strain gauges. The second phase of testing was performed to compare the effect of varying b_p , 10 mm or 15 mm, using the same prism type, bond length L_b and no strain gauges within the bond zone. Carbon FRP rupture and debonding failure modes were observed for the 10 mm and 15 mm strips, respectively. This also confirmed the premature failure of the specimens in phase one, since the debonding strain obtained in phase one was much lower than that of phase two. In phase 3 it was decided to use the 15 mm wide strip with increased bond length L_b and revised strain gauge arrangement (i.e. strain gauge spacing of 41 mm, as depicted in Figure 3.9 (c)). This phase of testing was mainly used to determine the influence of the specimen type. Therefore, the specimen type was varied, while keeping the embedment depth b_p and bond length L_b the same. Of concern was the impact to the bond strength of the presence of strain gauges within the bonded region. Thus, corresponding specimens without strain gauges in the bond region were also tested to quantify the effect, one of which had been tested in Phase 2. The final phase of testing involved using 15 mm

and 20 mm wide strips and different strip positions to assess the influence of the distance of the strip relative to the perpendicular joint, or its proximity to the hollow cores of the bricks.

A summary of the near surface mounted push-pull tests is included in Table 3.9, where P_{IC} is the recorded maximum applied load, ε_{max} is the maximum strain recorded in the strip prior to failure, and E_p is the Young's Modulus of each carbon FRP strip as determined from the experimental data. The observed failure modes include premature carbon FRP sliding failure, full debonding, carbon FRP strip rupture and strip partial debonding with rupture.

Table 3.9 Summary of experimental results for NSM test

Phase	Specimen	L_d	d_p	P_{IC}	ε_{max}	E_p	Failure Mode
		(mm)	(mm)	(kN)	($\mu\varepsilon$)	(GPa)	
1	HO1.5-2-10-0	158	10	19.9	11059	142.8	S
	St1.0-1-10-1/2	76	10	19.6	10086	153.6	S
	St1.0-2-10-1/2	159	10	17.5	10313	139.9	S
2	St1.0-3-10-1/2-NSG	244	10	27.6	18932	140.4	R
	St1.0-3-15-1/2-NSG	241	15	46.8	17899	146.9	FD
3	HO1.5-4-15-1/4	328	15	44.0	16807	149.8	FD
	HO1.5-4-15-1/4-NSG	334	15	50.7	18896	157.6	R
	HO1.0-4-15-0	328	15	38.3	13168	156.6	FD
	HO1.0-4-15-0-NSG	334	15	46.7	16575	159.9	FD
	St1.0-4-15-1/2	328	15	41.5	15409	153.6	PD-R
4	HO1.5-4-15-1/6	328	15	41.8	15938	150.9	PD-R
	HO1.5-4-15-1/4	328	15	38.3	15886	152.9	S-R
	HO1.5-4-20-1/2	328	20	49.4	13501	151.1	PD-R
	St1.0-4-20-AC	328	20	50.0	12901	154.1	FD
	St1.0-4-20-BC	328	20	51.2	13408	160.1	FD

Notes:

$b_m=355$ mm (HO1.5 prism) and 230 mm (HO1.0 and St1.0 prism); $t_p=1.2$ mm,

$E_p=P_{IC}/(A_p\varepsilon_{max})$; S=Sliding failure, R=FRP rupture, FD=FRP full debonding,

PD=FRP partial debonding.

3.4.2. Test Observations and Failure Modes

Test Observations

Based on the push-pull tests, a number of general observations were made. As the specimens were loaded, a series of small cracks began to form in the masonry at the loaded end along the strip. These cracks propagated at an approximate angle of 45 degrees to the strip. With further load, the extent of cracking propagated further along the length of the strip until failure. Figure 3.18 shows the propagation process of cracking, which has been marked in black.

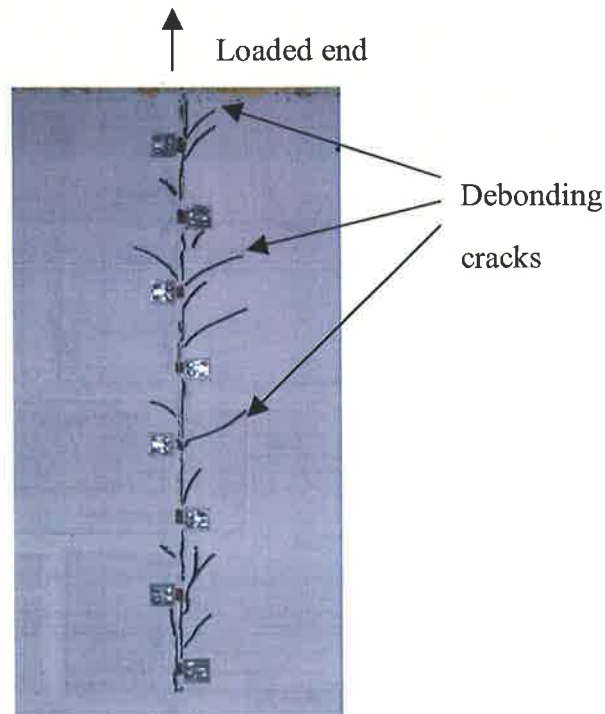


Figure 3.18 Cracking of NSM push-pull test

Failure Modes

Three types of failure modes were observed: (1) carbon FRP strip sliding; (2) carbon FRP strip full debonding; (3) carbon FRP strip rupture. Combinations of the failure modes (1) and (3) or (2) and (3) were also observed. Among the three failure modes, debonding failure occurred with masonry cracking and the FRP strip being completely

detached, and rupture failure was due to the rupture of FRP fibres, typically at the boundary of bonded end.

(1) Sliding failure

Sliding failure is regarded as a kind of premature failure, which occurred along the adhesive interface, while both the FRP strip and the masonry are not damaged, as shown in Figure 3.19. This type of failure was observed in the four specimens of phase one, where the large number of strain gauges reduced the adhesive bond area significantly. In this test phase, the ultimate load was less than 20 kN, and the maximum strain recorded was significantly lower than for the other specimens. This indicates that the capacity of the FRP strip was not fully used. As this failure could only be avoided by using fewer strain gauges, the strain gauge arrangements of subsequent specimens were revised as previously discussed in Section 3.2.3.

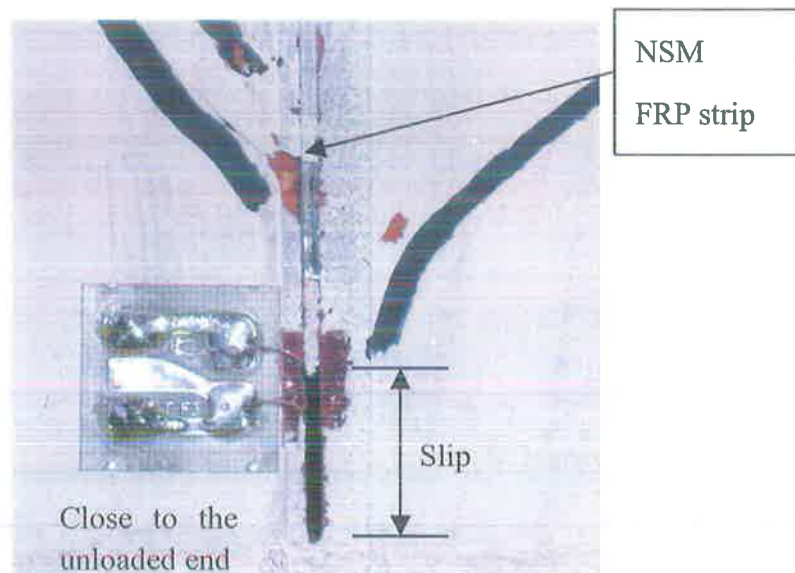


Figure 3.19 Sliding failure mode (St1.0-2-10-1/2)

(2) Debonding failure

Debonding failure occurred when the debonding crack in the masonry propagated the full length of the NSM strip. A number of these failures were quite explosive in nature, with sizeable pieces of masonry breaking away from the main specimen. In most

cases, part of the masonry was left on the strip attached to the adhesive, as shown in Figure 3.20. In debonding failure, debonding cracks initially formed in the brick unit at the loaded end. The shear cracks then started propagating along the length of the strip, until there was no length of bond left to transfer the load. The strip then completely debonded attached with the masonry components pulled out from the prism.

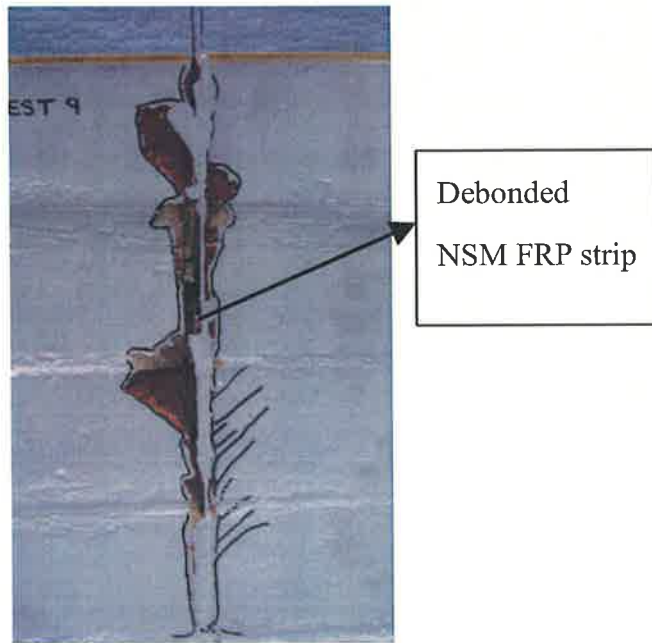


Figure 3.20 Debonding failure of CFRP NSM specimen (HO1.0-4-15-0-NSG)

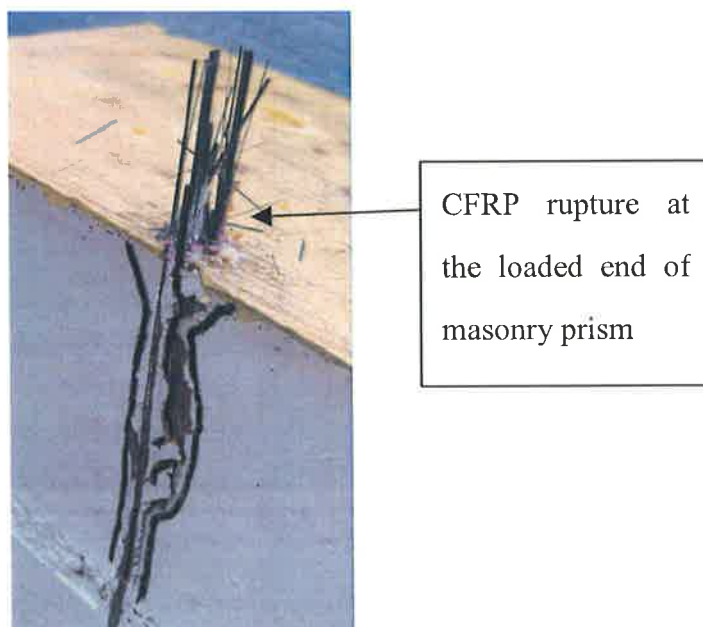


Figure 3.21 Rupture failure of NSM push-pull test specimen

(3) Rupture failure

Rupture failure of the carbon FRP strip occurred when the strain in the strip reached the carbon FRP material rupture strain, which was reported to be approximately 16,000 to 17,000 $\mu\epsilon$ (refer Table 3.2). Rupture typically occurred at the location where maximum strain was reached, especially at stress concentration regions such as the zone close to the boundary at loaded end, as shown in Figure 3.21. When rupture occurs the strip is being used to its full capacity. Failure due to pure carbon FRP strip rupture was observed in two cases. It should be noted that interface cracks still formed prior to rupture of the strip due to the high strain reached. Rupture also occurred combined with other failure modes (i.e. sliding or debonding) in four push-pull tests.

3.4.3. Effects on NSM Bond Strength

Based on the near surface mounted push-pull tests, a number of comparisons can be made in terms of the influence of bond dimensions, strip locations relative to the perpend joint and strip locations relative to the brick core. The comparisons are given below in terms of the ultimate load P_{IC} and the maximum strain ϵ_{max} . The effect of strain gauges was also studied to determine the influence of bond area reduction on bond strength.

Effect of FRP strip bond dimensions

(1) Bond length

In phase one, two different bond lengths L_b , one brick (76 mm) and two brick (~160 mm) lengths, were used while d_p was kept constant at 10 mm. The premature FRP sliding failure observed in these two specimens meant that the data recorded did not represent the actual bond behaviour, thus the effect of bond length could not be accurately compared. Two more bond lengths, three brick (~248 mm) and four brick

(~334 mm) lengths, were used in later tests. As other parameters were also varied, a direct comparison could not be made.

(2) Depth of embedment

The effect of embedment depth d_p was compared through the average P_{IC} for three embedment depths varied in the tests as shown in Figure 3.22. The test results of specimens with 10 mm embedment depth failed in premature sliding failure were excluded in this comparison. It can be seen that increase d_p can increase the near surface mounted FRP to masonry bond resistance. When d_p was increased from 10 mm to 15 mm (increased by 50%), P_{IC} was increased by 57.6%. However, when increasing d_p from 10 mm to 20 mm (by 100%), the increase in P_{IC} was found to be only 81.9%. The curve in Figure 3.22 suggests that the increase in P_{IC} may tend to be zero when the embedment depth reaches a critical value. In other words, there might be a critical embedment depth above which P_{IC} tends to be unchanged by increasing d_p . This critical d_p can probably be found if a solid brick is used in such a test, for 20 mm is the maximum value that can be achieved in cored bricks used in this test. There is currently no theoretical model that can predict the critical near surface mounted FRP to masonry embedment depth.

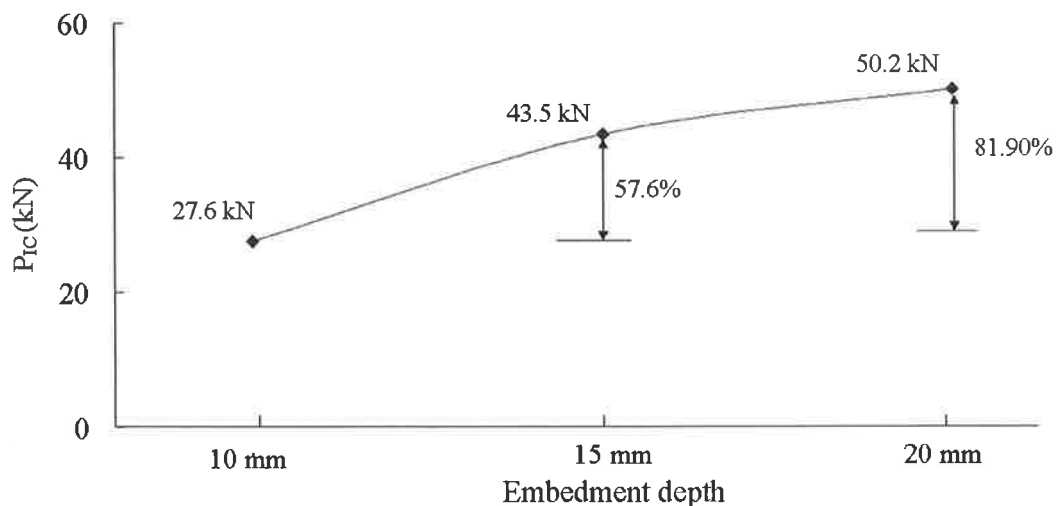


Figure 3.22 Effect of d_p on NSM bond strength

Effect of strip position

(1) Relative to perpend joints

The FRP strip position effect relative to perpend joints was compared using a series of specimens with same bond length and embedment depth as shown in Figure 3.23. The average result of two HO1.5-4-15-1/4 specimens was used. It can be seen from Figure 3.23 that P_{IC} increased when the distance from FRP position to the nearest perpend joint was increased. However, the change in bond strength was insignificant among the specimens with distances of 1/6, 1/4 and 1/2 brick length from perpend joints. It was found that P_{IC} could be increased by approximately 8.4% when locating an FRP strip at least 1/6 brick length away from perpend joints.

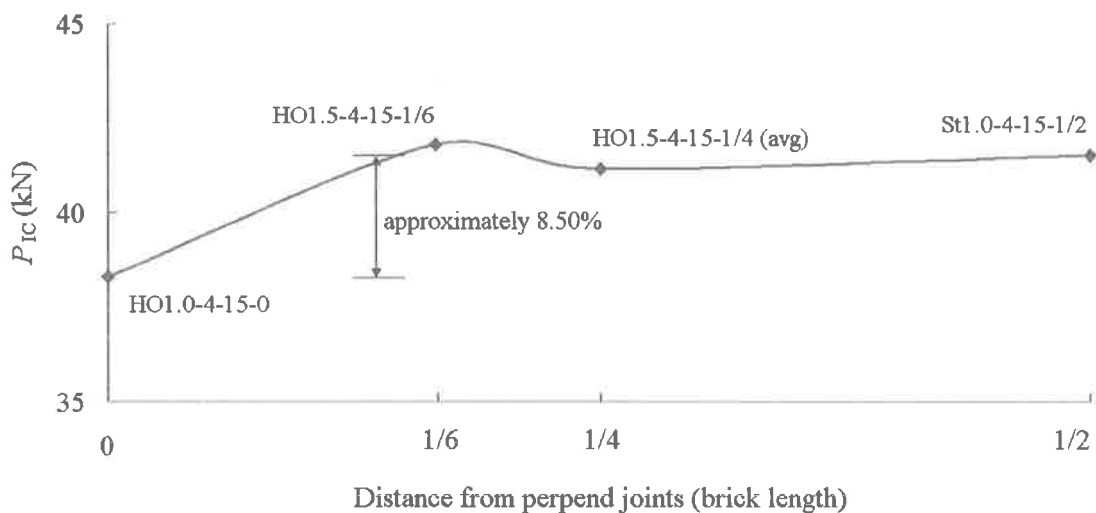


Figure 3.23 Effect of FRP position relative to perpend joints

(2) Relative to brick cores

Two different FRP strip positions in relation to the hollow brick cores were used to study the effect of brick confinements. Since the nominal distance from the edge of core to the exterior edge of the brick is 20 mm, a 20 mm wide strip was used to study the critical situation of a strip in core. In other words, using a 20 mm strip into a core

meant that in this case the back edge of the strip was breaking into one of the cores of the brick. The second position was that the strip was located directly between two cores, or in the web, in the most solid part of the brick cross section.

A direct comparison was made between the results of specimens ‘St1.0-4-20-AC’ and ‘St1.0-4-20-BC’ in phase four, as both of them failed in FRP debonding. Table 3.10 compared the results of these two specimens with the percentage increase in both P_{IC} and ε_{max} relative to specimen ‘St1.0-4-20-AC’.

Table 3.10 The effect of strip position relative to brick cores

Phase	Specimen	P_{IC}	% P_{IC}	ε_{max}	% ε_{max}	Failure mode
		(kN)	increase	($\mu\varepsilon$)	increase	
4	St1.0-4-20-AC	50.0	-	12901	-	FD
4	St1.0-4-20-BC	51.2	2.4	13408	3.9	FD

As can be seen, the difference in both P_{IC} and ε_{max} was minimal between these two cases. A slightly higher P_{IC} was recorded (~2%) for the specimen with the strip between cores. This increment in ultimate load was attributed to the increasing bond surface area, as the strip breaking into the core would lose its bond with the masonry brick at its back edge adjacent to the hollow core.

In conclusion, the test results suggest there is slight influence on the strength of the NSM bond in such a critical situation when strip back edge just met the core edge. However, it is not recommended to use a d_p greater than the depth of brick cover. Further tests are recommended to study the use of different types of brick and strip width.

3.5. PUSH-PULL TEST RESULTS ANALYSIS

The data recorded from each of the push-pull tests were used to produce a series of plots to highlight: the strain distribution; shear stress distribution; load-displacement response; and bond shear-slip curves. These plots were then used to analyse the load transfer mechanism of FRP-to-masonry bonded EB or NSM joints. The analysis method used for all the specimens is illustrated here using a typical test result for a glass FRP externally bonded specimen (GP-5-Gr-Q). The complete analysis results for each specimen are summarised in Appendix C.

3.5.1 Push-pull Test Data Processing

The applied load and the strain readings were recorded using a computer data acquisition system during each test. The Young's modulus of the FRP strip, E_p , was computed from strain readings within the unbonded region using Eq. 3-2. The axial stress at any strain gauge location σ_i (refer to Figure 3.24) was then computed from the corresponding strain readings using Eq. 3-3.

$$E_p = P / (A_p \cdot \varepsilon_{ub}) \quad \text{Eq. 3-2}$$

$$\sigma_i = E_p \cdot \varepsilon_i \quad \text{Eq. 3-3}$$

where P = applied load; A_p = cross section area of the FRP strip; ε_{ub} = strain reading within the unbonded region of the FRP strip; and ε_i = strain reading at section "i" within the bonded region.

The relative displacement across the adhesive layer between the FRP strip and the masonry is defined as the local slip, δ , which can be determined from the recorded

strain data along the FRP strip surface by assuming there is no slip at the unloaded end of the strip. The total slip at the loaded end is defined as the displacement of FRP strip, Δ , as shown in Figure 3.24.

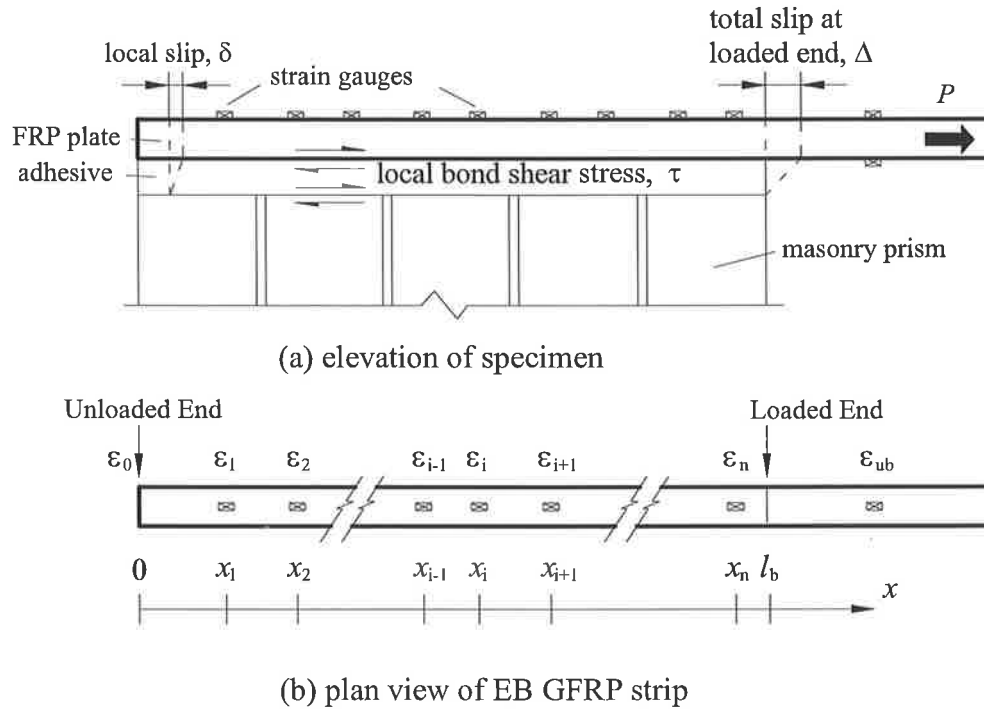


Figure 3.24 Symbols used in bond analysis

The local slip at each strain gauge location on the FRP strip is calculated by integrating the strains from the unloaded end, which can be expressed as

$$\delta(x) = \delta_0 + \int_0^x \varepsilon(x) dx \quad \text{where } \delta_0 = 0, \varepsilon_0 = 0 \quad \text{Eq. 3-4}$$

Using the data from the discrete strain gauge locations, the above expression can be evaluated using a trapezoidal rule method to evaluate the integral in Eq. 3-4:

$$\delta_i = \delta_{i-1} + \frac{1}{2} (\varepsilon_{i-1} + \varepsilon_i) (x_i - x_{i-1}), \quad \text{with } i=1, 2, \dots, n+1; \quad \text{Eq. 3-5}$$

The variation in strain along the bonded length of FRP strip was due to the transfer of force from the strip to the masonry through the shear stress, τ , acting along the bonded interface as shown in Figure 3.24 (a).

To compute the local shear stress acting between strain gauge locations along the bonding interface, a free body diagram (FBD) of strip between two strain gauges is shown for both the external bonding and near surface mounting applications in Figure 3.25. Considering equilibrium in the horizontal direction, the difference between the axial stresses σ_{i-1} and σ_i at two adjacent strain gauges is balanced by the shear stress, τ_i , which can be expressed as follows for the two bond methods:

EB:

$$\tau_0 = t_p E_p \frac{\varepsilon_1 - 0}{x_1 - 0}; \quad \tau_i = t_p E_p \frac{\varepsilon_i - \varepsilon_{i-1}}{x_i - x_{i-1}}, \text{ with } i=1, 2, \dots, n+1 \quad \text{Eq. 3-6}$$

NSM:

$$\tau_0 = \frac{b_p t_p E_p}{2b_p + t_p} \frac{\varepsilon_1 - 0}{x_1 - 0}; \quad \tau_i = \frac{b_p t_p E_p}{2b_p + t_p} \frac{\varepsilon_i - \varepsilon_{i-1}}{x_i - x_{i-1}}, \text{ with } i=1, 2, \dots, n+1 \quad \text{Eq. 3-7}$$

where b_p is the width of the FRP strip, t_p and E_p are the thickness and Young's modulus of FRP strip, respectively. For glass FRP, the thickness and Young's modulus of glass sheet is used.

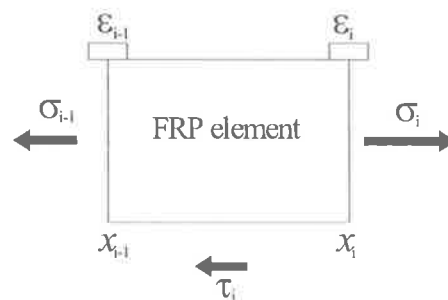


Figure 3.25 Shear stress analysis free body diagram

It should be noted here that the strain developed in the FRP strip at the loaded end should be excluded when processing and analysing the test data due to the presence of local bending effects near the loaded end (Van Gemert, 1980, Chen et al., 2001). Therefore, the strain data in the strip's unbonded region was not used to compute the stress and slip parameters at the last strain gauge location within the strip bonded region, ε_n , (refer Figure 3.24). Consequently, there is no data plotted for the region close to the loaded end.

3.5.2. Load Transfer Mechanism

This section discusses the load transfer mechanism in light of a number of observations during the loading process. These cover the strain distributions in the FRP strip along the bond length, the shear stress distribution along the FRP-to-masonry bond interface, the response of the load versus displacement at the loaded end, and the shear-slip bond model. The load transfer mechanism was seen to be quite similar for both external bonding and near surface mounting methods. The typical results obtained from specimen GP-5-Gr-Q are used throughout this section to illustrate the characteristics of FRP bonded to brick masonry.

Strain Distribution in FRP Strip

Figure 3.26 shows the distribution of the axial strain in the FRP strip at various loading levels. The abscissa represents the distance from the loaded end. The strain distribution along the bond length plateaus from the loaded end as the load increases and debonding cracks develop. This means that, as the load increases, redistribution of the bond stress along the bond length occurs as a result of changes in the state of the load transfer along the bond interface. With further increase of load, more of the FRP strip is mobilised as a result of crack propagation. It can be seen that at the initial

peak load (23 kN), three of the strain readings reached the peak strain of approximately $12000 \mu\epsilon$. When the force is transferred further down towards the unloaded end, the peak strain moves down correspondingly as a result of debonding propagation. The fluctuation of the peak strains is due to the strain being measured at the top surface, and also resulted from the different locations of strain gauges relative to cracks occurring nearby. However this does not influence the overall trend of strain development and distribution as shown in Figure 3.26.

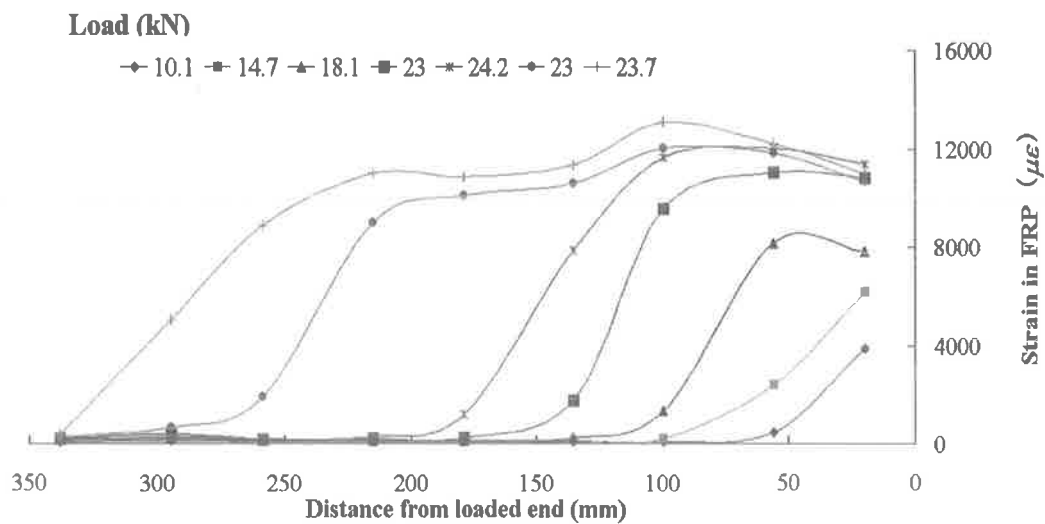


Figure 3.26 Strain distribution in FRP strip (GP-5-Gr-Q)

Shear Stress Distribution along the FRP Bond Interface

A typical shear stress distribution is shown in Figure 3.27, which not only depicts the development of shear stress along the bond interface, but also provides an experimental measure of the effective bond length, l_e , of the glass FRP strip. At lower load levels, shear stresses are only observed at the FRP loaded end, while the shear stress is zero at the unloaded end. As the load increases, the shear stress at the loaded end increases correspondingly until reaching a peak shear. At this stage of loading, microcracking develops at the loaded end and starts to propagate towards the unloaded end. With further increase of load, the peak of the shear stress gradually

shifts towards the unloaded end and the entire bond length is mobilised to resist the pulling force. The peak shear is an indication of the extent of cracking and debonding propagation. The effective bond length, l_e , may be estimated by the length of strip under a shear stress curve as shown in Figure 3.27 (stress distribution at the load of 18.4 kN), which is found to be around 130 mm for specimen GP-5-Gr-Q. Some of the curves, at high load levels, are in the shape of bimodal curves. The occurrence of sub-crests might be due to the existence of friction after debonding and also depends on the location of microcracks relative to the strain gauges as discussed previously.

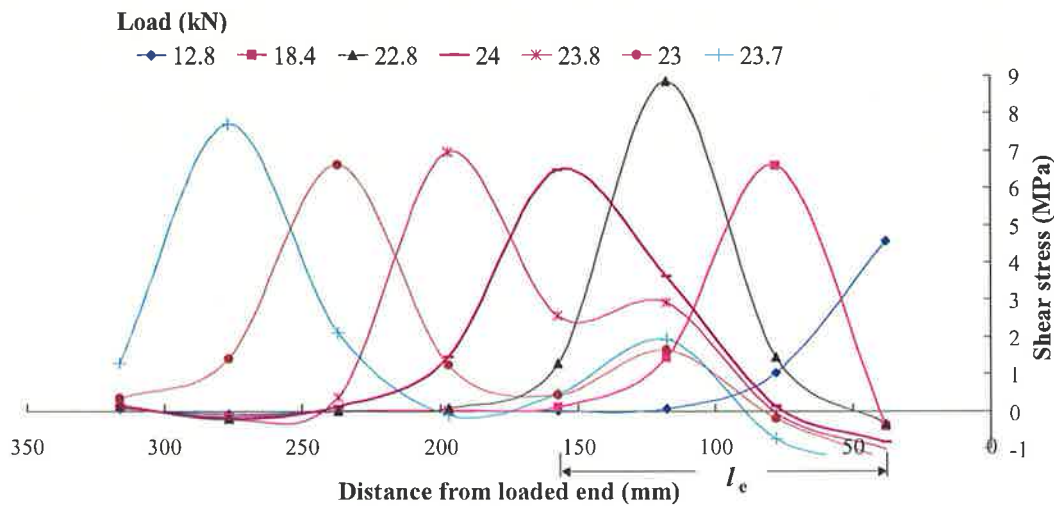


Figure 3.27 Shear stress distribution along FRP strip (GP-5-Gr-Q)

Load Versus Displacement Response

Figure 3.28 shows the typical load-displacement response of specimen GP-5-Gr-Q which was similar in shape for all specimens. Three stages can be observed from this curve. In stage one, from the origin to point A, the load increases approximately linearly, which is close to the observed cracking load, P_{cr} , 15.5 kN. The second stage, from point A to B, illustrates the softening stage of the bonded joint up to the peak load. From point B to C, the load is maintained and the shear stress is being transferred down towards the unloaded end of the strip as debonding propagates. The fluctuation of the curve at this stage is probably due to the crack developing from one

brick to another, which causes the little drop of the load. The load is generally maintained at this high level with the displacement increasing until the FRP strip fails at the end.

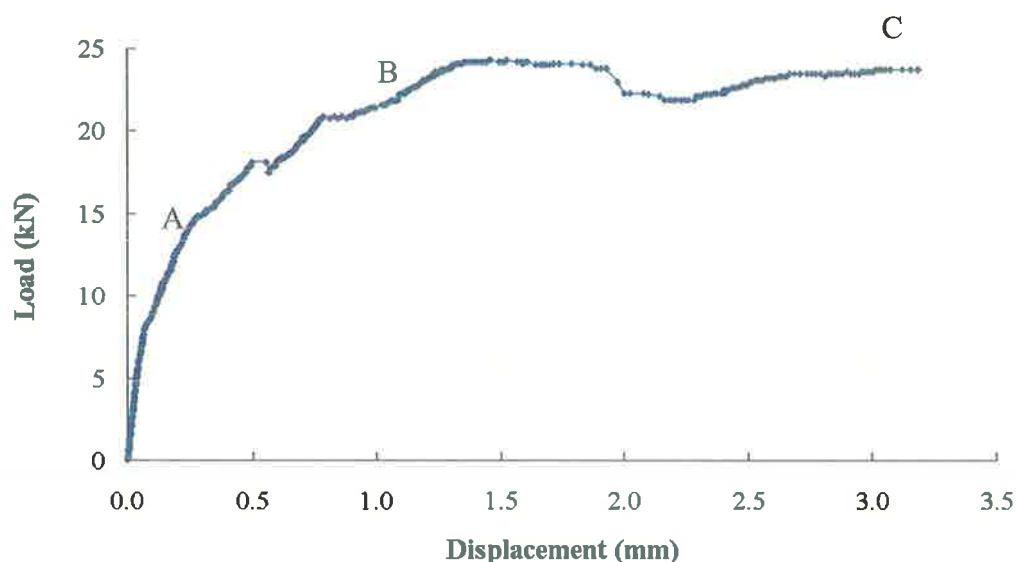


Figure 3.28 Load-displacement response at loaded end (GP-5-Gr-Q)

Shear-slip Bond Model

Slip and shear stress values computed as explained previously, can be combined to produce the local shear-slip curves. The shear stress versus slip response plotted for each pair of strain gauges is shown in Figure 3.29. This response is important for bond behaviour analysis, as it is this fundamental property for such bonded joints that is required for non-linear numerical simulation.

As the FRP bond length is long enough for the full shear stress redistribution, the descending branch of the shear-slip relationship can be clearly shown (Teng et al., 2002). Despite the significant degree of irregularity inherent to the strain gauge measurements and the unavoidable nonuniformity of interfacial properties, the local shear-slip behaviour is reasonably consistent between different locations on the same specimen and comparable with the other specimens. It can be seen from

Figure 3.29 that the peak shear stress at each location varies between 6 to 9 MPa corresponding to a slip value between 0.3 and 0.4 mm (approximately 0.32 mm for specimen GP-5-Gr-Q). The shear stress decreases to zero at slip in the order of 1.1 mm.

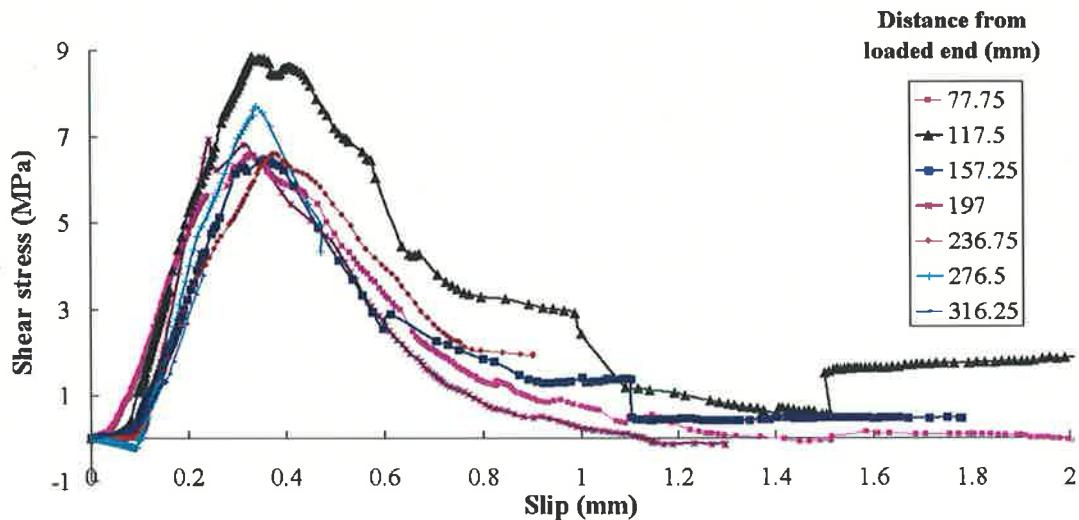


Figure 3.29 Local shear-slip response at various positions (GP-5-Gr-Q)

The peak shear stress, τ_f , at various locations for each specimen has been averaged and listed in Table 3.11 together with the corresponding slip at peak shear stress, δ_i , and slip at zero shear stress, δ_f . For externally bonded glass FRP, it excludes the two specimens without masonry surface preparation. For near surface mounted carbon FRP, it does not consider the specimens with bond length less than 3-bricks, as no clear descending branch was observed from the bond-slip model. The detailed experimental data for the individual specimen can be found in Appendix C.

Through averaging the value of τ_f , δ_i , and δ_f specimens, a typical average bond-slip model can be obtained for the externally bonded glass FRP and near surface mounted carbon FRP. This shape is quite similar to the experimental results of FRP bonded to concrete reviewed by Teng et al. (2002). Therefore, an idealised bi-linear bond-slip model for FRP bonded to masonry can be adopted, which features a linear ascending branch followed by a linear descending branch, as shown in Figure 3.30.

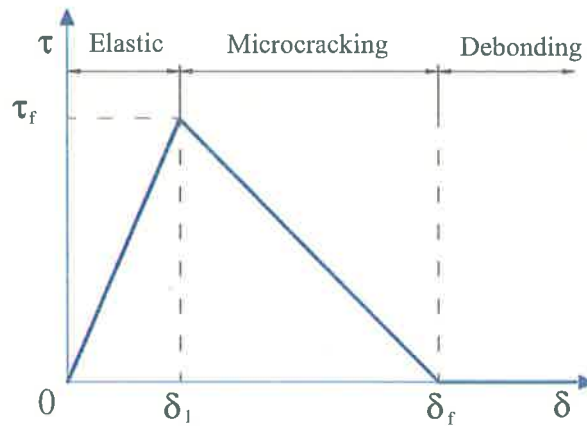


Figure 3.30 Idealised bi-linear bond-slip model

The average value of the shear-slip parameters derived from the test data are given in Table 3.11. Note, the bond-slip behaviour of externally boned carbon FRP masonry is quoted from a previous bond test conducted in the University of Adelaide (Tran, 2004). Typical experimental bond-slip curves and an idealised bi-linear curve as dashed lines are given for different FRP materials and bond techniques in Figure 3.31. It is clear for the external bonding technique that using glass FRP can achieve similar shear stress as using carbon FRP, while over four times more slip can be developed if using glass FRP. When using the same carbon FRP strip, the shear stress achieved by the near surface mounting technique is over twice as large as that by the external bonding technique and the slip developed by the near surface mounting technique is significantly higher than that by external bonding technique. These are representative comparisons based on tests to date.

Comparing the carbon FRP and glass FRP for the external bonding technique, it is seen that the peak shear, τ_f , is similar, but slip δ_1 and δ_f for glass FRP is significantly greater than that for carbon. The value of τ_f is clearly dependent on the masonry properties rather than FRP, for the same bonding technique. Due to the large slips, the fracture energy, G_f , defined as the area under the shear-slip model, is found to be approximately five times higher for the glass FRP compared to that of carbon FRP. Therefore, it is suggested that the glass FRP is more ductile than carbon.

Table 3.11 Average of shear-slip parameters for push-pull test specimens

Bonding technique	δ_1 (mm)	τ_f (MPa)	δ_f (mm)		
GFRP-EB					
GP-5-Ne-M-1	0.29	4.87	0.95		
GP-5-Ne-Q-1	0.34	6.70	0.78		
GP-5-Ne-M-2	0.27	5.62	0.91		
GP-5-Ne-Q-2	0.24	6.46	0.77		
GP-5-Sa-M	0.26	5.30	0.95		
GP-5-Sa-Q	0.26	5.69	0.99		
GP-5-Gr-M	0.20	5.12	0.77		
GP-5-Gr-Q	0.33	7.19	1.01	St Dev	COV
Mean	0.27	5.87	0.89	0.10	0.11
CFRP-NSM					
HO1.5-4-15-1/4	0.38	12.78	1.15		
St1.0-4-15-1/2	0.47	12.48	1.20		
HO1.5-4-15-1/6	0.35	14.44	1.25		
HO1.5-4-15-1/4	0.30	12.08	1.30		
HO1.5-4-20-1/2	0.38	12.65	1.27		
St1.0-4-20-AC	0.37	12.21	1.26		
St1.0-4-20-BC	0.49	13.14	1.12	St Dev	COV
Mean	0.39	12.83	1.22	0.07	0.05
Previous test data by Tran (2004)					
CFRP-NSM	0.39	12.83	1.22		

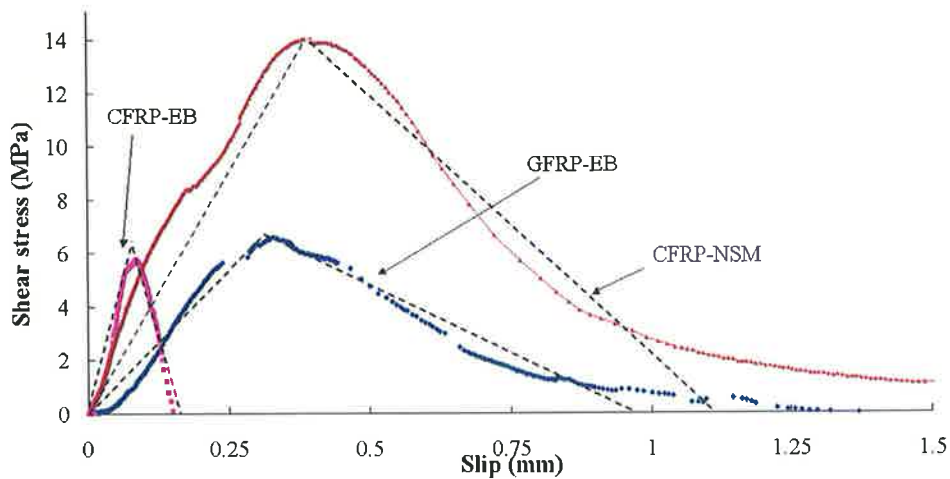


Figure 3.31 Comparison of local bond-slip models

Comparing the near surface mounted and external bonded shear-slip model for carbon FRP, the peak shear stress, τ_f , and corresponding slip at peak shear, δ_f , for the near surface mounting technique is more than double and approximately five times higher than that of external bonding technique, respectively. The maximum slip δ_f is also an order of magnitude greater. The fracture energy absorption, G_f , for the near surface mounted technique was approximately 14 times higher than for the external bonded technique. This demonstrates that near surface mounting is more efficient than external bonding, as both the bond strength and ductility are much higher.

3.6. SUMMARY

This chapter has presented the results of an experimental study of bond tests for externally bonded and near surface mounted FRP strips on clay brick masonry to simulate the bond behaviour for the intermediate debonding failure mode of FRP strengthened masonry walls in out-of-plane bending.

Using the externally bonded glass FRP technique, 12 push-pull specimens were carefully tested to study the effect of masonry surface preparation, masonry mortar substitutes and glass FRP strip bonding method. According to the test results, a sander is recommended for surface preparation for external bonding FRP. Mortar bed joints have minimal effect on the FRP-to-masonry bond strength. The results also show that using prefabricated glass FRP strips can achieve a slightly higher bond strength compared to the dry lay-up bonding method. However, using dry lay-up bonding method can significantly reduce the labour cost and solve time restraint problem, while achieving a good bond strength comparable to that of the prefabricated glass FRP strip bonding method. The average debonding strain for externally bonded glass FRP masonry was experimentally found to be 11045 $\mu\varepsilon$, approximately 92% of the glass FRP rupture strain 12000 $\mu\varepsilon$ (refer Table 3.3).

For the near surface mounting technique, 15 push-pull tests in four phases were carried out, in which the strip bond dimensions L_b and b_p , the masonry prism type, and the strip positions relative to both mortar perpend joints and brick cores were varied to investigate the influences on the near surface mounted FRP-masonry bond behaviour. The effect of bond length L_b was unable to be quantified due to premature sliding failure of the FRP strips although it was seen that longer FRP embedment depths would result in higher bond strength up to the point when the failure mode became FRP rupture. Secondly, the bond strength was seen to decrease when the FRP strip passed through mortar perpend joints. An 8.5% decrease was observed in this test program when locating the FRP strip in perpend joints compared to when the strip was offset from the perpend joints. Therefore, it is not recommended to position vertical near surface mounted FRP strips through perpend joints. After comparing the results of the specimens with varying distances from perpend joints, it was found that there was no obvious correlation between perpend offset distance and bond strength. A slightly higher P_{IC} was observed in specimens with strip between cores, which indicated the effect of brick confinement to FRP strip on bond strength.

The experimental bond test data was also analysed in this chapter. The general FRP-to-masonry bond behaviour and load transfer mechanism was found to be similar to that of FRP bonded to concrete. The fundamental bond-slip relationship has been determined for externally bonded glass FRP and near surface mounted carbon FRP.

It is recommended that further push-pull tests could be carried out to find the influence of other variables on both externally bonded and near surface mounted FRP-to-masonry bond strength. For the external bonding method, different brick units and masonry prism types could be used to study the influence of masonry types on bond behaviour. As to near surface mounting method, which is still quite new in FRP strengthening technique, there is certainly a lot of room for further development of the understanding of the bond behaviour.

4. THEORETICAL MODELLING: BOND TESTS

4.1. INTRODUCTION

This chapter presents the theoretical modelling of the bond strength for both FRP externally bonded and near surface mounted to masonry. As discussed in the literature review, there are two advanced bond strength models for FRP bonded to concrete: Chen & Teng's model (Teng et al., 2002) for FRP externally bonded to reinforced concrete (RC) and Seracino et al's model (2006) which caters for both externally bonded and near surface mounted FRP to concrete. Considering the similarities between masonry and concrete (both strong in compression and weak in tension), it was proposed that the above models could be adopted to simulate the strength of FRP-to-masonry bonded joints. Modifications were made for using these models to predict the maximum load, P_{1C} , and strain, ϵ_{db} at debonding failure.

4.2. THEORETICAL MODELLING

As discussed in Chapter Two, IC debonding was found to be one of the dominant failure modes in both RC and masonry flexural members retrofitted with longitudinal FRP strips. The IC debonding mechanism is idealised using small-scale shear specimens (Teng et al., 2002), including push-pull test. Hence, research relating to predicting the force in the strip at which IC debonding occurs, using the push-pull bond test, has received much attention worldwide. Chen and Teng's bond strength model (Teng et al., 2002) has been recently identified as the most accurate one to predict the IC debonding resistance of externally bonded FRP strip to reinforced concrete by Lu et al. (2005). More recently, Seracino et al. (2006) developed a generic model using a simplified linear-softening interface bond-slip

relationship, which is applicable to any adhesively bonded strip cross-section and material.

There is no published IC debonding model for FRP to masonry. Considering the similarity of the material properties between brick and concrete, and also as the mortar was found to have negligible impact on the bond strength, the existing models derived from reinforced concrete were used as a starting point in the present study to examine their applicability to FRP-to-masonry joints.

4.2.1. Chen and Teng's Bond Strength Model

Chen and Teng's bond strength model is a recent, simple and rational bond strength model for an FRP strip externally bonded to concrete which is based on fracture mechanics and experimental observations (Chen and Teng 2002). The predicted debonding load for FRP-to-concrete $(P_{IC})_{RC}$ is expressed as:

$$(P_{IC})_{RC} = \alpha \beta_{frp} \beta_l l_e b_p \sqrt{f_c'} \quad \text{Eq. 4-1}$$

where: α = the factor giving the mean or characteristic resistance corresponding to a particular type of structure (for FRP bonded to RC bond test, the mean value for α is 0.427); b_p = the width of FRP strip in mm; f_c' is the cylinder compressive strength of concrete in MPa; β_{frp} is the FRP width coefficient given by

$$\beta_{frp} = \sqrt{\frac{2 - b_p / b_c}{1 + b_p / b_c}} \quad \text{Eq. 4-2}$$

b_c = the width of concrete prism, β_l is the bond length coefficient given by

$$\beta_l = \begin{cases} 1.0 & \text{if } L_b \geq l_e \\ \sin \frac{\pi L_b}{2l_e} & \text{if } L_b < l_e \end{cases} \quad \text{Eq. 4-3}$$

and L_b and l_e are the FRP bond length and effective bond length in mm, respectively, where the latter is given by

$$l_e = \sqrt{\frac{E_p t_p}{\sqrt{f'_c}}} \quad \text{Eq. 4-4}$$

where E_p and t_p are Young's modulus of FRP in MPa and thickness of FRP in mm, respectively.

The model uses the cylinder compressive strength of concrete f'_c , which is the primary material property defining the concrete strength and other parameters. However, the concrete property that most affects the bond strength is the concrete tensile strength f_{ct} . The relation between splitting tensile strength of concrete f_{ct} and concrete cylinder compressive strength f'_c adopted in this model is expressed as follows (MacGregor 1988).

$$\sqrt{f'_c} = \frac{f_{ct}}{0.53} \quad \text{Eq. 4-5}$$

In this research, it was assumed that a similar relationship exists between the compressive and tensile strength for a clay brick masonry unit. Thus, if the terms in Eq. 4-5 are replaced by the corresponding values for clay brick units, f_{uc} and f_{ut} , the IC debonding strength and critical length for an externally bonded FRP strip on clay brick masonry can be computed by substituting the modified version of Eq. 4-5 into Eqs. 4-1 and 4-4 which can then be respectively expressed as

$$(P_{IC})_{URM} = \alpha \beta_{fp} \beta_l l_e b_p \frac{f_{ut}}{0.53} \quad \text{Eq. 4-6}$$

$$(l_e)_{URM} = \sqrt{\frac{E_p t_p}{\frac{f_{ut}}{0.53}}} \quad \text{Eq. 4-7}$$

where f_{ut} is the lateral modulus of rupture of the masonry units; β_{fp} and β_l are the same as the original model; for $E_p t_p$, the consistent values must be used (i.e. if the Young's modulus of the FRP strip is used, the overall thickness of the strip should be used; when using the property of the FRP fibre sheet, the thickness of the sheet only should be used).

This model is used later in Section 4.3 to predict the debonding load $(P_{IC})_{URM}$ for the push-pull EB test specimens. The theoretical value $(P_{IC})_{URM}$ is then compared with the experimental results to investigate its validity.

4.2.2. Seracino et al's Generic Model

More recently, a generic analytical model was derived by Seracino et al. (2006) to determine the debonding resistance of any adhesively bonded strip-to-concrete joint using a simplified linear-softening local interface bond-slip relationship. The bond-slip model is idealised by a single softening branch, which results in little effect on the predicted debonding response and no impact on the debonding resistance, as the area under the bond-slip curve is unchanged. This model uses a unique definition of the debonding failure plane and confinement ratio, which is suitable for both externally bonded and near surface mounted techniques as shown in Figure 4.1.

The generic equation for the maximum debonding resistance is expressed as

$$(P_{IC})_{RC} = \sqrt{\tau_f \delta_f} \sqrt{L_{per} (EA)_p} \quad \text{Eq. 4-8}$$

where $(EA)_p$ is the axial rigidity of the FRP strip; L_{per} is defined as the 'perimeter' length of the debonding failure plane cross-section, which can be expressed as

$$L_{per} = 2d_f + b_f \quad \text{Eq. 4-9}$$

To determine the first term in Eq. 4-8, $\tau_f \delta_f$, which by definition is twice the fracture energy G_f , a statistical analysis of experimental data was conducted to find the following relationship, with $t_b = t_d = 1$ mm (shown in Figure 4.1) to give

$$\tau_f \delta_f = 0.976 \phi_f^{0.526} f_c^{0.6} \quad (\text{mean}) \quad \text{Eq. 4-10}$$

Where φ_f is the IC debonding failure plane aspect ratio, expressed as

$$\varphi_f = \frac{d_f}{b_f} \quad \text{Eq. 4-11}$$

Where, d_f and b_f is the length of the failure plane perpendicular and parallel to the concrete surface, respectively, as shown in Figure 4.1.

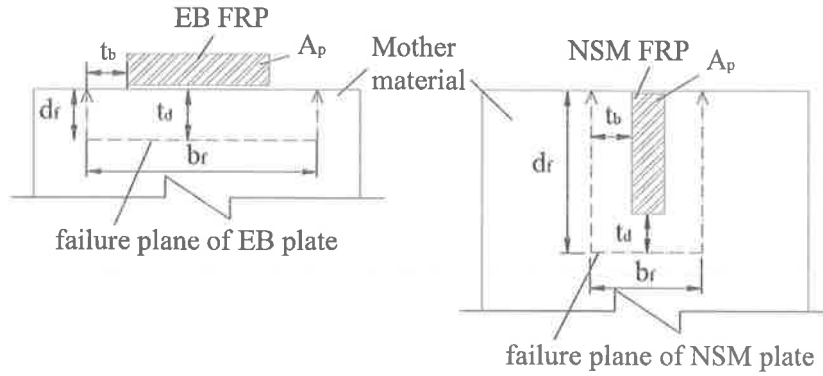


Figure 4.1 Definition of IC debonding failure plane (cross section)

Substituting Eq. 4-10 into Eq. 4-8, the maximum debonding resistance for FRP or metallic strips bonded to RC is expressed as

$$(P_{IC})_{RC} = \alpha_p 0.988 \varphi_f^{0.263} f_c^{0.3} \sqrt{L_{per} (EA)_{frp}} < \begin{cases} f_{rupt} A_p & \text{for FRP plates} \\ f_y A_p & \text{for metallic plates} \end{cases} \quad \text{Eq. 4-12}$$

$$\alpha_p = \begin{cases} 1.0 & \text{for mean} \\ 0.85 & \text{for lower 95\% confidence limit} \end{cases}$$

where units of N and mm are used, f_{rupt} is the rupture stress of an FRP strip, and f_y is the yield stress of a metallic strip.

The above model is only suitable when the bond length L_b is greater than the effective bond length l_e . In the case of $L_b < l_e$, a linear variation of $(P_{IC})_{RC}$ was recommended. The effective bond length l_e can be determined knowing τ_f and δ_f and is given by

$$l_e = \frac{\pi}{2\lambda} \quad \text{Eq. 4-13}$$

$$\text{where } \lambda^2 = \frac{\tau_f L_{per}}{\delta_f (EA)_p} \quad \text{Eq. 4-14}$$

and has been simplified by the assumption that $(EA)_c$ is very large relative to $(EA)_p$.

This model is a function of only material and geometric properties, and is applicable to any adhesively bonded technique and plate material. For the purpose of predicting FRP bonded to masonry, the same substitution used for Chen and Teng's model is used here, which can be expressed as

$$(P_{IC})_{URM} = 0.988 \phi_f^{0.263} \left(\frac{f_{ut}}{0.53} \right)^{0.6} \sqrt{L_{per} (EA)_p} < f_{rupt} A_p \quad \text{Eq. 4-15}$$

This model is then used to predict the debonding load of the masonry push-pull test specimens for both EB and NSM and the theoretical result is then compared with the experimental result to investigate its suitability. The comparisons are presented in the following section.

4.2.3. Prediction and Comparison of Theoretical Models

Both Chen & Teng's (C-T) model and Seracino et al's (S-R) model, modified as described in the preceding section, were used to predict the debonding load P_{IC} (for convenience, use P_{IC} for $(P_{IC})_{URM}$ from here on) for the push-pull test specimens. Comparisons are made with the corresponding experimental results and also between the theoretical predictions. As noted earlier, the test data of carbon FRP externally bonded to masonry brick units reported in Tran's test (2004) are included to study the validity of the two models to different FRP materials (glass FRP and carbon FRP) and different bond techniques (EB and NSM). There are no other published FRP-to-masonry push-pull test data available so far.

The C-T model, with $\alpha=0.427$, was used to predict the external bonding test results, whereas the S-R model, with $\alpha_p=1$, was used to predict both external bonding and near surface mounting test results. For the tests using the prefabricated externally bonded glass FRP strip, the Young's modulus of the strip, derived from the material tensile test, and nominal gross thickness of the strip were used. For dry lay-up glass FRP strip and carbon FRP, the manufacturer properties of the glass fibre sheet and the carbon FRP pultruded plate were used, respectively. For the S-R model, the average shear-slip parameters summarised in Table 3.11, and $t_b=t_d=1$ mm (shown in Figure 4.1) was adopted for the failure plane parameters. Therefore, the failure plane aspect ratio φ_f can be expressed as

$$EB : \varphi_f = \frac{1}{2 + b_p} \quad \text{Eq. 4-16}$$

$$NSM : \varphi_f = \frac{1 + b_p}{2 + t_p} \quad \text{Eq. 4-17}$$

For specimen St1.0-4-20-AC, with the 20 mm wide FRP strip located at the brick core, the failure plane parameters adopted were $t_b=1$ mm and $t_d=0$, as the inner edge of the FRP strip was adjacent to the edge of brick core so that no confinement was considered at this edge. Once the debonding resistance is predicted, the FRP strain at debonding can also be computed, which is another important parameter in the analysis of the FRP bonded section.

The theoretical predictions for the externally bonded tests are summarised in Table 4.1. The specimens without masonry surface preparation are excluded due to the weak bond effect and significant lower ultimate load. The comparisons of the validity for the two models are graphically shown in Figure 4.2. It can be seen that there is not much difference between the predictions of both models. The S-R's prediction is found to be a little bit greater than that of C-T, especially in the case of $l_b < l_e$ (i.e. specimens CP-1-Ne-M and CP-2-Ne-M).

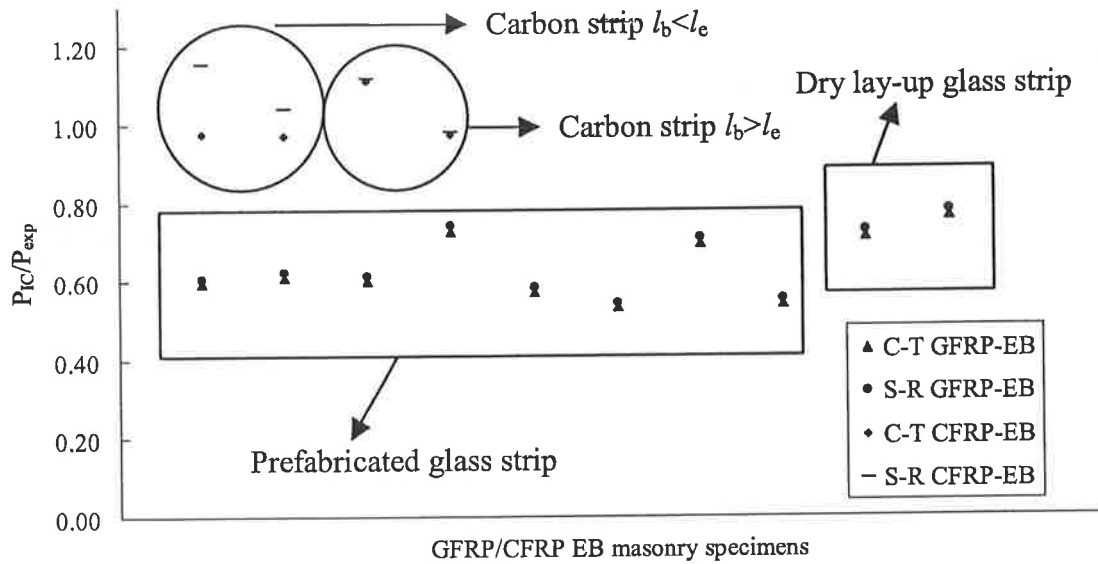


Figure 4.2 Validation of prediction for GFRP/CFRP-EB masonry

Good agreement was found between the predictions and experimental results for the externally bonded carbon FRP. The mean values of P_{IC}/P_{exp} were found to be 1.01 and 1.07 with the standard deviations of 0.07 and 0.08 for C-T and S-R models, respectively. The S-R model is slightly more unconservative, giving approximately 15% and 4% over-predictions for bond resistance and debonding strain, respectively.

However, the predictions of both models for the GFRP-EB series are significantly lower than the experimental debonding load. The mean value of P_{IC}/P_{exp} was found to be approximately 60%. The bond resistance underestimation for external bond glass FRP is likely due to the following two reasons. Firstly, the unconventional prefabrication of the GFRP strips in this test would have affected the test debonding loads. It was found that too much epoxy resin (i.e. saturant) was used in the fabrication of the GFRP strip compared to typical recommendation and practical use, which enhanced the bond resistance. Because less epoxy resin was used for the dry lay-up method, it was found that bond resistance was slightly lower and hence the predictions are slightly better. Secondly, the theoretical models were derived primarily using CFRP bond tests, and probably cannot predict GFRP bond test accurately, due to the different material stiffness.

Table 4.1 Summary of IC debonding resistance prediction for GFRP/CFRP-EB

Specimen	Material Details						Experimental Results					Predictions				Comparison with test data			
	FRP					URM unit						C-T Model		S-R Model		C-T Model		S-R Model	
	t_{frp} (mm)	b_{frp} (mm)	l_b (mm)	E_{frp} (MPa)	ϵ_{rup} ($\mu\epsilon$)		f_{ut} (MPa)	P_{cr} (kN)	P_{exp} (kN)	Failure mode	ϵ_{max} ($\mu\epsilon$)	P_{IC} (kN)	ϵ_{db}	P_{IC} (kN)	ϵ_{db}	P_{IC}/P_{exp}	$\epsilon_{db}/\epsilon_{max}$	P_{IC}/P_{exp}	$\epsilon_{db}/\epsilon_{max}$
GFRP-EB (Prefabricated plate)																			
GP-5-Ne-M-1	2	50	420	19300	12000	3.55	14.5	22.1	FD	12143	13.14	6806	13.40	6944	0.59	0.56	0.61	0.57	
GP-5-Ne-Q-1			395				14.3	21.5	FD	11257	13.14	6806	13.40	6944	0.61	0.60	0.62	0.62	
GP-5-Ne-M-2			419				12.8	21.9	FD	11433	13.14	6806	13.40	6944	0.60	0.60	0.61	0.61	
GP-5-Ne-Q-2			396				13.2	18.1	FD	9560	13.14	6806	13.40	6944	0.73	0.71	0.74	0.73	
GP-5-Sa-M			416				14.1	23.0	PD+R	12597	13.14	6806	13.40	6944	0.57	0.54	0.58	0.55	
GP-5-Sa-Q			394				13.3	24.7	FD	13529	13.14	6806	13.40	6944	0.53	0.50	0.54	0.51	
GP-5-Gr-M			423				12.7	18.9	PD+R	10710	13.14	6806	13.40	6944	0.70	0.64	0.71	0.65	
GP-5-Gr-Q			393				15.5	24.3	FD	12339	13.14	6806	13.40	6944	0.54	0.55	0.55	0.56	
GFRP-EB (Dry lay-up)																			
GD-5-Sa-Q-1	0.616	50	386	73000*	45000*	3.55	18	19.9	FD	10522	14.18	6306	14.47	6434	0.71	0.60	0.73	0.61	
GD-5-Sa-Q-2			386				16	18.6	FD	8619	14.18	6306	14.47	6434	0.76	0.73	0.78	0.75	
CFRP-EB																			
CP-1-Ne-M	1.2	50	70	160000*	14000*	3.16		16.3	FD	1712	15.90	1656	18.82	1960	0.98	0.97	1.15	1.14	
CP-2-Ne-M			140					26.8	FD	2900	26.01	2709	27.87	2904	0.97	0.93	1.04	1.00	
CP-3-Ne-M			210					24.9	FD	2824	27.64	2879	27.87	2904	1.11	1.02	1.12	1.03	
CP-4-Ne-M			280					28.4	FD	4056	27.64	2879	27.87	2904	0.97	0.71	0.98	0.72	
												GFRP	CFRP	GFRP	CFRP	GFRP	CFRP	GFRP	CFRP
Mean											0.63	1.01	0.60	0.91	0.65	1.07	0.62	0.97	
St Dev											0.08	0.07	0.07	0.14	0.08	0.08	0.07	0.18	
COV											0.13	0.07	0.12	0.15	0.13	0.07	0.12	0.19	

* manufacturer data; C-T Model = Chen & Teng's model, S-R Model= Seracino & Raizal's model;

R=rupture, FD=fully debonding, PD=partial debonding;

More external bond glass FRP to masonry push-pull tests using proper fabrication method need to be done to confirm the validity for these two models to predict the resistance for GFRP EB masonry. In the remaining of this report, the value of α was adjusted for both the C-T and S-R models to make the models suitable for predicting the bond resistance of the GFRP EB masonry tested in this study. This is discussed in Section 4.2.4.

The theoretical predictions of the carbon FRP near surface mounted tests are summarised in Table 4.2 and presented graphically in Figure 4.3. The mean value of P_{IC}/P_{exp} is 1.15 with the standard deviation of 0.13, excluding the specimens with premature sliding failure. Considering the no strain gauge (NSG) specimens alone, the mean and standard deviation of P_{IC}/P_{exp} turn to 1.01 and 0.06, respectively.

Thus, good agreement was found between the bond resistance prediction using S-R model and the experimental debonding load for the four specimens without strain gauges in the bond zone. The prediction for specimens with 10 mm to 15 mm FRP embedment depths are slightly unconservative because of the existence of strain gauges, which results in a slightly weakened bond and hence slightly lower experimental bond strength. For near surface mounted specimens with 20 mm FRP strip width, the model tends to over-predict the debonding load. This is probably due to the experimental loads being significantly reduced by the wider strips approaching the circular cores in the brickwork, thereby having less masonry confinement compared to the narrow 10 mm or 15 mm wide FRP strips. Although the reduced confinement effect was considered by reducing L_{per} (Eq. 4-9) in the S-R model, the predicted debonding loads were still approximately 30% over-predicted.

Generally speaking, the S-R model is valid to model the push-pull test resistance of carbon FRP near surface mounted to brick masonry. However, this model may over predict the resistance for cored masonry brick units when the FRP strips are located near the core.

Table 4.2 Summary of theoretical prediction for CFRP NSM IC debonding resistance

Specimen	Material Details					Experimental Results				Predictions				Comparison with test data			
	FRP					URM unit				C-T Model		S-R Model		C-T Model		S-R Model	
	t_{frp}	b_{frp}	l_b	E_{frp}	ϵ_{rup}					f_{ut}	P_{exp}	Failure Mode	ϵ_{max}	P_{IC}	ϵ_{db}	P_{IC}	ϵ_{db}
	(mm)	(mm)	(mm)	(MPa)	($\mu\epsilon$)	(MPa)	(kN)		($\mu\epsilon$)	(kN)		(kN)					
CFRP-NSM																	
HO1.0-2-10-0	1.2	10	158	16000*	14000*	3.55	19.9	S	11059	N/A	29.77	15503	N/A	1.50	1.40		
St1.0-1-10-1/2			76				19.6	S	10086		16.92	8812		0.86	0.87		
St1.0-2-10-1/2			159				17.5	S	10313		29.77	15503		1.70	1.50		
St1.0-3-10-1/2-NSG			244				27.6	R	18932		29.77	15503		1.08	0.82		
St1.0-3-15-1/2-NSG		15	241	46.8	FD		17899	47.55	16509		1.02	0.92					
HO1.5-4-15-1/4			328	44.0	FD		16807	47.55	16509		1.08	0.98					
HO1.5-4-15-1/4-NSG			334	50.7	R		18896	47.55	16509		0.94	0.87					
HO1.0-4-15-0			328	38.3	FD		13168	47.55	16509		1.24	1.25					
HO1.0-4-15-0-NSG			334	46.7	FD		16575	47.55	16509		1.02	1.00					
St1.0-4-15-1/2			328	41.5	PD+R		15409	47.55	16509		1.15	1.07					
HO1.5-4-15-1/6			328	41.8	PD+R		15938	47.55	16509		1.14	1.04					
HO1.5-4-15-1/4			328	38.3	S+R		15886	47.55	16509		1.24	1.04					
HO1.5-4-20-1/2		20	328	49.4	PD+R		13501	66.83	17403		1.35	1.29					
St1.0-4-20-AC			328	50.0	FD		12901	64.50	16797		1.29	1.30					
St1.0-4-20-BC			328	51.2	FD		13408	66.83	17403		1.31	1.30					
													Mean	1.15	1.07		
													St Dev	0.13	0.17		
													COV	0.11	0.16		

* manufacturer data; C-T Model = Chen & Teng's model, S-R Model= Seracino & Raizal's model;

S=Sliding, R=rupture, FD=fully debonding, PD=partial debonding;

Specimens with sliding failure are excluded from the calculation of Mean and St Dev;

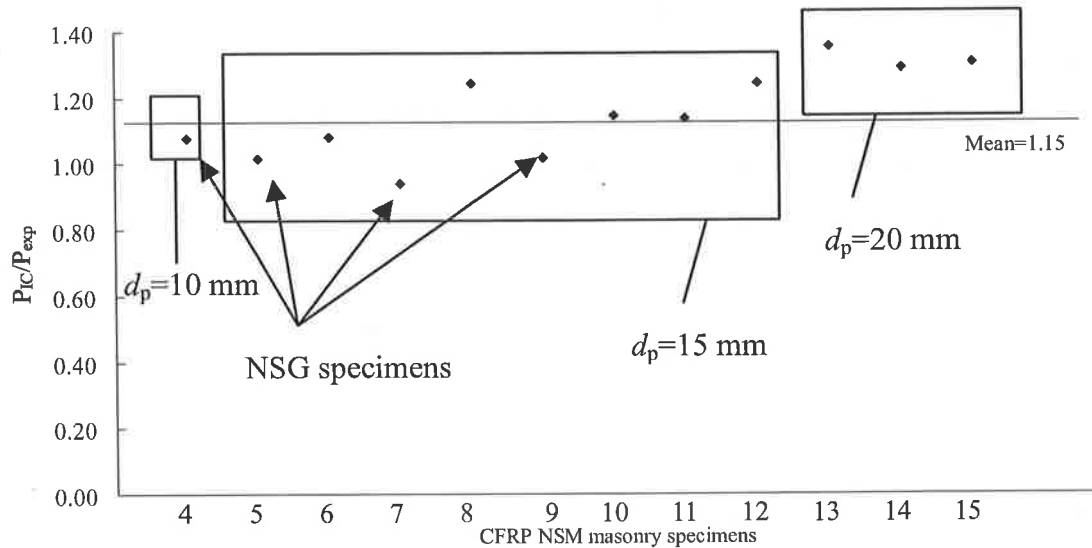


Figure 4.3 Validation of prediction for CFRP-NSM

4.2.4. Modification of GFRP EB Masonry Model

As discussed in the preceding section, the validity of the existing models for GFRP-EB could not be examined directly due to the glass FRP manufacture problems. However, it is believed that most of the main factors affecting the bond strength have been properly considered in both existing models. Hence, it was proposed to slightly modify the models for bond strength prediction which were used for the full-scale glass FRP repaired wall designs (Section 5.2.2). To amplify the prediction and make P_{IC}/P_{exp} tend towards 100%, the factor 'α' for both C-T and S-R models was adjusted. It should be noted that the modified factor may only be valid for the glass FRP externally bonded to masonry used in this study.

The modified models with adjusted factor α are shown for the C-T model for GFRP-EB as:

$$P_{IC} = 0.678\beta_{f_{fp}}\beta_{l_e}b_{f_{fp}}\frac{f_{lt}}{0.53} \quad \text{Eq. 4-18}$$

and for the S-R model for GFRP-EB in this study as:

$$P_{IC} = 1.645\phi_f^{0.263} \left(\frac{f_{ut}}{0.53}\right)^{0.6} \sqrt{L_{per} (EA)_p} \quad \text{Eq. 4-19}$$

The summary of the predictions for GFRP-EB using the modified factor is shown in Table 4.3. It can be seen that using the modified models, the mean values for P_{IC}/P_{exp} have been improved to 1.01 and 1.08 with the St Dev of 0.13 and 0.14 for C-T and S-R models, respectively.

Clearly, more experimental studies on glass FRP externally bonded to masonry are needed using the proper GFRP bonding approach to examine or confirm the validity of the existing or the modified models.

4.4. CONCLUSIONS

This chapter depicted the theoretical modelling for FRP bonded to masonry. By expressing the existing Chen and Teng's model and Seracino et al's model in terms of masonry tensile strength, both models were found to be suitable for predicting the externally bonded carbon FRP IC debonding resistance. Seracino et al's model is also valid in predicting the near surface mounted carbon FRP bond strength. Due to inappropriate fabrication of the glass FRP strip, the experimental debonding load was found to be significantly higher than predictions in this study. Modified factors were determined for both models to give improved predictions of the debonding resistance for the externally bonded glass FRP strips used in this study. These models are used to predict the debonding strain and force in the FRP at debonding for the FRP strengthening wall test designs in the next chapter.

Table 4.3 Summary of prediction for GFRP-EB with modified models

Specimen	Material Details						Experimental Results				Predictions				Comparison with test data				
	FRP					URM unit					C-T Model		S-R Model		C-T Model		S-R Model		
	t_{frp}	b_{frp}	l_b	E_{frp}	ϵ_{rup}						f_{ut}	P_{cr}	P_{exp}	Failure mode	ϵ_{max}	P_{IC}	ϵ_{db}	P_{IC}	ϵ_{db}
	(mm)	(mm)	(mm)	(MPa)	($\mu\epsilon$)	(MPa)	(kN)	(kN)		($\mu\epsilon$)	(kN)		(kN)						
GFRP-EB (Prefabricated plate)																			
GP-5-Ne-M-1	2	50	420	19300	12000	3.55	14.5	22.1	FD	12143	20.86	10807	22.31	11562	0.94	0.89	1.01	0.95	
GP-5-Ne-Q-1			395				14.3	21.5	FD	11257	20.86	10807	22.31	11562	0.97	0.96	1.04	1.03	
GP-5-Ne-M-2			419				12.8	21.9	FD	11433	20.86	10807	22.31	11562	0.95	0.95	1.02	1.01	
GP-5-Ne-Q-2			396				13.2	18.1	FD	9560	20.86	10807	22.31	11562	1.15	1.13	1.23	1.21	
GP-5-Sa-M			416				14.1	23.0	PD+R	12597	20.86	10807	22.31	11562	0.91	0.86	0.97	0.92	
GP-5-Sa-Q			394				13.3	24.7	FD	13529	20.86	10807	22.31	11562	0.84	0.80	0.90	0.85	
GP-5-Gr-M			423				12.7	18.9	PD+R	10710	20.86	10807	22.31	11562	1.10	1.01	1.18	1.08	
GP-5-Gr-Q			393				15.5	24.3	FD	12339	20.86	10807	22.31	11562	0.86	0.88	0.92	0.94	
GFRP-EB (Dry lay-up)																			
GD-5-Sa-Q-1	0.616	50	386	73000*	45000*	3.55	18	19.9	FD	10522	22.51	10013	24.08	10712	1.13	0.95	1.21	1.02	
GD-5-Sa-Q-2			386				16	18.6	FD	8619	22.51	10013	24.08	10712	1.21	1.16	1.29	1.24	
															GFRP	GFRP	GFRP	GFRP	
															Mean	1.01	0.96	1.08	1.02
															St Dev	0.13	0.12	0.14	0.12
															COV	0.13	0.12	0.13	0.12

* manufacture C-T Model = Chen & Teng's model, S-R Model= Seracino & Raizal's model;

R=rupture, FD=fully debonding, PD=partial debonding;

5. EXPERIMENTAL PROGRAM – FULL-SCALE WALLS

5.1. INTRODUCTION

The promising results of the existing one-way bending tests of FRP retrofitted masonry wall panels led to extending the current research program to examine the effectiveness of the proposed FRP rehabilitation techniques in enhancing the out-of-plane resistance of full-scale masonry walls under two-way bending. The FRP-to-masonry bond model, derived in Chapter 4, was used to determine the strain and force in FRP at debonding failure.

Four masonry wall specimens were tested in this program. These walls had been previously tested to failure by Griffith and Vaculik (2005) to study the out-of-plane behaviour of masonry walls under two-way bending. The original unstrengthened masonry walls failed in typical two-way bending failure modes. The previous test results are briefly introduced in this chapter. Both external bonding and near surface mounting methods were used, whereas only vertical FRP strips were applied according to the design criteria of this project. The test variables include the FRP material (carbon FRP or glass FRP), and FRP strip width and spacing.

The content of this chapter is limited to reporting on the design of strengthening schemes, set-up of wall specimens, test method and observations of test results. The materials used in this experimental program are identical with those of push-pull tests. Thus, the material properties are found in Section 3.3.

5.2. FULL-SCALE WALL TEST PROGRAM

5.2.1. Masonry Wall Specimens

As part of ongoing research at The University of Adelaide investigating the out-of-plane behaviour of masonry walls, three rectangular and one square full-scale walls (with window openings) were tested under both two-way unidirectional static and reversed-cyclic loading (Griffith and Vaculik, 2005). The outer dimensions of rectangular and square walls are $4.0\text{ m} \times 2.5\text{ m} \times 0.11\text{ m}$ and $2.5\text{ m} \times 2.5\text{ m} \times 0.11\text{ m}$, respectively. Each wall contained one $1.2\text{ m} \times 1.0\text{ m}$ window opening and two 0.48 m long return walls. The window opening was eccentrically positioned in the three rectangular walls and centrally positioned for the one square wall as shown in Figure 5.1.

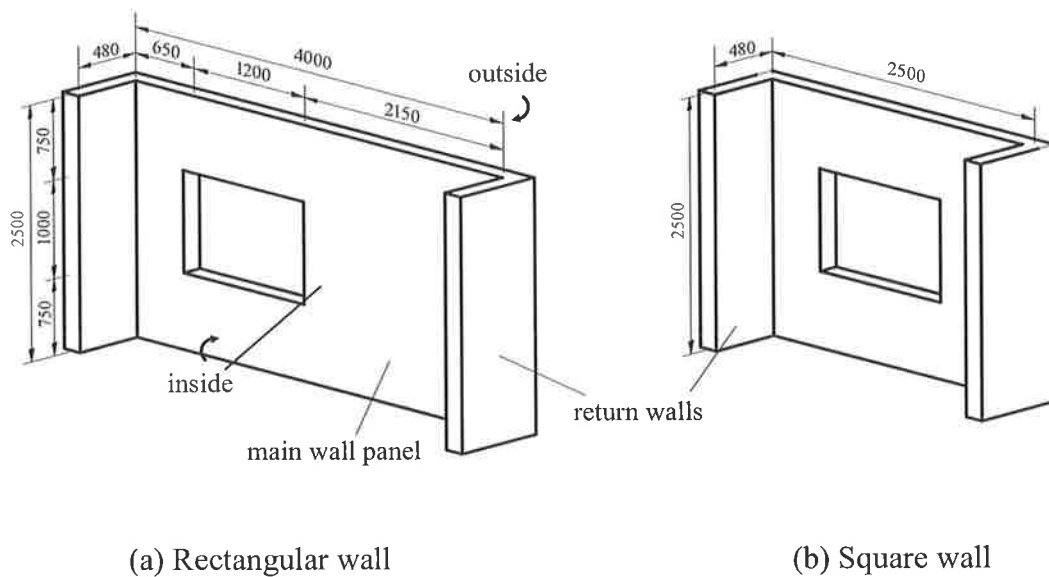


Figure 5.1 Masonry wall specimens

The previous research of masonry wall under out-of-plane loading had considered various parameters including wall geometries, effect of axial precompression and

different boundary conditions. The general configurations of the masonry walls previously tested are illustrated in Table 5.1.

Table 5.1 Masonry wall configurations in previous experimental study

	Wall Geometry and Support Conditions
Rectangular wall	<p style="text-align: center;">vertical precompression</p>
Square wall	<p style="text-align: center;">vertical precompression</p>

Notes: F= Fixed support; SS=Simple support;

idealised cracking pattern is shown on the walls.

In the previous tests, the vertical edges of each wall were restrained against rotation by the vertical returning walls, and thus considered to be full moment restraints with intermediate fixity. All top and bottom horizontal edges were treated as simply supported. Vertical precompression was exerted on the top of the walls as shown in Table 5.1.

Each wall was tested in two distinct phases. The first test phase was a unidirectional static test, during which pressure was applied only to the outside face (see Figure 5.1) of the wall using the airbags until cracking occurred and its ultimate load capacity reached. Therefore, the static strength and the collapse mechanisms of the masonry wall specimen were both determined. The second, cyclic testing was subsequently conducted on the cracked walls, during which loading was alternated between the positive and negative directions, by means of airbags positioned on both sides of the wall. Thus, the post-cracking strength of the masonry walls under out-of-plane cyclic loading and the resulting load-displacement behaviour were observed and studied.

The previous masonry wall test results are used in this study as reference data for comparison of the out-of-plane bending behaviour with the test results of FRP repaired damaged masonry walls. One rectangular wall and one square wall, tested under the same boundary conditions as the current FRP repaired wall test, were considered as the control wall and hereafter called Wall_{RC} and Wall_{SC}, respectively. The test results of the two reference walls are described as below.

Figure 5.2 shows the static behaviour and envelope of cyclic behaviour of both Wall_{RC} and Wall_{SC} under two-way out-of-plane bending. The original and residual capacity of Wall_{RC} was 5.1 kPa and 2.4 kPa, respectively, while the original strength of Wall_{SC} was 8.7 kPa and the residual strength was 4.9 kPa at completion of the cyclic test.

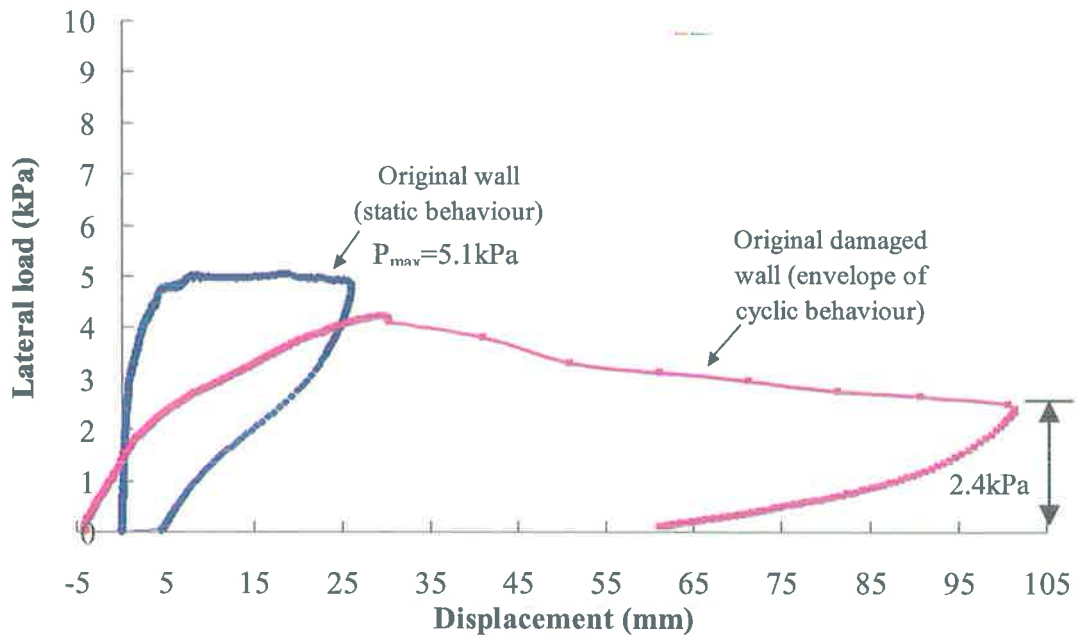
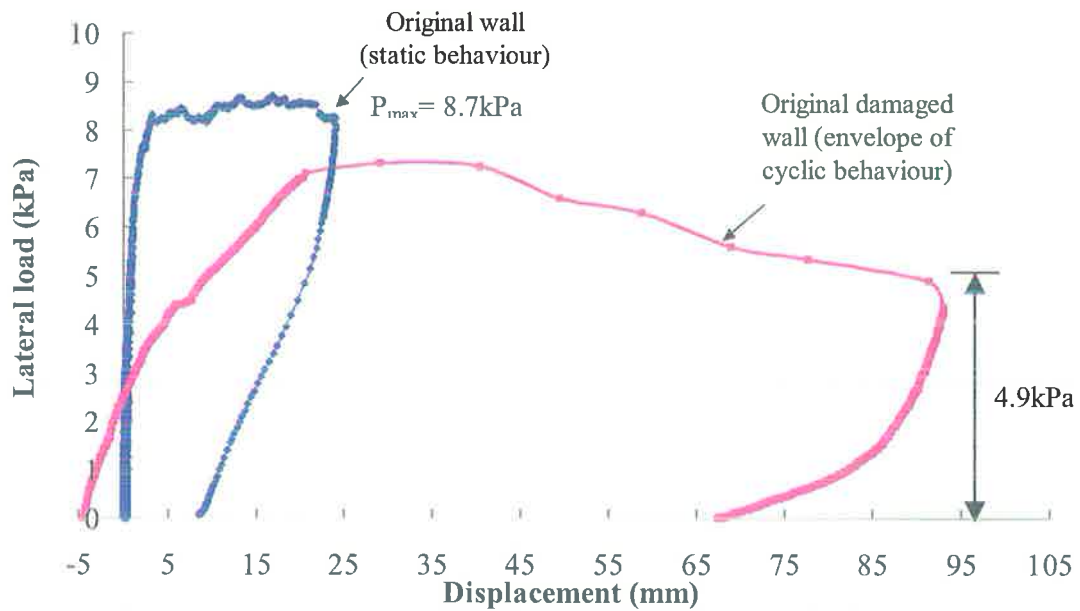
(a) Rectangular control wall ($Wall_{RC}$)(b) Square control wall ($Wall_{SC}$)

Figure 5.2 Load-displacement behaviour of control walls

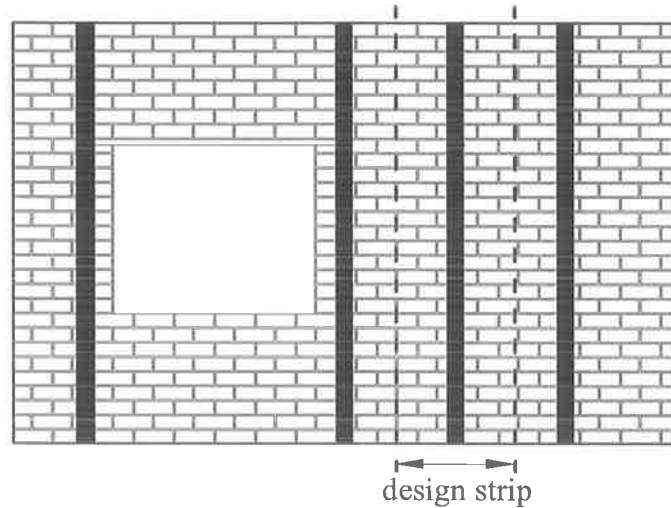
5.2.2. Design for FRP Strengthening Schemes for Damaged Masonry Walls

As discussed in Chapter Two, the cross section analysis method can be used to predict the one-way vertical bending capacity of FRP retrofitted masonry panel by simply beam theory. A similar method, based on strain compatibility, was used to design the vertical FRP strips assuming an idealised failure mode, namely FRP strip debonding failure at the same time as the ultimate compressive crushing strain is reached in the masonry. As shown in Figure 5.3, to determine the geometry of FRP strip for a wall design strip (Figure 5.3 (a)) at the idealised failure mode, this design strip can be represented as a masonry beam with an FRP strip fixed to its tension face (Figure 5.3(b)). The strain and stress distribution is shown in Figure 5.3 (c).

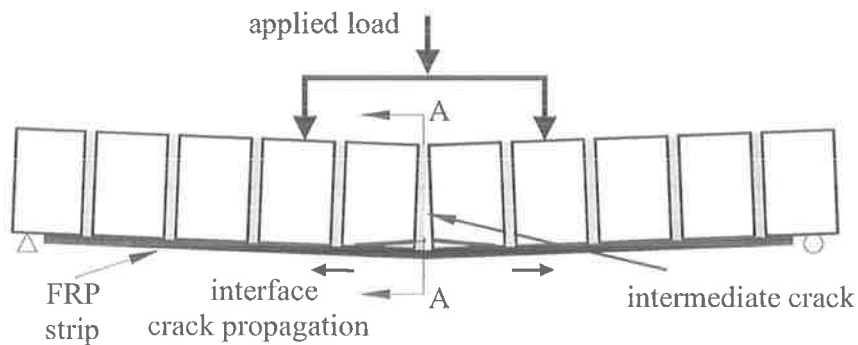
For preliminary design of the FRP strip, strain compatibility without slip was assumed along the cross-section so that the tensile force developed in FRP strip, T_p , and compressive force in masonry, C_m , the depth of neutral axis c , geometry of the FRP strip and the nominal bending moment M_n could be determined. The FRP strip debonding strain ε_{db} used in the design was determined using the FRP-to-masonry bond model developed in Chapter 4.

Three strengthening schemes were designed for the previously tested three rectangular masonry wall specimens by varying the FRP material (carbon FRP or glass FRP) and FRP strip spacing. The resulting design, together with the nominal vertical bending moment capacity, M_{cv} , are summarised in Table 5.2 for the four walls strengthened with FRP strips and tested in this study. Wall 1 was strengthened by four 50 mm wide x 1.2 mm thick CFRP pultruded strips spaced at 650 mm with two strips placed adjacent to the opening as shown in Table 5.2 (a). Wall 2 (Table 5.2 (b)) was repaired using four 100 mm wide x 2.0 mm thick prefabricated GFRP strips with the identical positioning as for wall 1. In order to study the effect of the FRP spacing, Wall 3 (Table 5.2 (c)) was designed to have the same M_{cv} as Wall 2, which was repaired with five 77

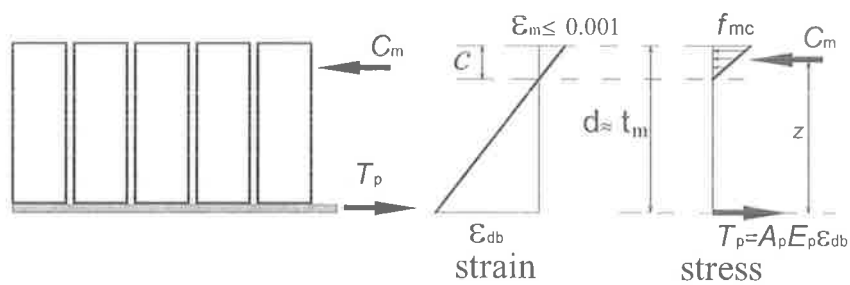
mm wide x 2.0 mm thick prefabricated GFRP strips spaced at 500 mm, with two strips also placed adjacent to the window opening.



(a) FRP retrofitted masonry wall



(b) Vertical bending of a wall design strip

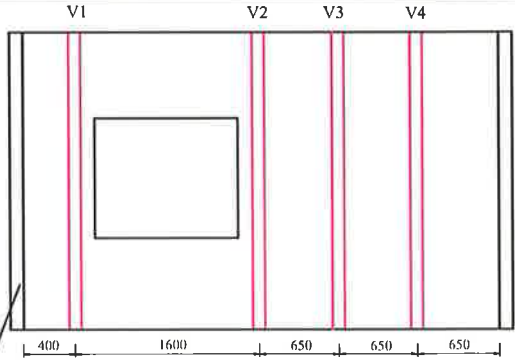
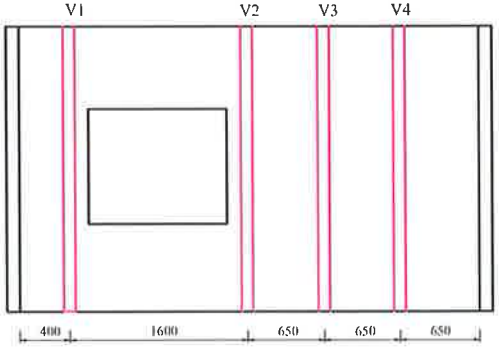


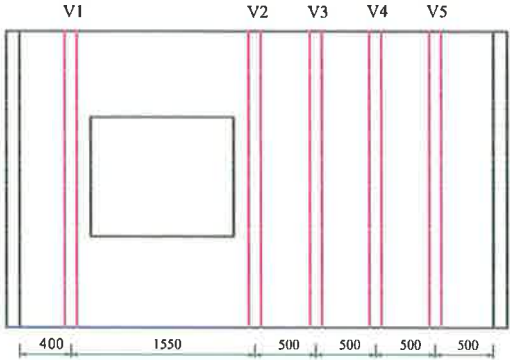
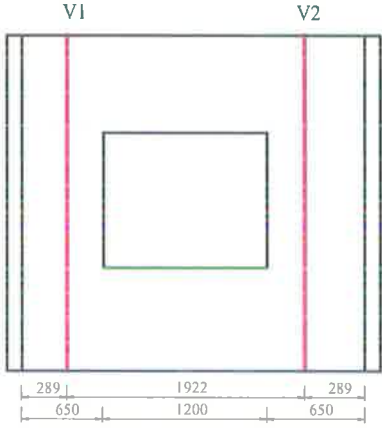
(c) Strain and stress distribution at section A-A

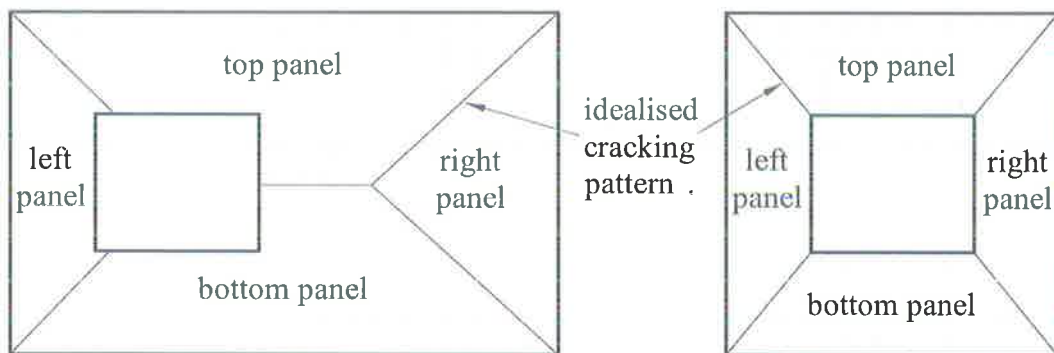
Figure 5.3 FRP strip design

A similar analysis method was used to design the CFRP NSM square wall repair. Two CFRP strips, 20 mm wide x 1.4 mm thick, were applied to repair wall 4 using the NSM method. The full design process is given in Appendix D. All four FRP repaired walls were tested under 0.1 MPa of vertical precompression with the same edge support conditions as the control masonry wall tests (i.e. simply supported along top and bottom, intermediate rotational fixing along two vertical edges). For simplicity, the FRP strips are labeled as V1 to V4 (or V5) going from left to right (see Table 5.2), and the wall sub-panels were labelled as left panel, right panel, top panel and bottom panel as shown in Figure 5.4.

Table 5.2 Strengthening schemes of FRP retrofitting masonry wall test

Wall	Strengthening Schemes	b_p (mm)	s (mm)	M_{cv}
				(kNm)
1	 <p>(a) EB CFRP Wall 1</p>	50	650	5.3
2	 <p>(b) EB GFRP Wall 2</p>	100	650	7.75

<p>3</p>	 <p>(c) EB GFRP Wall 3</p>	<p>77</p>	<p>500</p>	<p>7.75</p>
<p>4</p>	 <p>(d) NSM CFRP Wall 4</p>	<p>20</p>	<p>-</p>	<p>7.0</p>



(a) rectangular wall

(b) square wall

Figure 5.4 Definition of wall sub-panels

5.2.3. FRP Retrofitted Masonry Wall Test Set-up

The FRP strengthened wall test set-up included the wall surface preparation, FRP plating, set-up of steel reaction frame, four-side supports and airbags. The pre-existing cracks in the wall specimens were not repaired except for those in wall 3. Because wall 3 was previously tested without any support along the top edge, the pre-existing cracking pattern of wall 3 was different from those for the 4-side supported walls (i.e. wall 1 and wall 2). To avoid the impact that this alternate cracking pattern might have on the behaviour of the wall after strengthening, the pre-existing cracks in wall 3 were repaired prior to apply the FRP strips. Therefore, the impact of crack repair on wall behaviour was also investigated through comparison of the behaviour of wall 3 with that of wall 1 and wall 2.

Surface preparation of masonry wall specimens

Before applying externally bonded FRP strips, the masonry wall surface was prepared by a sander as this was found to be the most effective method (refer to Section 3.3.3). The inside-face of the wall was first marked where the FRP strips were to be bonded. Then the masonry surfaces were sanded and also cleaned up using a wire brush and compressed air. Figure 5.5 shows the prepared wall surface of wall 1. Wall 3 was repaired using mortar with the same mix that was used in the original wall construction.

For the near surface mounted retrofitting method, wall 4 was first marked with the position for the two FRP strips, and then vertical straight grooves were cut through brick units, approximately 1/4 brick length away from the perpend joints, using a circular saw. Figure 5.6 shows the grooves cut in wall 4. These grooves were later vacuumed thoroughly and washed by acetone before bonding the FRP strips.

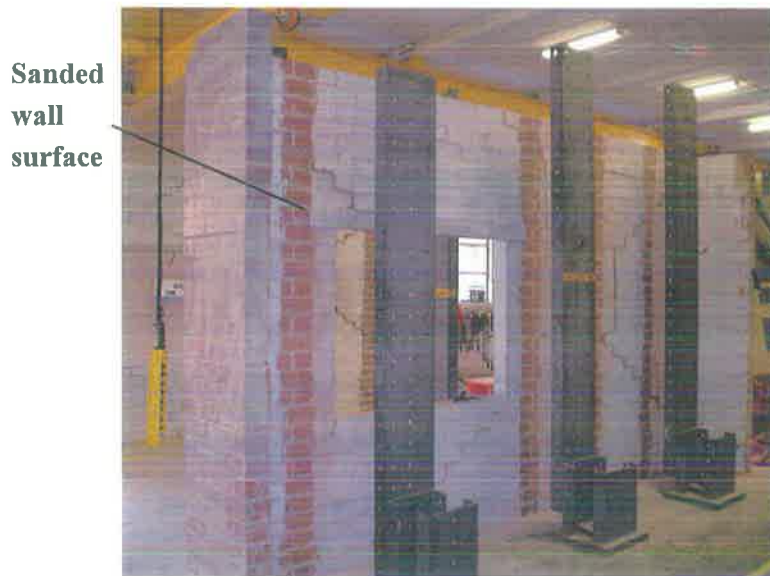


Figure 5.5 Surface preparation of FRP EB wall (Wall 1)

Grooves cut 1/4 brick length away from perpend joints

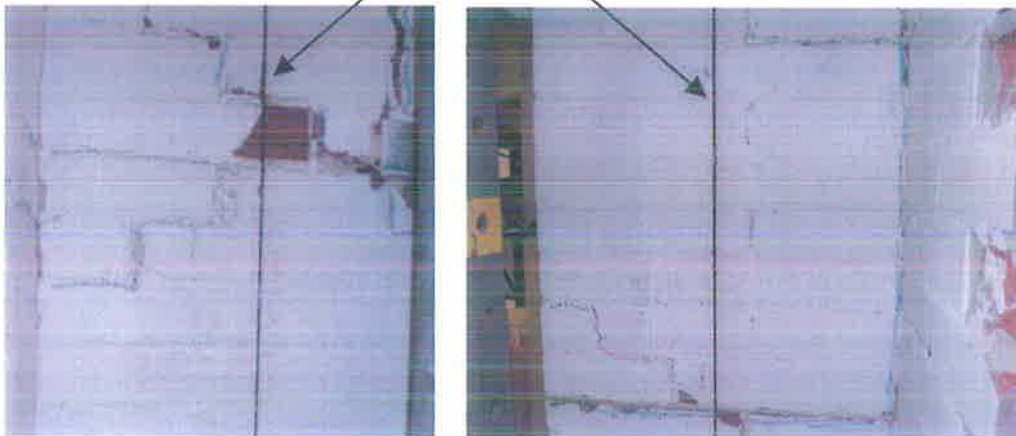


Figure 5.6 Grooves cut in masonry wall (Wall 4)

FRP installation

The glass FRP strips were prefabricated from two-layer glass fibre sheet as that used in the FRP-to-masonry bond tests (refer to Section 3.2.2 prefabricated method). The carbon FRP was 50 mm wide x 1.2 mm thick pultruded strip that was ready to use for Wall₁. The two 20 mm wide x 1.2 mm thick near surface mounted carbon FRP strips for wall 4 were cut from the 50 mm pultruded strips.

Before bonding the FRP strips onto the masonry wall, the bonding surfaces of both masonry walls and FRP strips were washed with acetone to remove any foreign substances. The adhesive was then plastered onto the contact surfaces of both the masonry and FRP strips as shown in Figure 5.7 (a). Subsequently, the FRP strip was carefully installed onto the masonry wall at the proper position as shown in Figure 5.7 (b). The top surface of FRP was then rolled using a metal roller in order to impregnate properly the FRP strip with adhesive. Finally, a uniformly distributed load was exerted on the FRP strip using a plywood batten together with a steel strut, supported by the steel frame using a group of timber wedges, as shown in Figure 5.7 (c). The excess adhesive squeezed out was scraped off the masonry wall. The exerted pressure was withdrawn after 24 hours and the adhesive was cured for at least seven days prior to testing.

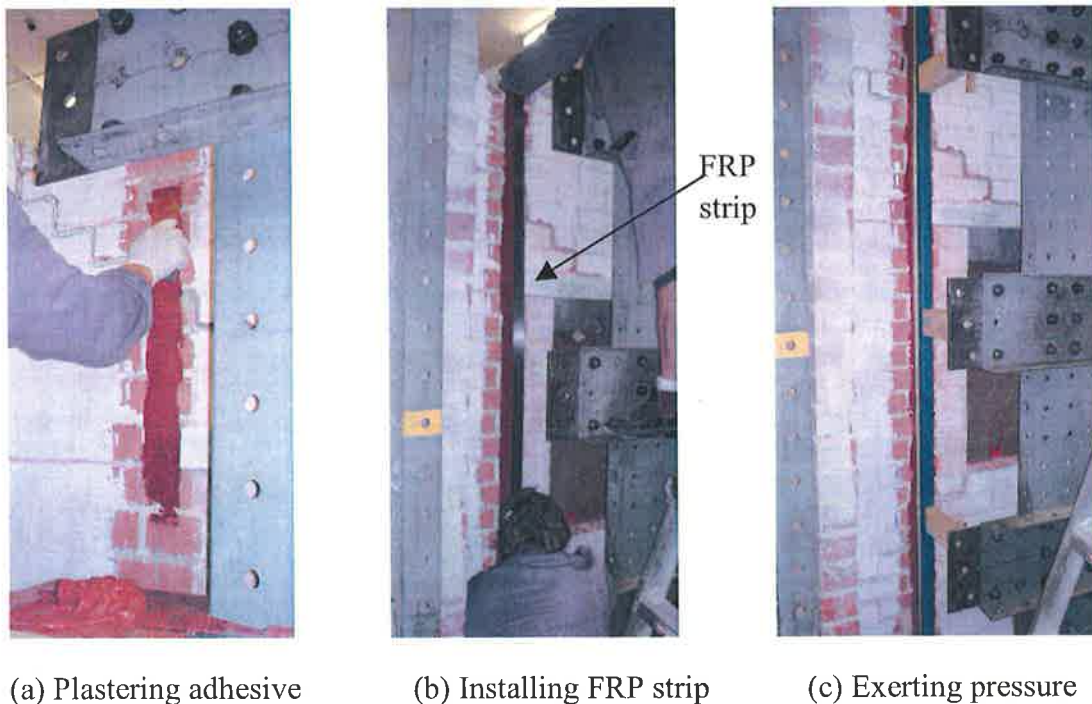


Figure 5.7 FRP EB onto the masonry wall

The FRP strip installation for the near surface mounting method of wall 4 was similar to that of the CFRP-to-masonry bond test. The near surface mounted carbon FRP strips were strain gauged before being plated into the grooves. The strain gauge

positions for wall 4 are reported in Section 5.2.4. The application process for the NSM CFRP strips consisted of the following steps (after the grooves have been cut):

- 1) applying dust tape along the outer sides of FRP strip locations on the masonry wall surface;
- 2) washing both the masonry grooves and CFRP strips with acetone;
- 3) strain gauging the CFRP strips at design locations;
- 4) plastering adhesive onto the contact surfaces of both the masonry grooves and CFRP strips; and,
- 5) embedding the CFRP strips into the adhesive-filled grooves and removing excess adhesive and dust tapes.

The strengthened wall specimen was left for seven days before testing, to allow the full bond to develop.

Boundary conditions

An important aspect of these tests was the care taken to achieve precise boundary conditions along the four edges of the wall. The detailing used to provide restraint to the walls, and their implications for analysis are briefly discussed in this section, because it is similar to the previous tests. For full details, please refer to Griffith and Vaculik's study (2005).

(1) Vertical edges

As mentioned in preceding sections, all four wall specimens used in this experimental study were tested to failure in previous tests by Griffith and Vaculik (2005). The connection zones between the main wall and return walls were also badly cracked, as shown in Figure 5.8, which means that the return walls could no longer provide full moment restraint along the two vertical edges of the main wall. However, when supported by the side steel frames, the return walls were still expected to restrain the

lateral movement of the main wall during loadings, as shown in Figure 5.9 (b).

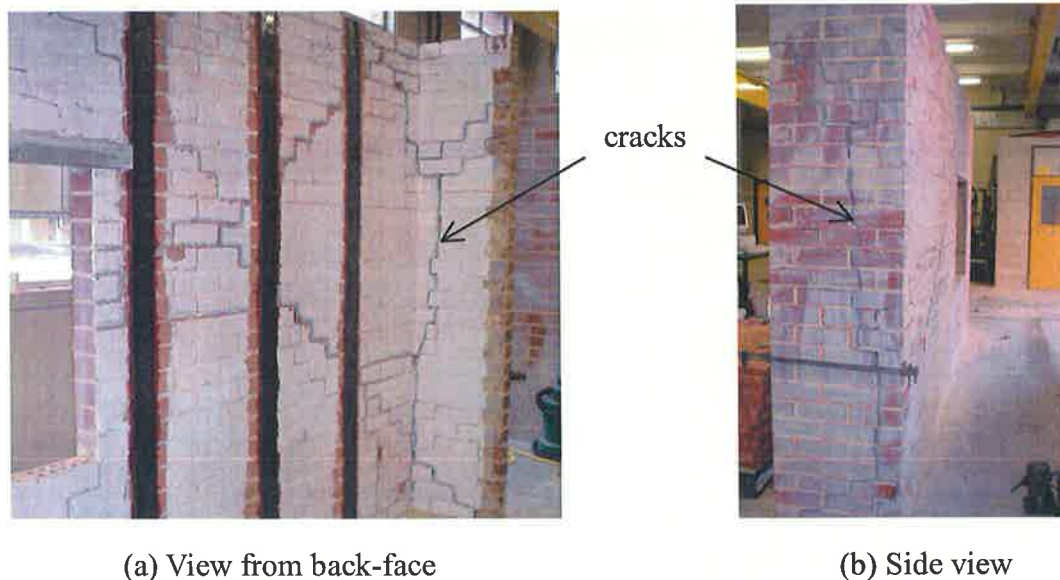


Figure 5.8 Damaged connection between main wall and return wall

(2) Bottom edge support

The arrangement of supports is depicted in Figure 5.9 (a). A similar arrangement of bottom edge support was adopted. This consisted of a steel member placed adjacent to the full length of the bottom edge of the wall specimens and connected back to rigid steel bases using a group of steel struts as shown in Figure 5.9 (c). A simple support was then achieved along the bottom edge, which allowed the rotation of the main wall and restrained the lateral movement at this edge.

(3) Top edge support

A long steel member was firmly connected onto each sideward steel frame. On the same side as the FRP strips, another steel member was connected to the previous one through a group of steel angles to provide the restraint of lateral movement along the top edge, while the rotation of the main wall panel was allowed along this edge as shown in Figure 5.9 (d). Therefore, the top edge was regarded as a simple support. Unlike the arrangement in previous tests, the top edge support in this test program was designed to be separate from the vertical precompression system to avoid the

potential mutual influences during loading and improve the accuracy of the support conditions.

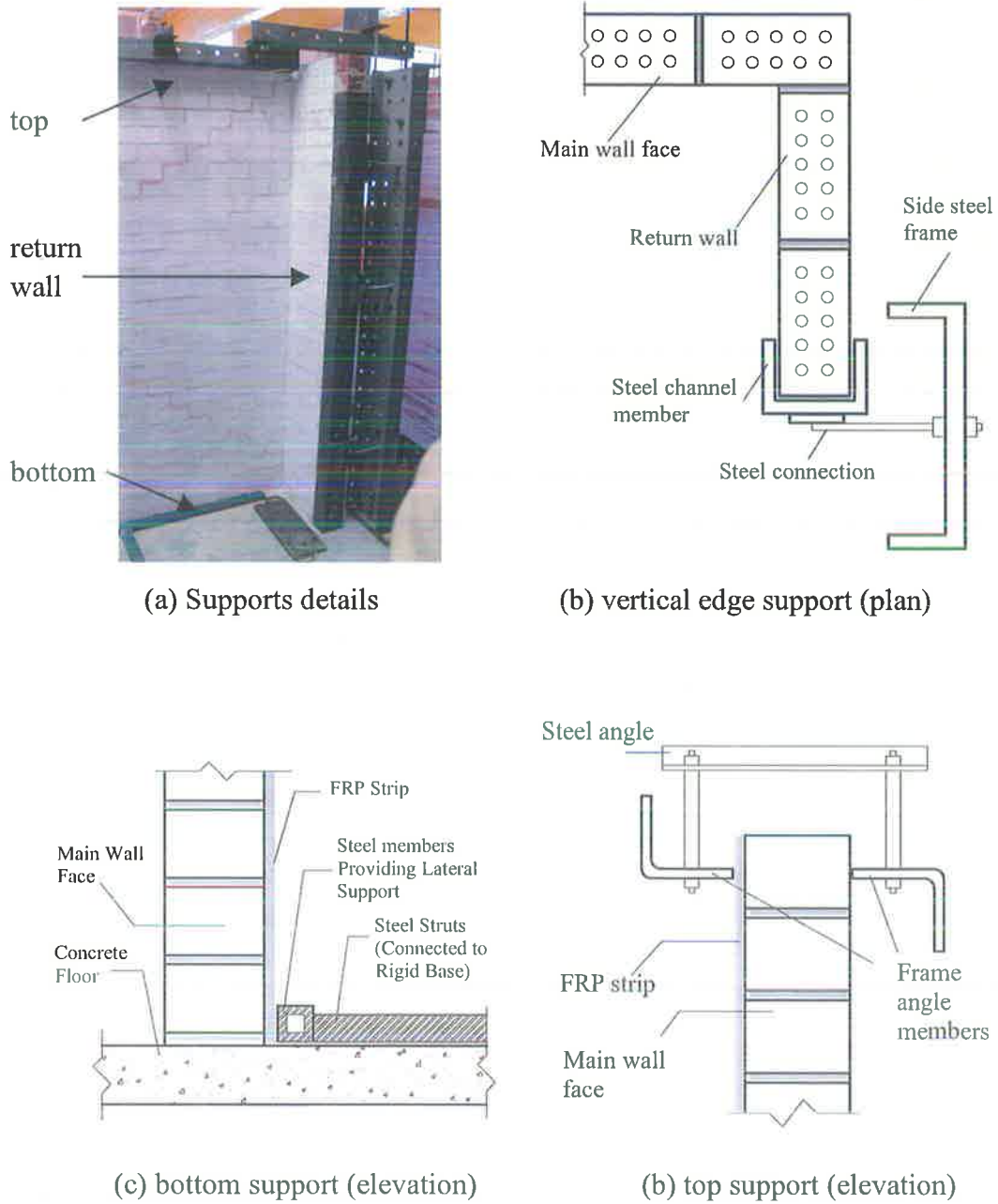


Figure 5.9 Wall support details

Vertical precompression

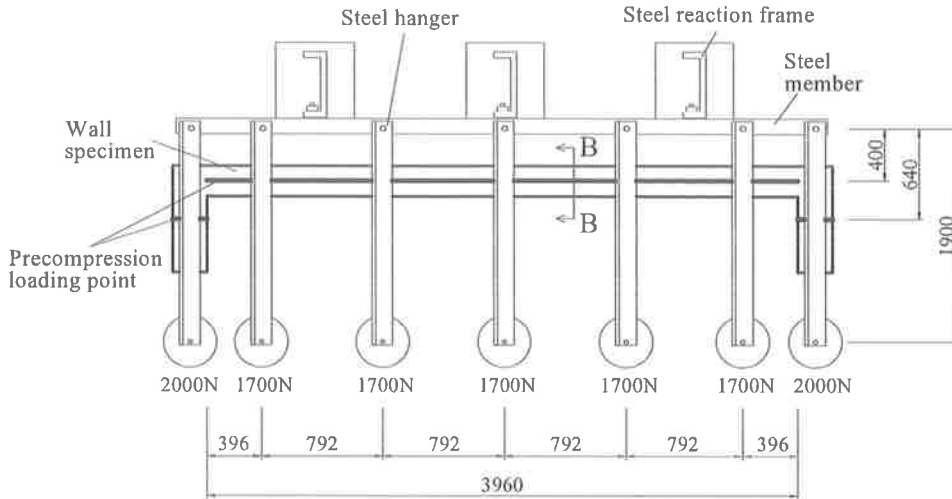
Because the walls were “pre-cracked from the prior cyclic test by Griffith and

Vaculik (2005), all the FRP repaired masonry wall specimens were tested under 0.1 MPa vertical precompression. This could be expected to reduce the effect of gaps due to pre-existing cracks, and also increase the friction in masonry bed joints, consequently improving the integration of the wall specimens. The arrangement used to achieve this is illustrated in Figure 5.10 (a). Five steel hangers were distributed evenly along the top of the main wall, plus one hanger on each return wall. These seven steel hangers were supported by a steel bar used to apply the vertical reaction as a point load in order to give precise control over the length of the lever arm. Weights of 1700 N and 2000 N were hung from the steel hangers set on the top of the main wall and return walls, respectively, which exerted a magnified force onto the wall by leverage. It is obvious from Figure 5.10 (a) that the lever ratio is 4.75 (1900 mm / 400 mm) and 2.97 (1900 mm / 640 mm) for the main wall and return walls, respectively. The weight of the steel hangers were also considered in the arrangement of precompression.

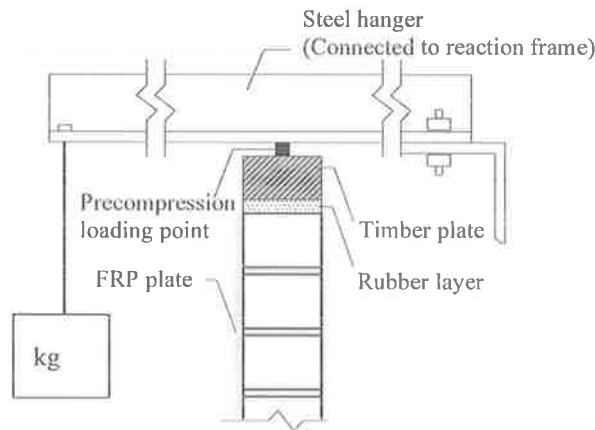
Timber plates and a layer of rubber were matted underneath the thin steel bar in order to transmit the load uniformly and result in more even distribution of the vertical pressure onto the wall as detailed by Figures 5.10 (b) and (c) for main wall and return wall, respectively.

Airbags and steel resisting frames

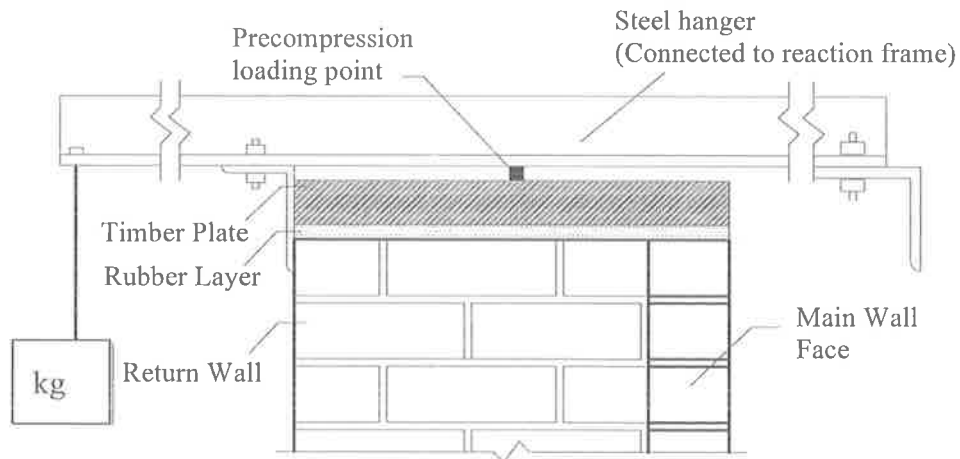
In each wall test, lateral pressure was applied onto the test wall using airbags mounted on a rigid backing board consisting of plywood and a steel frame (see Figure 5.11 (a)). In turn, the backing board was supported by four load cells, which were connected to the rigid back steel frames. A number of small bags were used instead of a single large bag, because this arrangement could minimise the membrane action in the airbags during loading. It should also be noted that in testing the walls with opening, load was applied only onto the solid portions of the wall, and not onto the window opening.



(a) Plan view of precompression arrangement



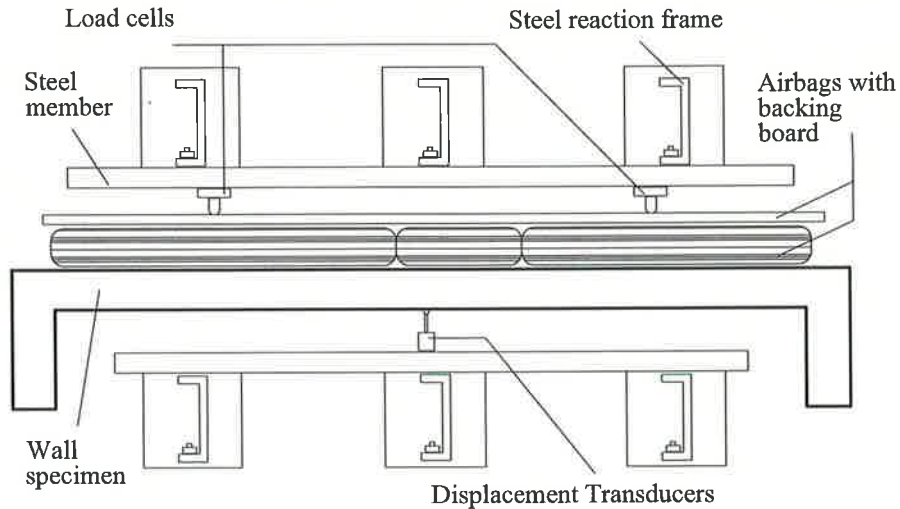
(b) Cross section of Precompression arrangement on main wall (B-B)



(c) Elevation view of Precompression arrangement on return wall

Figure 5.10 Details of precompression arrangement

During each test, the airbags were slowly inflated using an electric pump regulated by an electronic pressure controller to apply a uniform lateral pressure onto the face of the wall. The lateral force exerted on the wall was equal and opposite to the total reaction force exerted onto the backing frame, which was measured by four load cells shown in Figure 5.11 (a).



(a) Plan view of overall test arrangement



(b) Front view of overall test arrangement of wall 1

Figure 5.11 Overall test arrangement

5.2.3. Instrumentations

Load measurement

As shown in Figure 5.12, load cells were installed between the airbag backing board and the steel reaction frame to measure the reaction force exerted onto the wall face and conveyed the data to an acquisition system. The load cells were first calibrated to measure loads up to 50 kN. Considering that the maximum airbag pressure was 20kPa, four load cells were able to carry and measure the reaction forces within its measuring capacity. In the determination of load cell positioning for the test walls (see Figure 5.13), consideration was given to ensuring that the loads exerted onto each of the load cells were of similar magnitude.



Figure 5.12 Load cell connections

In addition to the load cells, which were used as the primary load measurement system, two pressure transducers were used inside the airbags to monitor the air pressure. Because of inherent inefficiencies involved in the conversion of the air pressure inside the airbags to a surface pressure acting onto the wall face, these measurements of the air pressure were recognised to overestimate the actual load exerted on the main wall face and were used only as indicative estimates to control

the pressure within the airbags during testing. It was noted from the previous study that the actual face pressure based on the reaction forces measured by load cells was typically 75%-80% of the air pressure measured within the airbags (Griffith and Vaculik, 2005).

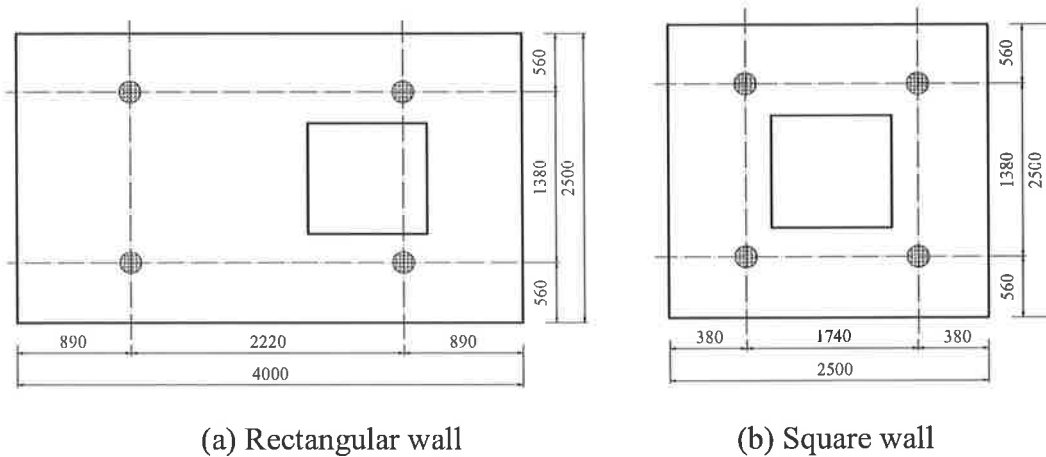


Figure 5.13 Load cell positioning (view from wall outside face)

Strain and displacement measurement

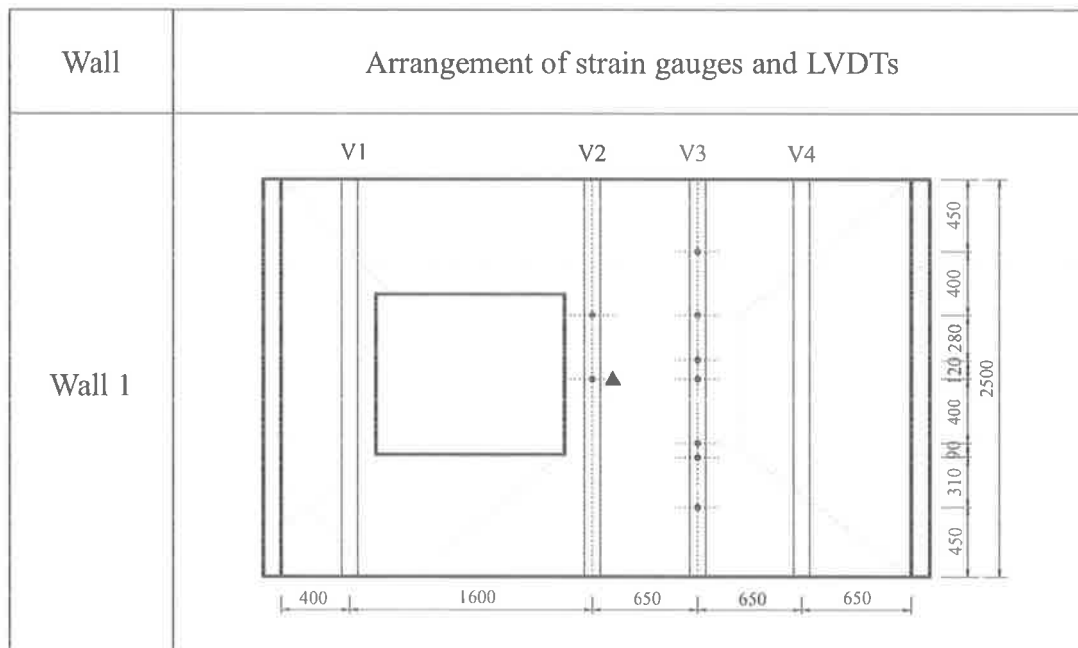
The mid-height of FRP strip was considered to be the location to measure the maximum strain, as this was where horizontal cracks already existed. However, the pre-existing cracks were regarded to have some impact on the tensile force in an FRP strip when it crossed a crack line, for there might be stress concentration in the FRP strip at the intersection with a crack line caused by the opening of the crack when loading. Due to the limitation of data acquisition channels, only nine strain gauges were used for wall 1, 2 and 4. Strain gauges were only located at the most critical positions on FRP strips of the three walls. The data acquisition system was upgraded for the test of wall 3 to allow 31 strain gauges to be used and distributed evenly along all five FRP strips for wall 3.

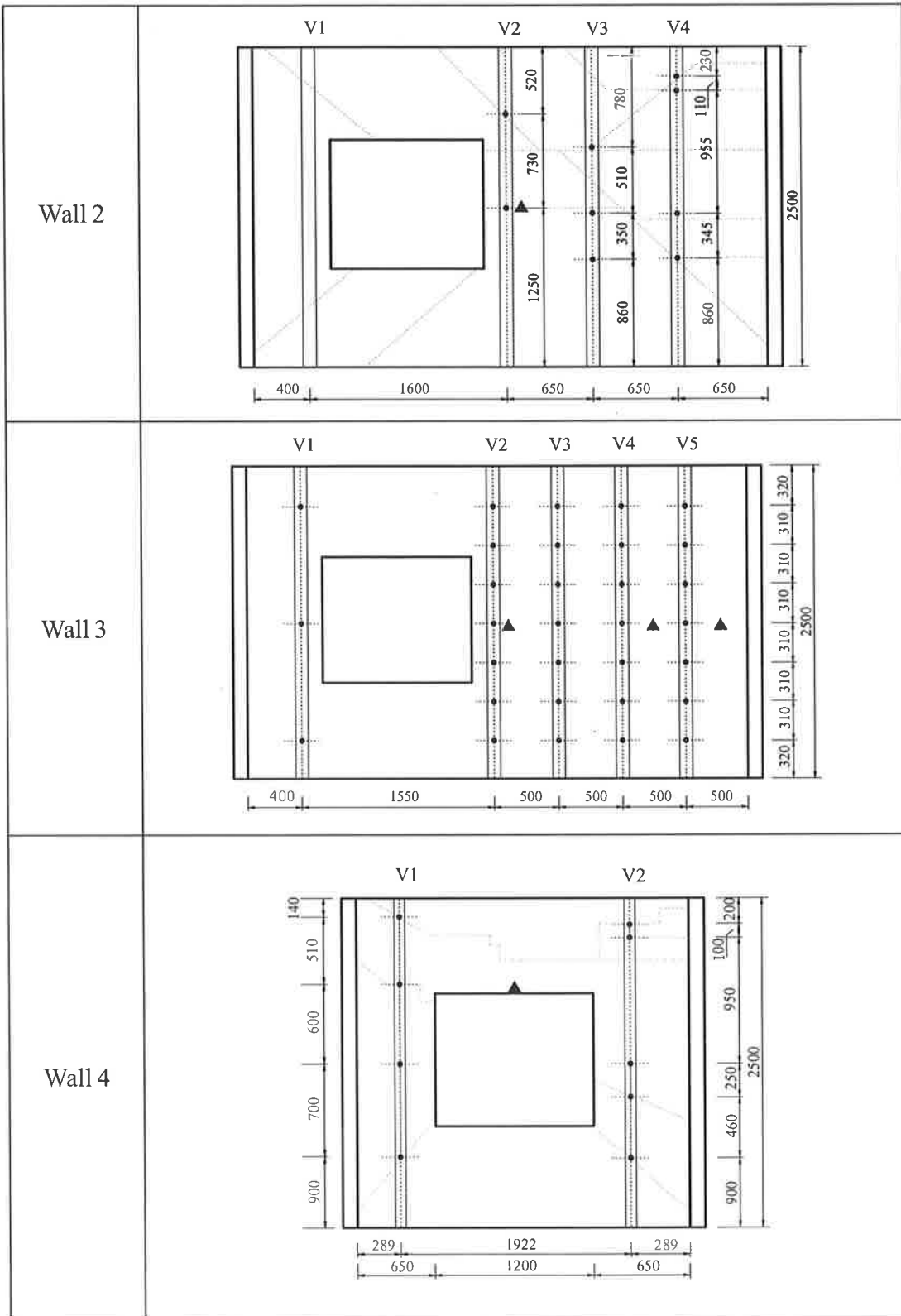
Linear variable differential transformers (LVDTs), accurate to ± 0.01 mm, were used to measure the displacement of the wall during loading. As the centre of the wall was deemed to experience the maximum deflection, the LVDT was positioned at the

centre of each rectangular wall, while adjacent to the centre of the upside edge of opening for the square wall. Due to an upgraded data acquisition system for the test of wall 3, two additional channels were used for LVDTs placed along the mid-height to study the deflection profile of the repaired wall.

The arrangement of strain gauges and LVDTs for each wall is shown in Figure 5.14. The major pre-existing cracking patterns for each wall except wall 3 are shown in light dashed lines. It can be seen that the FRP strips near the vertical edges (e.g. strip V1 and V4 or V5 for the rectangular walls, and V1 and V2 for the square wall) were typically intersected by diagonal cracks near their ends. On the contrary, the strips near the centre (e.g. V2 for the rectangular walls) were mainly intersected by mid-height horizontal cracks. And strip V3 was intersected by both diagonal and horizontal cracks.

Figure 5.14 Arrangement of strain gauges and LVDTs





Legend ● strain gauges ▲ LVDTs — major pre-existing cracks
 All dimensions in mm

5.3. EXPERIMENTAL RESULTS OF FULL-SCALE WALL TESTS

5.3.1. Overall Behaviour of FRP Retrofitted Masonry Wall

The results for the FRP strengthened walls tested under static monotonic out-of-plane load are briefly summarised in Table 5.3 together with the results of the unstrengthened control walls reported from Griffith and Vaculik's study (2005). The FRP repaired walls were significantly stronger in out-of-plane bending and maintained this strength for very large displacement (see Figure 5.15). It can be found from the test results that the out-of-plane strength had been doubled and the displacement of the repaired wall at which peak load was reached was also increased significantly.

Table 5.3 Results of the FRP repaired full-scale wall test

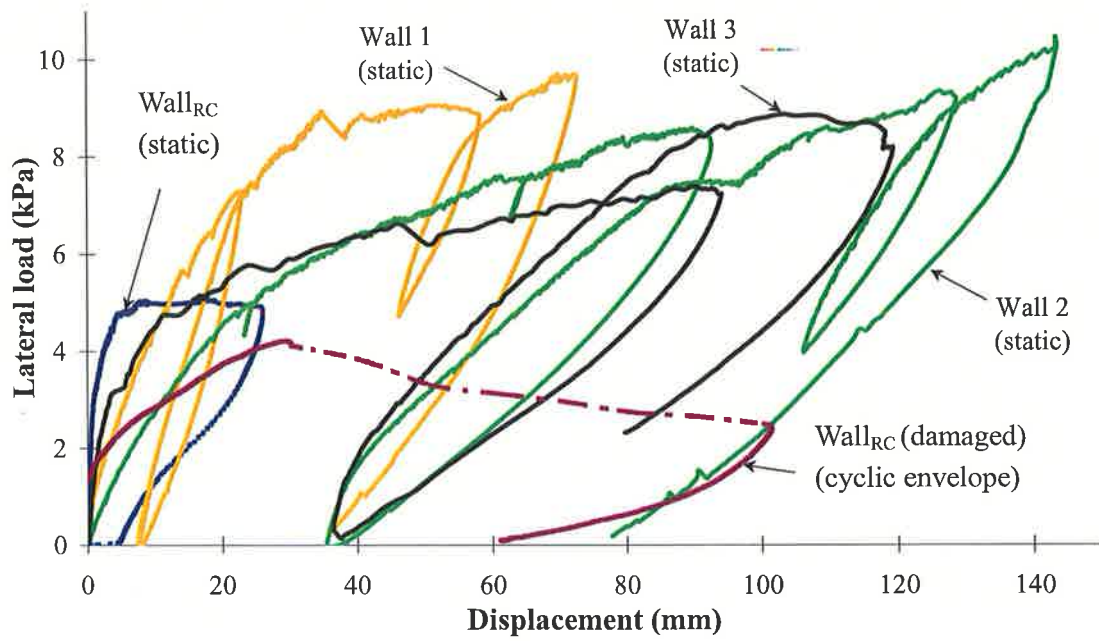
Specimen	P_u (kPa)	$\Delta_u^{(b)}$ (mm)	$\epsilon_{p, \max}$ ($\mu\epsilon$)	Mode of Failure	
				Masonry	FRP
Wall _{RC} ^(a)	5.1	25.2	-	Two-way bending	-
Wall 1	9.7	72.7	4729	Cracking	Debonding V4
Wall 2	10.5	143.5	12412	Cracking & collapse	No FRP failure
Wall 3	12.1	119.4*	10117	Cracking & collapse	Debonding V5
Wall _{SC} ^(a)	8.7	26.5	-	Two-way bending	-
Wall 4	8.2	101.7 [†]	5897	Cracking	Debonding V2

Note: Wall_{RC} = Rectangular control wall; Wall_{SC} = Square control wall

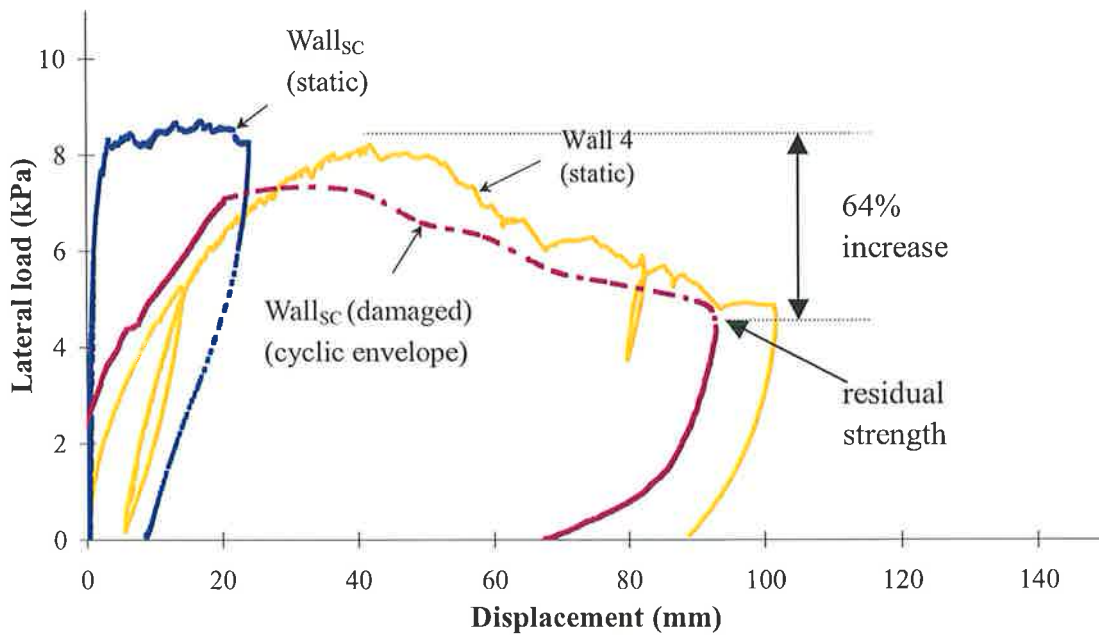
(a) Data reported in Griffith and Vaculik's study;

(b) Ultimate displacement at centre;

*: Ultimate displacement did not occur at the maximum load



(a) Rectangular walls



(b) Square wall

Figure 5.15 Comparison of load-displacement behaviour for walls

The FRP strips proved to be effective in improving the out-of-plane strength and the ductility of masonry walls, for they not only carried the tensile forces in the tension side, but also helped to hold the masonry units together and restrained the cracking of

masonry in the horizontal direction due to vertical bending. The pre-existing horizontal cracks enlarged and there was almost no new horizontal cracking observed during testing. Even the displacement measured at the centre of the wall exceeded 70 mm and reached 143.5 mm for Wall 2. The maximum measured strains mostly occurred at either the FRP mid-height or at intersections with pre-existing cracks, where tensile forces were concentrated. In addition to the structural response, the masonry cracking patterns of repaired walls were found to be similar to the control walls at lower load levels but changed significantly at higher load levels. For the rectangular walls, when the lateral pressure was under approximately 5-6 kPa (i.e. the capacity of original undamaged masonry wall), the pre-existing cracks were only slightly increased, while no new cracking occurred until the displacement exceeded approximately 30 mm. The behaviour and modes of cracking and failure of each wall will be later discussed separately. The lateral load used in the study is the face pressure acting on the wall, which was computed by dividing the total reaction force exerted on the wall measured through the four load cells by the net wall area assumed to equal the sum of the surface area of total air bags.

For simplicity, the wall segment between two FRP vertical strips i and $i+1$, is simply called segment V_{i-i+1} , and the left and right vertical edges are denoted by 'LE' and 'RE'. For example, segment V_{4-RE} denotes the wall segment between vertical strip V_4 and the wall right vertical edge.

5.3.2. Individual Behaviour of FRP Retrofitted Masonry Wall

Wall 1 (Externally bonded carbon FRP retrofitted wall)

The load-deflection response of Wall 1 is shown in Figure 5.16. The loading process consisted of three phases (phase 1: A-B-C; phase 2: C-D-E; phase 3: E-F-G). The load was first increased slowly to B (at around $P=7.3$ kPa and $\Delta=23.3$ mm), and one load

cell was found to be out of order due to a wire connection problem. The wall was unloaded to C. After the load cell was fixed, the wall was reloaded in the second phase from C with an initial displacement of 7.6 mm, during which the pre-existing cracks were found enlarged. After the load reached the first peak at point H, (approximately $P=8.9$ kPa and $\Delta=35.1$ mm), a number of new cracks occurred in wall segment V_{1-2} . After a small drop in strength, the load climbed up again and was maintained at a high level of around 9 kPa, while the displacement increased to about 55 mm.

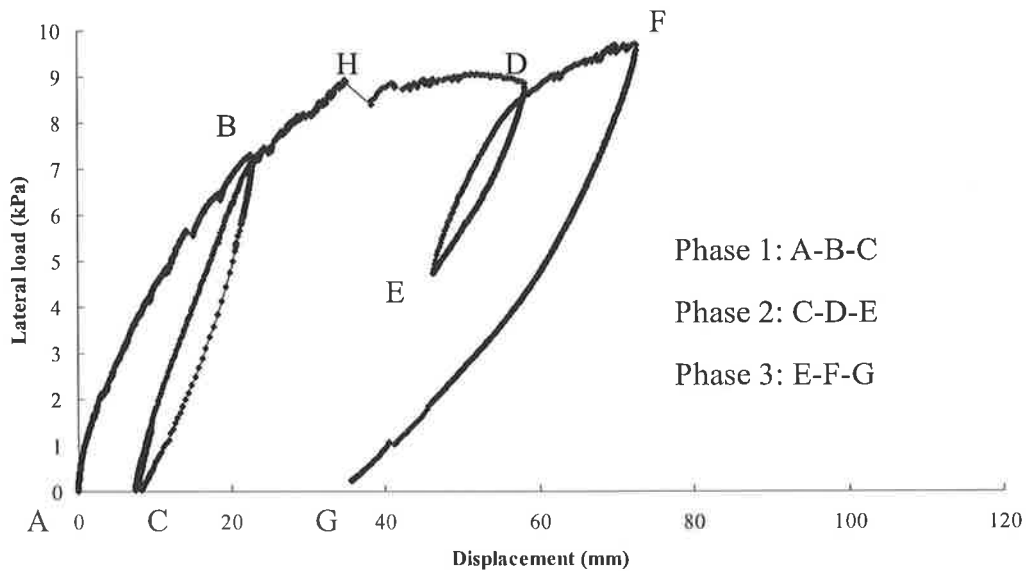


Figure 5.16 Lateral load-Displacement behaviour for Wall 1

During this increase in displacement ($H \rightarrow D$), the new cracks continued to form as well as the major pre-existing cracks enlarged. The wall was then unloaded from D (at approximately $P=8.9$ kPa, $\Delta=58$ mm) to E (at approximately $P=4.7$ kPa, $\Delta=46$ mm), where the load was held for closer inspection of cracking development. As shown in Figure 5.17, the new cracking mainly consisted of diagonal cracks above the window, and a series of short vertical cracks in the segment V_{3-4} , which connected the pre-existing horizontal cracks and also propagated towards the top and bottom of this wall segment. After this crack inspection, the loading was increased again, starting from E, until strip V4 debonding failure occurred at F (at $P_u=9.7$ kPa, $\Delta_u=72.7$ mm).

The debonding failure originated from the intersection of a major bottom diagonal pre-existing crack, and the strip V4 (location 'circled' in Figure 5.17) due to the large relative displacement between the masonry units sitting above and beneath the diagonal crack. The rotation of the right wall panel (refer Figure 5.4 for the definition of wall sub-panels) about the right vertical edge was comparatively larger than the top and bottom panels, because the vertical strips restrained the rotation of wall sub-panel about the horizontal edges more effectively. A maximum local offset displacement of 52 mm was measured along the boundary between the right and bottom panels (refer Figure 5.18). The FRP strips were effective in holding the wall panel and prevent the failure of the wall until shear failure occurred in the masonry units at the intersection of the lower diagonal pre-existing crack and strip V4 due to the peeling action in both the vertical and horizontal directions. The debonding of FRP then propagated both upwards and downwards until the segment of FRP below the diagonal crack was completely debonded.

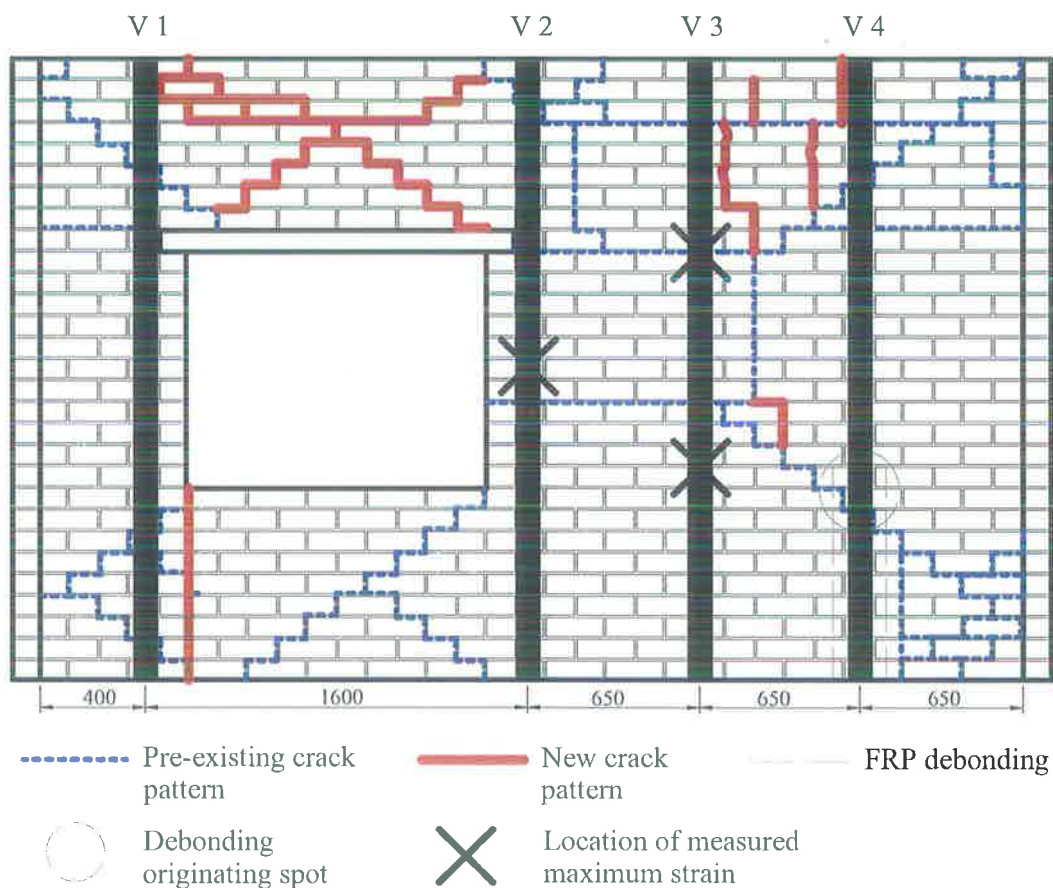


Figure 5.17 Schematic of cracking pattern and FRP debonding of Wall 1

Unlike IC debonding, this debonding failure mode was caused by the peeling action due to the differential displacement between wall sub-panels and was not at all simulated by the push-pull test. This peeling debonding is a new debonding failure mode that has not been quantified. It can be simulated as shown in Figure 5.18, through observing the failed masonry unit at the debonding point of origin and analysing the behaviour of right portion of the main wall panel. Figure 5.18 (a) shows the peeling action acting on the FRP strip due to the relative displacement between wall sub-panels, mainly caused by rotation of the right panel about the right vertical edge during out-of-plane loading. Figure 5.18 (b) shows a schematic of the action on bricks at the origin of FRP debonding.

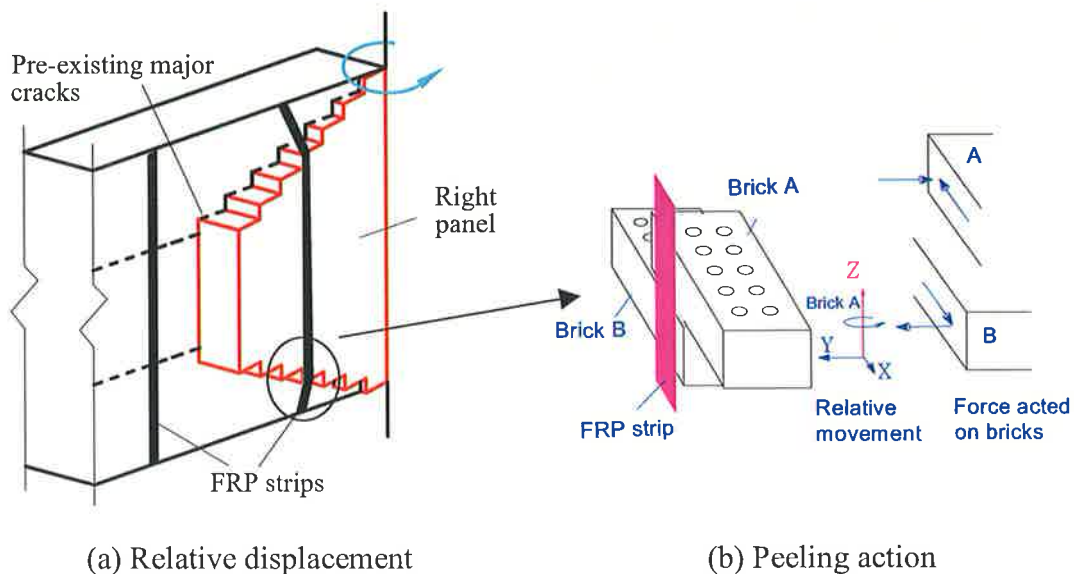


Figure 5.18 Schematic of the peeling debonding failure mode for Wall 1

The presence of vertical FRP strips proved to be effective in controlling the deflection of the wall. They acted like flexible vertical supports so that the bending and local failure modes of wall segments could become critical in the horizontal direction rather than vertical. For example, segment V_{1-2} above the opening can be deemed that the two vertical FRP strips V_1 and V_2 acted as two vertical supports for this sub-panel and induced a typical two-way bending cracking pattern under four-side support condition (cracking pattern shown in Figure 5.17). The new vertical cracks that occurred in the top of segment V_{3-4} are further evidence that horizontal bending

became dominant in the wall segments between FRP strips due to the vertical stiffening by the vertical FRP strips.

The strain distribution profile for FRP strip V3 is shown in Figure 5.19. The locations of measured maximum strain in FRP strips are denoted in Figure 5.17 with an 'X' symbol. The maximum strain recorded in strip V2 was $4478 \mu\epsilon$ measured at the mid-height where a pre-existing horizontal crack was located. The maximum strains of $4729 \mu\epsilon$ and $4548 \mu\epsilon$ were recorded in strip V3 at 950 mm from the top and 850 mm from the bottom. Both locations were at intersections with a major pre-existing horizontal crack. This suggested that pre-existing cracks have an impact on the force in FRP due to stress concentrations in FRP strips where pre-existing cracks were located. The measured maximum strain was close to the debonding strain of $5000 \mu\epsilon$ (reported by Tran 2004) for CFRP EB masonry, but premature peeling debonding occurred where FRP strain is much lower near base of wall in this case which indicates that the failure observed in this test by peeling action is a premature failure mode. If this premature failure can be prevented, the strength of the repaired wall can be further increased.

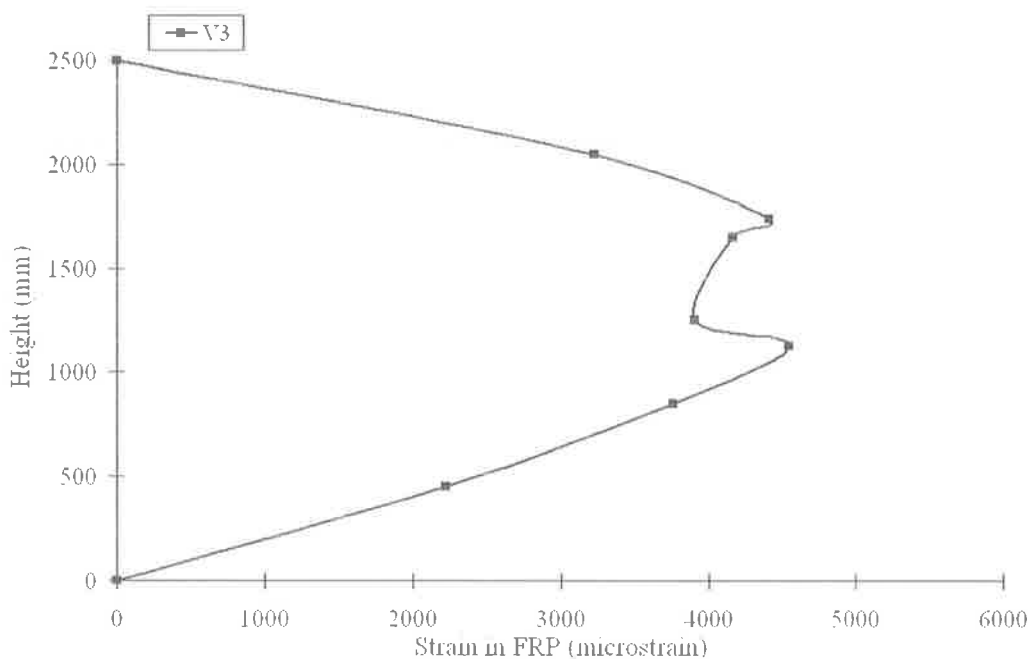


Figure 5.19 Strain distribution in carbon FRP strip V3 of Wall 1

Wall 2 (Externally bonded glass FRP retrofitted wall)

The load-deflection response of Wall 2 is shown in Figure 5.20. The loading process consisted of three phases (phase 1: A-B-C; phase 2: C-D-E; phase 3: E-F-G). The load was initially increased slowly to point B (at around $P=8.5$ kPa, $\Delta=92.4$ mm), where the LVDT measurement capacity was reached. The wall was then unloaded to C and the LVDT was adjusted. The cracking pattern during this first phase was similar to that observed in Wall 1. The pre-existing cracks enlarged and a series of new diagonal and horizontal cracks were observed in the wall segments V_{1-2} above and below the window as shown in Figure 5.21.

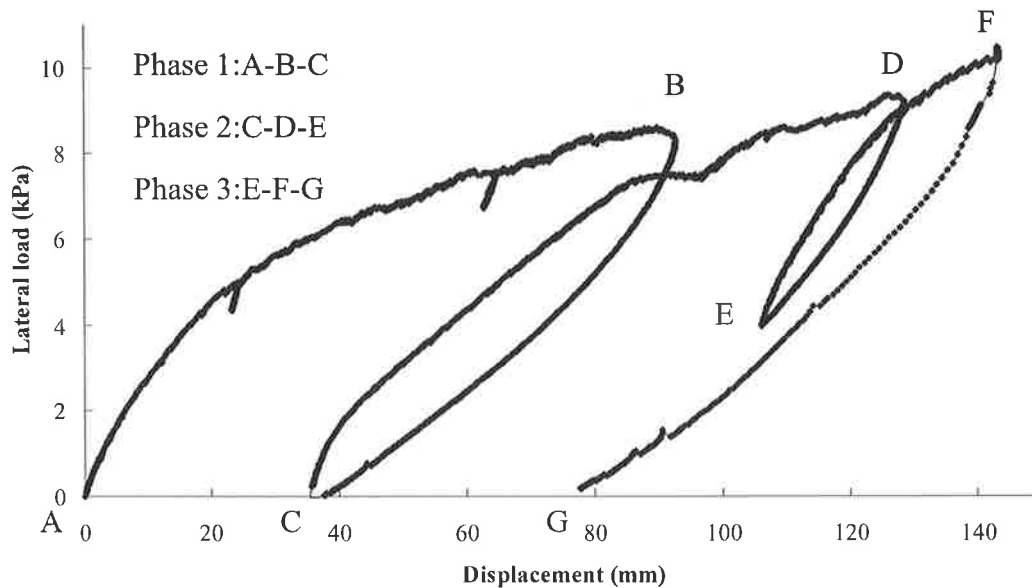


Figure 5.20 Lateral load-Displacement behaviour for Wall 2

The second phase of loading commenced from C at the displacement of 34.5 mm and loaded up to D (at approximately $P=9.23$ kPa, $\Delta=128.6$ mm), during which two significant vertical cracks occurred in wall segment V_{4-RE} (along the right edge of GFRP strip V4 and adjacent to the wall vertical edge through both mortar joints and brick units, which also connected the pre-existing cracks) as shown in Figure 5.21. The wall was then unloaded to E for crack inspection. Finally, in the third phase, the

wall was loaded from E until failure. The maximum lateral load and corresponding central displacement reached 10.38 kPa and 143.5 mm, respectively. The wall failed in masonry fracture and collapse due to horizontal bending in segment V_{4-RE} and there was no FRP debonding.

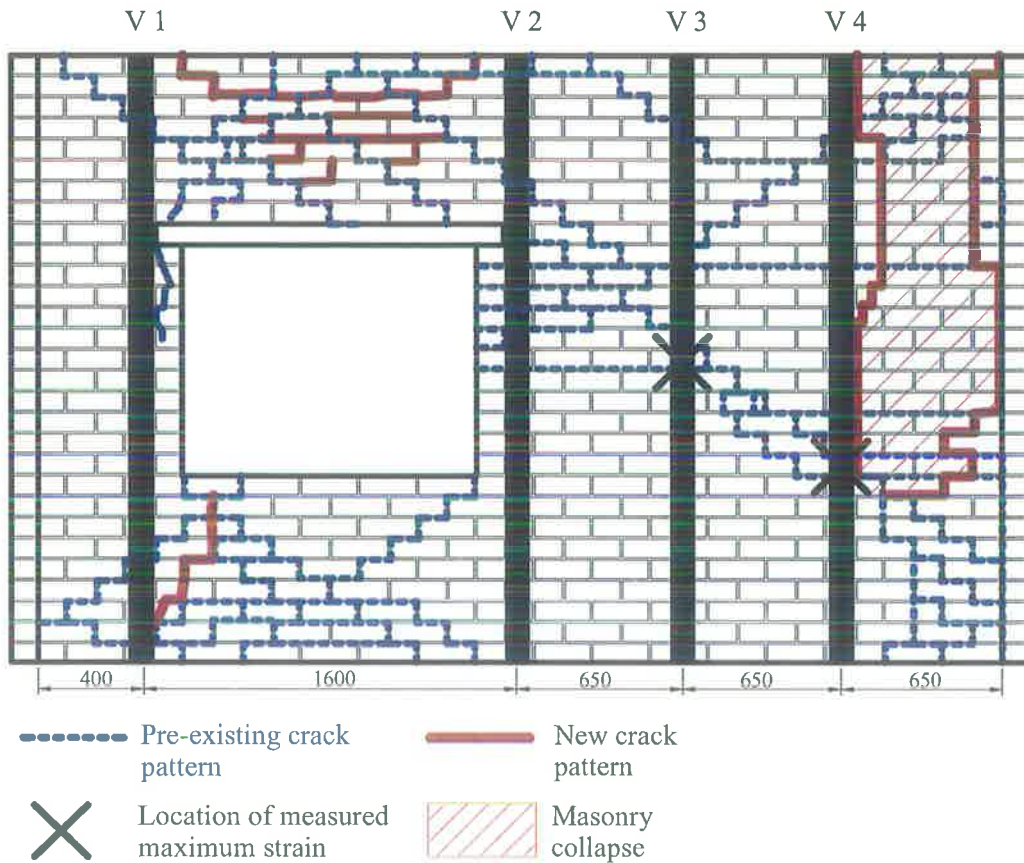


Figure 5.21 Schematic of cracking pattern and wall failure of Wall 2

The masonry horizontal bending failure initiated in the second loading phase. With further loading in phase 3 the masonry reached its horizontal bending capacity and vertical cracks significantly expanded. Subsequently, most of the wall segment V_{4-RE} collapsed as shown in Figure 5.22.

The strain distribution profile for FRP strips V3 and V4 is shown in Figure 5.23. The locations of measured maximum strain in FRP strips are also shown in Figure 5.21. The maximum strain on strip V3 was 12412 $\mu\epsilon$ recorded at the mid-height, where a major horizontal crack was located. The maximum strain on strip V4 was 11227 $\mu\epsilon$

occurred 860 mm from the bottom where a major diagonal crack crossed the strip. The maximum strains are very close to or exceed the glass FRP debonding strain of $12000 \mu\epsilon$, reported in Chapter Three. This means the glass FRP strips were close to debonding at the stage of masonry collapse. In fact, tiny cracking was seen along the bonding adhesive and it is believed that debonding would have occurred if the masonry did not fail in segment V_{4-RE}.

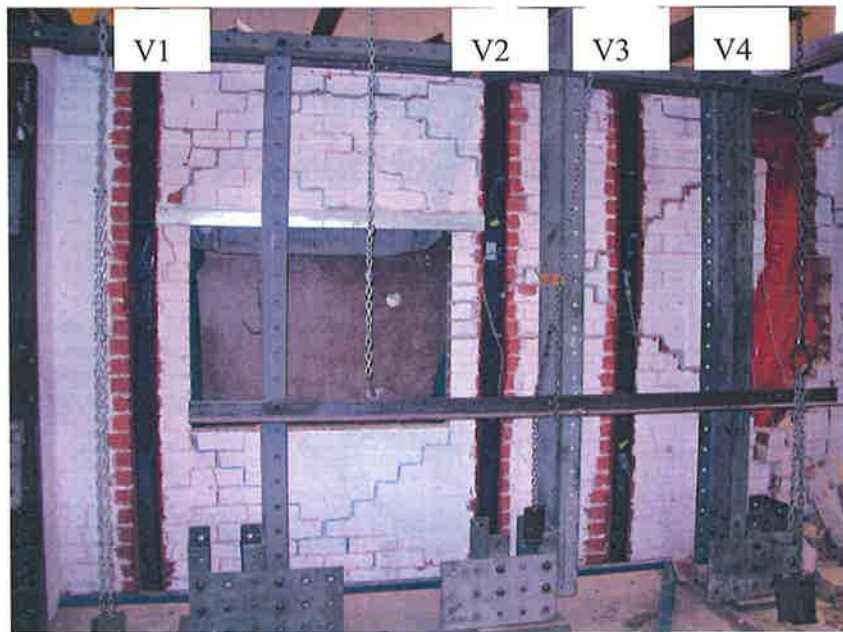


Figure 5.22 Photo for cracking and failure patterns of Wall 2

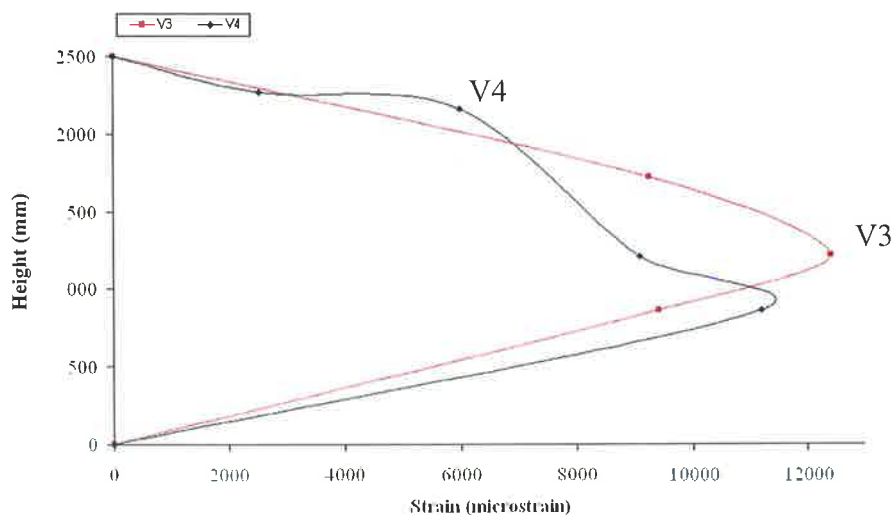


Figure 5.23 Strain distributions in glass FRP strip V3 and V4 of Wall 2

Wall 3 (Externally bonded glass FRP retrofitted wall)

To investigate the layout effect of FRP spacing, 77 mm wide GFRP strips were used at a reduced spacing of 500 mm, while keeping the same design capacity as for Wall 2. The pre-existing cracks were fixed for this wall specimen to investigate the impact of pre-existing cracks. Three LVDTs were used to measure the displacements at the centre of the main wall panel (LVDT1) and wall segments V₄₋₅ (LVDT2) and V_{5-RE} (LVDT3) to study the horizontal deflection profile along the wall surface at the solid half side.

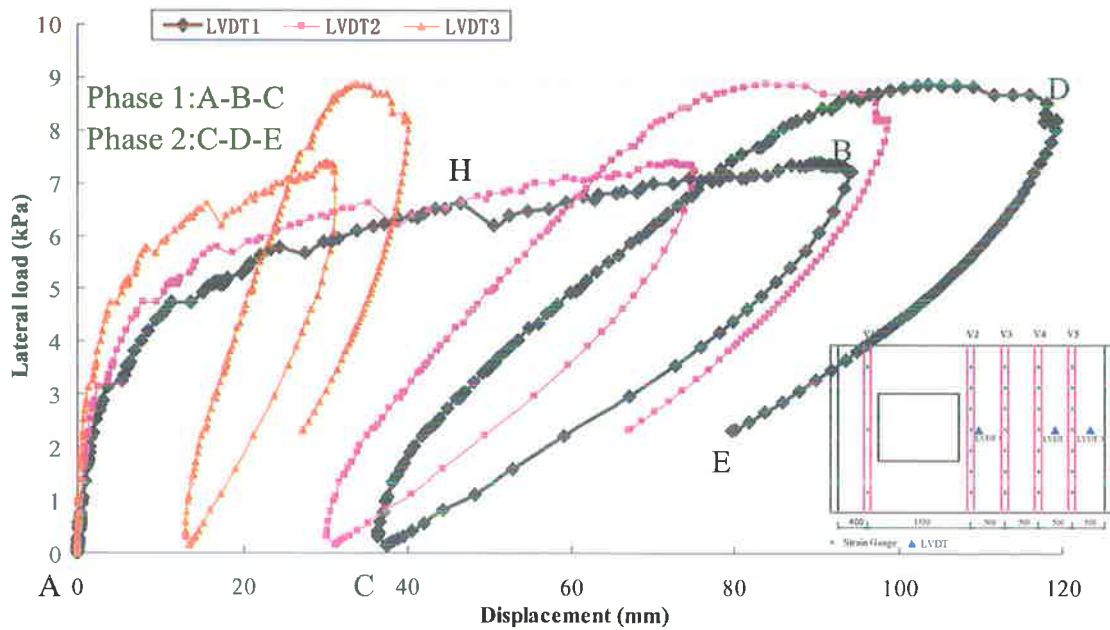


Figure 5.24 Lateral load-Displacement behaviour for Wall 3 (Phase 3 excluded)

The load-deflection response of specimen Wall 3 is shown in Figure 5.24. The loading process included three phases. The load was initially increased slowly in phase 1 to point H at approximately 6 kPa when new diagonal cracks occurred in wall segment V₁₋₂ above and below the window opening as shown in Figure 5.25. With further loading from point H the repaired pre-existing diagonal cracks at the bottom right portion of the main wall panel cracked again and slightly expanded (Figure 5.25).

Meanwhile, a new diagonal crack occurred from the upper right hand corner and continuously propagated towards the right edge of strip V5 (Figure 5.25). When the load approached 7 kPa, a series of new vertical cracks occurred in wall segments V_{LE-1} , V_{2-3} , V_{4-5} and V_{5-RE} , as well as the previous diagonal and vertical cracks. Finally the load was increased to point B of LVDT1 curve (at approximately $P=7.3$ kPa, $\Delta=94.2$ mm), where the LVDT1 measurement capacity was reached. The wall was then unloaded to C and the LVDT1 was adjusted.

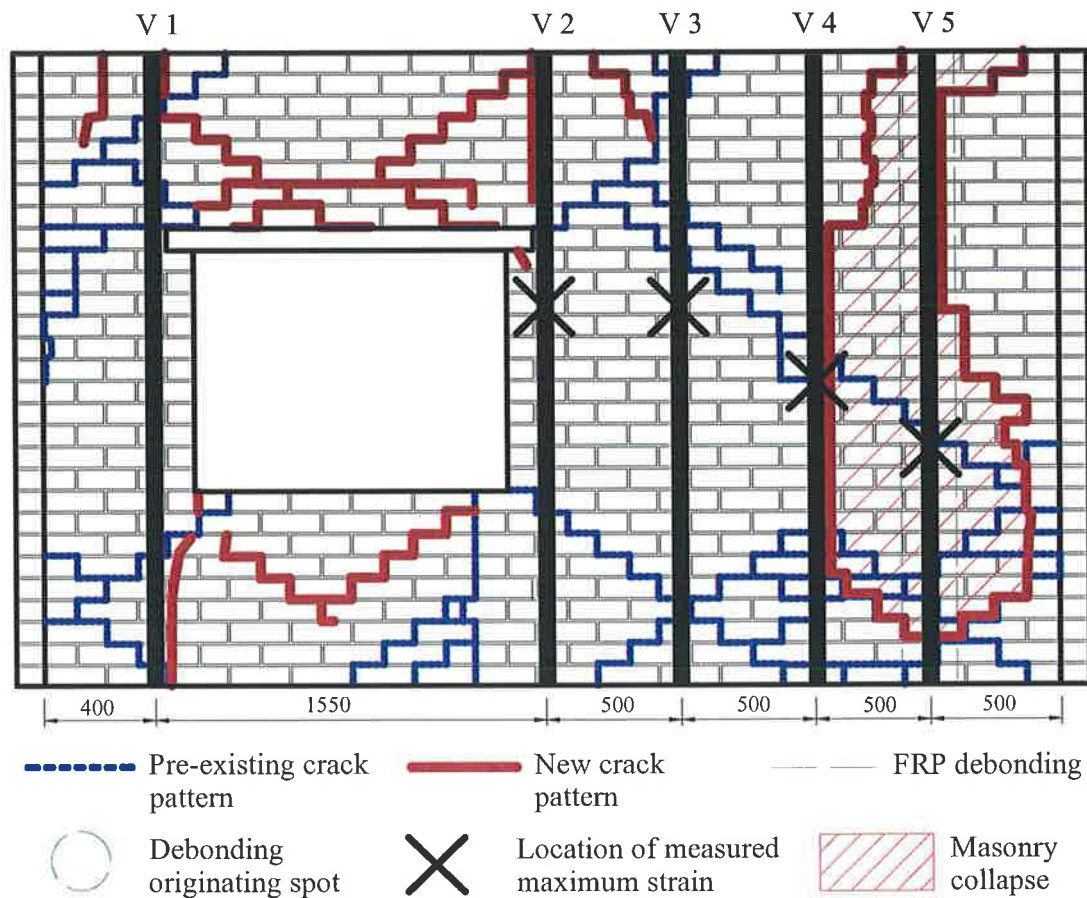


Figure 5.25 Schematic of cracking pattern and FRP debonding of Wall 3

The second phase of loading commenced from C ($\Delta=37.4$ mm) and was loaded up to D (at $P=8.9$ kPa, $\Delta=118$ mm) when it was stopped due to severe cracking and deformation in wall segment V_{1-2} below the window, where the masonry bricks almost collapsed. During the second phase, the new vertical cracks near strip V5 were significantly enlarged due to the fractured masonry as shown in Figure 5.26 (b).

In order to fail this strengthened wall while preventing any further damage to wall segment V_{1-2} , the lateral load was only applied to the right half portion of the main wall panel (from V_2 to wall right vertical edge) in phase 3. This was done by disconnecting the air pipe connected to the airbags behind the left portion of the main wall panel (from left edge to V_2). No displacements were recorded in phase 3 while the strain gauges and load cells kept recording. Therefore the load versus displacement curve is not available for this phase. The load was applied from point E until wall failure. The failure seems to have occurred initially in micro cracking of strip V_5 and masonry fracture along the midline behind the strip V_5 . This caused the complete debonding of strip V_5 . The two masonry wall segments either side of strip V_5 (V_{4-5} and V_{5-RE}) were pushed out of the main wall as shown in Figure 5.26 (c). The debonding of the glass FRP strip occurred suddenly. The masonry collapse region is observed in Figure 5.25.

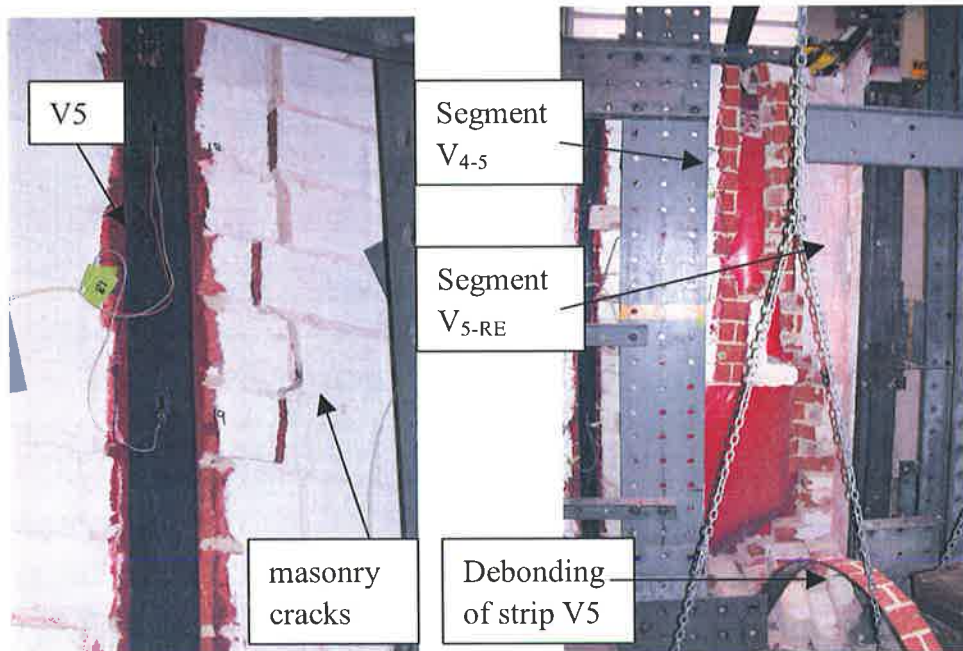
The strain distribution profile for each FRP strip is shown in Figure 5.27. The locations of measured maximum strain in FRP strips are denoted in Figure 5.25. The maximum strain recorded in GFRP strip V_2 , V_3 , V_4 and V_5 was $9463 \mu\epsilon$, $10626 \mu\epsilon$, $10550 \mu\epsilon$, and $10939 \mu\epsilon$, respectively. These maximum strains all occurred either close by the wall mid-height or to a major crack. The maximum strains are close to the GFRP debonding strain $12000 \mu\epsilon$, indicating that the load carried by the right four FRP strips was comparable and the strips acted effectively to distribute the load evenly on the FRP strengthened part of the wall.

Figure 5.28 shows the deflection profile, recorded by the three LVDTs, at the mid-height of the right half portion of the main wall panel. As the lateral load increased, the differences between the LVDT3 and LVDT2 became larger, while the deflections at LVDT1 and LVDT2 were comparable. Curvature of the wall at mid-height seemed to be concentrated in the transition zone at GFRP strip V_5 , where the stresses were probably concentrated. Therefore, it is quite reasonable that cracks

mainly occurred in segment V_{4-5} and V_{5-RE} , and the wall failed suddenly in masonry fracture and collapse.



(a) Overall view of failed Wall 3



(b) Vertical cracks in wall segment V_{5-RE} (c) Debonding of FRP strip V5

Figure 5.26 Photos for cracking and failure patterns of Wall 3

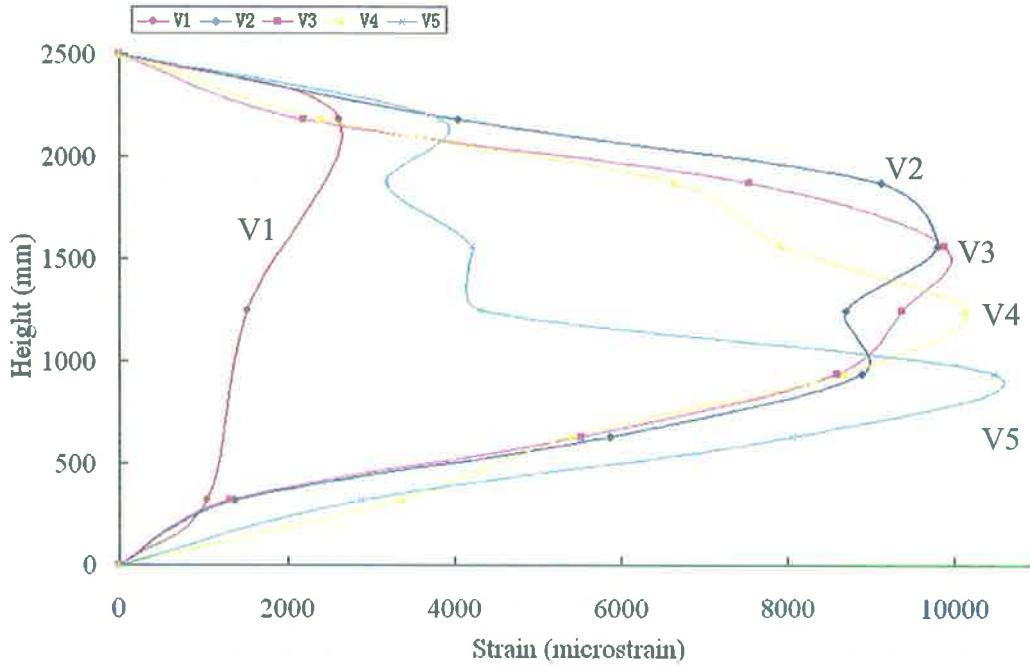
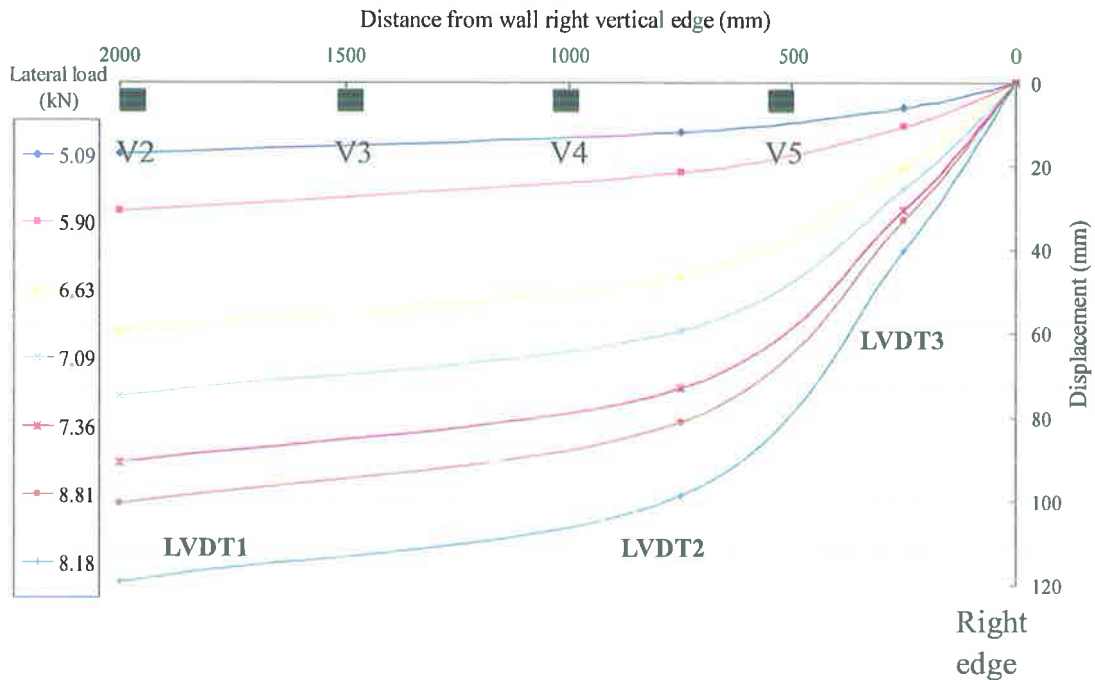


Figure 5.27 Strain distributions in all five glass FRP strips of Wall 3



Note: LVDTs are at mid-height of wall

Figure 5.28 Horizontal deflection profile of Wall 3

Wall 4 (Near surface mounted carbon FRP retrofitted wall)

The lateral load-deflection relationship of Wall 4 is shown in Figure 5.29, including three loading phases. The loading went from A to B ($P=5.2$ kPa, $\Delta=14$ mm) when the pre-existing cracks in wall segment V_{1-2} and the diagonal cracks from the corners of the window opening enlarged significantly and started to propagate towards the corner of the wall (refer Figure 5.30). The wall was unloaded to C for crack inspection and then reloaded in phase 2 from C to D ($P=5.9$ kPa, $\Delta=82$ mm). In this phase, debonding of strip V2 occurred at point H ($P=8.2$ kPa, $\Delta=41.9$ mm) close to the intersection with a new diagonal crack and propagated to the bottom of the wall as shown in Figure 5.31 (b). The wall was unloaded from D to E for close inspection. In order to test the ductility of the wall, it was loaded again in phase 3 from E to F ($P=4.9$ kPa, $\Delta=101.7$ mm). In this phase, the strength of the wall kept decreasing gradually with the increasing of central displacement. The wall was then unloaded to point G.

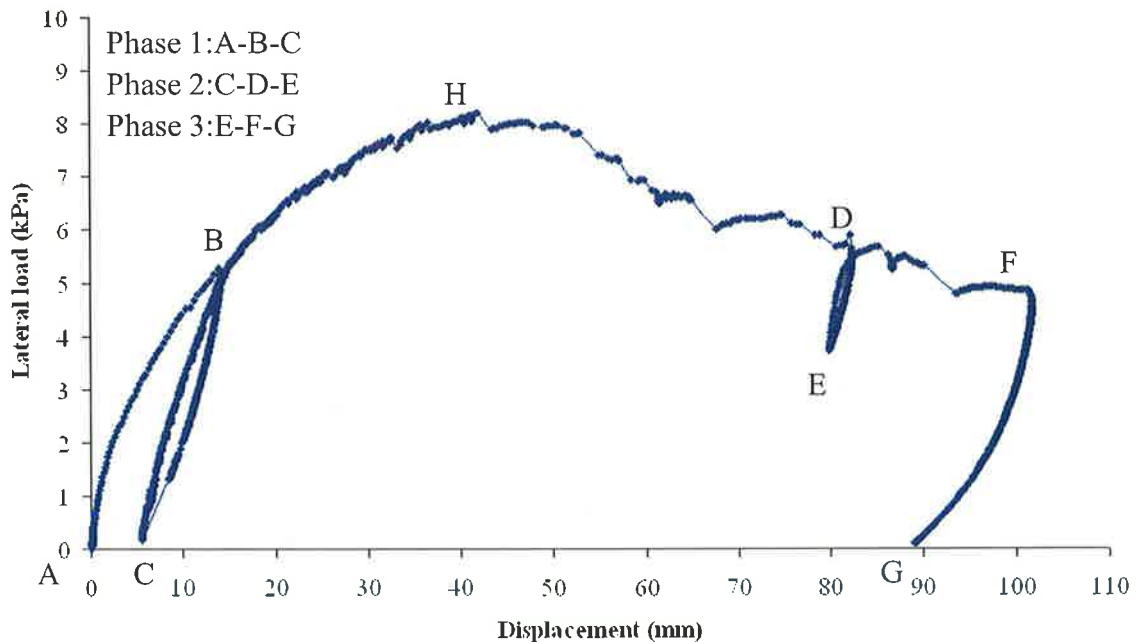


Figure 5.29 Lateral load-Displacement behaviour for Wall 4

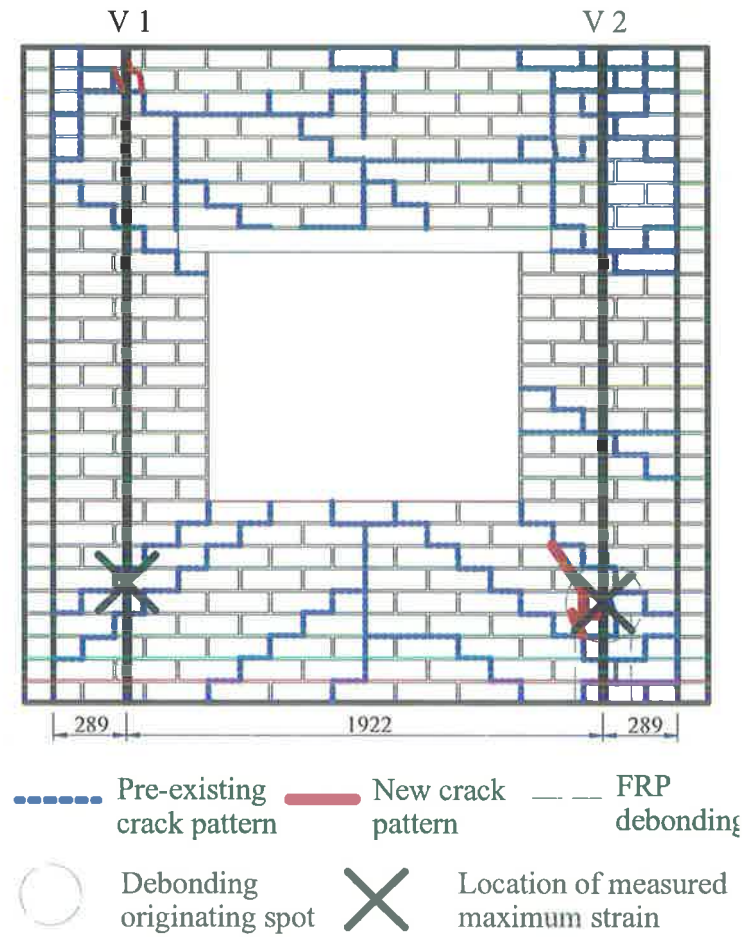
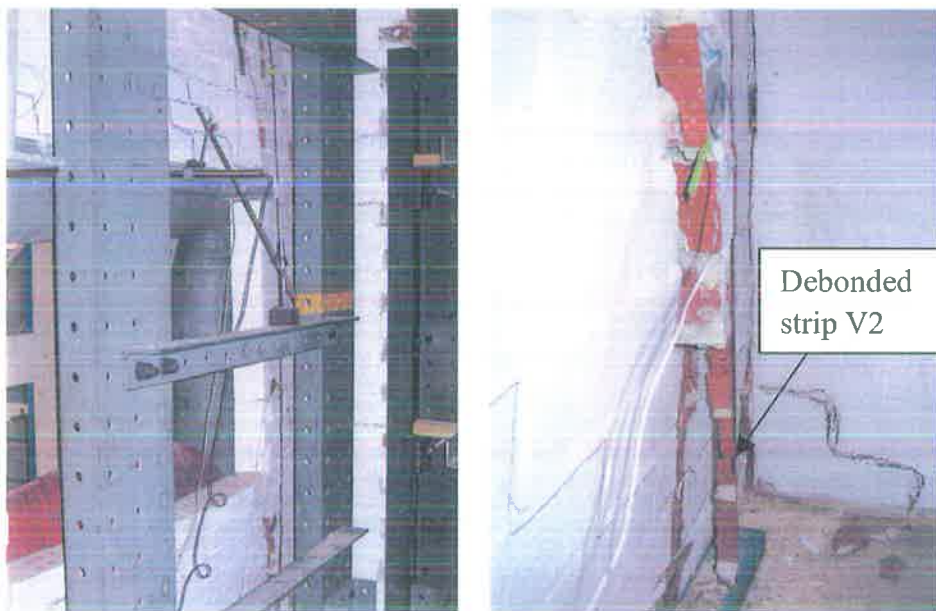


Figure 5.30 Schematic of cracking pattern and FRP debonding of Wall 4



(a) Overall view of failure

(b) Debonding of strip V2

Figure 5.31 Photos for cracking and failure patterns of Wall 4

It was seen that the wall behaved like four rigid trapeziform bodies: top, bottom, right and left panels, rotating about the four edges with the increase of loading and opened up along the edges of window opening. The diagonal cracks continuously propagated to the carbon FRP strips either through pre-existing stepped cracks or through new cracks. Crack propagation was blocked when they reached the edge of FRP strips where the cracks then developed along the FRP strip edges towards the base. The cracks kept enlarging with increasing load until the FRP strip V2 debonded (point H in Figure 5.29) at a load of 8.2 kPa.

The FRP debonding failure observed in this test was caused by the cleavage action due to differential rotation occurred between two sub-panels (i.e. right and bottom sub-panels). The near surface mounted carbon FRP was debonded and pulled out from the bottom sub-panel of the wall when the shear failure occurred in the masonry brick units as shown in Figure 5.31 (b).

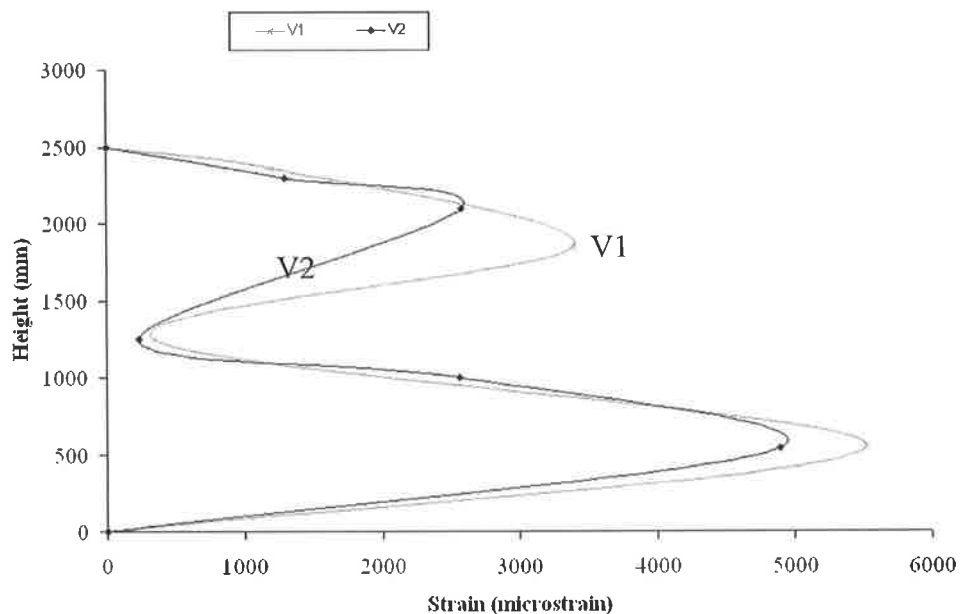


Figure 5.32 Strain distributions in carbon FRP strips of Wall 4

The strain distribution profile for each FRP strip is shown in Figure 5.32. The locations of measured maximum strain in FRP strips are also denoted in Figure 5.30. The maximum strains recorded on CFRP strips V1 and V2 were $5897 \mu\epsilon$ and $5000 \mu\epsilon$,

respectively. These maximum strains both occurred close to the major bottom diagonal cracks. The maximum strains were significantly lower than the experimental debonding strain for CFRP near surface mounted to masonry of approximately $18000 \mu\epsilon$, as derived from the push-pull tests in Chapter Three. This indicates that near surface mounted FRP strip has a great tendency to debond in 'cleavage' mode at lower FRP strain which is believed to be caused by the similar 'peeling' action as observed in Wall 1.

5.4. CONCLUSIONS

By comparing the load-deflection of FRP repaired walls and control walls, the following findings can be drawn:

1. For the rectangular masonry walls, all three FRP strengthening schemes increased the strength, compared to the original static strength, significantly: by approximately 90% for Wall 1, 106% for Wall 2, and 137% for Wall 3. The displacements at which the maximum strength for the FRP repaired walls were also much larger.
2. For near surface mounted carbon FRP strengthened wall, the ultimate load was increased by 64% over the residual cyclic strength of approximately 5 kPa and was comparable to the original static strength of 8.7 kPa as shown in Figure 5.15. The load-displacement curve of Wall 4 closely followed the envelope of the cyclic loading for the original wall, while restoring the strength to be that of the original masonry wall. The ductile behaviour of Wall 4 was also much better than for the original wall.
3. The stiffness of externally bonded carbon FRP repaired wall (Wall 1) was greater

than the stiffness for the two externally bonded glass FRP strengthened walls (Wall 2 and Wall 3). However, the displacement capacity of externally bonded glass FRP walls was greater than that for Wall 1 since larger strains were achieved in the glass FRP strips.

4. The stiffness of the four strengthened walls were lower than that of the original unreinforced masonry wall under initial loading, but higher than the original masonry wall at the end of its cyclic loading when cracking patterns were developed. This is due to the impact of pre-existing cracks, which made the wall stiffness lower. However, the stiffness was effectively increased by applying vertical FRP strips. Comparing the three reinforced rectangular walls (Figure 5.15 (a)), it is seen that the initial stiffness of Wall 1, using stiffer carbon material and Wall 3 where the pre-existing cracks were repaired, were comparable and both clearly stiffer than that of Wall 2. However, at higher loads and displacements, the stiffness of the externally bonded carbon FRP repaired wall (Wall 1) was significantly higher than either of the externally bonded glass FRP repaired Walls (Wall 2 and Wall 3). It is also interesting to note that the stiffness of Wall 3, where cracks were repaired, decreased quickly and tended to be comparable with Wall 2, once the load went beyond the capacity of original masonry wall, which was approximately 5 kPa.
5. Comparing the ultimate strength of Walls 2 and 3, it was found that an increase of 15% in the ultimate strength was achieved by increasing the number of strips while keeping the same design capacity. Due to a lack of central displacement data for Wall 3 at the loading phase 3, the differences in ultimate deflection could not be studied.
6. New premature FRP strip peeling debonding failure mode were observed in externally bonded carbon FRP retrofitted wall (Wall 1) which was caused by the peeling action due to large differential displacement between wall sub-panels. The

FRP cleavage debonding failure was observed in the near surface mounted carbon FRP strengthened wall (Wall 4) due to an angle occurred between two sub-panels. If these two premature failures can be prevented, the strengthened wall capacity is believed to be governed by the FRP strip IC debonding or the stability of the wall (i.e. the out-of-plane wall displacement).

6. THEORETICAL MODELLING: RETROFITTED WALLS

6.1. INTRODUCTION

The experimental results presented in Chapter 5 have demonstrated the ability of both externally bonded and near surface mounted vertical FRP strip strengthening techniques to improve the out-of-plane strength of masonry walls. The subject of this chapter is to predict the lateral load capacity of masonry walls strengthened with only vertical FRP strips subjected to biaxial out-of-plane bending and to provide strengthening design recommendations based on allowable critical displacements for FRP repaired masonry walls to prevent a sudden masonry failure due to the excessive wall displacement as observed in the experimental study.

Based on the observation of the wall tests, the one-way vertical bending capacity (with an FRP IC debonding failure mode) of a vertical strip can be deemed to give a lower bound load capacity for a masonry wall strengthened with FRP vertical strips under two-way bending. On the other hand, in order to provide recommendations on wall acceptable displacements, rigid body theory is used in this chapter to develop a relationship between the wall displacements and the FRP response.

6.2. LATERAL RESISTANCE OF THE WALL UNDER BIAIXAL BEDNING

The only two recent published studies on biaxial bending behaviour of FRP reinforced masonry wall (Ghobarah and Galal 2004 and Korany, 2005) were discussed earlier in Chapter Two. Ghobarah tested a series of concrete block masonry walls strengthened with externally bonded carbon FRP strips oriented mainly in the vertical direction.

The failure modes include masonry cracking along the sides of FRP strips and cracking in the mortar and blocks at unbonded regions, debonding of unanchored FRP strips and FRP strip rupture at the anchorage region. The failure mechanism of the strengthened wall was found to be significantly changed compared with the unreinforced masonry wall. However, the experimental observation from Korany's tests (two-wythe brick wall strengthened with bi-directional NSM intermittently bonded CFRP cables) is quite different. Korany concluded that the cracking patterns of the strengthened walls were similar to that of the unreinforced masonry wall and that failure occurred due to masonry wall cracking and debonding or rupture of the carbon FRP.

According to the behaviour of four strengthened walls investigated in this study, it is suggested that the strengthened wall cracking pattern is similar to the unreinforced masonry wall except for some vertical cracks occurred between FRP strips at higher loads and it behaved elastically between diagonal cracks. Therefore, one-way vertical bending capacity could be studied to predict the lower bound flexural capacity of the walls retrofitted with vertical strips. Assuming displacement is governed by rotations along cracks, rigid body theory could be used to study the relationship between wall displacements at different locations and relate the FRP behaviour to the critical displacements, which helps to provide recommendations on acceptable wall displacement.

6.3. ONE-WAY VERTICAL BENDING CAPACITY

As discussed in Chapter 2, beam theory can be used to predict the lateral load capacity of a strengthened wall under one-way vertical bending. An important underlying assumption applied to the analysis and design of reinforced members is that plane sections remain plane. The strain at failure in an FRP strip can vary from the IC

debonding strain to the ultimate strain at rupture corresponding to different FRP failure modes. In this study, the masonry wall was designed with the expectation that FRP debonding would occur before either masonry compression failure or FRP rupture failure. Therefore, in a unit width strip of FRP retrofitted masonry wall, the vertical flexural capacity was governed by the maximum tensile force in the FRP strip.

According to beam theory, the moment capacity is derived based on strain compatibility. Considering a cross section of a unit width wall strip bonded with a FRP strip at its tension face, subject to bending, the cross section analysis is based on the following assumptions:

- plane sections remain plane after bending,
- full composite action between FRP strip and masonry surface,
- the thickness of the FRP strip is negligible compared to the thickness of the masonry wall, t_m , and
- tensile resistance of the brick masonry can be neglected.

Due to the design assumption that FRP debonding occurs prior to FRP rupture or masonry crushing, the stress-strain relation for masonry brick is within the elastic range, so a triangular stress block distribution can be used for the masonry brick as shown in Figure 6.1.

Applying internal force equilibrium and strain compatibility to the section, the following equations can be obtained.

$$T_p = C_m, \quad \text{gives} \quad A_p E_p \varepsilon_{db} = \frac{1}{2} \varepsilon_m E_m \cdot s \cdot c \quad \text{Eq. 6-1}$$

$$\frac{\varepsilon_m}{\varepsilon_{db}} = \frac{c}{t_m - c} \quad \text{Eq. 6-2}$$

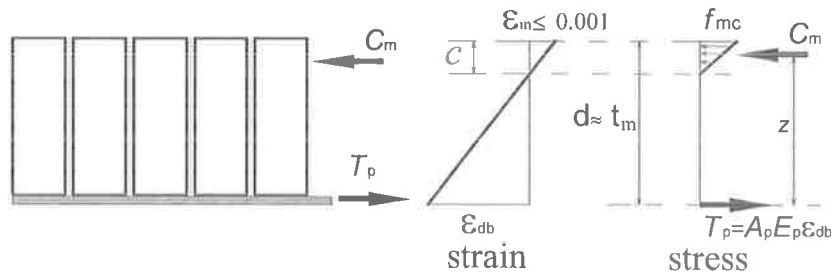
where, T_p is the tensile force in FRP strip; C_m is the compressive force in masonry;
 s is the spacing FRP strips, also equivalent to the wall design strip width,
 c is the depth from the compression face to the neutral axis;
 ε_{db} is the strain in FRP when debonding failure occurred.

Therefore, the ultimate bending moment capacity of the section, M_{cv} , and the corresponding lateral load capacity for this wall design strip, w_{pre} , can be obtained as

$$M_{cv} = A_p E_p \varepsilon_{db} \left(t_m - \frac{c}{3} \right) \quad \text{Eq. 6-3}$$

$$w_{pre} = \frac{8M_{cv}}{H^2} \quad \text{Eq. 6-4}$$

where H is the wall height. Assume simple-support at wall top and bottom



(a) left part of a FRP retrofitted masonry beam (b) strain and stress distributions

Figure 6.1 IC Debonding failure of FRP under-reinforced URM wall

Once the FRP debonding strain, ε_{db} , is known, the T_p , C_m , c and ε_m can be determined. If the ε_m and c are checked to be less than the ultimate compressive strain of the masonry and the depth of brick top cover, respectively, the vertical bending moment capacity of the vertical masonry wall strip is given by Eq. 6-3. Hence, the value of the IC debonding strain ε_{db} is critical and sensitive in order to predict the flexural capacity of the strengthened wall using this model.

In published existing studies, experimental data of debonding strain were used as the value of ε_{db} for several types of FRP material for theoretical computation. This situation is improved in this study since an FRP-to-masonry theoretical bond model has been developed (refer Chapter 4) which can be used to predict the maximum force and strain in FRP at debonding in terms of the fundamental FRP material properties. Thus, the one-way vertical bending capacity for a vertical wall strip can be predicted by using the FRP material properties and the geometry of FRP strip. As summarised in Table 6.1, T_p and ε_{db} were determined using the modified Chen and Teng's model and Seracino et al's model as discussed in Chapter Four for the externally bonded case and near surface mounted case, respectively. The maximum vertical bending moment and the lateral load capacity computed using Equations 6-3 and 6-4 are listed in Table 6.1.

Table 6.1 Summary of one-way vertical bending capacity prediction

	s	b_p	E_p	T_p	ε_{db}	ε_m	c	M_{cv}	w_{pre}	w_{exp}	w_{pre}/w_{exp}
	(mm)	(mm)	(GPa)	(kN)			(mm)	(kNm)	(kPa)	(kPa)	
Wall 1	650	50	160	32.4	0.0034	0.0005	13.4	5.31	6.8	9.7	0.70
Wall 2	650	100	73	47.1	0.0105	0.0010	9.3	7.75	9.9	10.5	0.94
Wall 3	500	77	73	36.2	0.0105	0.0010	9.3	7.75	9.9	12.1	0.82
Wall 4	1000	20	160	72.2	0.0161	0.0010	7.6	7.05	9.0	8.2	1.10
Notes:										Mean	0.89
1. T_p and ε_{db} are determined using FRP-to-masonry theoretical bond model,										St Dev	0.17
2. ε_m , c and M_{cv} are determined using cross sectional analysis method.										COV	0.19

Compared to the experimental lateral load, w_{exp} , for the FRP strengthened walls under two-way bending, the predictions are slightly conservative, on average, by 11%. In the case of Wall 2, the predictions were more accurate than for the other three cases as the prediction for FRP debonding strain was more accurate than for the others. It is because of the smaller spacing of FRP strips used for Wall 3, that a higher strength

was achieved compared with Wall 2, which had the same design capacity. For Wall 1, the predicted ε_{db} of 0.0034 was much lower than the measured ultimate strain, hence the prediction for the load capacity was 30% lower than the test result. For wall 4, on the contrary, the lateral load capacity was over-predicted by 10%, due to the FRP premature cleavage debonding and hence ε_{db} was over-predicted.

It can be concluded that the cross sectional analysis method can be used with a vertical strip to give lower bound prediction for the lateral load capacity of two-way bending masonry walls strengthened with vertical FRP strips. However, this conclusion is based only on the current vertical FRP strengthening schemes and the corresponding experimental results.

6.4. RIGID BODY DEFLECTION ANALYSIS

6.4.1. Observed Rigid Body Behaviour

From the experimental observation, due to the presence of the pre-existing crack lines, the resulting sub-panels behaved largely as rigid bodies that rotated around the axes of the supports and crack lines when subject to out-of-plane loading (refer Figure 6.2). Most of the significant deformations and rotations took place at the contact zones along major crack lines as most of the maximum strains were measured in FRP strips at the intersections with crack lines. As stated in Section 6.2, Korany's tests (2005) also indicated that the rigid body behaviour of a strengthened masonry wall is similar to that for an unreinforced masonry wall. This suggests that it is reasonable to analyse the displacement response of an FRP retrofitted masonry wall using rocking rigid body principles.

Premature peeling or cleavage debonding tends to occur in FRP strips across diagonal cracks where there is a large differential displacement or large rotations between

sub-panels. Hence, the main purpose of the following rigid body analysis was to estimate the wall displacement at the FRP-diagonal crack intersections in order to predict the lateral displacement of a strengthened wall at which the premature debonding modes, such as peeling or cleavage debonding failure observed in Walls 1 and 4, respectively, will occur.

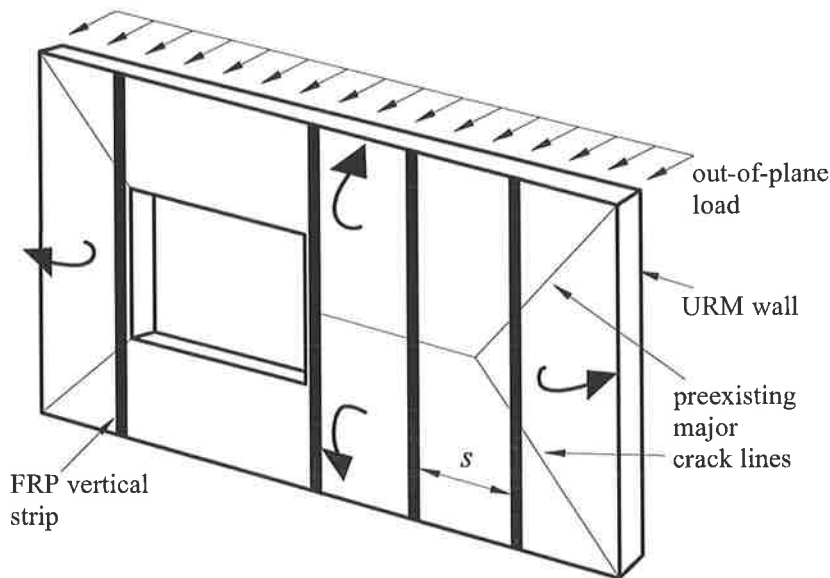


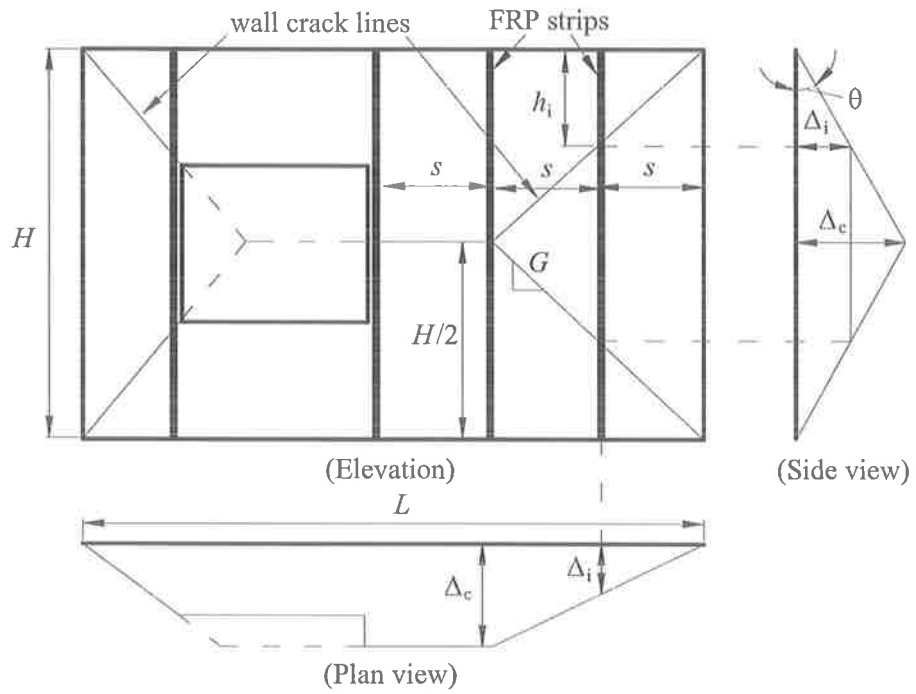
Figure 6.2 Rotation of sub-panels of FRP strengthened URM wall

6.4.2. Wall Displacement at the FRP-Diagonal Crack Intersections

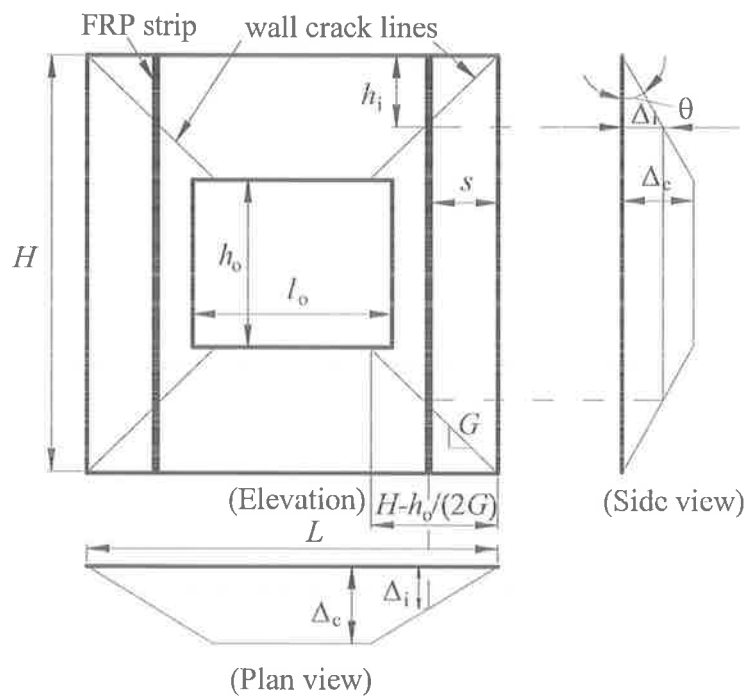
The geometry of the theoretical crack lines can be determined by the crack line slope G , which is substantially determined by the geometry of the masonry units and mortar joints. Consequently, the theoretical wall crack lines can be determined as shown in Figure 6.3 (only suitable for the case in this study, different wall or masonry unit geometry may result in different crack line slope G).

$$G = \frac{2(h_u + t_j)}{l_u + t_j} \quad \text{Eq. 6-5}$$

where, h_u and l_u are the height and length of the masonry unit, respectively; and t_j is the thickness of the mortar joint.



(a) Rectangular wall



(b) Square wall

Figure 6.3 Crack lines and deflections of FRP strengthened URM wall

When the location of the FRP strip to diagonal crack line intersection is known, the relationship between the wall central displacement, Δ_c , and the displacement at any FRP-to-diagonal crack line intersection, Δ_i , can be identified as

$$\Delta_i = \frac{2h_i}{H} \Delta_c \quad (\text{Rectangular wall}) \quad \text{Eq. 6-6}$$

$$\Delta_i = \frac{2h_i}{H - h_o} \Delta_c \quad (\text{Square wall}) \quad \text{Eq. 6-7}$$

where, h_i is the distance from the nearest horizontal edge to the FRP-diagonal crack intersection; h_o is the height of window opening.

In the current study, the central displacement, Δ_c , was measured during the tests from which the Δ_i was calculated using the above equations. The calculations are summarised in Table 6.2. It is noted that this model suggests that the carbon FRP peeling and cleavage debonding failure for Wall 1 and Wall 4 occurred at the local displacement of 27.1 mm and 28.2 mm, respectively. The above simple model is used to relate Δ_i and Δ_c based on the current observation. The wall displacement at the FRP-diagonal crack intersections is as critical as the central displacement, for FRP cleavage debonding may occur at the FRP-diagonal crack intersections at a smaller displacement. Therefore, it is useful to provide an allowable value of Δ_i for design purpose, which can prevent the premature FRP cleavage debonding failure.

Table 6.2 Wall displacement at FRP-diagonal crack intersection

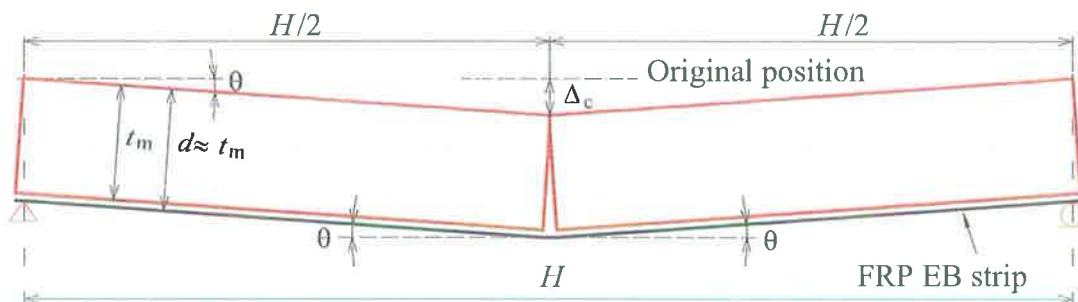
	s (mm)	h_i (mm)	$\Delta_{c,exp}$ (mm)	Δ_i (mm)
Wall 1 (V4)	650	466	72.7	27.1
Wall 2 (V4)	650	466	143.5	53.5
Wall 3 (V5)	500	358	119.4	34.2
Wall 3 (V4)	1000	717	119.4	68.5
Wall 4 (V2)	289	207	101.7	28.1

Note: $L = 2500$ mm, $G = 0.717$.

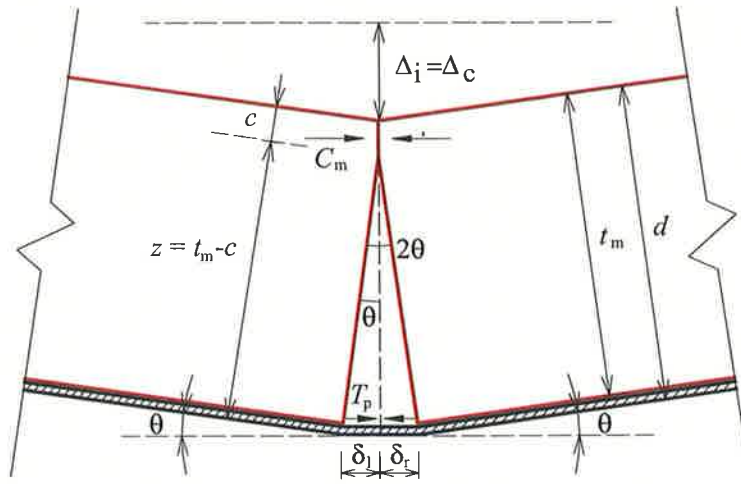
6.4.3. Modelling of Wall Displacements

This section discusses the relationship between the wall displacements and FRP bond behaviour based on rigid body theory. Displacement in the case of rigid body analysis is governed by rotation at a crack rather than curvature as would be the case in the classic bending theory. There are generally two critical displacements based on the experimental observation. One is the central displacement and the other is the FRP-diagonal crack intersectional displacement. Therefore, discussion in this section includes two general cases of a masonry wall panel: (1) includes a single midspan crack, representing the central portion of the wall with a major horizontal crack intersecting the FRP strip at mid-height (Figure 6.4 (a)), and (2) represents the side portion of a wall where two diagonal cracks intersect the FRP strip (Figure 6.5 (a)).

The two cases of FRP-reinforced masonry members (see Figures 6.4 and 6.5) are used in this section to explain the application of rigid body analysis to predict the post-cracking lateral displacement at which debonding might occur. The members are of unit width, thickness t_m and are strengthened with externally bonded FRP strips on the tension face. The members are also simply supported in one-way bending and are loaded under a uniform pressure w .

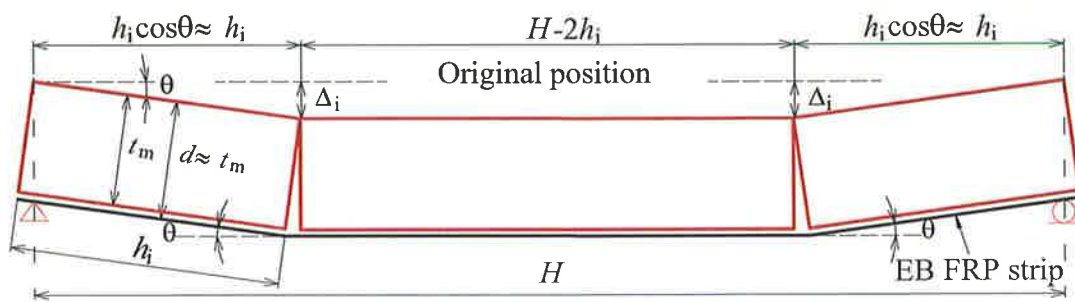


(a) One-way masonry member

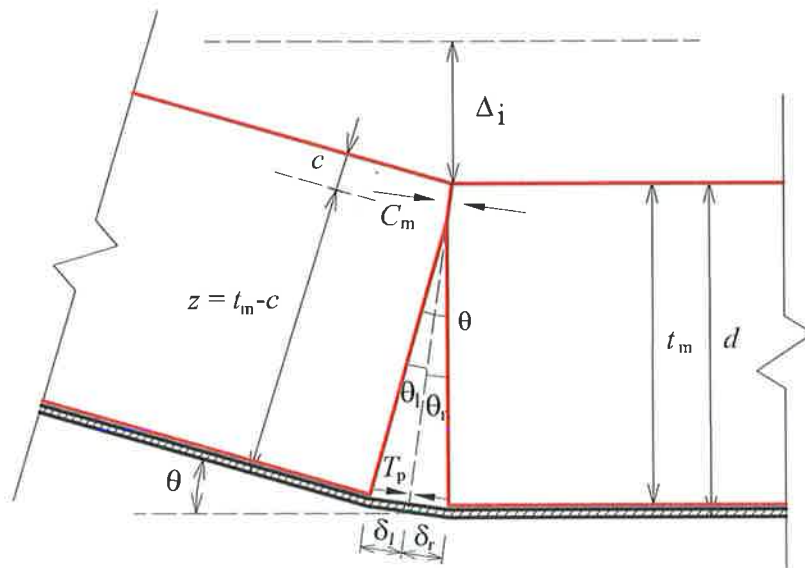


(b) Rotations at crack location

Figure 6.4 Rigid body representation of a member with a single midspan crack



(a) One-way masonry member



(b) Rotations at crack location

Figure 6.5 Rigid body representation of a member with two cracks

The single horizontal crack normally occurred at the mid-height of the wall, as shown in Figure 6.4 (a), when considering a strip in the central portion of a masonry wall. After cracking, the member acts as two separate segments connected by an FRP strip. Under pressure, these segments are assumed to rotate rigidly around the axes of the supports, which results in a displacement Δ_c at the crack location (i.e. at the midspan). To form such a rotation, the deformation in masonry at the crack location has to form a contact zone between the two segments as shown in Figure 6.4 (b). Rotation at the crack location is considered to occur around the intersection between the two segments. Therefore, when the rotation of the member is θ , the total rotation between adjacent cracks at the crack location is 2θ in this case. The forces acting on the cross section of the left hand rigid segment are the tension force in the FRP strips T_p and the compressive force in masonry C_m at the contact zone. The length of the FRP slip spanning the crack opening is considered to be the sum of the accumulated local slip that occurs between the FRP and masonry to both the left and right side of the crack, which are denoted by δ_l and δ_r , respectively. An equal length of slip is assumed for equal length of segments. If the accumulated slip is more than can be delivered by the bonded length of FRP to one side of the crack, then debonding is predicted to occur.

For small deflections relative to usual wall heights, crack angles are very small. From the geometry of the member shown in Figure 6.4, the rotation θ and the displacement Δ_c of the member with a single midspan crack can be obtained as

$$\theta = \frac{\delta_l}{z} \quad \text{Eq. 6-8}$$

$$\Delta_c = \theta \cdot H / 2 \quad \text{Eq. 6-9}$$

where, $z = t_m - c$, c is the depth of neutral axis of the cross section, which can be determined from Eq. 6-1 and Eq. 6-2.

A member with two cracks as shown in Figure 6.5 (a) is used to simulate the case of an FRP strip on a side portion of a four-sided simply-supported wall where the FRP strip crosses two diagonal cracks. Considering the same loading situation as before, the two side segments are assumed to rotate rigidly around the axes of the supports, which result in a rotation at the crack location and a displacement Δ_i at the two crack locations (i.e. at the FRP-diagonal crack intersections). To form the same rotation θ of the member as that in the former case, the rotation at the crack location is θ in this case as shown in Figure 6.5(b). However, due to the different length of the rigid body segments, which forms the same crack, the local slip accumulated between the FRP and the masonry on each side of the crack, δ_l and δ_r , are different according to the different loading stages, which may result in the different rotation angles θ_l and θ_r . From the geometry of the member shown in Figure 6.5, the rotation θ and the displacement Δ_i of the member with two cracks can be obtained as

$$\theta = \theta_l + \theta_r = \frac{\delta_l}{z} + \frac{\delta_r}{z} \quad \text{Eq. 6-10}$$

$$\Delta_i = \theta \cdot h_i \quad \text{Eq. 6-11}$$

where, $z = t_m - c$, c is the depth of neutral axis of the cross section; h_i is the distance from the FRP-diagonal crack intersection to the nearest horizontal support.

Therefore, when the total slip of FRP at the cracking end of the segment can be predicted, the maximum central displacement Δ_c and the critical displacement for the FRP-diagonal crack intersection Δ_i can be estimated by the simple model above. Among the existing FRP bond models, the generic model for full-range behaviour of FRP bond joints developed by Yuan et. al. (2004) can be used to quantify the response of FRP strips crossing a crack opening. Predictions of FRP strip using Yuan's model are depicted in the next section.

6.4.4. Prediction for FRP Slip Crossing Crack Openings

Yuan et. al. (2004) developed a generic model to predict the entire debonding propagation process for FRP IC debonding failure mode based on the realistic bi-linear local bond-slip law. It is a closed-form analytical solution, which can be used to predict the FRP post-debonding response. It is found that the FRP bond length and the FRP plate stiffness affect the behaviour of the FRP bond joints.

As discussed in the above section, the upper bound of the critical wall displacements can be predicted by considering the FRP slip at the crack location . Therefore, in the current study the maximum slip of FRP strip crossing a crack opening must be predicted, which is simply the response of FRP at the post-debonding stage. The post-debonding is referred to as the stage between elastic-softening-debonding stage (refer Figure 3.30) and softening-debonding stage defined in Yuan's model. The former stage is the initiation of debonding, when debonding commences and propagates along the interface from the cracking end of a rigid body segment. The slip of the FRP at the loaded end can be quantified to be the δ_f from the FRP local bond-slip model at this stage, which is the slip when the shear stress decreases to zero at the loaded end. The latter stage represents the end of the debonding process, when the tensile force in FRP starts to decrease theoretically. The slip in FRP at this stage is theoretically defined as the maximum displacement δ_{max} , which can be developed through the total bond length. Unlike the five-brick masonry prism used in the FRP push-pull bond tests, the masonry segments in a cracked wall member may vary from a few hundred to 1250 mm in this case. It is believed that the slip at the loaded end (i.e. the cracking end of a rigid body segment) can be continuously developed if the bond length is long enough. Thus, the slip of FRP at the cracking end of a rigid body segments can develop from δ_f to δ_{max} during the post-debonding stage and the δ_{max} can be quantified by Yuan's model according to the FRP and masonry properties, the FRP bond length and the FRP-to-masonry bond-slip model.

The analytical solution of Yuan's model for elastic-softening-debonding stage ($\delta > \delta_f$) can be described as follows.

$$T_p = \frac{\tau_f b_p}{\lambda_2 \sin(\arctan(\frac{\lambda_1}{\lambda_2}))} \quad \text{Eq. 6-12}$$

$$\delta_{fp} = \delta_f (1 + \frac{T_p \lambda^2 l_d}{\tau_f b_p}) \quad \text{Eq. 6-13}$$

where, λ , λ_1 , λ_2 are dimensionless parameters, and defined respectively by Yuan as follows:

$$\lambda^2 = \frac{\tau_f}{\delta_f} \left(\frac{1}{E_p t_p} + \frac{b_p}{b_m E_m t_m} \right),$$

$$\lambda_1^2 = \lambda^2 \frac{\delta_f}{\delta_1} = \frac{\tau_f}{\delta_1} \left(\frac{1}{E_p t_p} + \frac{b_p}{b_m E_m t_m} \right)$$

$$\lambda_2^2 = \lambda^2 \frac{\delta_f}{\delta_f - \delta_1} = \frac{\tau_f}{\delta_f - \delta_1} \left(\frac{1}{E_p t_p} + \frac{b_p}{b_m E_m t_m} \right)$$

l_d is the length of debonding developed along FRP-to-masonry interface.

The maximum slip δ_{\max} can be obtained when the peak shear propagates to the support end of rigid body segment and the force in FRP begins to decrease. In this case, it is also described as

$$l_d = L_b - \frac{\pi}{2\lambda_2} \quad \text{Eq. 6-14}$$

$$\delta_{\max} = \delta_f \left(1 + \frac{\lambda^2 (L_b - \frac{\pi}{2\lambda_2})}{\lambda_2 \sin(\arctan(\frac{\lambda_1}{\lambda_2}))} \right) \quad \text{Eq. 6-15}$$

where L_b is FRP bond length.

Therefore, the upper bound of the FRP slip at the end of rigid body segment can be predicted by Yuan's model. The bond-slip parameters (τ_f , δ_l , δ_f) used in this prediction are derived from the author's FRP-to-masonry bond test (refer to Table 4.2).

6.4.5. Prediction and Comparison for Wall Displacements

Upper bound estimate of the wall displacements using the model developed in Section 6.4.3 are also based on the following assumptions:

- only IC debonding is developed along the FRP-to-masonry interface,
- the central displacement and the FRP-diagonal crack intersectional displacement of the wall are simulated by a rigid body member with a single midspan crack or two cracks, respectively,
- the debonding action is equally developed either side of a crack,
- the ultimate displacement is governed by the maximum slip of the rigid body segment with the shortest FRP bond length.

The displacement predictions summarised in Table 6.3 are compared with the experimental displacements at which FRP debonding failure occurred (Wall 1, 3 and 4) or ultimate displacements (Wall 2). It can be seen from Table 6.3 (a) that the predictions for externally bonded glass FRP walls (Wall 2 and 3) are in good agreement, because the predicted upper bound central displacements are approximately 8% and 30% higher than the experimental results. Although Wall 2 failed in local masonry collapse, it is believed that the FRP strips were very close to debonding based on the experimental strain recorded at that time. The prediction for externally bonded carbon FRP wall is only approximately half of that measured in the test. This is believed to be due to the following two reasons: (1) movements were found along the top horizontal support during this wall test, and hence the actual relative displacement was probably less than the measured value; (2) the

CFRP-to-masonry bond-slip parameters were derived from only four test specimens from Tran's study (2004), and may not accurately represent the bond behaviour.

Table 6.3 Upper bound prediction for the critical displacements of the wall

	L_b	$\delta_{\max,pre}$	z	$\theta_{\max,pre}$	$\Delta_{c,pre}$	$\Delta_{c,exp}$	$\Delta_{c,pre}/\Delta_{c,exp}$
	(mm)	(mm)	(mm)	radian	(mm)	(mm)	
Wall 1	1250	2.78	96.6	0.029	36.0	72.7	0.49
Wall 2	1250	12.50	100.7	0.124	155.2	143.5	1.08
Wall 3	1250	12.50	100.7	0.124	155.2	119.4	1.30

(a) Central displacement

	h_i	$l/2l_{mid}$	L_b	$\delta_{\max,pre}$	z	$\theta_{\max,pre}$	$\Delta_{i,pre}$	$\Delta_{c,pre}$	$\Delta_{c,exp}^*$	$\Delta_{c,pre}$	$\Delta_{c,exp}$
	(mm)	(mm)	(mm)	(mm)	(mm)	radian	(mm)	(mm)	(mm)	(mm)	(mm)
Prediction with theoretical crack line slope and h_i											
Wall 1 (V4)	466	784	466	0.99	96.6	0.020	9.6	25.6	72.7	0.35	
Wall 2 (V4)	466	784	466	4.43	100.7	0.088	41.0	110.0	143.5	0.77	
Wall 3 (V5)	358	892	358	3.36	100.7	0.067	23.9	83.4	119.4	0.70	
Wall 3 (V4)	717	533	533	5.11	100.7	0.101	72.8				
Wall 4 (V2)	207	1043	207	1.36	92.4	0.029	6.1	22.1	41.9	0.53	
Prediction with measured h_i											
Wall 1 (V4)	680	570	570	1.20	96.6	0.025	16.9	31.1	72.7	0.43	
Wall 2 (V4)	690	560	560	5.35	100.7	0.106	73.3	132.8	143.5	0.93	
Wall 3 (V4)	602	648	602	5.79	100.7	0.115	69.2	122.1	119.4	1.02	
Wall 3 (V5)	516	734	516	4.92	100.7	0.098	50.4				
Wall 4 (V2)	387	863	387	2.72	92.4	0.059	22.8	44.2	41.9	1.05	

Notes: l_{mid} = the length of middle segment; $L_b = \text{MIN}(h_i, l_{mid})$; $\Delta_{c,pre}$ is computed by Eq.6-6 and 6-7
 $\Delta_{c,exp}^*$ = experimental central displacement at debonding;

(b) FRP-diagonal crack intersectional displacement

For FRP-diagonal crack intersectional displacement Δ_i , a direct comparison cannot be made because there are no experimental data measured at this location. The FRP-diagonal crack intersectional displacement predictions were converted into the central displacements (Table 6.3 (b)) using Eq. 6-6 and 6-7. Two parts are included in this table. The first part is the prediction with theoretical crack line slope (i.e. theoretical h_i). In order to examine the validity of the displacement model and eliminate the inaccuracy caused by the difference between theoretical and experimental h_i , the prediction based on the measured distance h_i are also reported in the second part of Table 6.3 (b). Both wall displacements at strips V4 and V5 of Wall 3 were predicted, and the minimum value is reported and used for comparison.

It can be seen from Table 6.3 (b) that the predicted displacement for Wall 1 is significantly lower than the test results as previously observed in Table 6.3 (a) for the same two reasons discussed above. The predictions for the other walls using the theoretical h_i (part 1 of Table 6.3 (b)) are generally lower than the test results (23% lower for Wall 2, 30% for Wall 3 and 47% for Wall 4). It is believed that this inaccuracy is caused by firstly the movements of wall top edge support resulting in larger experimental displacement than the actual value, secondly the inaccuracy due to using the theoretical h_i . Therefore the measured h_i is used for prediction in the second part of Table 6.3 (b). The predictions are found in good agreement with the test results. The prediction to test result ratio is found to be 0.93, 1.02 and 1.05 for Wall 2, 3 and 4, respectively. Hence, it is believed this model is valid to predict the upper bound wall displacements for GFRP EB and CFRP NSM techniques. The underestimate using theoretical h_i is mainly due to the high variation of masonry properties and therefore the variation in cracking pattern.

6.5. CONCLUSIONS

This chapter discussed the application of the beam theory to predict the load capacity of one-way vertical bending capacity M_{cv} of a FRP retrofitted wall design strip. The FRP-to-masonry bond model developed in Chapter Four was used to predict the force and strain in FRP at IC debonding. Based on the experimental observation, M_{cv} can be regarded as the lower bound of the load capacity of the retrofitted wall under two-way bending. In general, a good agreement is found between predictions and the experimental results.

It can also be concluded that the rigid body theory is suitable to model the post-cracking behaviour of the wall with FRP strips based on the current experimental conditions and observations. The geometry and relationship between wall displacements and the FRP post-debonding behaviour were investigated. Simulating with a wall member including a single midspan crack or two cracks, the Δ_c and the Δ_i are related to the slip of FRP strip developed at the cracking end of a rigid body segment according to Yuan's generic FRP bond model. It is also found that the prediction is highly sensitive to the location of FRP-diagonal crack intersection (i.e. l_i). It is found that the wall displacement predictions using measured l_i for GFRP EB and CFRP NSM techniques are in good agreement with the test results, while it is over 50% under-estimate for CFRP EB technique.

Based on these results, recommendations for FRP retrofitted masonry wall strength and displacement design can be made: assuming IC debonding as weak link to gain more ductile response than if masonry crushing or FRP tensile rupture start to occur, and the midheight displacement of retrofitted URM wall should be controlled within the wall thickness to prevent wall collapse.

However, tests on FRP strengthened original URM walls without any existing cracks

are required to confirm the suitability of the rigid body theory for the FRP strengthened masonry wall. The FRP peeling/cleavage debonding response is recommended to be quantified, for it is a new failure mode and the failure tends to occur at a lower FRP tensile force and smaller wall displacement. More externally bonded carbon FRP to masonry bond tests are recommended to further quantify the bond-slip parameters.

7. CONCLUSIONS AND RECOMMENDATIONS

7.1. SUMMARY AND CONCLUSIONS

Earthquake damage to masonry buildings has shown the vulnerability of masonry walls to out-of-plane failure. This study focused on enhancing the flexural strength and behaviour of masonry walls subjected to out-of-plane loading. FRP rehabilitation techniques have been widely used for reinforced concrete structures for many years due to the advantages of FRP materials including lightweight, high strength, durability and moldability. The application of this technique for masonry buildings is not so well developed and so the FRP-masonry bond behaviour and failure mechanism are still not fully understood.

Twelve externally bonded glass FRP masonry and fifteen near surface mounted carbon FRP masonry push-pull tests were conducted to investigate the FRP-to-masonry bond behaviour. The variables included: masonry surface preparation method; location of FRP (relative to perpend joints and brick cores); FRP embedment depth and, FRP bond length. The FRP debonding failure model and load transfer mechanism along the FRP-to-masonry interface was studied, from which a local shear-slip model was determined for both externally bonded glass FRP and near surface mounted carbon FRP masonry were derived. The FRP-to-masonry bond strength models were developed based on FRP-concrete bond models by Chen and Teng, and Seracino et al. The predicted results given by the new model compared well with the experimental bond test results of near surface mounted carbon FRP and externally bonded carbon FRP techniques. Due to the inappropriate fabrication of the glass FRP strips, the experimental bond strength for the externally bonded glass FRP bond test was higher than predictions by the new model.

To investigate the effectiveness of retrofitting masonry walls using vertical externally bonded or near surface mounted strips, four full-scale walls, simply supported along four sides, were tested under distributed load imposed by air bags. The four masonry walls (with window openings) had previously been tested under reversed-cyclic loading, and were in a severely damaged state before the FRP retrofit schemes were applied. The full-scale wall tests showed that the flexural capacity of damaged masonry walls can be improved significantly using vertical FRP strips. The strengthened walls were as strong or stronger and more ductile than the original walls. Premature failure modes, called FRP peeling debonding and cleavage debonding, were observed in externally bonded carbon FRP strengthened wall and near surface mounted carbon FRP strengthened wall, respectively. The other two walls (repaired with externally bonded glass FRP strips) failed in horizontal bending of the masonry between two vertical FRP strips.

Based on these tests, a lower bound mechanics based analysis approach was developed to predict the out-of-plane bending capacity of masonry walls retrofitted with adhesively bonded vertical FRP strips. Rigid body theory was used to develop a model to predict the maximum wall displacement assuming that the debonding slip in the FRP crossing the wall crack could be fully developed. The predictions compared well with the experimental results for three of the four walls using the shear-slip bond parameters summarised in this study. The significant under-prediction of displacement for externally carbon FRP strengthened wall was probably due to the fact that the shear-slip model reported for externally bonded carbon FRP-masonry in Tran's study (2004) was not accurate as this was derived from only four push-pull tests. The validity of strain predictions for C-T and S-R bond model are limited to IC debonding. When peeling or cleavage debonding occurred, these two bond models might over-predict the FRP debonding strain.

It should also be noted that the development of the current model was based on

single-wythe walls, but it is believed that it is still applicable to multi-wythe walls if wythe wall tied together with good head joints. As for cavity walls, the applicability of the current model may be dependent on the wall construction form. If applying FRP on both exterior faces of both wall leaves and assuming wall ties to ensure the displacement compatibility of two wall leaves, it is believed the retrofitting method is still effective to improve the cavity wall out-of-plane capacity. However, further researches are recommended on this topic.

In summary, it could be concluded that reinforcing masonry walls with externally bonded or near surface mounted vertical FRP strips is an effective scheme to enhance the out-of-plane flexural resistance of masonry walls.

7.2. RECOMMENDATIONS FOR FURTHER RESEARCH

During the course of completing this study, some related aspects requiring further research have become apparent. These are summarised as follows:

- Further push-pull tests could be carried out to find the influence of other variables on both externally bonded and near surface mounted FRP-to-masonry bond strength. For the external bonding method, different types of brick units should be tried which has varying tension strength so that the accuracy of the material based bond-slip model can be verified. For the near surface mounting method, a series of bond tests should be conducted to establish more accurate values for critical bond length and depth of FRP embedment. More externally bonded carbon FRP-masonry bond tests are also recommended to more accurately quantify the bond-slip parameters previously reported by Tran (2004).

- The validity of the two models for externally bonded glass FRP strips applied in accordance with the manufacturer's recommendations should be performed.
- Tests on FRP strengthened masonry walls without pre-existing cracks are required to verify whether the failure mechanisms and cracking patterns are similar to those observed in walls with pre-existing cracks. The suitability of the rigid body theory for FRP strengthened masonry walls need to be further confirmed and the models developed in this study need to be validated by more test data.
- FRP peeling debonding and cleavage debonding response should be quantified as they are new critical failure modes and the failure tends to occur before IC debonding in two of the four walls considered in this research.
- It is worthwhile to investigate the behaviour of FRP retrofitted URM walls subject to different loading conditions. Cyclic loading and reversed cyclic loading are recommended to examine the behaviour of URM walls retrofitted by FRP on both faces.

NOTATIONS

A_c	= cross section area of the concrete prism
A_p	= cross section area of the FRP strip
b_c	= the width of concrete prism
b_f	= the length of the failure plane parallel to the concrete surface
b_m	= the width of a wall design strip
b_p	= FRP strip width
C_m	= compressive force in masonry
c	= the depth of neutral axis
d_f	= the length of the failure plane perpendicular to the concrete surface
d_p	= depth of embedment for NSM FRP strip
E_c	= the modulus of elasticity of concrete
E_f	= the modulus of elasticity of fibre sheet
E_p	= the modulus of elasticity of FRP strip
E_m	= the modulus of elasticity of epoxy resin
f_{ct}	= concrete tensile strength
f_{rupt}	= the rupture stress of an FRP strip
f_t	= the ultimate stress of FRP at rupture
f_{ut}	= the lateral modulus of rupture of masonry units
f_y	= the yield stress of a metallic strip
G	= masonry wall crack line slope
H	= wall height
h_o	= height of wall opening
h_i	= distance from the top of the wall to the FRP-diagonal crack intersection
h_u	= height of the masonry unit
L_b	= FRP bond length
L_{per}	= the length of the debonding failure plane (in cross-section)
l_d	= the length of debonding developed along FRP-to-masonry interface

l_e	= effective bond length
l_u	= length of the masonry unit, respectively
M_{cv}	= nominal vertical bending moment capacity
M_n	= nominal bending moment
P_{cr}	= Load when the first crack is observed visually
P_i	= applied load
$(P_{IC})_{RC}$	= FRP-to-concrete debonding load
P_u	= ultimate load
s	= spacing between FRP strips
T_p	= tensile force in FRP strip
t_p	= FRP strip thickness
t_j	= the thickness of the mortar joint
V_f	= the volume fraction of fibre in the FRP strip
w_{pre}	= lateral load capacity
β_{frp}	= FRP width coefficient
β_l	= bond length coefficient
ε_{db}	= the debonding strain of FRP
ε_l	= strain reading with the FRP bonded region
ε_p	= axial strain in the FRP strip
ε_u	= ultimate strain
ε_{ub}	= strain reading within the unbonded region of the FRP strip
ε_{ult}	= the ultimate strain of FRP at rupture
Δ_c	= central displacement
Δ_i	= FRP-to-diagonal crack intersectional displacement
Δ_u	= ultimate displacement
Δ	= slip at the FRP strip at the loaded end
δ	= slip in FRP strip
δ_f	= slip at zero shear stress
δ_{frp}	= slip in FRP strip
δ_l	= slip at peak shear stress

φ_f	= the IC debonding failure plane aspect ratio
σ_p	= axial stress in the FRP strip
λ	= dimensionless parameter defined by Eq 6-12
λ_1	= dimensionless parameter defined by Eq 6-13
λ_2	= dimensionless parameter defined by Eq 6-14
τ_f	= peak shear stress

REFERENCES

- ACI 440.2R-02. (2002). "Emerging Technology Series. Guide for the Design and Construction of Externally Bonded FRP Systems for Strengthening Concrete Structures." *Reported by ACI Committee 440. American Concrete Institute, Farmington Hills, Michigan, USA.*
- ACI 318-89 (1989). "Building Code Requirements for Reinforced Concrete (318-89) and Commentary (318R-89)." *American Concrete Institute (ACI), Farmington Hills, Michigan, USA.*
- AS1700.4. (1993). "Minimum Design Loads on Structures - Earthquakes Codes." *Standards Australia 1993, The Crescent, Homebush, NSW 2140.*
- Albert, M. L., Elwi, A. E., and Cheng, J. J. R. (2001). "Strengthening of Unreinforced Masonry Walls Using FRPs." *Journal of Composites for Construction*, 5(2), 76-84.
- Chapman, A., Hamann, M., Moon, L., and Stoechel, A. (2005). "Seismic Strengthening of Unreinforced Masonry Using Near Surface Mounted FRP." *Final Year Research Report, School of Civil and Environmental Engineering, University of Adelaide, November, Adelaide.*
- Chen, J. F., Yang, Z. J. and Holt, G. D. (2001). "FRP or steel plate-to-concrete bonded joints: effect of test methods on experimental bond strength", *Steel and Composite Structures-An International Journal*, 1(2), 231-244.
- Concrete Society Technical Report No. 55. (2000). "Design guidance for strengthening concrete structures using fibre composite materials." *The Concrete Society. Century House, Telford Avenue, Crowthorne, Berkshire, UK.*
- Deslauriers, F., Pall, A., and Pall, R., (1997). "Seismic rehabilitation of Federal Building in Sherbrooke, Quebec", *Proceedings, Annual Conference - Canadian Society for Civil Engineering*, v 4, Second Symposium on Applied Mechanics Structures: Seismic Engineering, 1997, 339-347.

- Ehsani, M. R. and Saadatmanesh, H. (1997). "Method of Strengthening Masonry and Concrete Walls With Composite Strap and High Strength Random Fibers." *U.S. Patent* No.5,640,825.
- Ehsani, M. R., Saadatmanesh, H., and Velazquez-Dimas, J. I. (1999). "Behaviour of Retrofitted URM Walls under Simulated Earthquake Loading." *Journal of Composites for Construction*, 3(3), 134-142.
- Ghobarah, A., and Galal, K. E. M. (2004). "Out-of-Plane Strengthening of Unreinforced Masonry Walls with Openings." *Journal of Composites for Construction*, 8(4), 298-305.
- Gilstrap, J. M. and Dolan, C. W. (1998). "Out-of-plane Bending of FRP-reinforced Masonry Walls", *Composites Science and Technology*, 58(8), 1277-1284.
- Griffith, M. C. and Klopp G. (1998). "Seismic Analysis of Unreinforced Masonry Buildings", *Australian Journal of Structural Engineering*, vol. SE1, No.2,1998.
- Griffith, M. C. and Vaculik, J. (2005). "Flexural Strength of Unreinforced Clay Brick Masonry Walls." *Proceedings of the 10th Canadian Masonry Symposium*, Banff, Alberta.
- Hamilton III, H. R., and Dolan, C. W. (2001). "Flexural Capacity of Glass FRP Strengthened Concrete Masonry Walls." *Journal of Composites for Construction*, 5(3), 170-178.
- Hamoush, S. A., McGinley, M. W., Mlakar, P., Scott, D., and Murray, K. (2001). "Out-of-Plane Strengthening of Masonry Walls with Reinforced Composites." *Journal of Composites for Construction*, 5(3), 139-145.
- Hamoush, S., McGinley, M. W., Mlakar, P., and Terro, M. J. (2002). "Out-of-plane behavior of surface-reinforced masonry walls." *Construction and Building Materials*, 16(6), 341-351.
- Hassan, T. and Rizkalla, S. (2003). "Investigation of Bond in Concrete Structures Strengthened with Near Surface Mounted Carbon Fiber Reinforced Polymer Strips." *Journal of Composites for Construction*, 7(3), 248-257.

- Hendry, A. W., Sinha, B. P., and Davies S. R. (1981). "An Introduction to Load Bearing Brickwork Design". Chichester : E. Horwood ; New York : Halsted Press, ISBN: 0-8531-2216-4.
- Hollaway, L. C. and Leeming, M. B. (1999). *Strengthening of Reinforced Concrete Structures*, CRC Press ISBN 0-8493-1715-0.
- Ing, L. K., Jones, N., Page, M. and Ward., S. (2004). "Intermediate Crack Debonding of Near Surface Mounted Strips." *Final Year Research Report*, School of Civil and Environmental Engineering, University of Adelaide, November, Adelaide.
- Kaiser, H. P. (1989). "Strengthening of reinforced concrete with epoxy-bonded carbon-fiber plastics." *Doctoral Thesis*, Diss. ETH, Nr.8918, ETH Zurich, Ch-8092 Zurich, Switzerland.
- Korany, M. D., Elwi, A. E., and Cheng, J. J. R. (2005). "Flexural Resistance of Unbonded and Intermittently Bonded FRP-Reinforced Masonry Panels." *10th Canadian Masonry Symposium*, Banff, Alberta, June 8-12, 2005.
- Kuzik, M. D., Elwi, A. E., and Cheng, J. J. R. (2003). "Cyclic Flexure Tests of Masonry Walls Reinforced with Glass Fiber Reinforced Polymer Sheets." *Journal of Composites for Construction*, 7(1), 20-30.
- Lee, C. L., Leong, T. H., Tay, I. C., Wong, W.L. (2005). "Failure Mechanism of FRP Plated Steel Beams", *Final Year Research Report*, School of Civil and Environmental Engineering, University of Adelaide, May, Adelaide.
- Lu, X. J., Teng, J. G., Ye, L. P. and Jiang, J. J. (2005). "Bond-slip models for FRP sheets/plates bonded to concrete." *Engineering Structures*, 27, 920-937.
- MacGregor, J. G. (1988). "Reinforced Concrete: Mechanics and Design", Prentice Hall, Englewood Cliff, New Jersey, USA.
- Meier, U. (1987a) "Bridge Repair With High Performance Composite Material", *Mater Technik* 15,125-128.
- Meier, U. (1987b)"Brückensanierungen mit Hochleistungs-Faserverbundwerkstoffen" *Material und Technik*; 15. Jahrgang, Heft No 4,125-128.
- Meier, U. and Kaiser, H. P. (1991). "Strengthening of structures with CFRP laminates",

- Proc Advanced Composite Material in Civil Engineering Structures, Mats Div ASCE*, Las Vegas, Jan 1991, 224-232.
- Oehlers, D. J., Ju, G., Liu, I. S. T., and Seracino, R. (2004). "Moment redistribution in continuous plated RC flexural members-Part-I: Neutral axis depth approach and tests." *Engineering Structures*, 26, 2197-2207.
- Oehlers, D. J., and Seracino, R., (2004). "Design of FRP and Steel Plated RC Structures: Retrofitting of Beams and Slabs for Strength, Stiffness and Ductility." Kidlington, Oxford, UK: Elsevier.
- Seracino, R., Raizal Saifulnaz, M. R. and Oehlers, D. J. (2006). "Generic Intermediate Crack Debonding Resistance of EB and NSM Plate-to-Concrete Joints." *Journal of Composites for Construction*, ASCE, (tentatively accepted February 8, 2006).
- Shrive, N. G. (2006). "The use of fibre reinforced polymers to improve seismic resistance of masonry." *Construction and Building Materials*, 20(4), 269-277.
- Spyrakos, C. C. and Vlassis, A. G. (2003). "Seismic Retrofit of Reinforced Concrete Bridges." *Advances in Earthquake Engineering*, v 13, Earth Resistant Engineering Structures IV, 79-88.
- Tan, K. H., and Patoary, M. K. H. (2004). "Strengthening of Masonry Walls against Out-of-Plane Loads Using Fiber-Reinforced Polymer Reinforcement." *Journal of Composites for Construction*, 8(1), 79-87.
- Teng, J. G., Chen, J. F., Smith, S. T., and Lam, L. (2002). "FRP strengthened RC structures." Chichester, England: John Wiley and Sons Ltd.
- Tran, L. G. (2004). "Strengthening of Masonry Beams Using FRP Plate." *Masters Thesis*, School of Civil and Environmental Engineering, University of Adelaide, Adelaide.
- Triantafillou, T. C. (1998). "Strengthening of Masonry Structures Using Epoxy-Bonded FRP Laminates." *Journal of Composites for Construction*, 2(2), 96-104.
- Tumialan, G., Tinazzi, D., Myers, J. J., and Nanni, A. (2000). "Field Evaluation of Unreinforced Masonry Walls Strengthened with FRP Composites Subjected to

Out-of-Plane Loading." *Structures 2000*, 176.

- Tumialan, J. G., Galati, N., and Nanni, A. (2003). "Fibre-reinforced polymer strengthening of unreinforced masonry walls subject to out-of-plane loads." *ACI Structural Journal*, 100(3), 321-9
- Tumialan, J. G., Micelli, F., and Nanni, A. (2001). "Strengthening of Masonry Structures with FRP Composites." *Structures 2001*, 130.
- Turco, V., N.Galati, G.Tumialan, and A.Nanni. (2003) "Flexural strengthening of URM walls with FRP systems." *FRPRCS-6: Applications in Masonry and Steel Structures*, Singapore, 1219-1228.
- Van Gemert, D. (1980). "Force transfer in epoxy-bonded steel-concrete joints.", *International Journal of Adhesion and Adhesives*, 1, 67-72.
- Velazquez-Dimas, J. I., and Ehsani, M. R. (2000). "Modeling Out-of-Plane Behavior of URM Walls Retrofitted with Fiber Composites." *Journal of Composites for Construction*, 4(4), 172-181.
- Yuan, H., Teng, J.G., Seracino, R., Wu, Z.S. and Yao, J. (2004). "Full-range behavior of FRP-to-concrete bonded joints." *Engineering Structures*, 26(5), 553-564.

APPENDIX A: FRP RETROFITTED URM WALL TESTS DATABASE

This database includes the available externally bonded FRP strip retrofitted masonry wall tests from the published literatures. Only static monotonic or cyclic one-way out-of-plane bending tests are included in this database. The details of masonry, FRP and test results are summarised according to the original publications. Predictions are provided for specimens with FRP debonding or rupture failure only, using cross sectional analysis method.

Ehsani, Saadatmanesh and Velazquez-Dimas (1999)

BEHAVIOR OF RETROFITTED URM WALLS UNDER SIMULATED EARTHQUAKE LOADING

The wall tests of this study are included in Velazque-Dimas and Ehsani (2000)
Please refer to the specimens S75/25, S40/20 and S30/30 in that test summary

Velazque-Dimas and Ehsani (2000)

MODELING OUT-OF-PLANE BEHAVIOR OF URM WALLS RETROFITTED WITH FIBER COMPOSITES

Test descriptions:

Masonry wall: half-scale single wythe (S) or half-scale double wythe (D)

Masonry wall geometry (mm) (Height * Width * Thickness): 1) short wall 710 * 1220 * 50; 2) slender wall 1420 * 1220 * 5

FRP retrofit scheme: GFRP vertical strips without anchorage (retorfitting on both sides of the wall)

Masonry wall test conditions: Simply supported one-way static cyclic one-way bending (No axial precompression)

Test variables: 1) Masonry wall types, 2) Amount of FRP materials

Wall Failure modes: 1) Flexural-shear (Fe-Sh); 2) FRP rupture (Ru)

Due to lack of data, Dimas and Ehsani's predictions are reported

Specimen	Masonry Details				FRP Details			Test Results			Prediction	
	H/t _m	Face	f _{mc}	ε _{mu}	Reinforcement ratio	f _{ut}	ε _{pu}	W _{exp}	ε _{max}	Failure Mode	W _{pre}	M _{pre} /M _{exp}
			(MPa)	(με)		(kN/mm)	(%)	(kPa)	(%)		(kPa)	
Half -scale brick units												
S75/25	14	North			0.75			31.0	1.2	De	34.3	1.11
	14	South			0.25			12.4	1.0	Dc	N/A	
S20/40	14	North			0.20			10.3	1.2	De	9.2	0.9
	14	South			0.40			18.6	1.0	De	18.3	0.99
S30/30	14	North			0.30			15.5	0.7	De	N/A	
	14	South			0.30			16.6	1.0	Ru	N/A	
S100/100	28	North	26.7	0.003	1.00	0.37	2.0	11.7	1.0	Ru+De	11.3	0.97
	28	South			1.00			11.7	0.9	De	N/A	
S300/300	28	North			3.00			16.7	0.5	N/A	N/A	
	28	South			3.00			22.7	0.3	Shear	33.4	1.47
S200/50	28	North			2.00			20.7	1.1	De	22.3	1.08
	28	South			0.50			6.2	1.3	Ru	5.7	0.92
D100	28	North			1.00			9.8	0.8	De	N/A	

Hamilton III and Dolan (2001)

FLEXURAL CAPACITY OF GLASS FRP STRENGTHENED CONCRETE MASONRY WALLS

Test descriptions:

Masonry wall geometry (mm) (Height * Width * Thickness): 1) 1800 * 610 * 200; 2) 4700 * 1220 * 200

FRP retrofit scheme: 1) One vertical GFRP strip for for short walls without anchorage

2) Four vertical GFRP strip for tall walls (1 layer * 4 strips for T1, 2 layers * 2 strips for T2) without anchorage

Masonry wall surface prepared by wire brushing

Masonry wall test conditions: Simply supported one-way static monotonic one-way bending

Test variables: 1) Masonry wall geometry, 2) FRP layers, 3) Masonry unit types

Wall Failure modes: 1) FRP debonding (De); 2) FRP rupture (Ru); 3) Combination of FRP rupture and debonding (Ru+De)

Predictions: Due to lack of FRP material properties, Hamilton et al's predictions based on beam theory are reported

Series	Specimen	Masonry Details				FRP Details							Test Results		Prediction	
		b_m	H_m	f_{mc}	ϵ_{m1}	layer * strips	t_p	b_p	A_p	f_{ut}	E_p	ϵ_{pu}	w_{exp}	Failure Mode	w_{pre}	M_{pre}/M_{exp}
		(mm)	(mm)	(MPa)	($\mu\epsilon$)		(mm)	(mm)	(mm^2)	(MPa)	(MPa)	(%)	(kPa)		(kPa)	
Normal concrete masonry unit																
S	S1	610	1800	14.5	0.003	1 * 1	0.35	69.9	24.47	N/A	1.5	15.0	De	20.4	1.36	
	S2	610	1800	14.5	0.003	1 * 1	0.35	69.9	24.47	N/A	1.5	18.4	Ru+De	20.4	1.11	
Lightweight concrete masonry unit																
											1.5					
S	S3	610	1800	10.9	0.003	1 * 1	0.35	69.9	24.47	N/A	1.5	21.3	Ru	26.9	1.26	
	S4	610	1800	10.9	0.003	1 * 1	0.35	69.9	24.47	N/A	1.5	23.7	Ru+De	26.9	1.14	
T	T1	1220	4700	15.0	0.003	1 * 4	0.35	279.6	97.86	N/A	1.5	5.9	Ru+De	5.9	1.00	
	T2	1220	4700	15.0	0.003	2 * 2	0.35	279.6	97.86	N/A	1.5	4.8	Ru	5.9	1.23	

Hamoush, McGinley, Mlakar, Scott, Murray (2001)

OUT-OF-PLANE STRENGTHENING OF MASONRY WALLS WITH REINFORCED COMPOSITES

Test descriptions:

Masonry wall geometry (mm) (Height * Width * Thickness): 1) 1800 * 1200 * 200

FRP retrofit scheme: 1) two layers of bi-directional GFRP webbing (i.e. glass sheet) without anchorage

2) 300 mm wide vertical and horizontal unidirectional GFRP strips with a clear spacing of 150 mm, without anchor

Masonry wall surface prepared by sand blasting or wire brushing

Masonry wall test conditions: Simply supported one-way static monotonic one-way bending

Test variables: 1) FRP configurations, 2) Masonry surface preparation

Wall Failure modes: 1) FRP debonding (De); 2) FRP rupture (Ru); 3) Combination of FRP rupture and debonding (Ru+De)

Predictions can not be made due to the lack of FRP Failure modes

Set No.	Specimen	Masonry Details				Surface preparatio	Patterns	FRP Details							Test Results	
		b_m	f_{mc}	ϵ_{m1}				t_p	Layer		b_p (mm)		A_p (Vert)	E_p	ϵ_{pu}	w_{exp}
		(mm)	(MPa)	($\mu\epsilon$)		(mm)	Vert	Hori	Vert	Hori	(mm^2)	(MPa)		(kPa)		
Concrete masonry units																
1	1				Wire brush	Strips	1.3	1	1	900	1200	1170	13790	0.015	15.40	Shear
2	2				Wire brush	Web	0.4	2	0	1200	1800	480	27579	0.020	24.27	Shear
5	3				None	Control	None	None	None	None	None	None	N/A	-	-	
5	4				None	Control	None	None	None	None	None	None	N/A	0.68	Bending	
5	5				None	Control	None	None	None	None	None	None	N/A	1.43	Bending	
1	6				Wire brush	Strips	1.3	1	1	900	1200	1170	13790	0.015	29.72	Unfaile
2	7				Wire brush	Web	0.4	2	0	1200	1800	480	27579	0.020	22.40	Shear
1	8	200	13.7	0	Wire brush	Strips	1.3	1	1	900	1200	1170	13790	0.015	17.10	Shear
2	9				Wire brush	Web	0.4	2	0	1200	1800	480	27579	0.020	14.47	Bending
3	10				Sandblast	Strips	1.3	1	1	900	1200	1170	13790	0.015	16.30	Shear
4	11				Sandblast	Web	0.4	2	0	1200	1800	480	27579	0.020	19.71	Shear
3	12				Sandblast	Strips	1.3	1	1	900	1200	1170	13790	0.015	22.06	Shear
4	13				Sandblast	Web	0.4	2	0	1200	1800	480	27579	0.020	27.71	Shear
3	14				Sandblast	Strips	1.3	1	1	900	1200	1170	13790	0.015	16.11	Shear
4	15				Sandblast	Web	0.4	2	0	1200	1800	480	27579	0.020	23.69	Shear

Note: Vert = Vertical direction, Hori = Horizontal direction

Albert, Elwi and Cheng (2001)

STRENGTHENING OF URM WALLS USING FRPS

Test descriptions:

Masonry wall geometry (mm) (Height * Width * Thickness): 4000 * 1200 * 190

FRP retrofit scheme: two or four vertical strips or diagonal strips without anchorage

Masonry wall test conditions: Simply supported one-way static monotonic one-way bending

Two point concentrated load at 1.4 m and 2.7 m above the base of the wall.

Test variables: 1) Masonry unit types, 2) FRP material types, 3) FRP strip width b_p , 4) Retrofit patterns

Wall Failure modes: 1) Flexural-shear (Fl-Sh); 2) FRP rupture (Ru)

Predictions are made for Ru failure specimens with vertical strips only.

Series	Specimen	Masonry Details			FRP Details								Test Results			Prediction	
		b_m	f_{mc}	ϵ_{m1}	Type	No. of strips	t_p	b_p	A_p	f_{ut}	E_p	ϵ_{pu}	P_{max}	M_{exp}	Failure Mode	M_{pre}	M_{pre}/M_{exp}
		(mm)	(MPa)	($\mu\epsilon$)			(mm)	(mm)	(mm ²)	(MPa)	(MPa)	(%)	(kN)	(kNm)		(kNm)	
Metric dimension masonry block																	
1	MU1				None	N/A	-	N/A	N/A				1.0	0.7	Mortar Shear		N/A
	MCS2-1				carbon strip	2	1.27	50	127	2749	185181	1.48	12.0	8.4	N/A		N/A
	MCS3-2				carbon strip	2	1.27	50	127	2749	185181	1.48	21.8	15.3	Mortar slip		N/A
	MCST4	190	7.3	N/A	carbon sheet	2	0.73	250	365	581	47475	1.30	28.9	20.2	N/A		N/A
	MGST5				glass sheet	2	1.81	250	903	106	17770	0.63	36.0	25.2	Fl-Sh		N/A
	MCS6				carbon strip	4	1.27	50	254	2749	185181	1.48	46.4	32.5	Fl-Sh		N/A
	MCST7-4				carbon sheet	2	0.73	250	365	473	47475	1.30	32.7	22.9	Fl-Sh		N/A
Imperial dimension block																	
2	ICST8				carbon sheet	2	0.73	250	365	581	47475	1.30	50.2	35.1	Fl-Sh		N/A
	ICST9				carbon sheet	2	0.73	250	365	581	47475	1.30	33.0	23.1	N/A		N/A
	ICST10				carbon sheet	2	0.73	125	182	581	47475	1.30	20.9	14.6	Ru	10.4	0.71
	ICST11	193	13.4	N/A	carbon sheet	2	0.73	250	365	581	47475	1.30	41.7	29.2	Fl-Sh		N/A
	ICST12				carbon sheet diagonal 1 strips	10	0.73	125	911	581	47475	1.30	22.7	15.9	Ru		N/A
	ICST13				carbon sheet	2	0.73	250	365	581	47475	1.30	37.7	26.4	Fl-Sh		N/A

Tumialan ,Galati and Nanni (2003)

FRP STRENGTHENING OF URM WALLS SUBJECT TO OUT-OF-PLANE LOADS

Test descriptions:

Masonry wall geometry (mm) (Height * Width * Thickness): 1200 * 600 * 95

FRP retrofit scheme: one vertical strip without anchorage

Masonry wall test conditions: Simply supported one-way static monotonic one-way bending.

Test variables: 1) Masonry surface preparation, 2) FRP material types, 3) FRP strip width b_p , 4) Masonry unit types

Wall Failure modes: 1) FRP debonding (De); 2) FRP rupture (Ru); 3) Masonry shear flexural(SF); Masonry shear sliding shear (SS)

Predictions based on beam theory are made for De and Ru failure specimens.

According to the experimental results, FRP debonding strain $\varepsilon_{db} = \alpha \varepsilon_{pu}$ ($\alpha=0.65$ for AFRP, $\alpha=0.7$ for GFRP)

Series	Specimen	Masonry Details				FRP Details							Test Results		Prediction	
		b_m	f_{mc}	ε_{mu}	Surface Preparation	FRP Type	t_p	b_p	A_p	f_{ut}	E_p	ε_{pu}	M_{exp}	Failure Mode	M_{pre}	M_{pre}/M_{exp}
		(mm)	(MPa)	($\mu\varepsilon$)			(mm)	(mm)	(mm ²)	(MPa)	(MPa)	(%)	(kNm)		(kNm)	
Concrete block																
COG	COG3							75	26.3				2.05	De	2.6	1.28
	COG3R							75	26.3				3.22	De	2.6	0.81
	COG5							125	43.8				3.33	De	4.3	1.30
	COG5R	600	10.5	0.0025	No	Glass	0.35	125	43.8	1690	92900	1.8	5.37	Ru	6.7	1.24
	COG7							175	61.3				3.74	De	6.0	1.60
	COG9							225	78.8				5.23	SF	N/A	
	COG12							300	105				6.06	SF	N/A	
COA	COA3							75	26.3				2.54	De	2.9	1.13
	COA5							125	43.8				3.57	De	4.8	1.33
	COA7	600	10.5	0.0025	No	Aramid	0.35	175	61.3	1876	115200	1.6	4.66	SF	N/A	
	COA9							225	78.8				5.25	SF	N/A	
	COA12							300	105				6.33	SF	N/A	
Clay brick																
CLG	CLG3							75	26.3				3.23	De	2.9	0.88
	CLG3R							75	26.3				3.88	Ru	4.0	1.03
	CLG5							125	43.8				4.89	De	4.7	0.96
	CLG5R	600	17.1	0.0035	Putty	Glass	0.35	125	43.8	1690	92900	1.8	5.37	Ru	6.7	1.25
	CLG7							175	61.3				6.58	De	6.6	1.00
	CLG7R							175	61.3				7.2	De	6.6	0.91
	CLG9							225	78.8				6.94	SS	N/A	
	CLG12							300	105				6.16	SS	N/A	
CLA	CLA3							75	26.3				2.94	De	2.9	0.99
	CLA5							125	43.8				5.23	Ru	7.3	1.40
	CLA7	600	17.1	0.0035	Putty	Aramid	0.35	175	61.3	1876	115200	1.6	6.13	De	6.7	1.09
	CLA9							225	78.8				8.45	De	8.50	1.01
	CLA12							300	105				5.9	SS	N/A	

Kuzik, Elwi and Cheng (2003)

CYCLIC FLEXURE TESTS OF MASONRY WALLS REINFORCED WITH GLASS FRP SHEETS

Test descriptions:

Masonry wall geometry (mm) (Height * Width * Thickness): 4000 * 1200 * 200

FRP retrofit scheme: Two vertical strips without anchorage

Masonry wall test conditions: Walls were tests in a vertical position under constant axial precompression with fully reversed cyclic out-of-plane lateral load.

Two-line concentrated loads were applied at 1200 mm from top and bottom.

Test variables: 1) Amount of GFRP sheets, 2) Amount of steel reinforcement, 3) Level of axial precompression

Wall Failure modes: 1) Flexural-shear failure (Fl-Sh); 2) Serviceability failure (Serv)

Predictions are not made due to flexural-shear failure.

Specimen	Masonry Details			FRP Details				Test Results		
	Steel reinforcement	Axial load	f_{mc}	l_p	b_p	E_p	ε_{pu}	P_{max}	M_{exp}	Failure Mode
	(bar type)	(kN)	(MPa)	(mm)	(mm)	(MPa)	(%)	(kN)	(kNm)	
Concrete masonry block										
Wall 1	2-10M	28.6			500			57.1	34.3	Fl-Sh
Wall 2	None	31.7			500			38.1	22.9	Fl-Sh
Wall 3	2-10M	30.1			260			39.0	23.4	Fl-Sh
Wall 4	2-10M	30.1			130			28.4	17.0	Serv
Wall 5a	2-10M	32.1	10.3	N/A	None	27521	2.2	15.2	9.1	Fl-Sh
Wall 5b	2-10M	30.8			500			53.2	31.9	Fl-Sh
Wall 6	2-10M	15.5			500			65.3	39.2	Fl-Sh
Wall 7	2-10M	46.5			500			69.1	41.5	Fl-Sh
Wall 8	2-15M	29.4			500			84.1	50.5	Fl-Sh

Turco, Galati, Tunialan and Nanni (2003)

FLEXURAL STRENGTHENING OF URM WALLS WITH FRP SYSTEMS

Test descriptions:

Masonry wall geometry (mm) (Height * Width * Thickness): 1200 * 600 * 95

FRP retrofit scheme: Vertical strips without anchorage

Masonry wall test conditions: Simply supported one-way static monotonic one-way bending.

Two-line concentrated load was applied at 200 mm spacing.

Test variables: 1) FRP material types, 2) FRP strip width b_p , 3) Masonry unit types

Wall Failure modes: 1) FRP debonding (De); 2) Flexural failure (FRP rupture or masonry crushing) (Fe);

3) Masonry shear failure (Shear)

Predictions based on beam theory are made for De and Ru failure specimens.

The reported FRP debonding strain was used for predictions (ε_{db} =1.4% for concrete block and 1.54% for clay brick).

Series	Specimen	Masonry Details		FRP Details							Test Results		Prediction	
		b_m	f_{mc}	FRP Type	t_p	b_p	A_p	f_{ut}	E_p	ε_{pu}	M_{exp}	Failure Mode	M_{pre}	M_{pre}/M_{exp}
		(mm)	(MPa)		(mm)	(mm)	(mm ²)	(MPa)	(MPa)	(%)	(kNm)		(kNm)	
Concrete block														
CLG	CLG3					75	28				2.05	De	3.3	1.61
	CLG3R					75	28				3.22	De	3.3	1.02
	CLG5					125	46				3.33	De	5.4	1.62
	CLG5R	600	10.5	Glass	0.37	125	46	1690	92900	1.82	5.37	De	5.4	1.01
	CLG7					175	65				3.74	De	7.6	2.03
	CLG9					225	83				5.23	Fe	N/A	
	CLG12					300	111				6.06	Fe	N/A	
CLA	CLA3					75	22				2.54	De	3.3	1.28
	CLA5					125	36				3.57	De	5.3	1.48
	CLA7	600	10.5	Aramid	0.29	175	51	1876	115200	N/A	4.66	Fe	N/A	
	CLA9					225	65				5.25	Fe	N/A	
	CLA12					300	87				6.33	Fe	N/A	
Clay masonry brick														
BLG	BLG3					75	28				3.23	De	4.5	1.39
	BLG3R					75	28				3.88	Ru	4.5	1.16
	BLG5					125	46				4.89	De	5.2	1.06
	BLG5R	600	17.1	Glass	0.37	125	46	1690	92900	1.82	5.37	Ru	6.7	1.25
	BLG7					175	65				6.58	De	7.1	1.08
	BLG7R					175	65				7.20	De	7.1	0.99
	BLG9					225	83				6.94	Shear	N/A	
	BLG12					300	111				6.16	Shear	N/A	
BLA	BLA3					75	22				2.94	De	3.1	1.05
	BLA5					125	36				5.23	Ru	7.3	1.40
	BLA7	600	17.1	Aramid	0.29	175	51	1876	115200	N/A	6.13	De	6.8	1.11
	BLA9					225	65				8.45	De	8.7	1.03
	BLA12					300	87				5.90	Shear	N/A	

APPENDIX B: GFRP MATERIAL TEST RESULTS

Three 50 mm wide prefabricated glass FRP strips were tested. Two strain gauges were attached at the centre of the on both sides. The test results are summarised in Table A.1. The load-strain responses for each strip are depicted in Figures A.1 to A.3.

Table B.1 Summary of Prefabricated GFRP Strip Tensile Test

GFRP strip	t_p	b_p	P_u	ϵ_u	σ_u	$E_{p,ave}$
	(mm)	(mm)	(mm)	($\mu\epsilon$)	(MPa)	(MPa)
1	2.0	50	21.4	10766	214	20.3
2	2.0	50	19.8	11729	198	16.2
3	2.0	50	25.3	11943	253	21.5
Mean			22.2	11479	221.7	19.3
St Dev			2.31	511.91	23.10	2.27
COV			0.10	0.04	0.10	0.12

Load-strain responses:

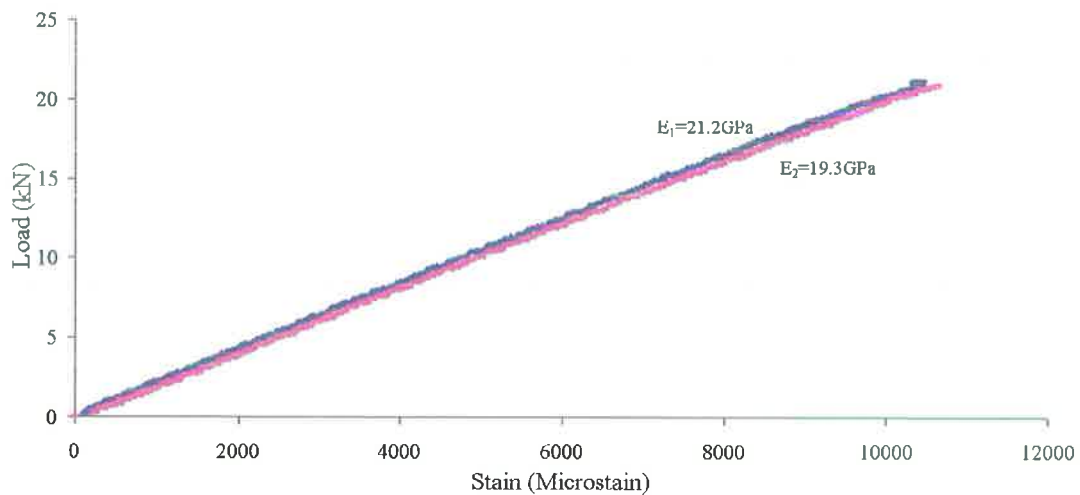


Figure B.1 Load-strain response of GFRP strip 1

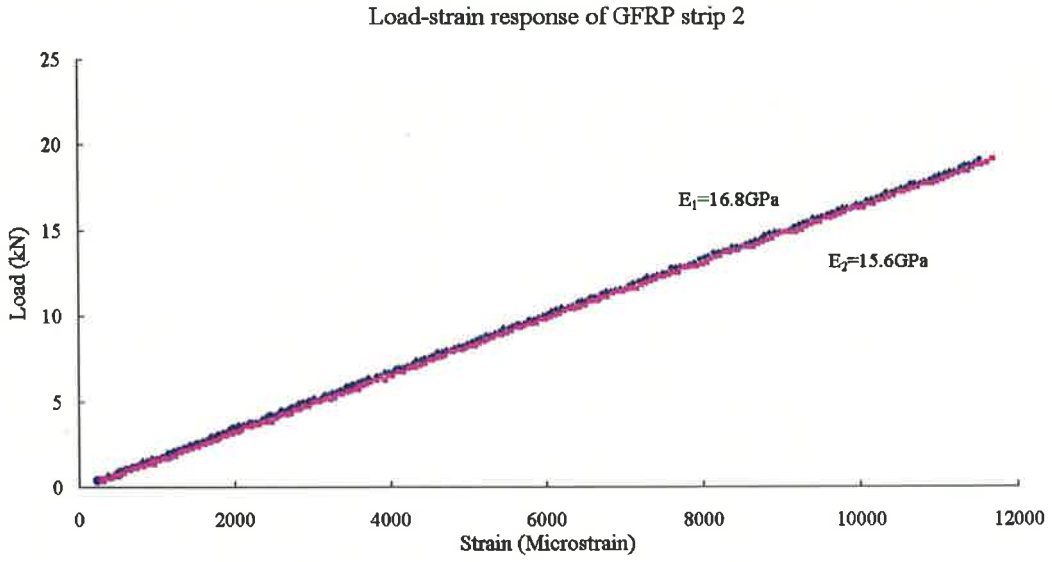


Figure B.2 Load-strain response of GFRP strip 2

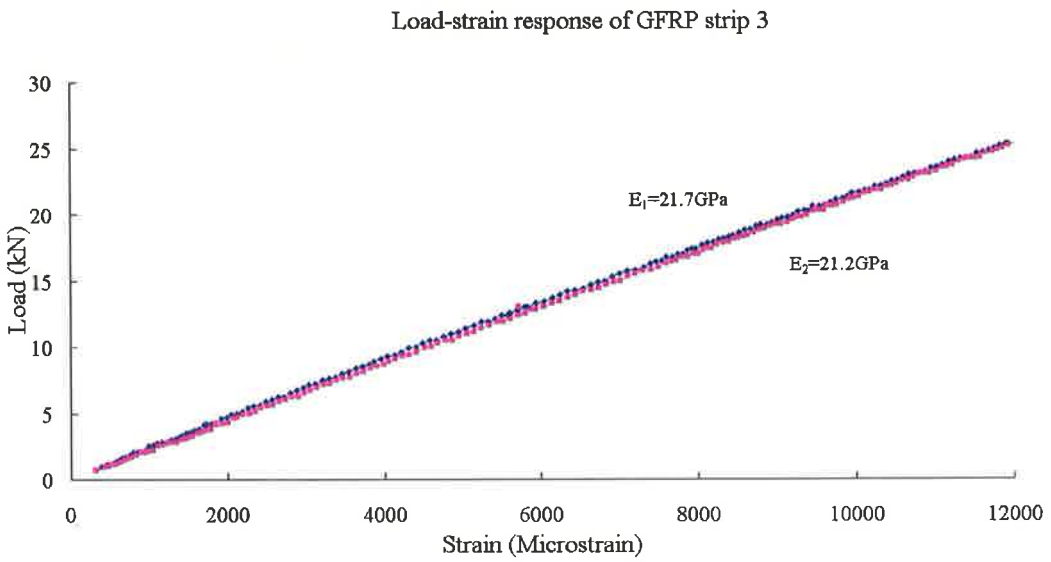


Figure B.2 Load-strain response of GFRP strip 3

APPENDIX C: FRP TO MASONRY BOND TEST RESULTS

C.1. GFRP Externally Bonded Masonry Push-pull Test Results

Specimen: GP-5-Ne-M-1

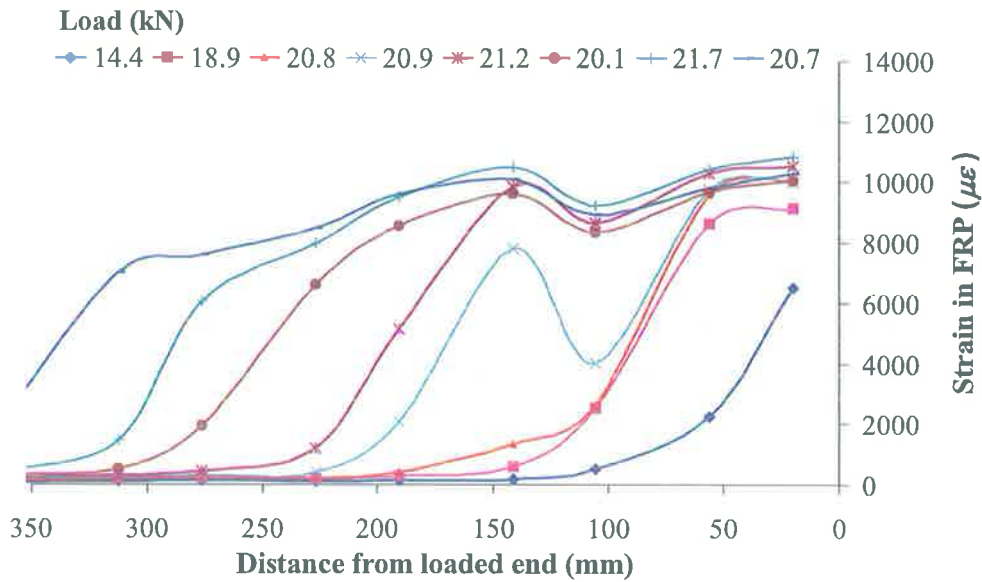


Figure C.1 (a) Strain distribution in FRP plate (GP-5-Ne-M-1)

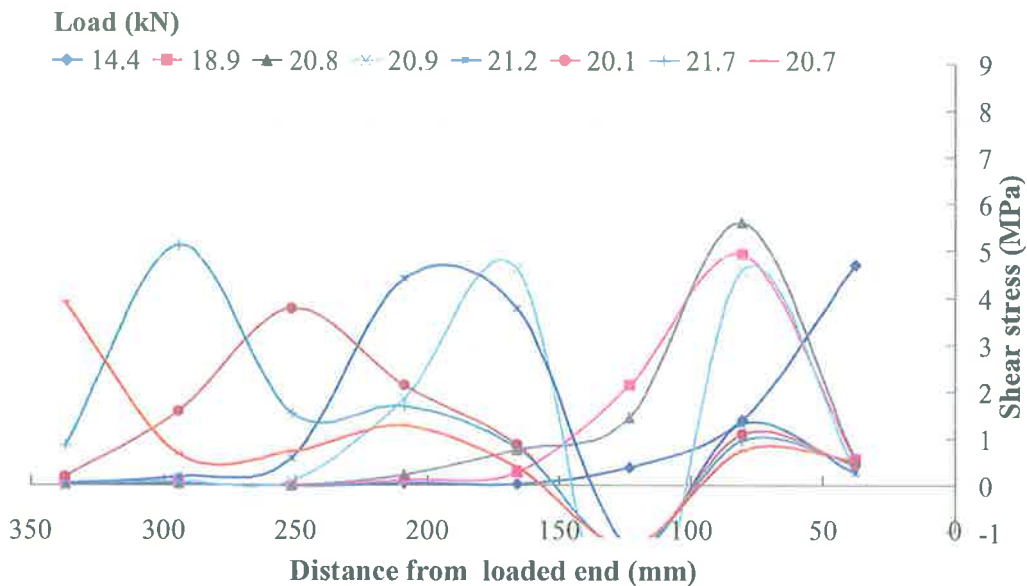


Figure C.1 (b) Shear stress distribution along FRP plate (GP-5-Ne-M-1)

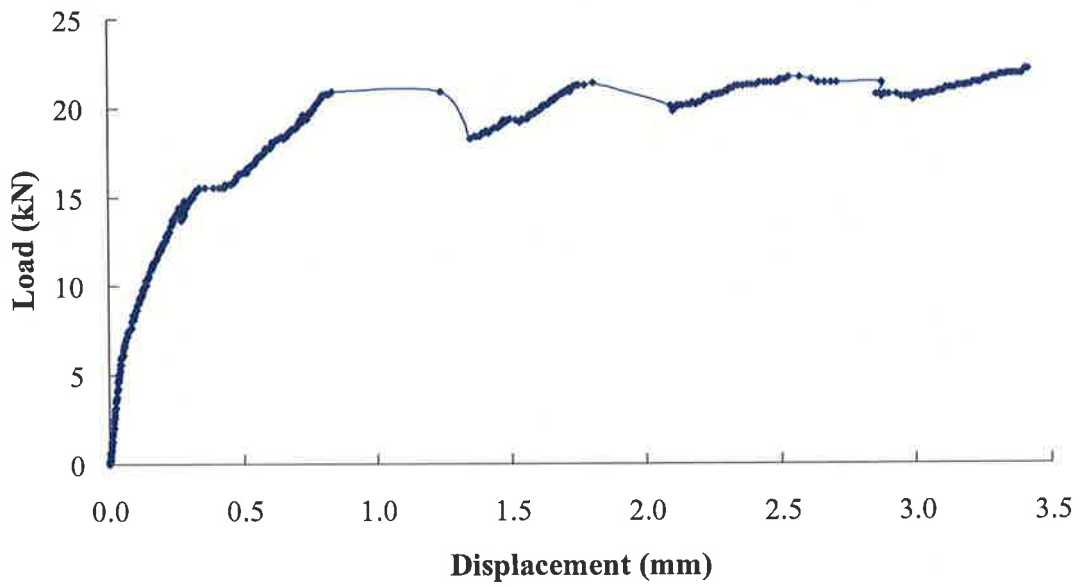


Figure C.1 (c) Load-displacement Response (GP-5-Ne-M-1)

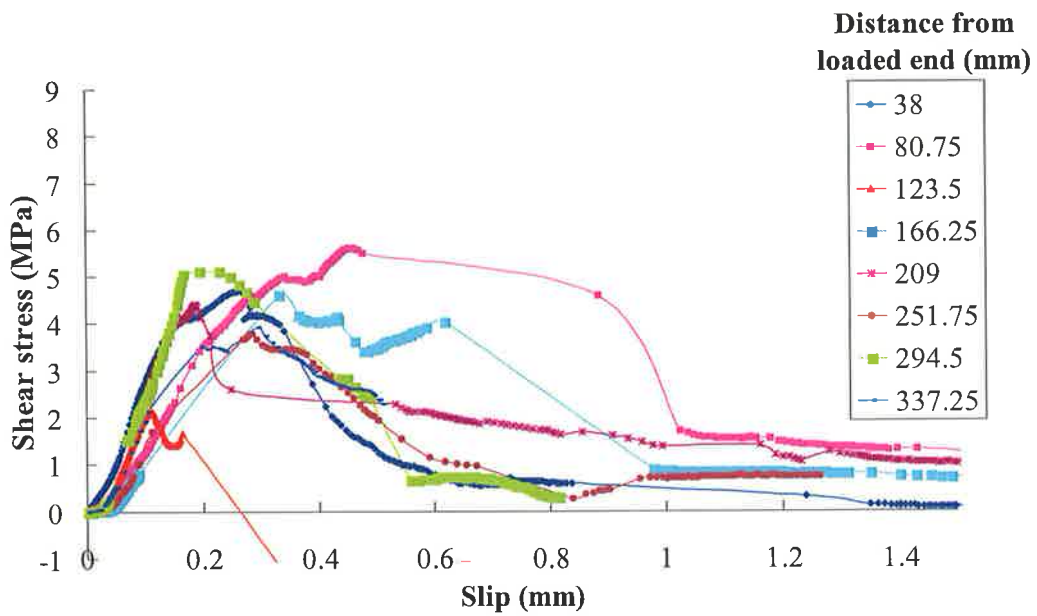


Figure C.1 (d) Local shear-slip response at various positions (GP-5-Ne-M-1)

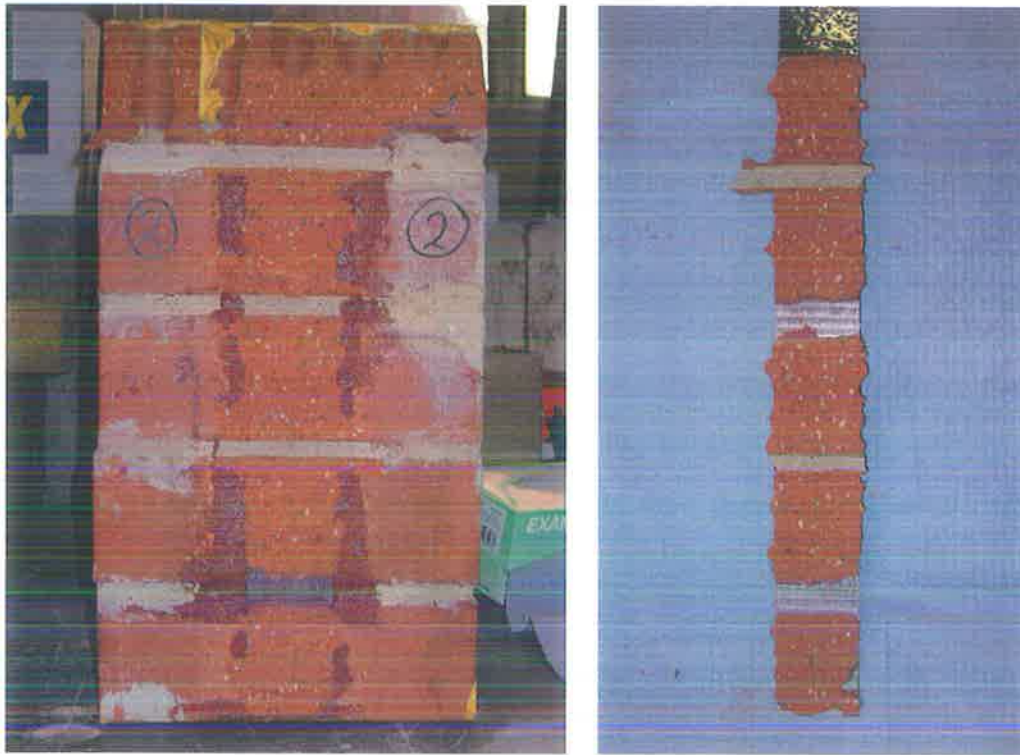


Figure C.1 (e) Failure mode (GP-5-Ne-M-1)

Specimen: GP-5-Ne-Q-1

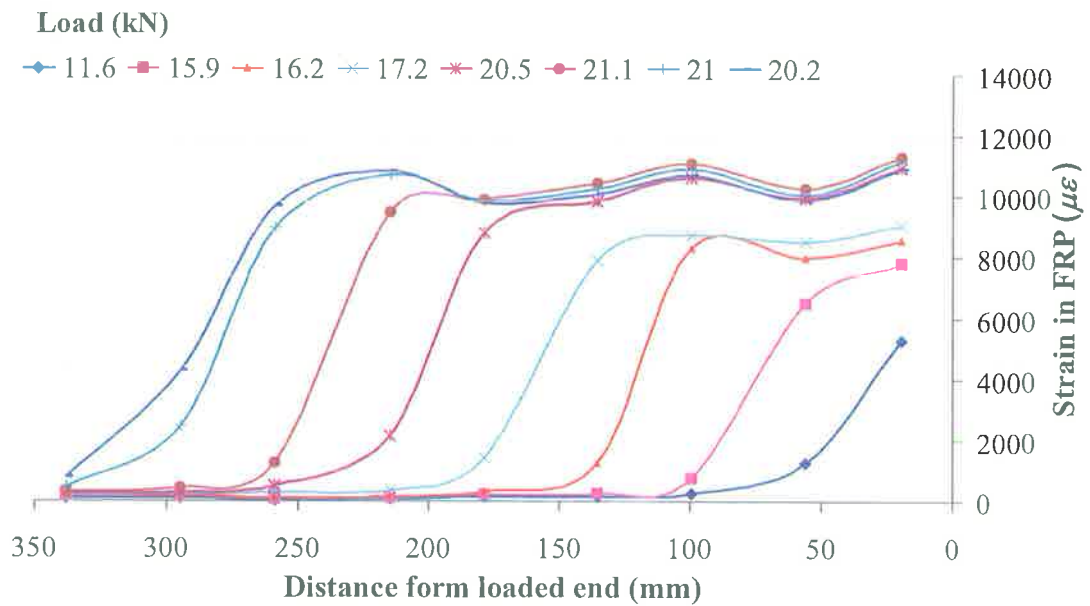


Figure C.2 (a) Strain distribution in FRP plate (GP-5-Ne-Q-1)

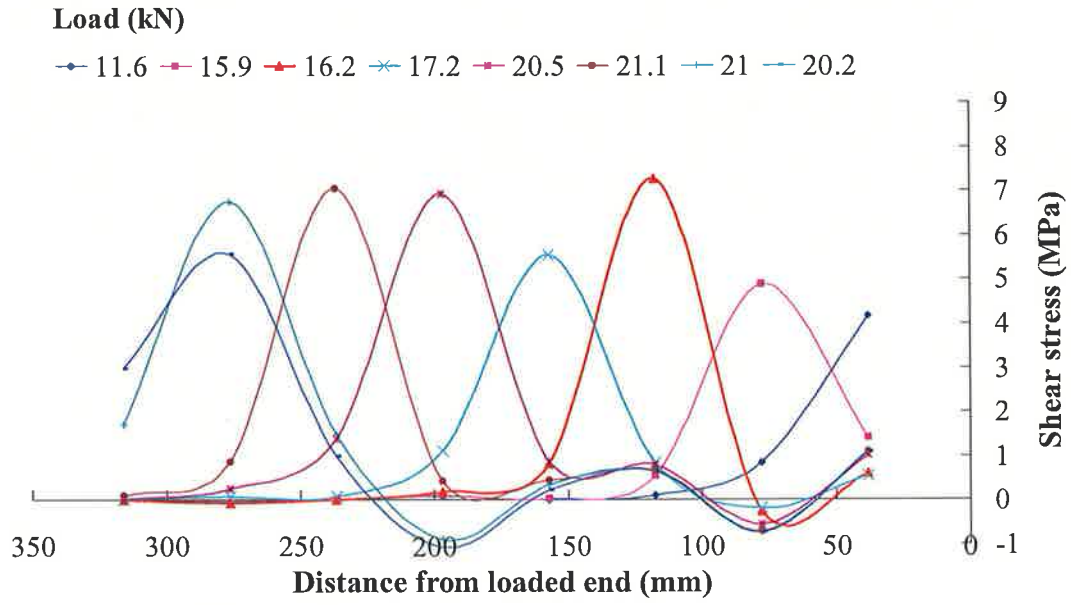


Figure C.2 (b) Shear stress distribution along FRP plate (GP-5-Ne-Q-1)

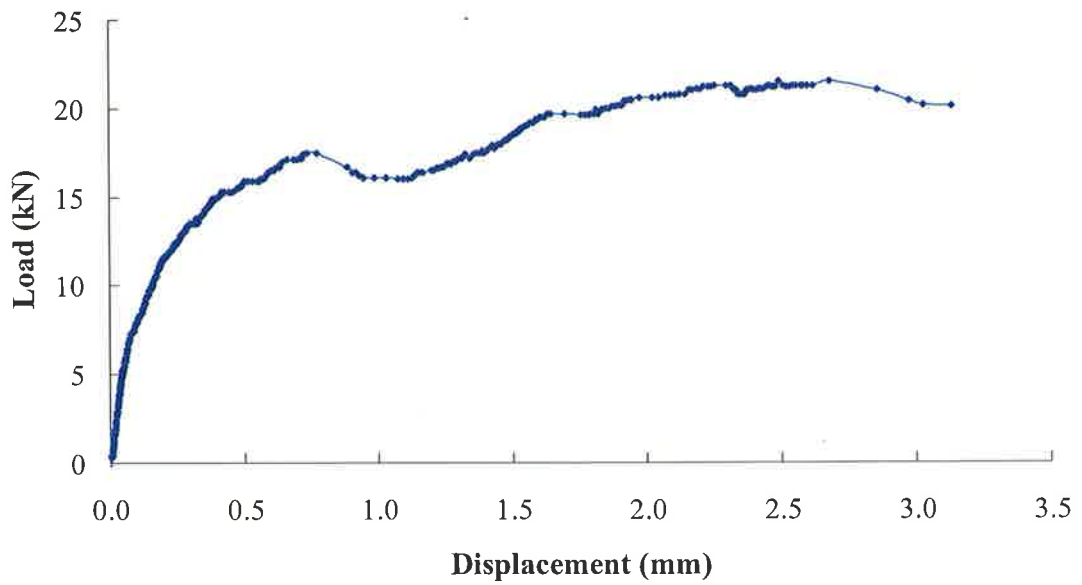


Figure C.2 (c) Load-displacement Response (GP-5-Ne-Q-1)

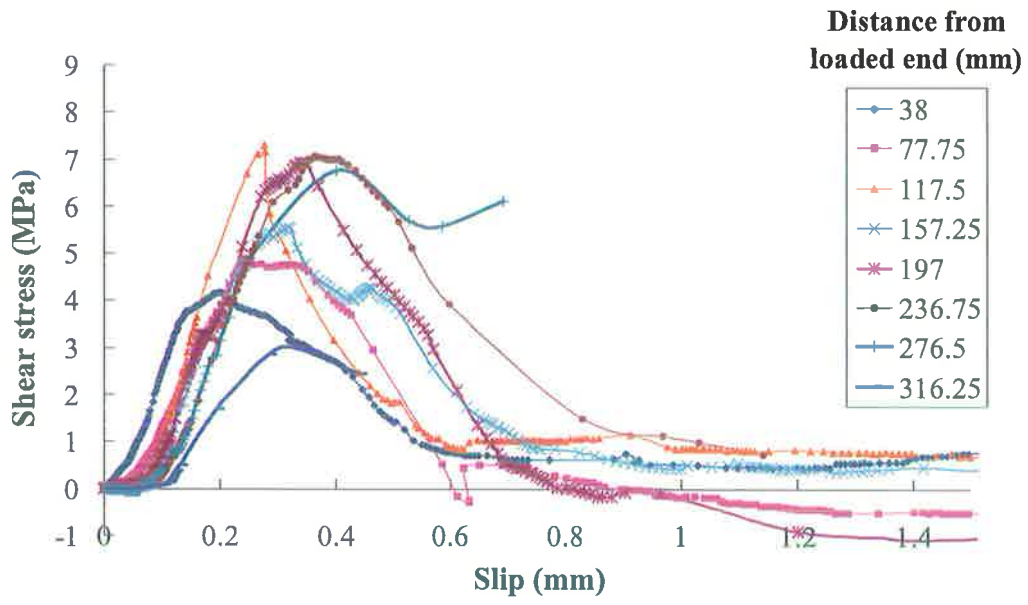


Figure C.2 (d) Local shear-slip response at various positions (GP-5-Ne-Q-1)

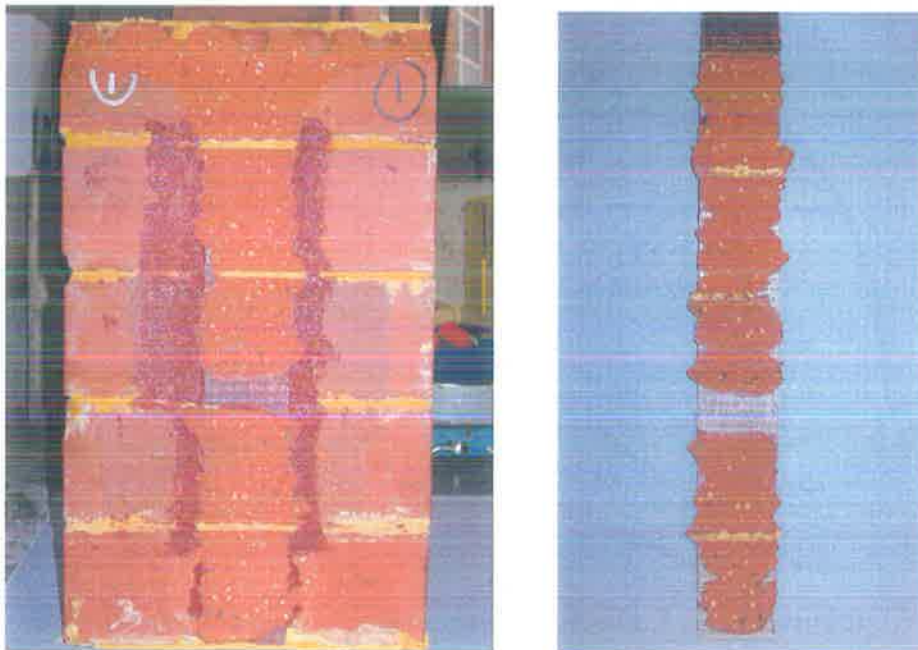


Figure C.2 (e) Failure mode (GP-5-Ne-Q-1)

Specimen: GP-5-Ne-M-2

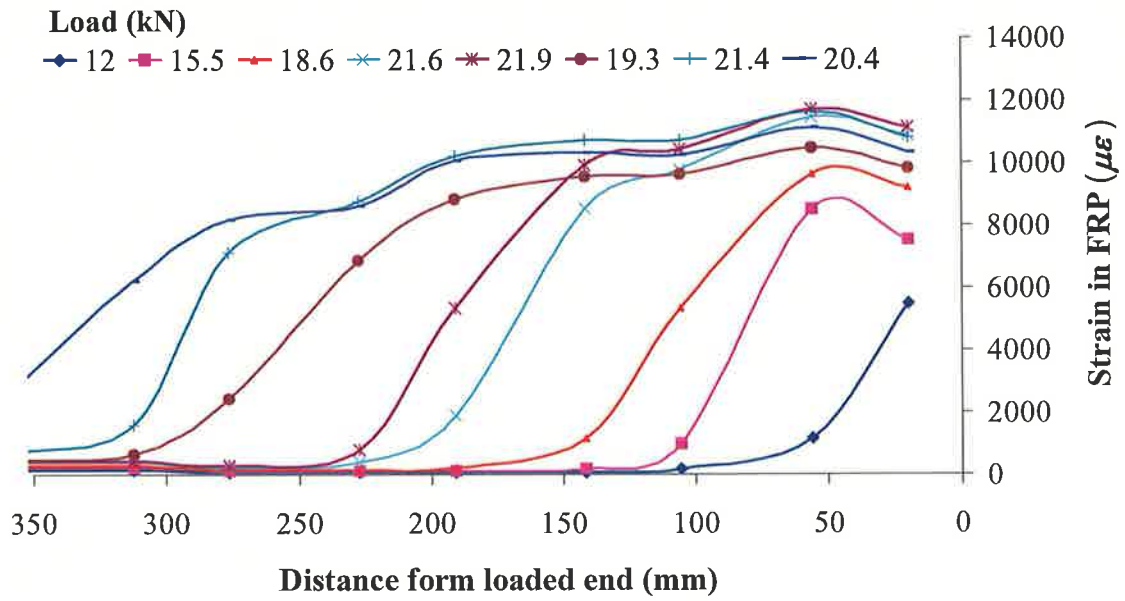


Figure C.3 (a) Strain distribution in FRP plate (GP-5-Ne-M-2)

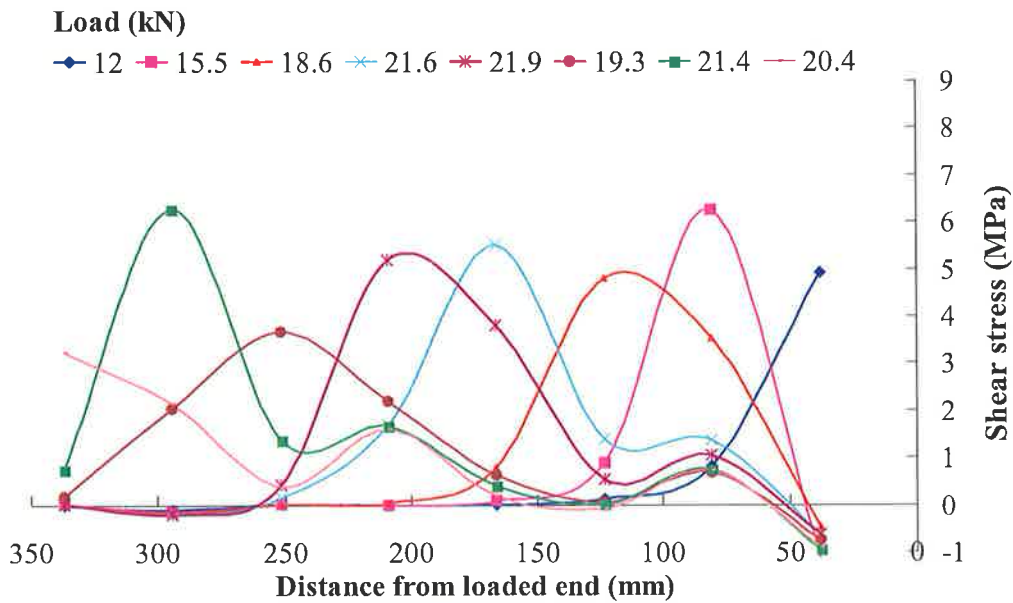


Figure C.3 (b) Shear stress distribution along FRP plate (GP-5-Ne-M-2)

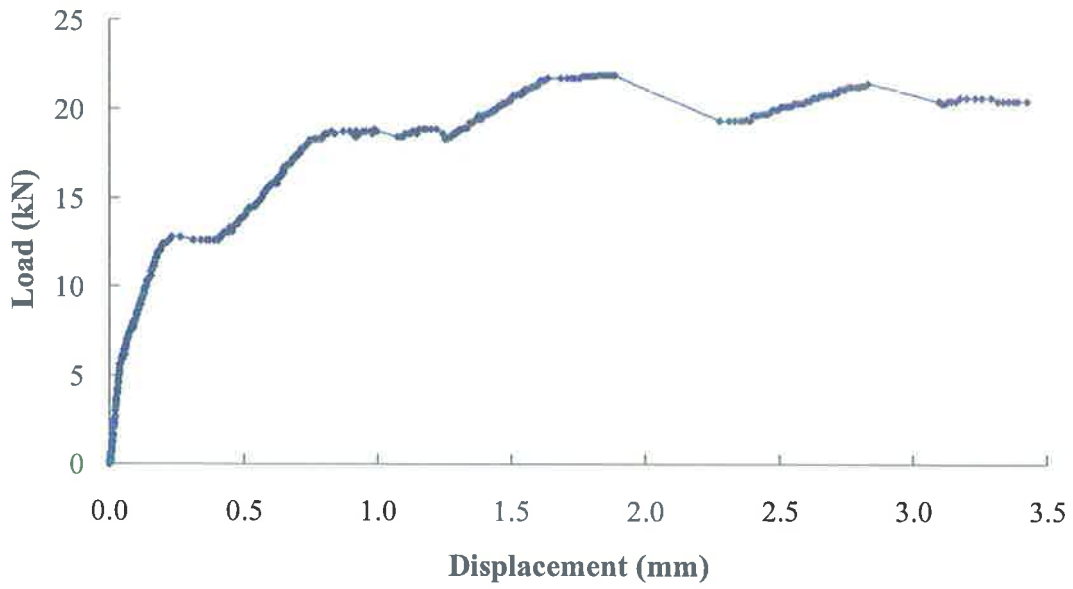


Figure C.3 (c) Load-displacement Response (GP-5-Ne-M-2)

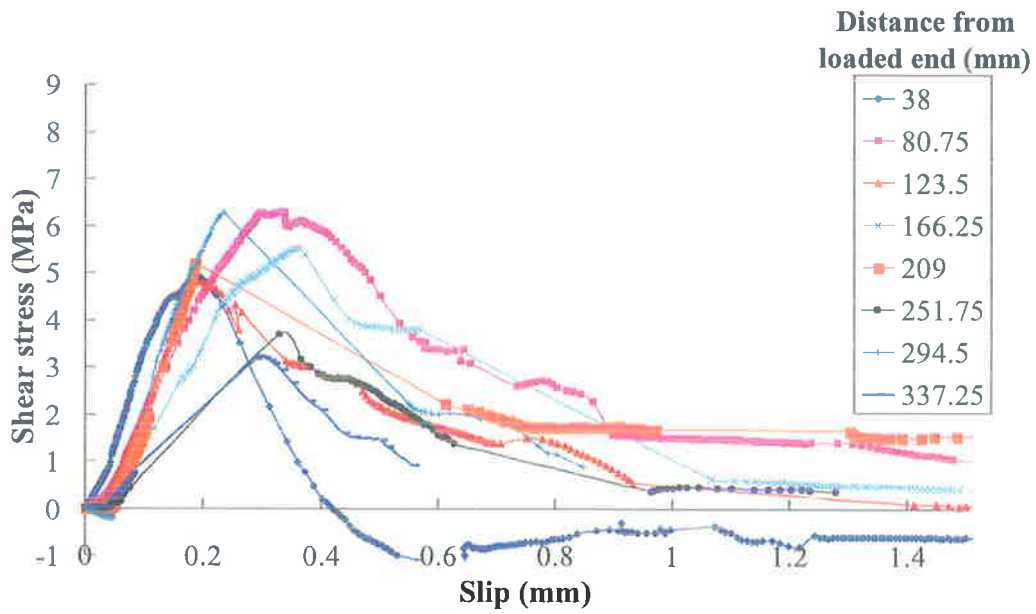


Figure C.3 (d) Local shear-slip response at various positions (GP-5-Ne-M-2)

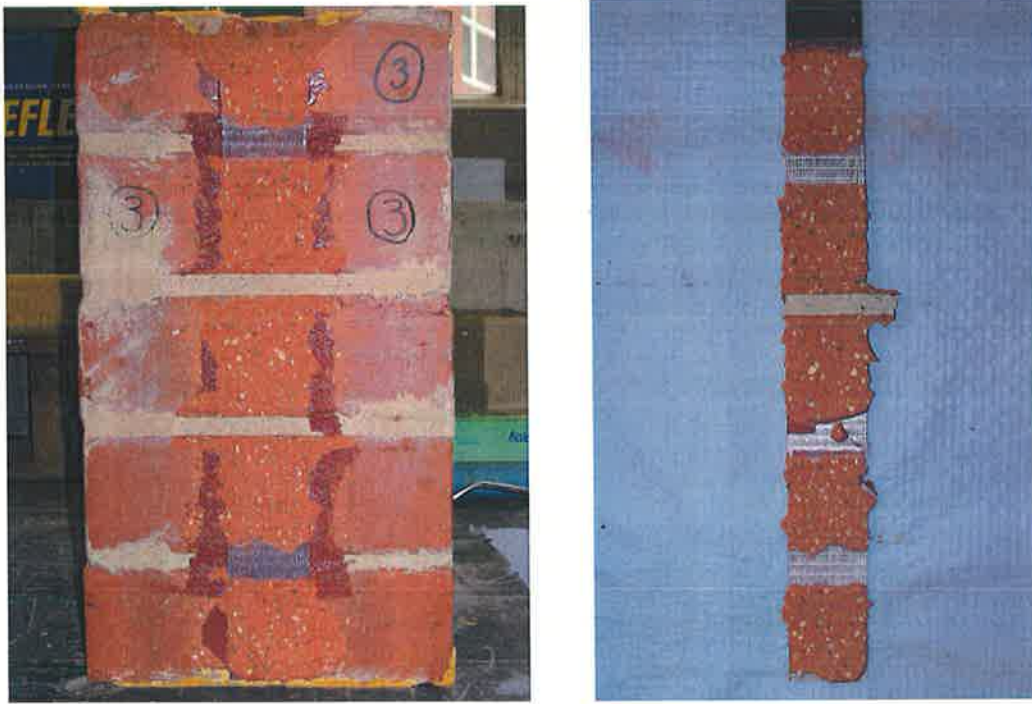


Figure C.3 (e) Failure mode (GP-5-Ne-M-2)

Specimen: GP-5-Ne-Q-2

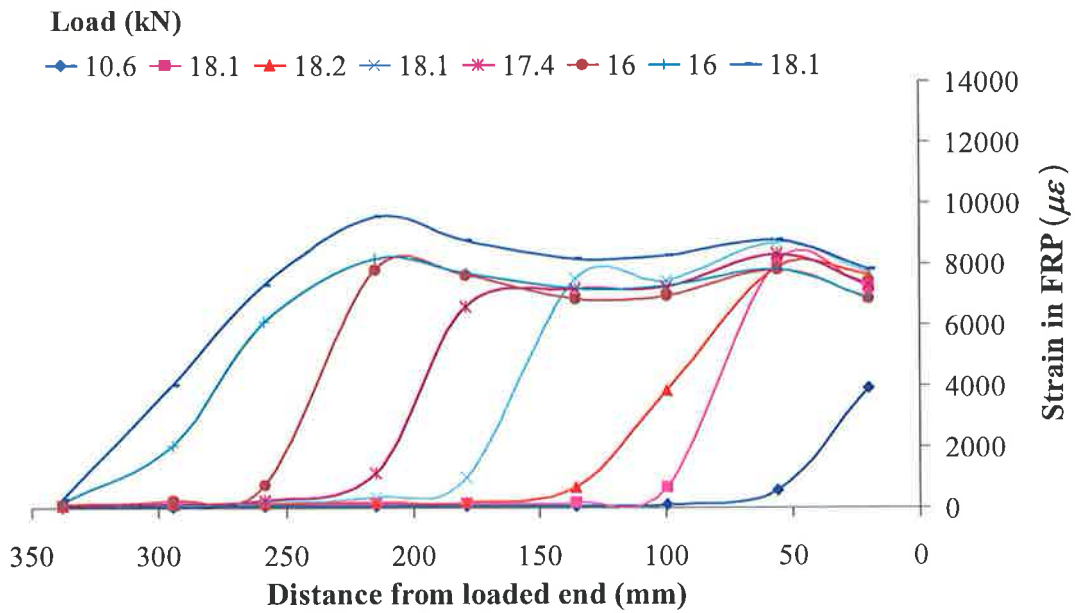


Figure C.4 (a) Strain distribution in FRP plate (GP-5-Ne-Q-2)

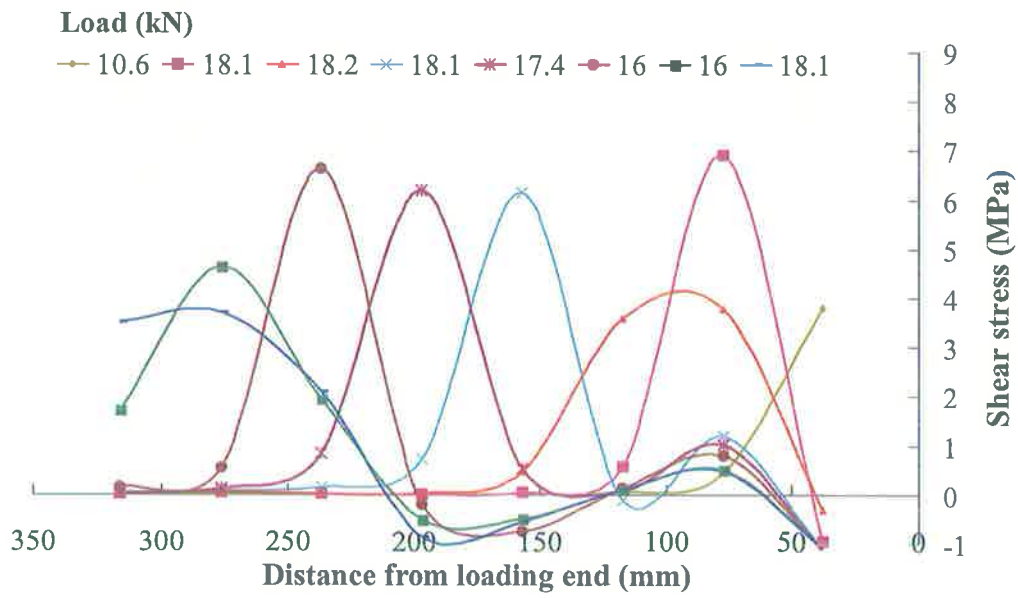


Figure C.4 (b) Shear stress distribution along FRP plate (GP-5-Ne-Q-2)

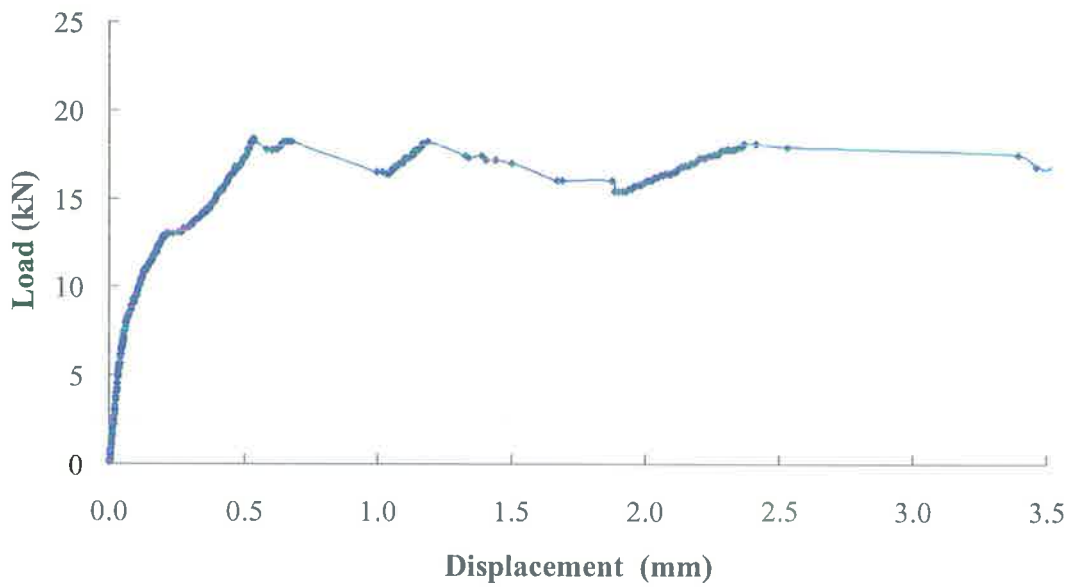


Figure C.4 (c) Load-displacement Response (GP-5-Ne-Q-2)

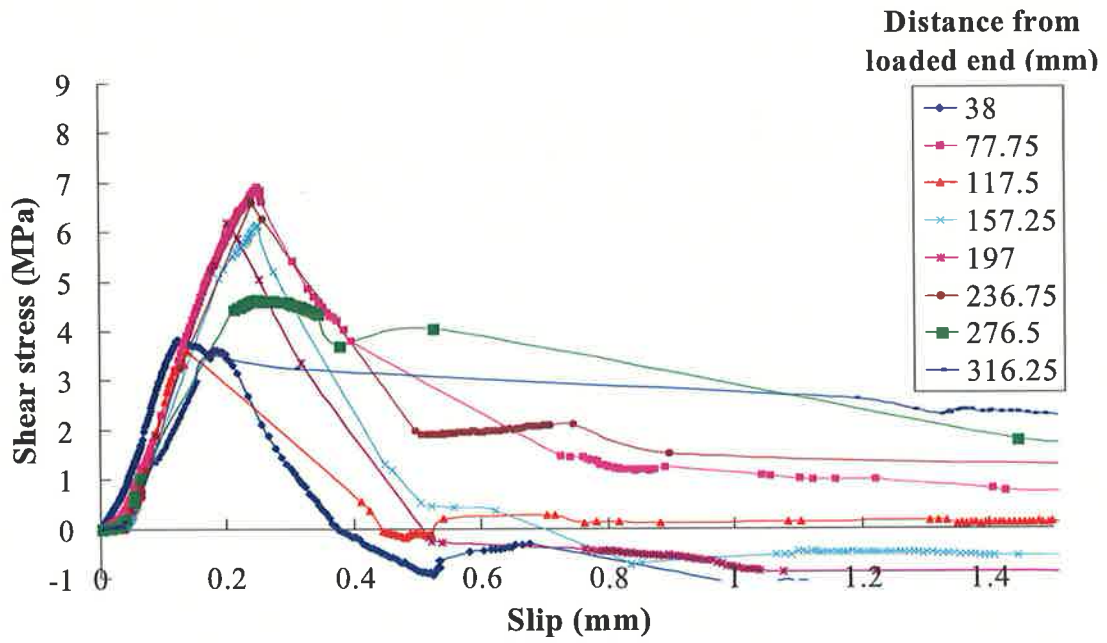


Figure C.4 (d) Local shear-slip response at various positions (GP-5-Ne-Q-2)

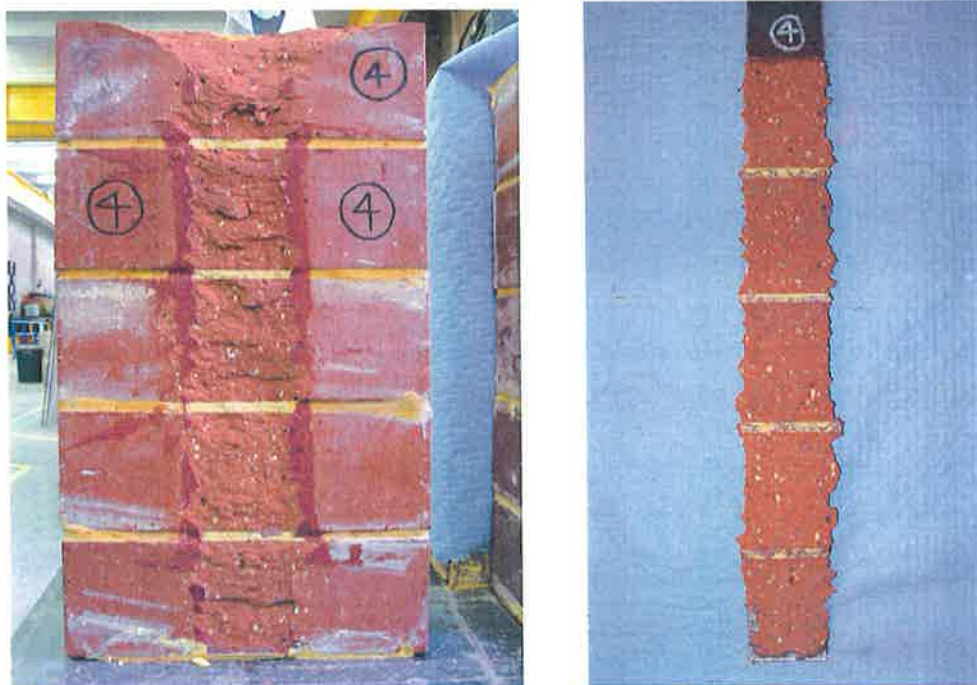


Figure C.4 (e) Failure mode (GP-5-Ne-Q-2)

Specimen: GP-5-Sa-M

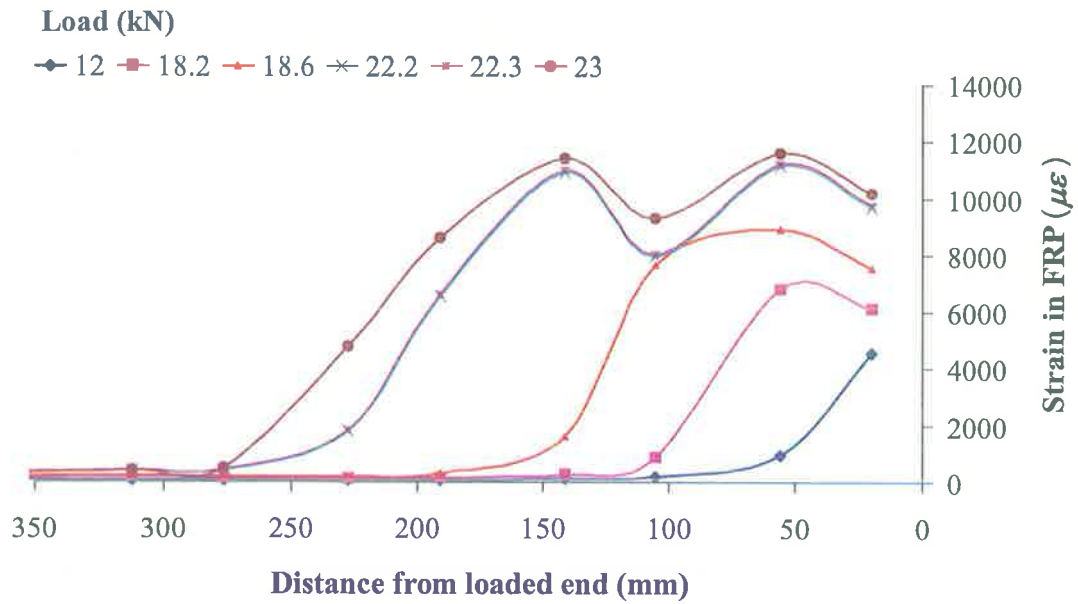


Figure C.5 (a) Strain distribution in FRP plate (GP-5-Sa-M)

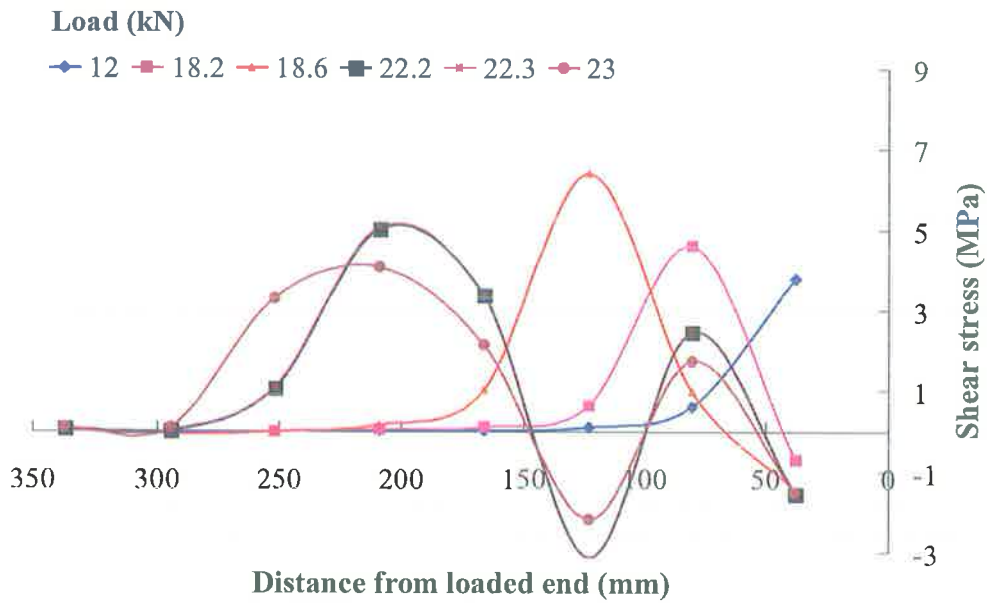


Figure C.5 (b) Shear stress distribution along FRP plate (GP-5-Sa-M)

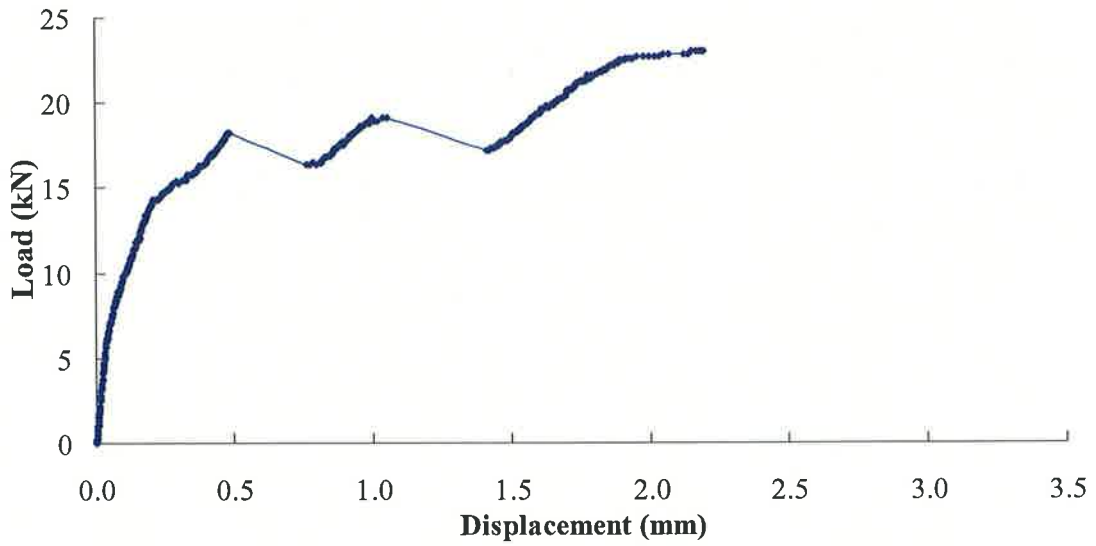


Figure C.5 (c) Load-displacement Response (GP-5-Sa-M)

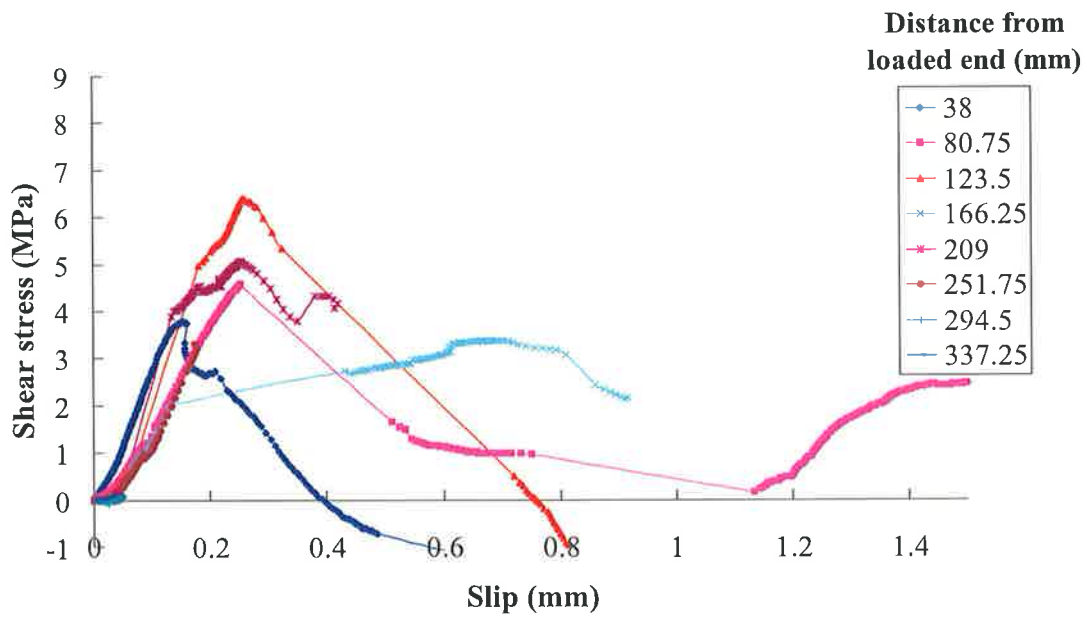


Figure C.5 (d) Local shear-slip response at various positions (GP-5-Sa-M)



Figure C.3 (d) Failure mode (GP-5-Sa-M)

Specimen: GP-5-Sa-Q

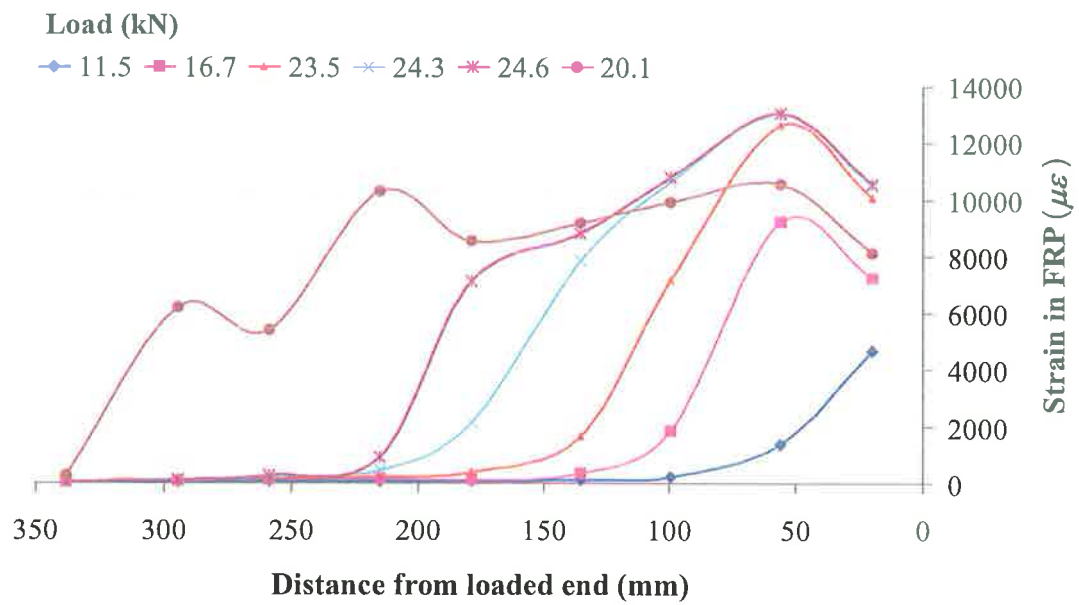


Figure C.6 (a) Strain distribution in FRP plate (GP-5-Sa-Q)

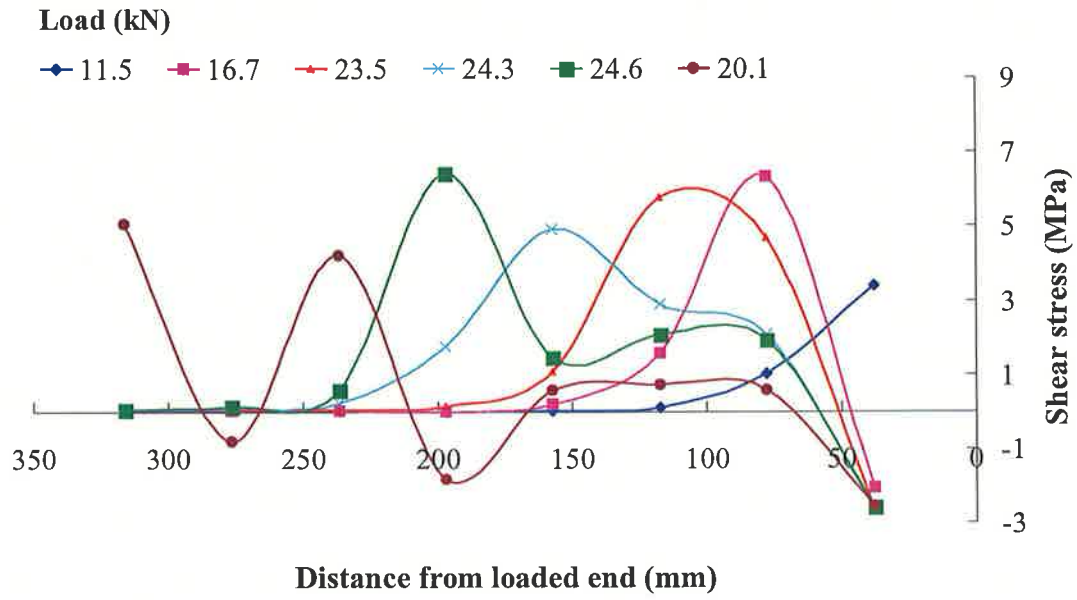


Figure C.6 (b) Shear stress distribution along FRP plate (GP-5-Sa-Q)

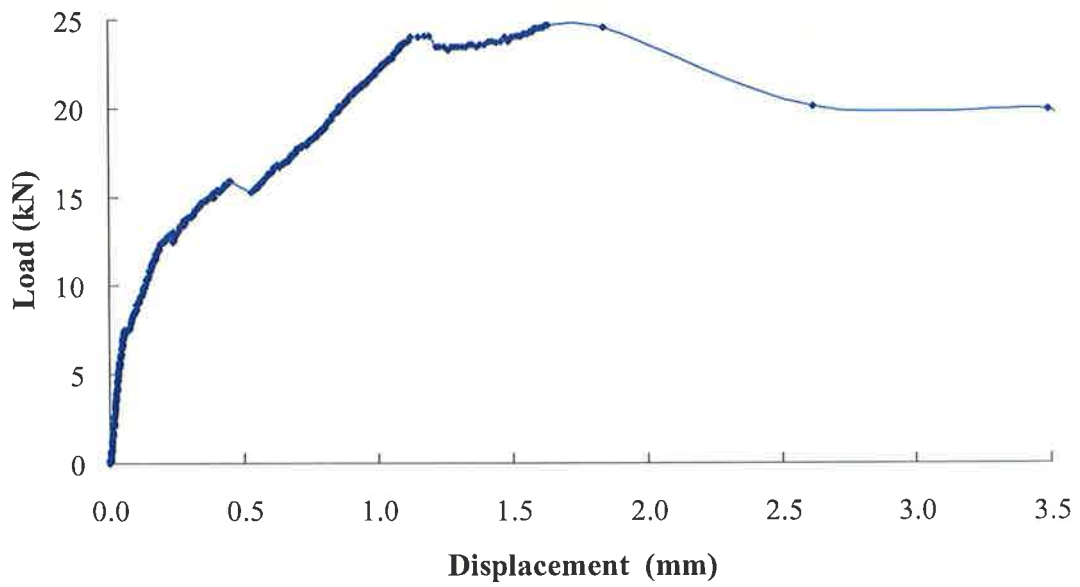


Figure C.6 (c) Load-displacement Response (GP-5-Sa-Q)

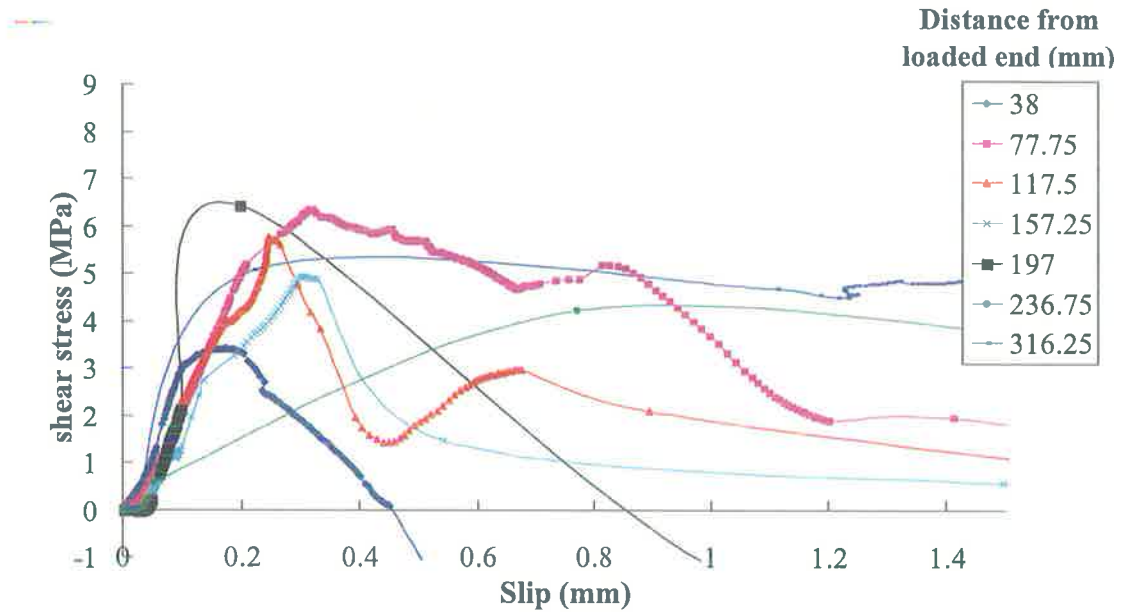


Figure C.6 (d) Local shear-slip response at various positions (GP-5-Sa-Q)

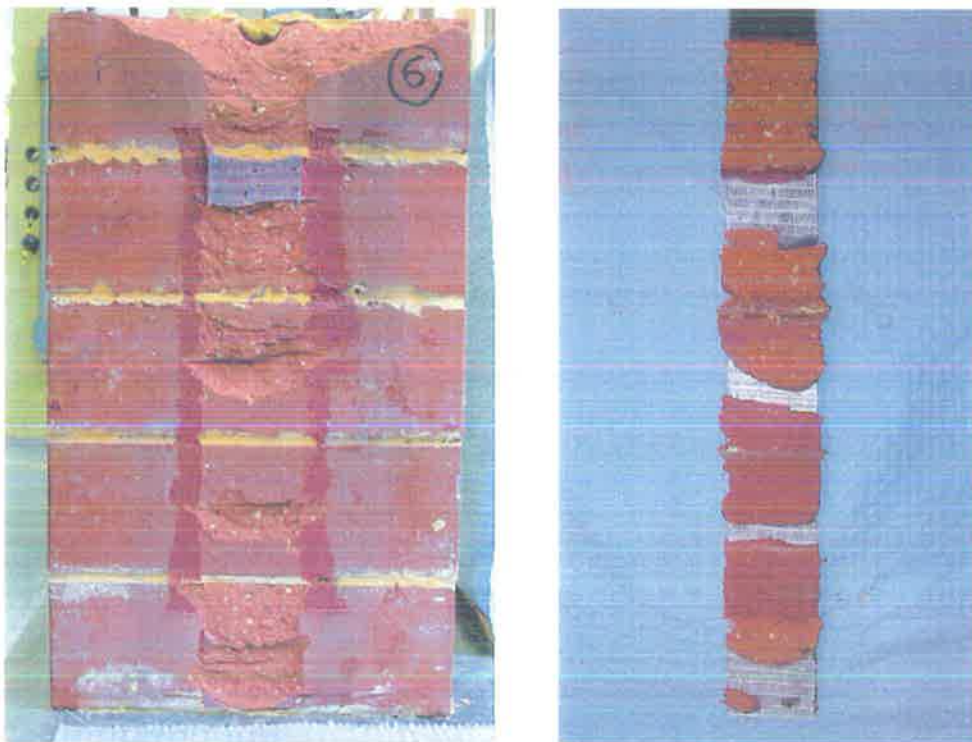


Figure C.6 (e) Failure mode (GP-5-Sa-Q)

Specimen: GP-5-Gr-M

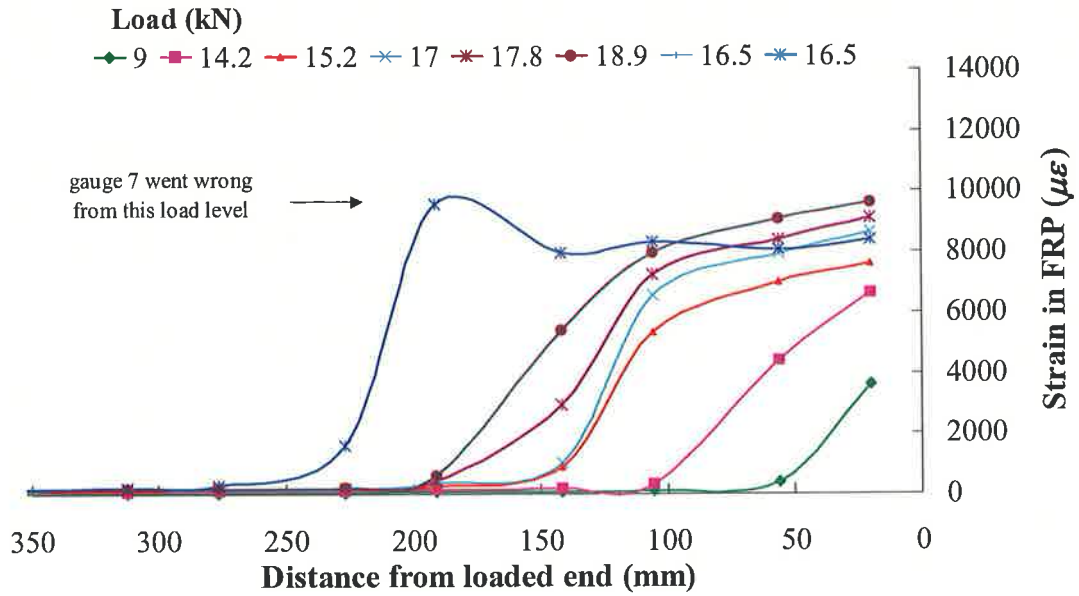


Figure C.7 (a) Strain distribution in FRP plate (GP-5-Gr-M)

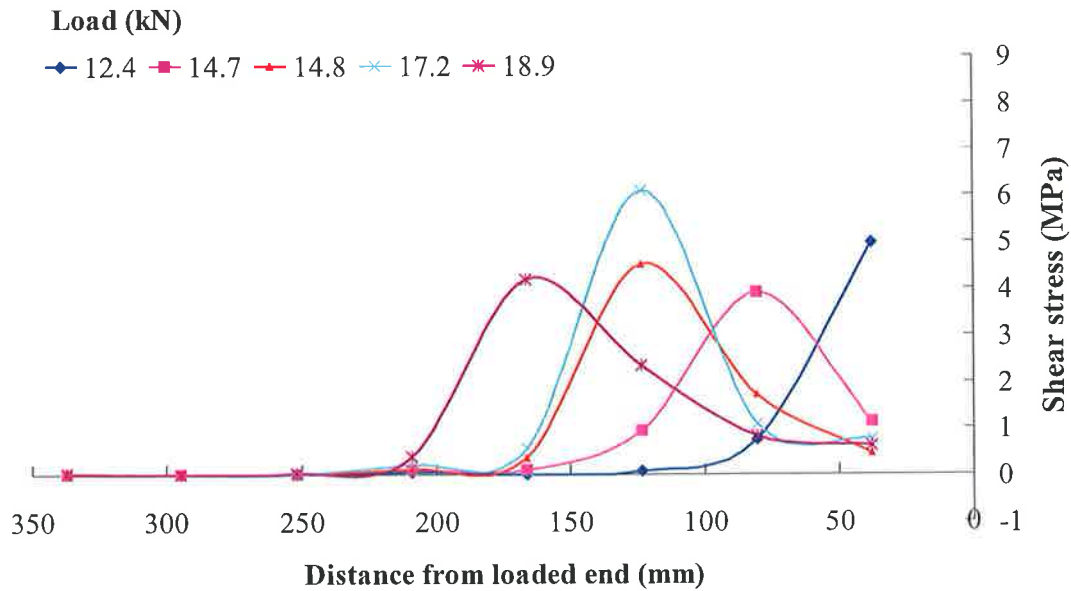


Figure C.7 (b) Shear stress distribution along FRP plate (GP-5-Gr-M)

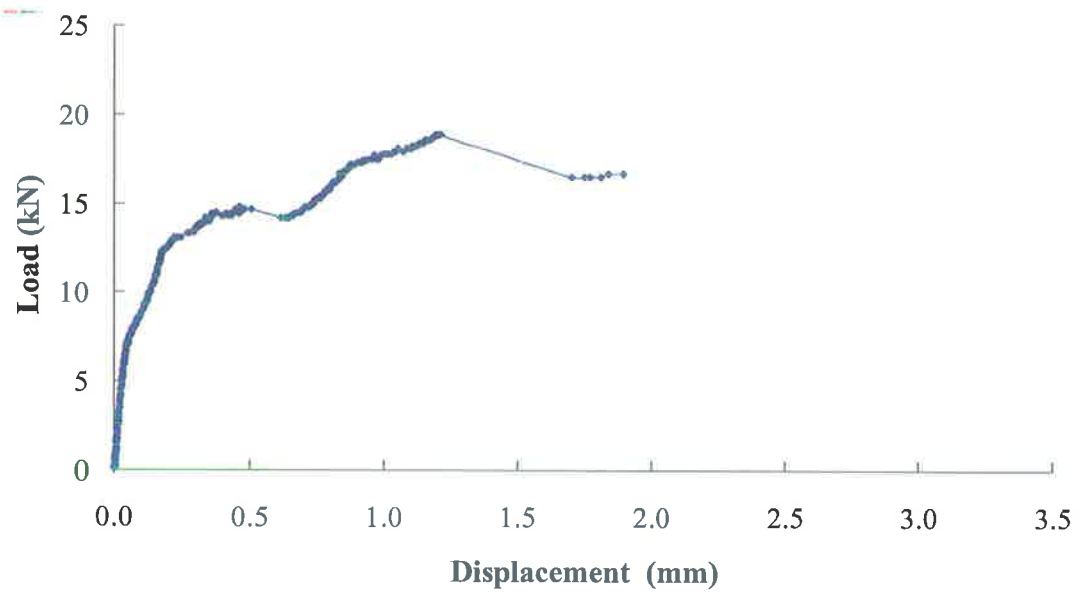


Figure C.7 (c) Load-displacement Response (GP-5-Gr-M)

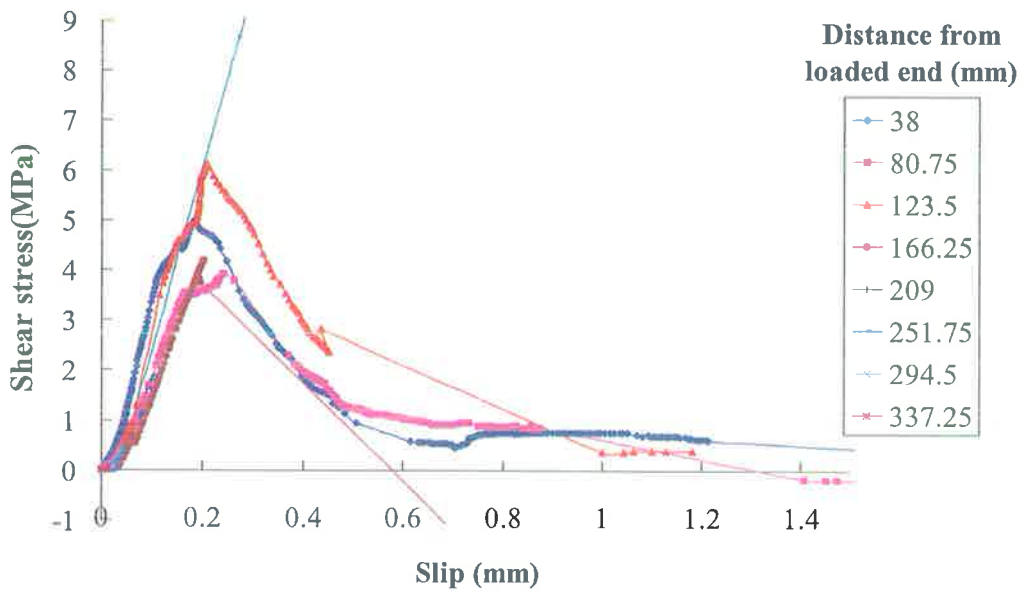


Figure C.7 (d) Local shear-slip response at various positions (GP-5-Gr-M)



Figure C.7 (e) Failure mode (GP-5-Gr-M)

Specimen: GP-5-Gr-Q

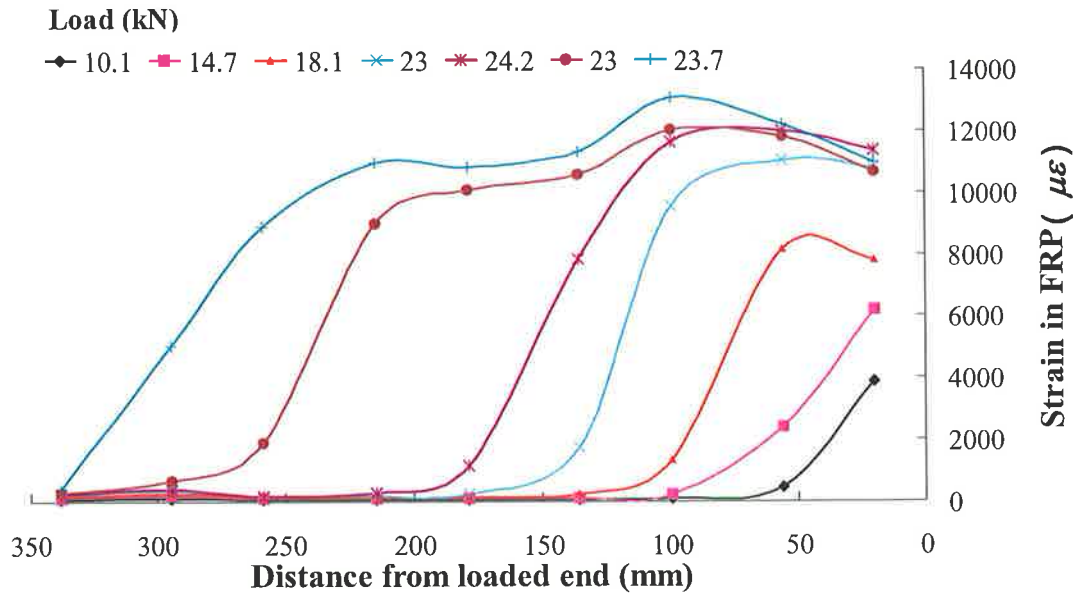


Figure C.8 (a) Strain distribution in FRP plate (GP-5-Gr-Q)

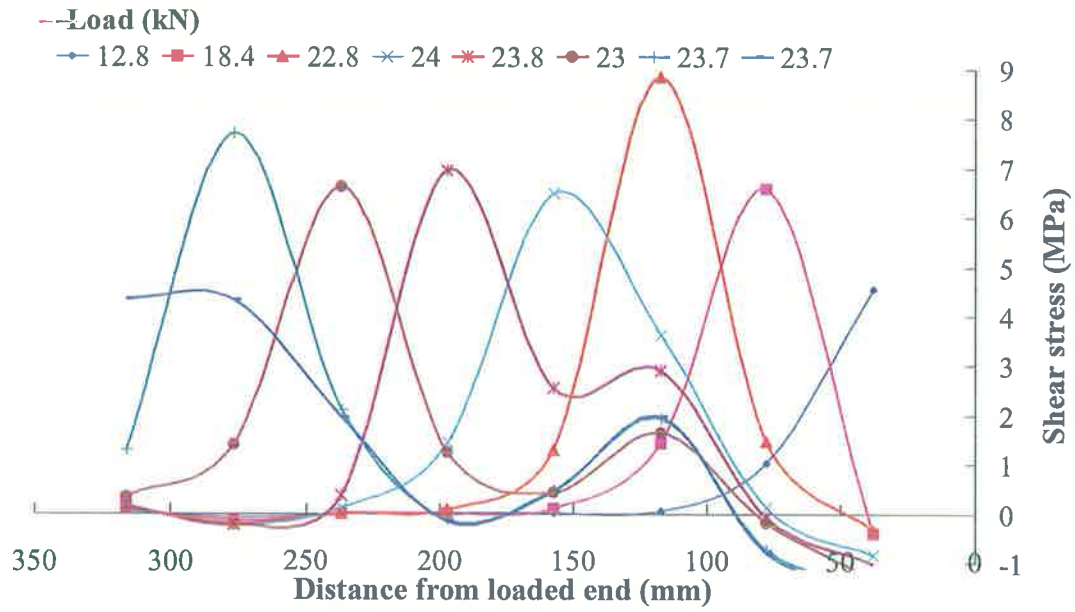


Figure C.8 (b) Shear stress distribution along FRP plate (GP-5-Gr-Q)

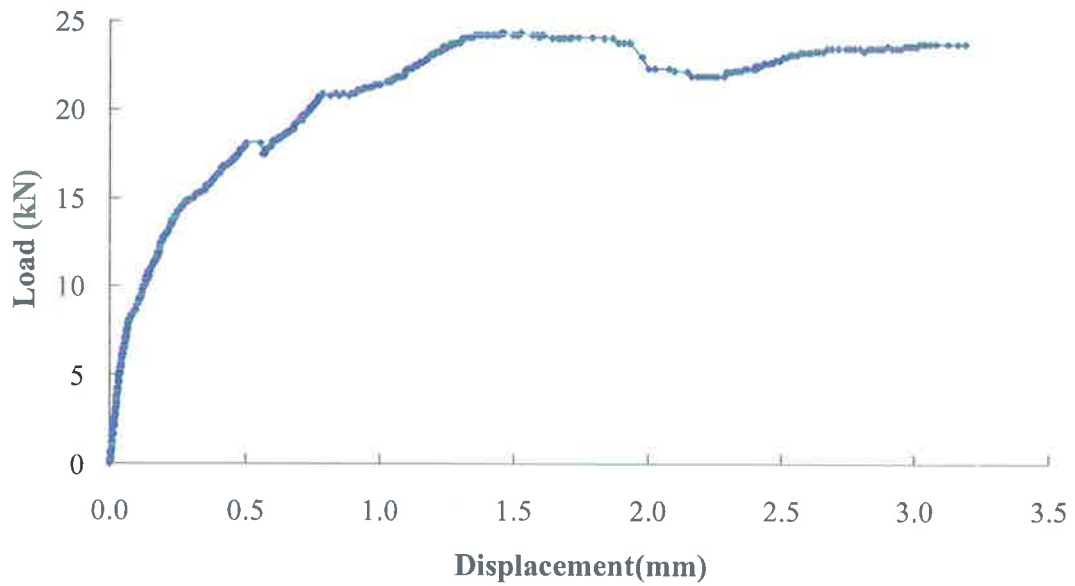


Figure C.8 (c) Load-displacement Response (GP-5-Gr-Q)

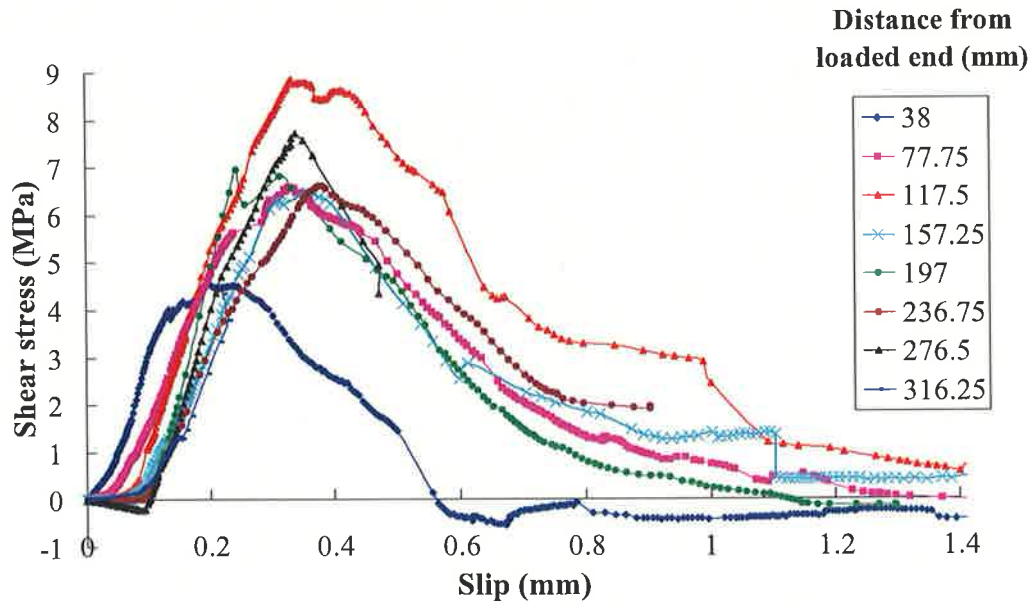


Figure C.8 (d) Local shear-slip response at various positions (GP-5-Gr-Q)

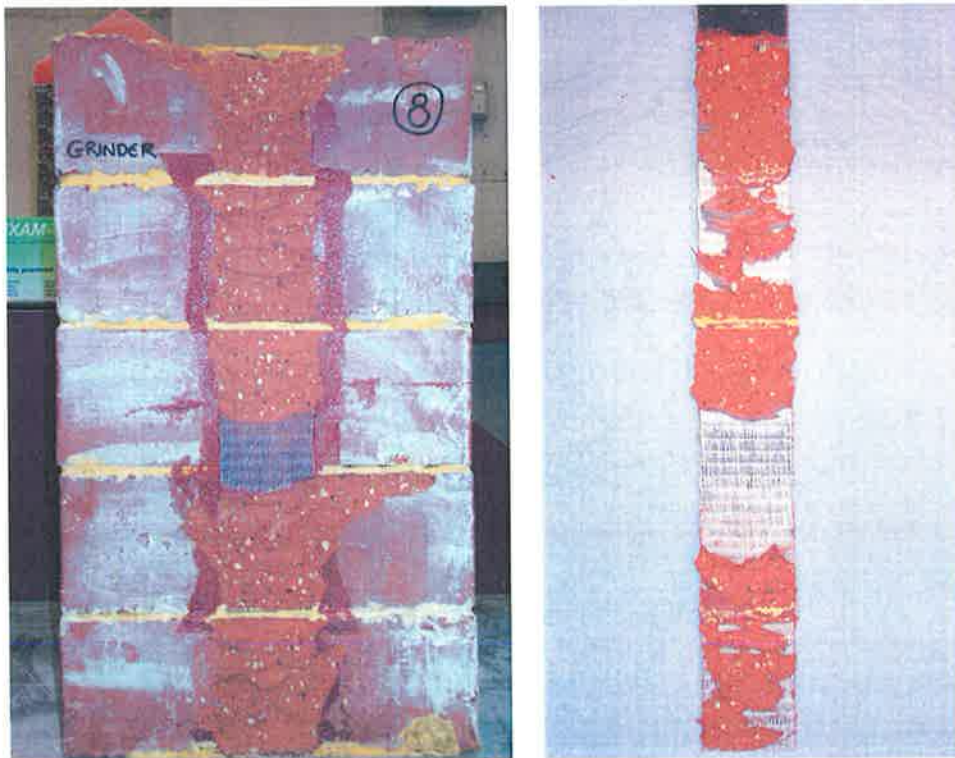


Figure C.8 (c) Failure mode (GP-5-Gr-Q)

Specimen: GP-5-Re-M

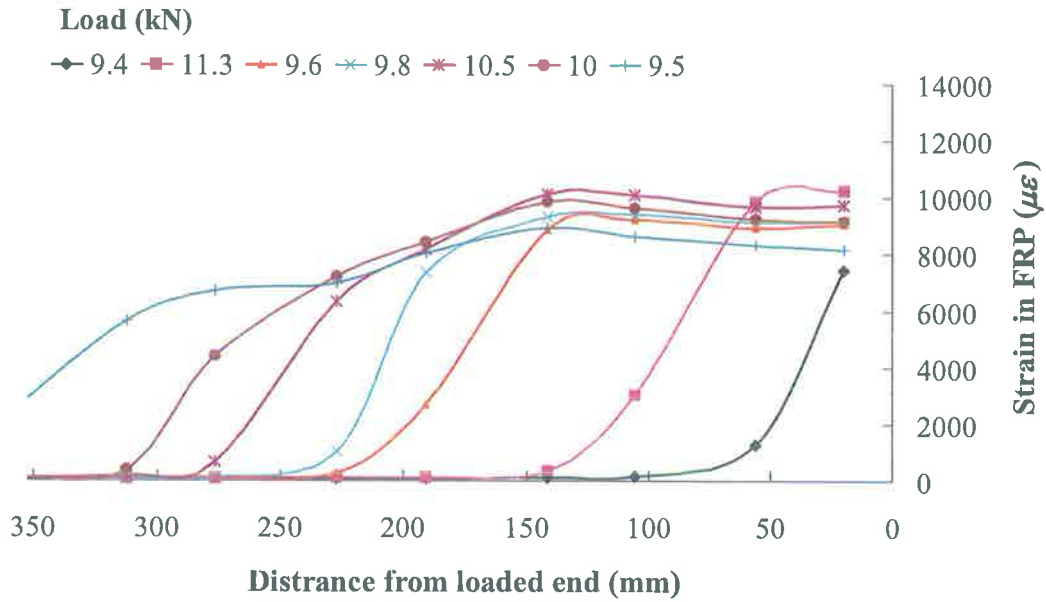


Figure C.9 (a) Strain distribution in FRP plate (GP-5-Re-M)

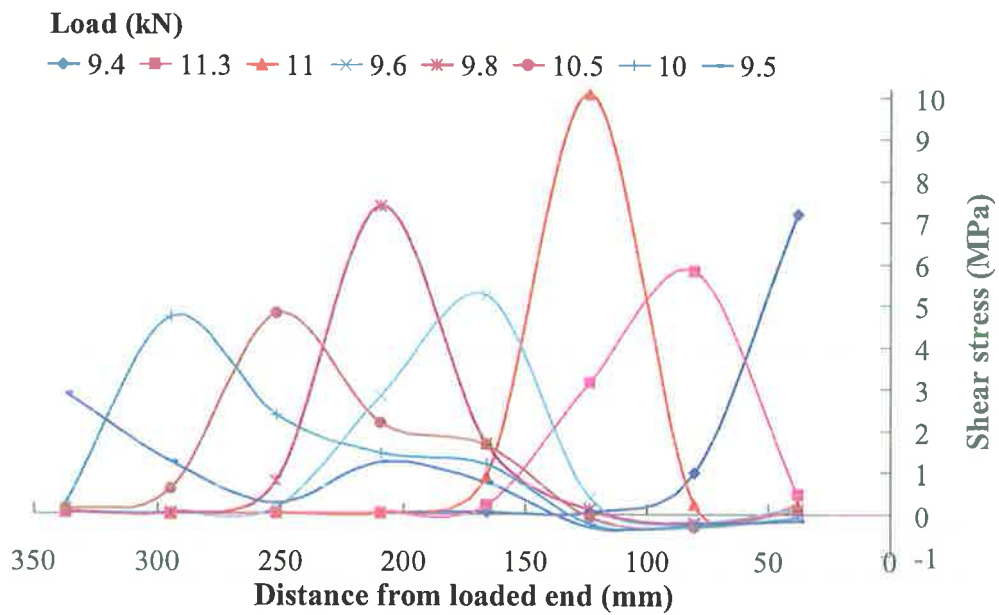


Figure C.9 (b) Shear stress distribution along FRP plate (GP-5-Re-M)

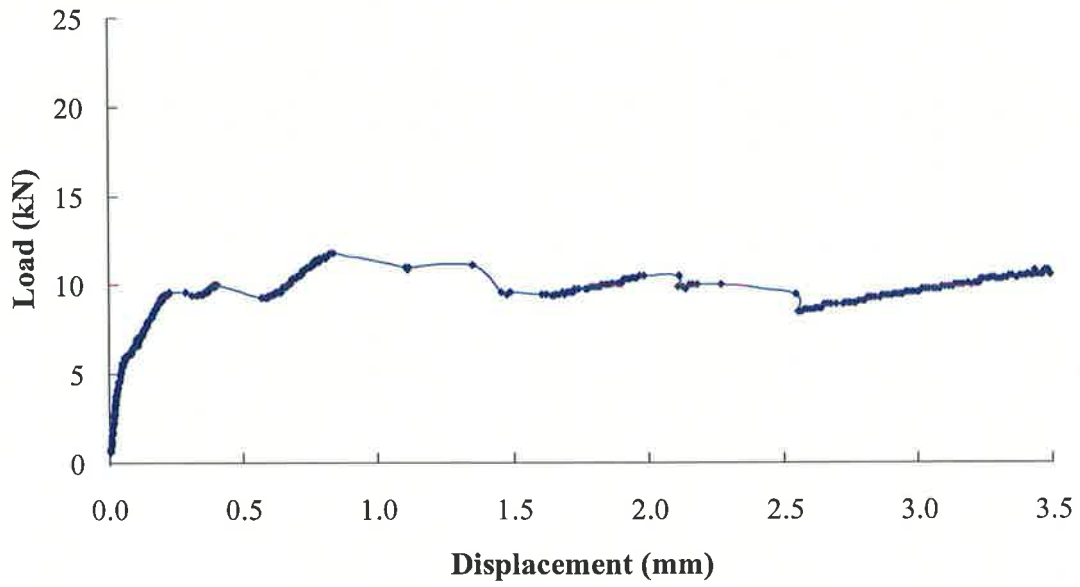


Figure C.9 (c) Load-displacement Response (GP-5-Re-M)

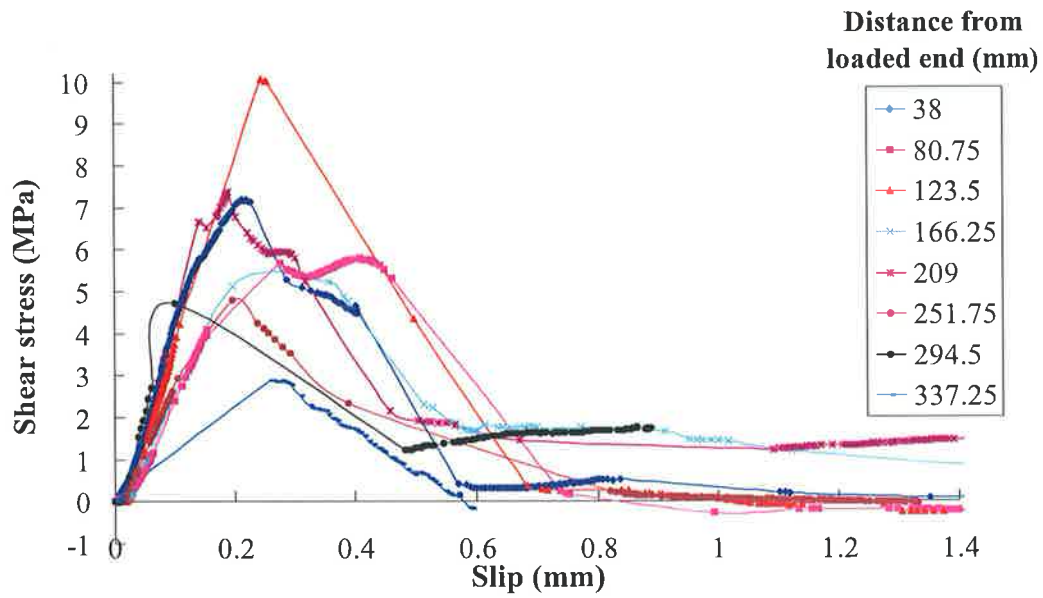


Figure C.9 (d) Local shear-slip response at various positions (GP-5-Re-M)

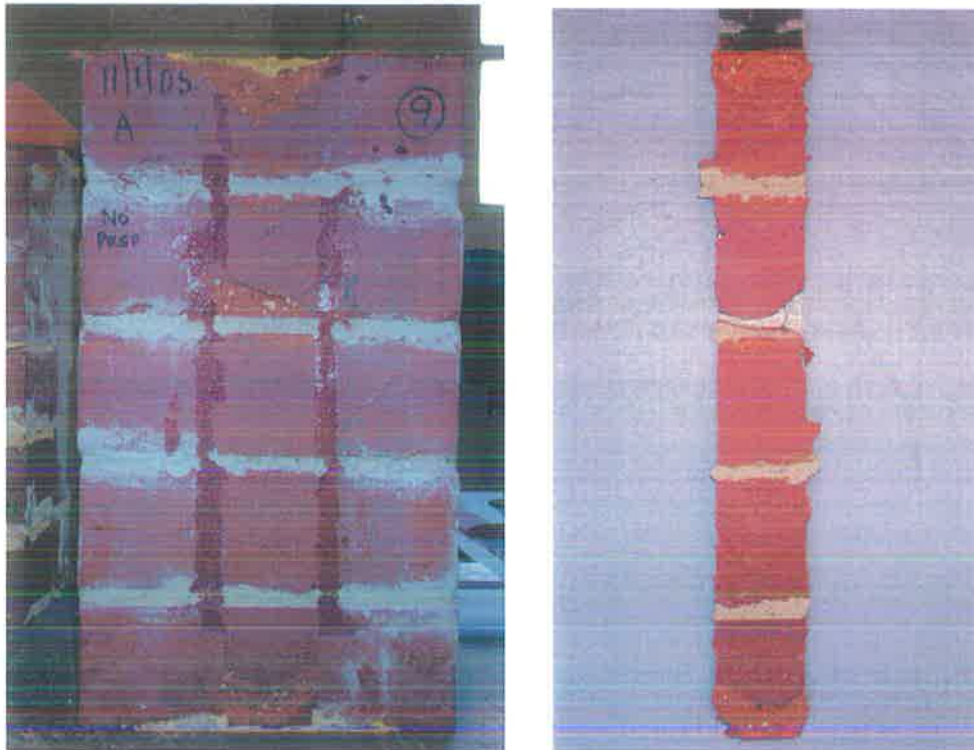


Figure C.9 (e) Failure mode (GP-5-Re-M)

Specimen: GP-5-Re-Q

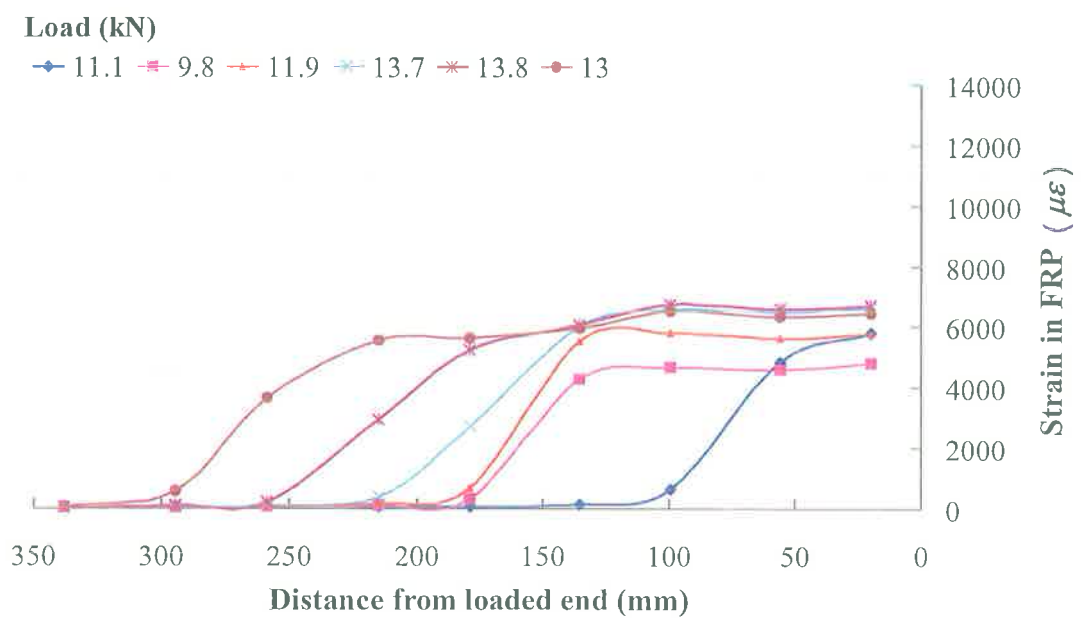


Figure C.10 a) Strain distribution in FRP plate (GP-5-Re-Q)

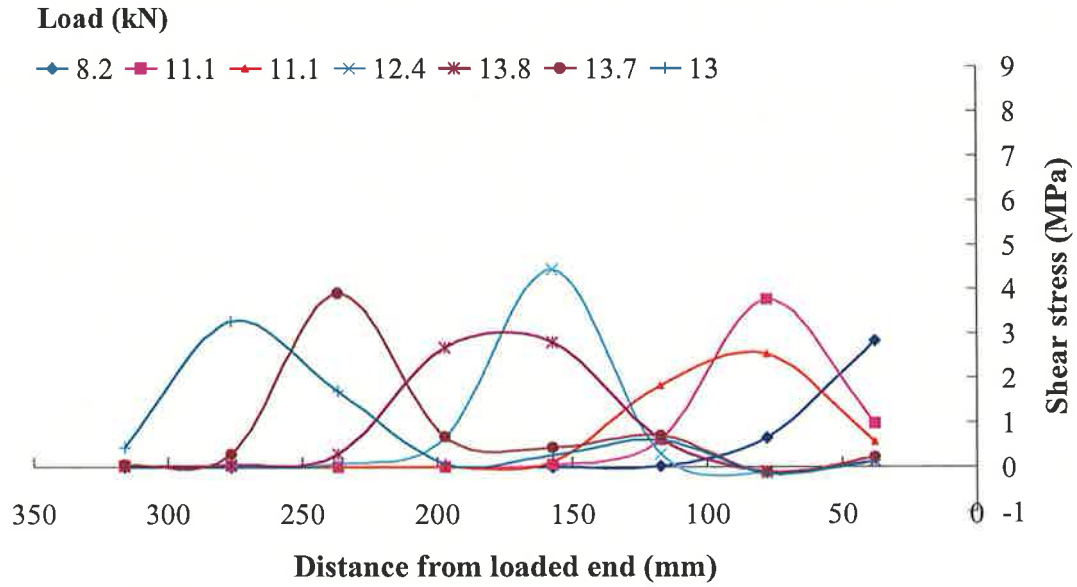


Figure C.10 (b) Shear stress distribution along FRP plate (GP-5-Re-Q)

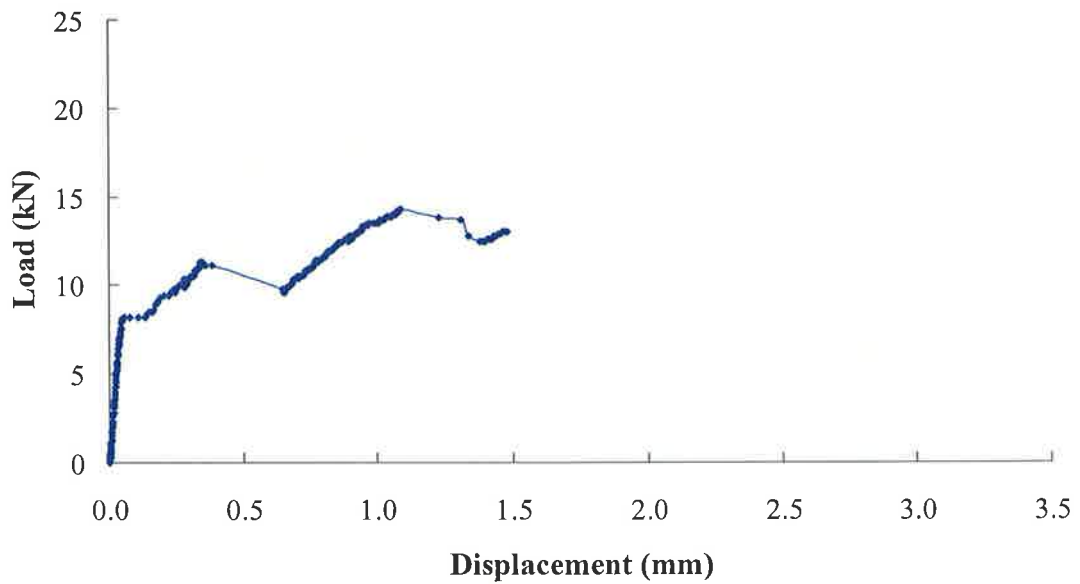


Figure C.10 (c) Load-displacement Response (GP-5-Re-Q)

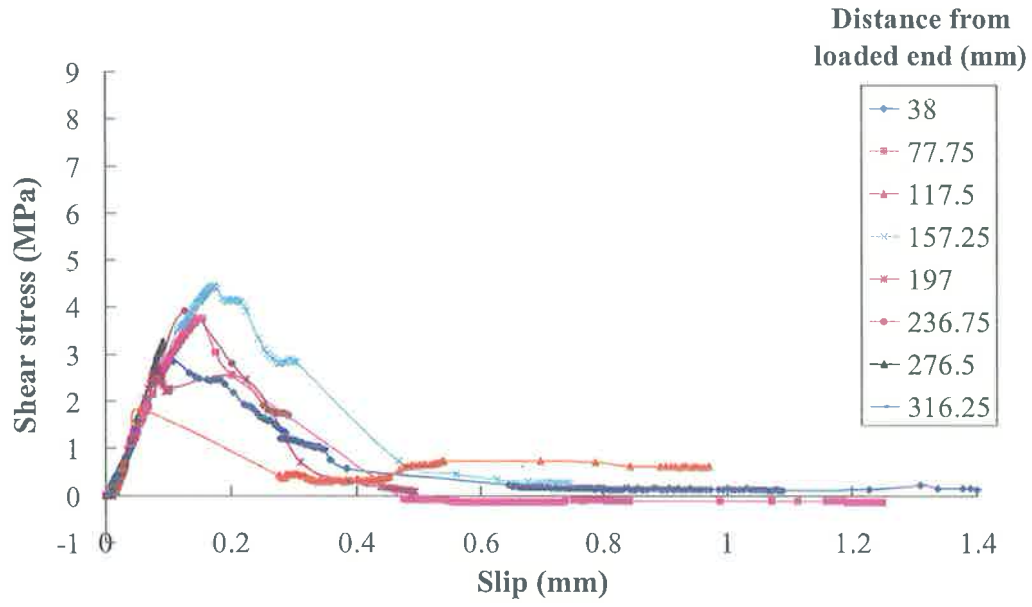


Figure C.10 (d) Local shear-slip response at various positions (GP-5-Re-Q)

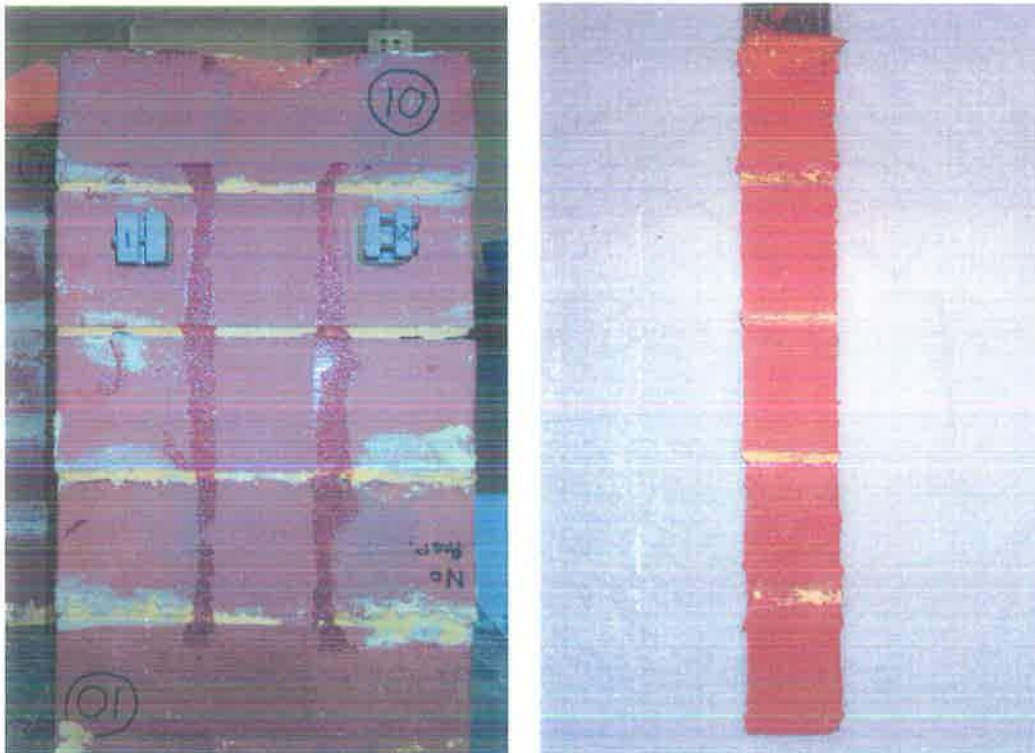


Figure C.10 (e) Failure mode (GP-5-Re-Q)

Specimen GD-5-Sa-Q-1

Plots are not available for this specimen because there was no strain gauge attached along the FRP strips.

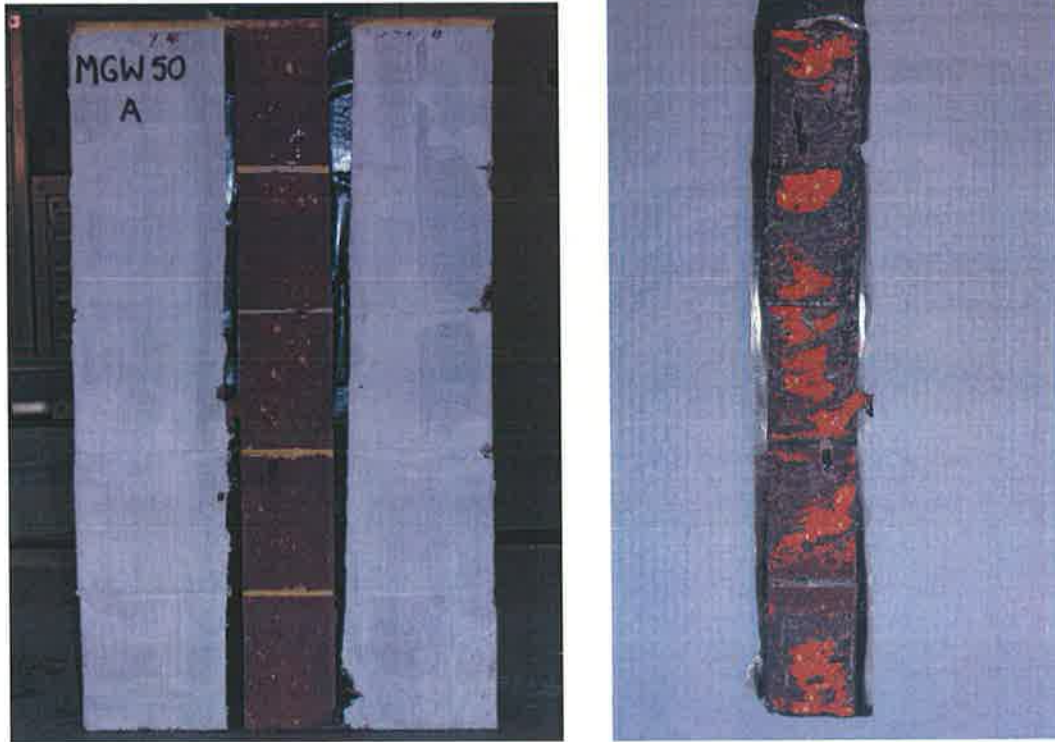


Figure C.11 Failure mode (GD-5-Sa-Q-1)

Specimen GD-5-Sa-Q-2

Plots are not available for this specimen because there was no strain gauge attached along the FRP strips.

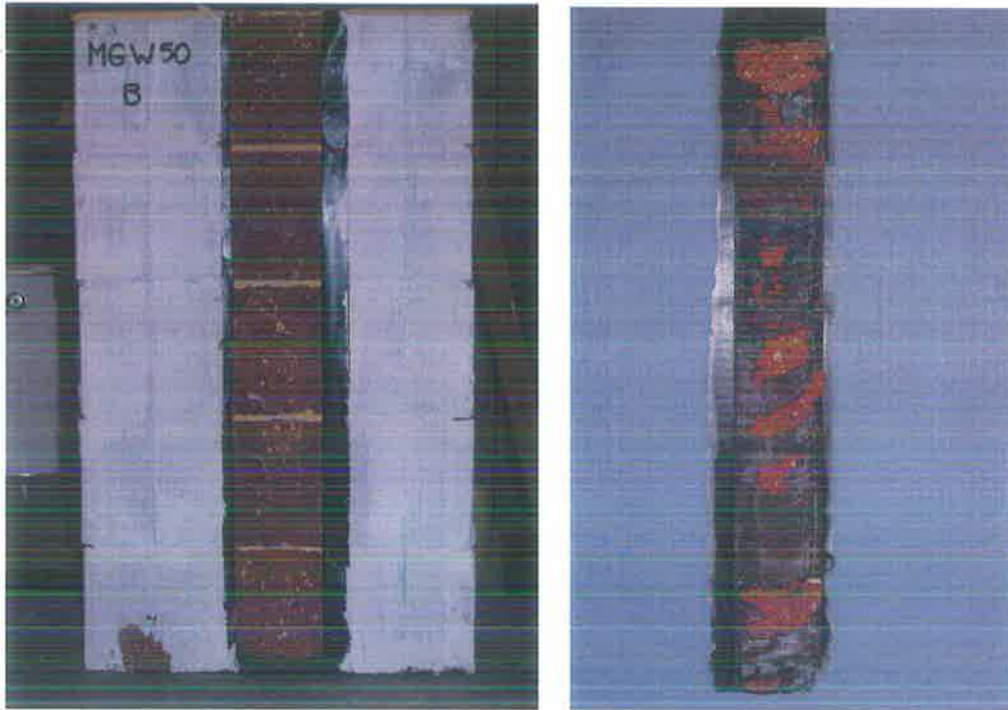


Figure C.12 Failure mode (GD-5-Sa-Q-2)

C.2 CFRP Near Surface Mounted Masonry Push-pull Test Results

The carbon FRP near surface mounted masonry push-pull tests were conducted with the assistance of final year students: Chapman A., Hamann M., Moon, L., and Stoechel A. For detailed test results, please refer to the final year research report of this school (Chapman et al., 2005).

APPENDIX D: DESIGN FOR FRP RETROFITTED WALL TESTS

Consider a one-meter wide wall design strip (i.e. $b_m = 1$ m). The strain and stress distributions of the cross section can be depicted by Figure C.1. The strain is assumed compatible along the cross section. The cross section is designed to an idealised failure mode, namely FRP strip fails in debonding while the ultimate strain is reached in the masonry extreme fibre. The tensile force developed in FRP strip is T_p and compressive force in masonry is C_m . The FRP strip debonding strain ϵ_{db} used in the design was determined by the FRP-to-masonry bond model developed in Chapter 4.

Masonry properties: $f'_{mc} = 16$ MPa; $\epsilon_{mu} = 0.001$; $E_m = 3539$ MPa;

CFRP properties: $E_p = 160$ MPa; $t_p = 1.2$ mm;

CFRP-EB $\epsilon_{db} = 0.003$ (refer to Table 4.3);

CFRP-NSM $\epsilon_{db} = 0.016$ (refer to Table 4.4);

GFRP properties: $E_f = 73$ MPa; $t_f = 0.616$ mm; $\epsilon_{db} = 0.011$ (refer to Table 4.5).

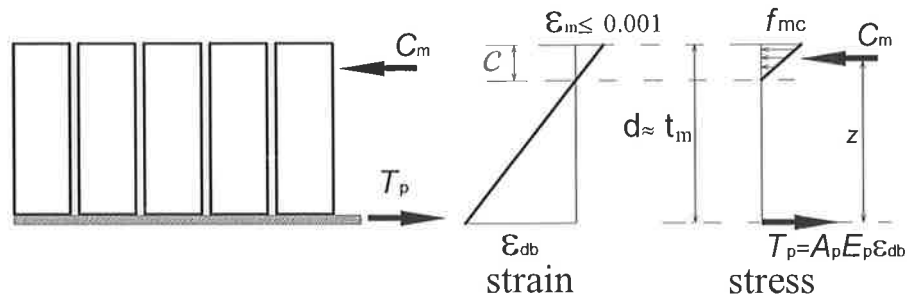


Figure D.1 The flexural strain and stress diagrams of the design wall strip

Compute the nominal flexural capacity:

$$T_p = C_m, \quad \text{gives} \quad A_p E_p \epsilon_{db} = \frac{1}{2} \epsilon_m E_m b_m$$

$$\frac{\epsilon_m}{\epsilon_{db}} = \frac{c}{t_m - c}$$

⇒ determine the required A_p

then, check $\varepsilon_m \leq 0.001$ and $c \leq$ brick shell cover (i.e. 20mm in this case)

the one-way vertical bending capacity:

$$M_{cv} = A_p E_p \varepsilon_{db} \left(t_m - \frac{c}{3} \right)$$

The three wall design schemes are summarised in Table C.1

Table D.1 Summary of wall design schemes

	E_{frp} (GPa)	ε_{db}	b'_p (mm/m)	T_p (kN/m)	ε_m	c (mm)	M_{cv} (kNm/m)	w_{pre} (kPa)	s (mm)	b_p (mm)
Wall 1	160	0.0034	77	44	0.0005	13.4	5.3	6.8	650	50
Wall 2	73	0.0105	154	76	0.0010	9.3	7.75	9.9	650	100
Wall 3	73	0.0105	154	76	0.0010	9.3	7.75	9.9	500	77
Wall 4	160	0.0161	20	72	0.0010	7.6	7.0	9.0	1000	20

Note: b'_p = FRP design strip width per meter wide wall;

s = adopted FRP strip spacing;

b_p = adopted FRP strip width (i.e. $b_p = b'_p s / 1000$)

APPENDIX E: FRP RETROFITTED WALL TEST RESULTS

E.1 WALL 1

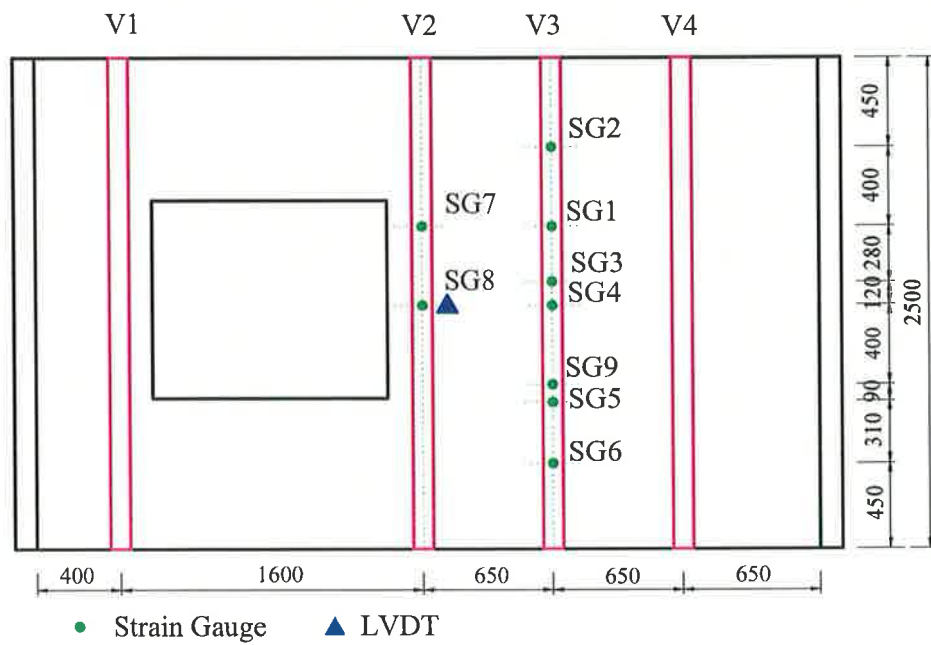


Figure E.1 (a) Test scheme and instrumentation layout of Wall 1

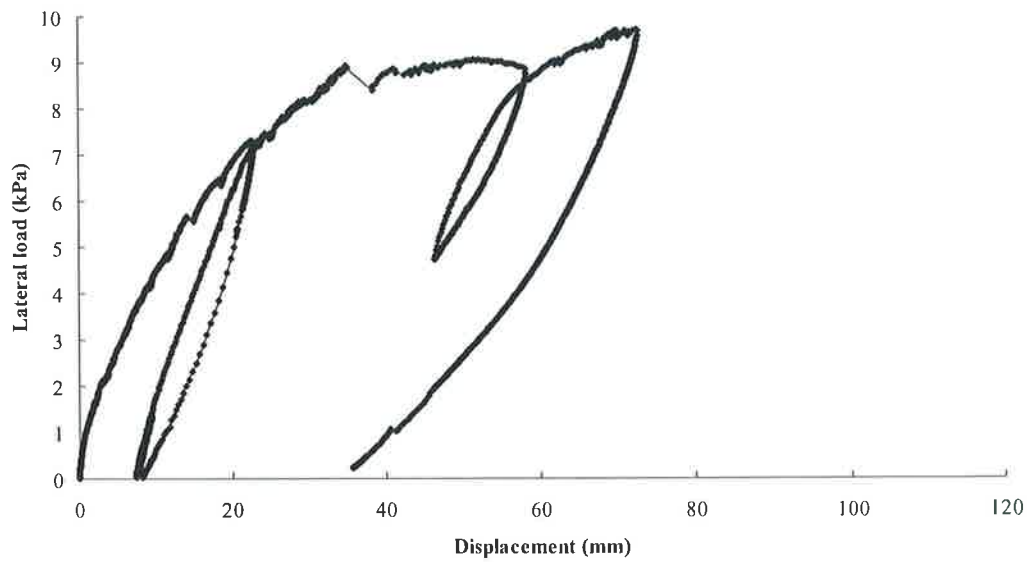
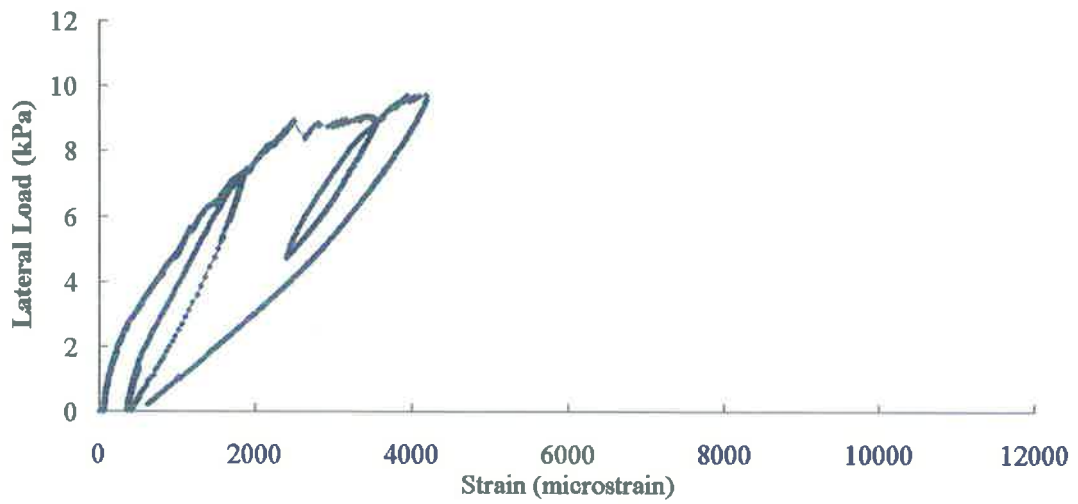
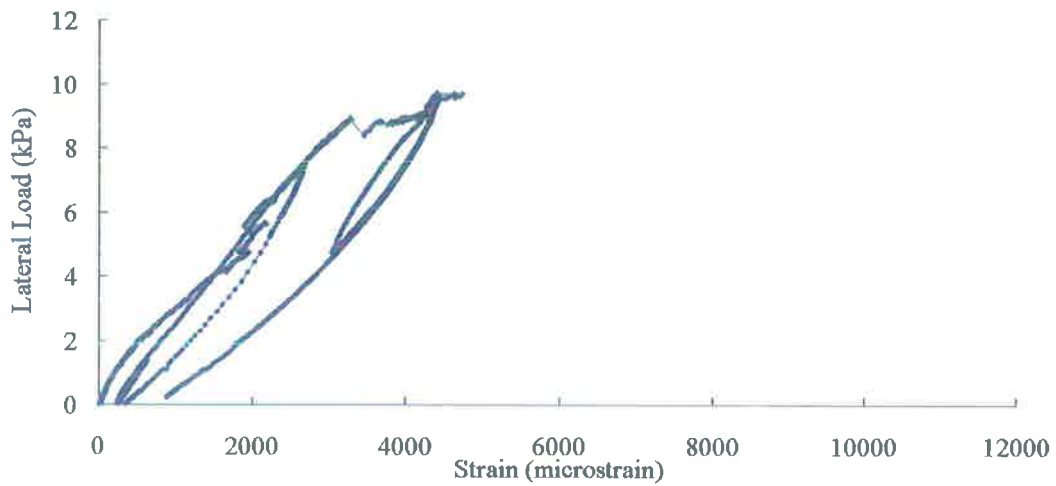


Figure E.1 (b) Lateral load-Displacement behaviour of Wall 1

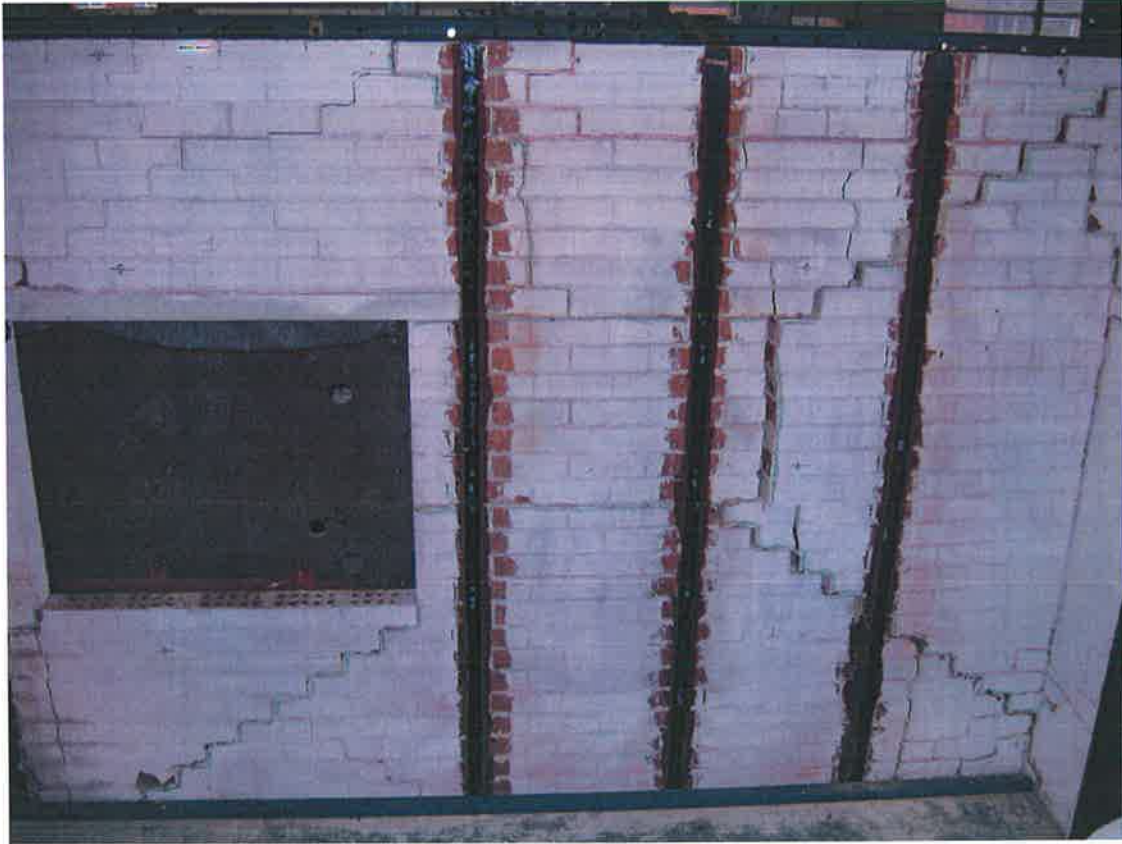


SG7 on Wall 1 FRP strip V2

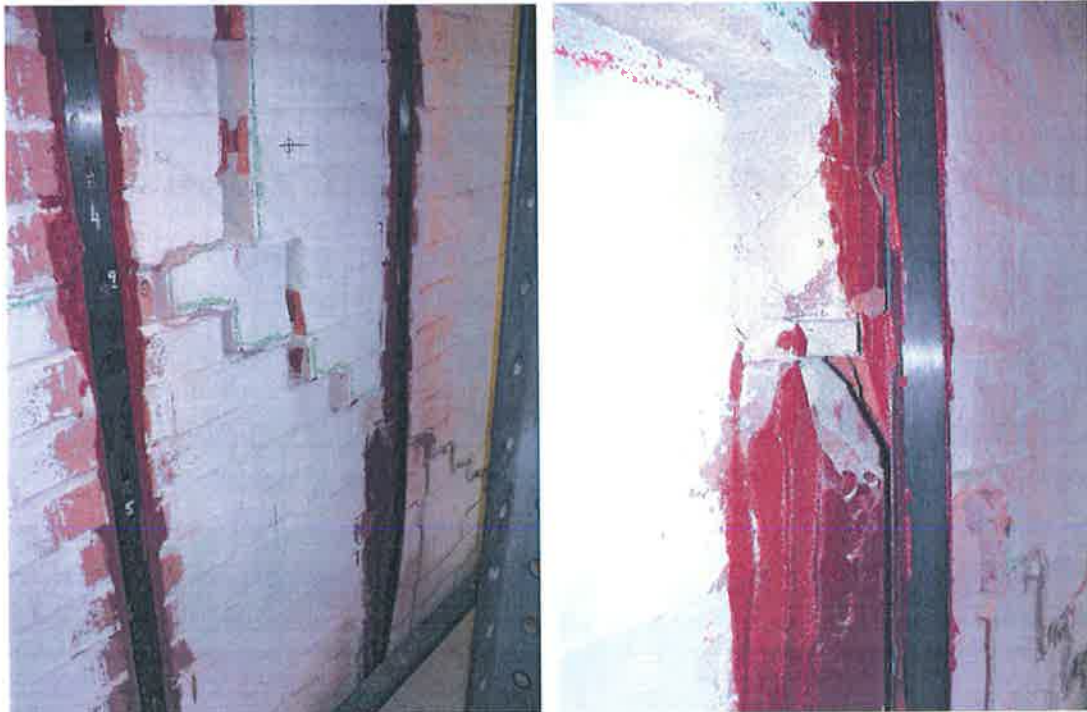


SG1 on Wall 1 FRP strip V3

Figure E.1 (c) Load-strain response for maximum strains on each FRP strip



Overall cracking pattern of Wall 1



Differential displacement of sub-panels

FRP debonding

Figure E.1 (d) Cracking patterns and failure mode of Wall 1

E.2 WALL 2

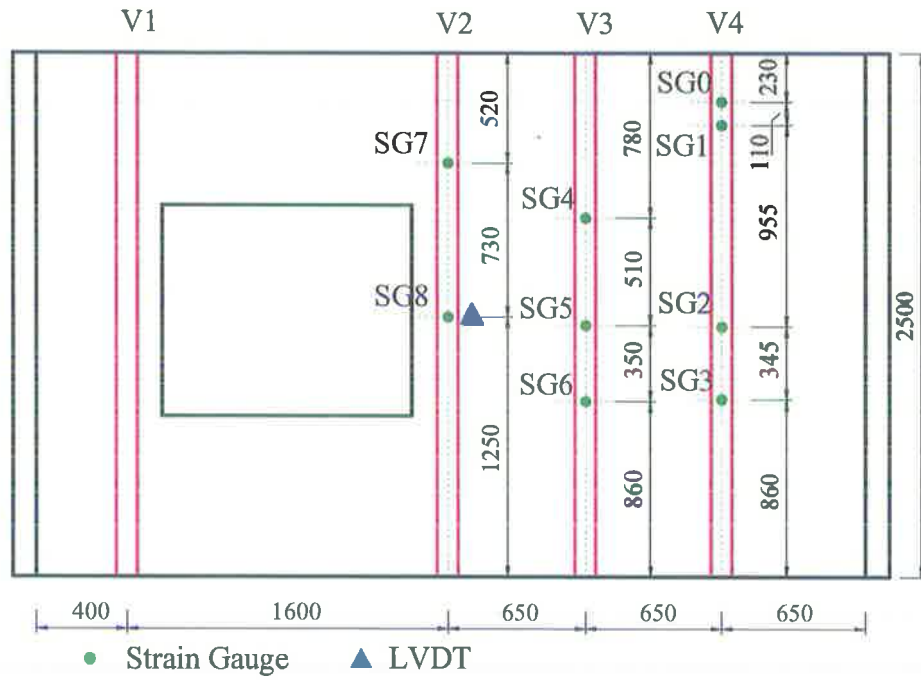


Figure E.2 (a) Test scheme and instrumentation layout

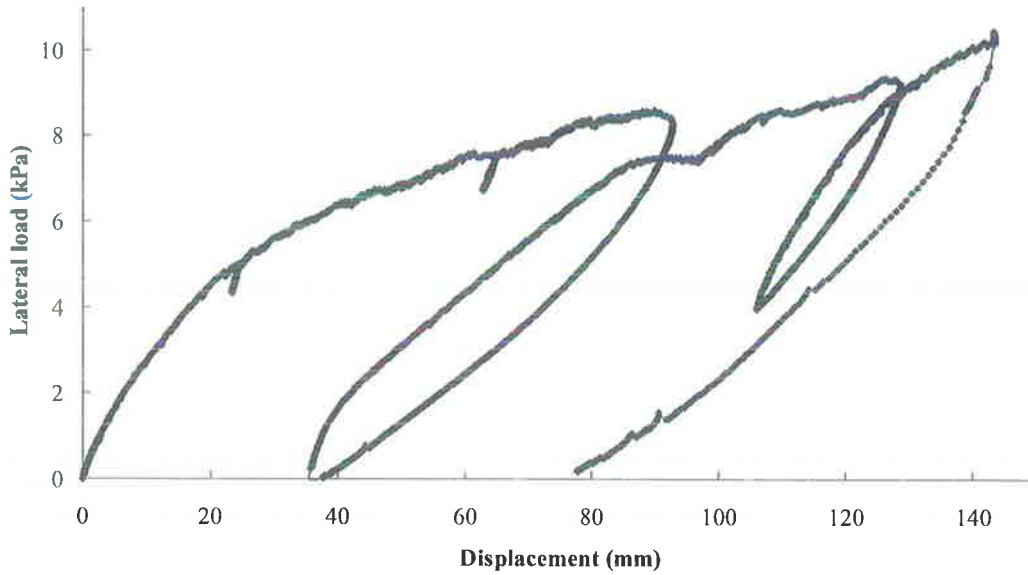
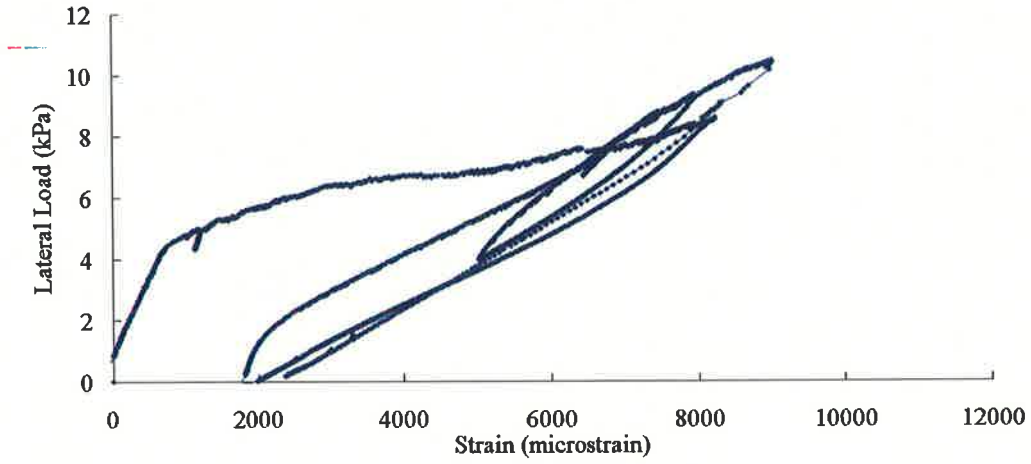
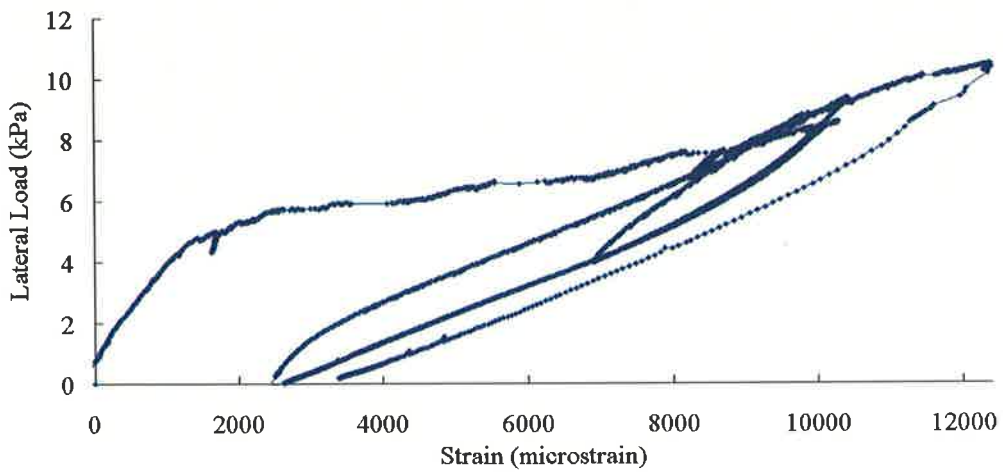


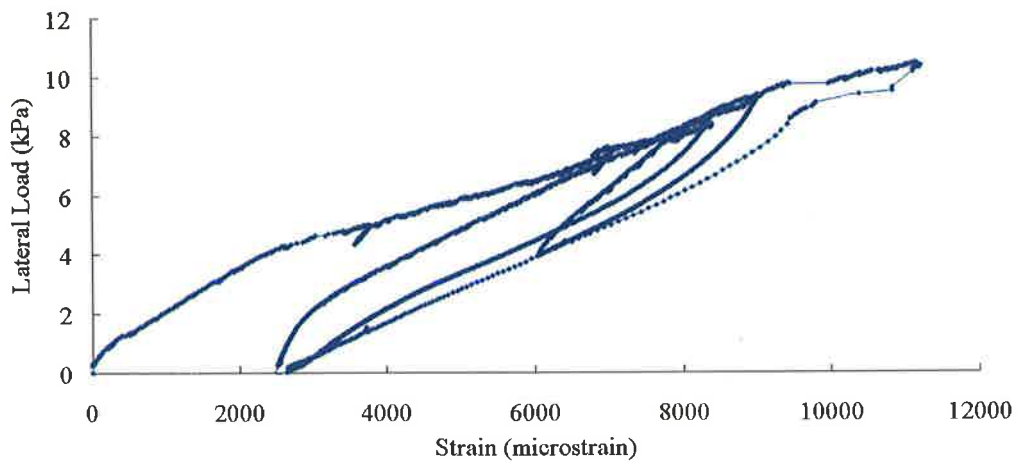
Figure E.2 (b) Lateral load-Displacement behaviour of Wall 2



SG8 on Wall 2 FRP strip V2



SG5 on Wall 2 FRP strip V3



SG3 on Wall 2 FRP strip V4

Figure E.2 (c) Load-strain response for maximum strains on each FRP strip



Overall cracking and failure patterns of Wall 2



Cracking above the window



Masonry collapse

Figure E.2 (d) Cracking patterns and failure mode of Wall 2

E.3 WALL 3

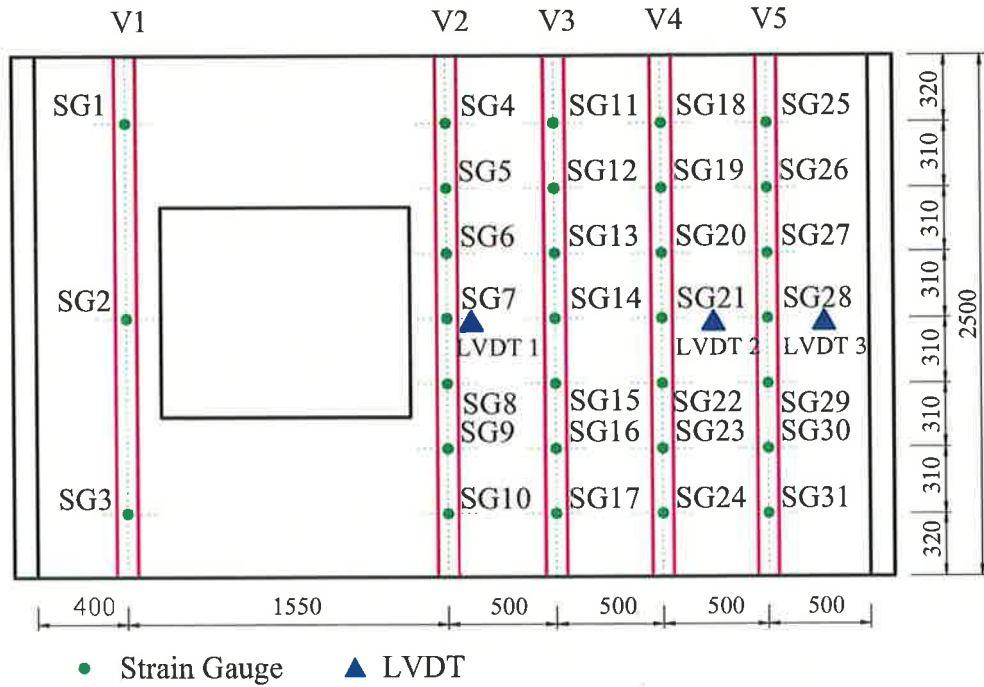


Figure E.3 (a) Test scheme and instrumentation layout of Wall 3

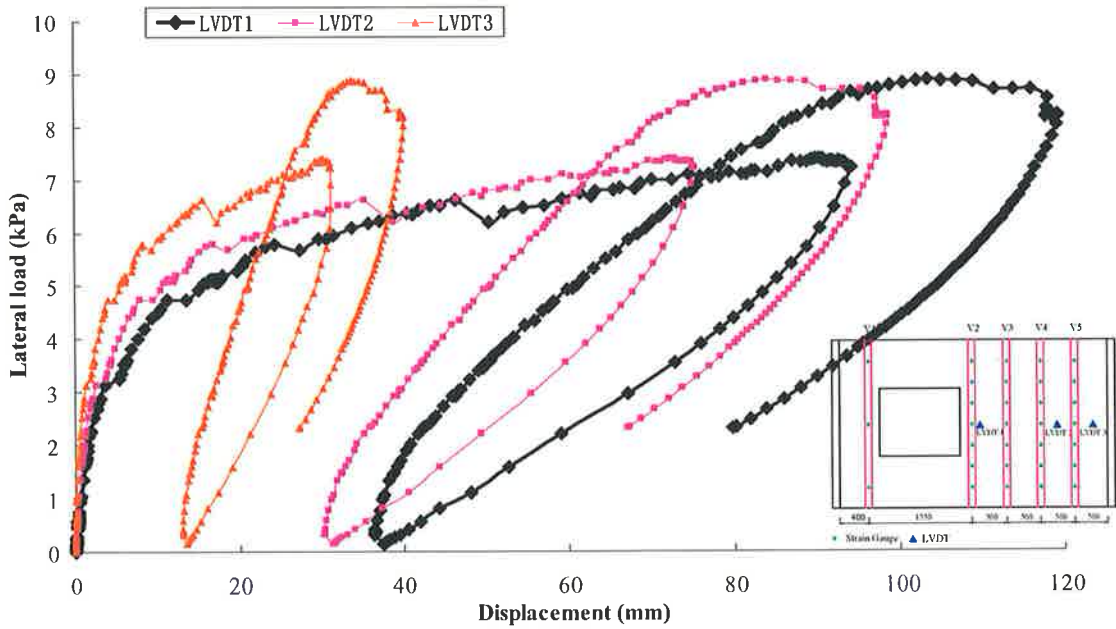
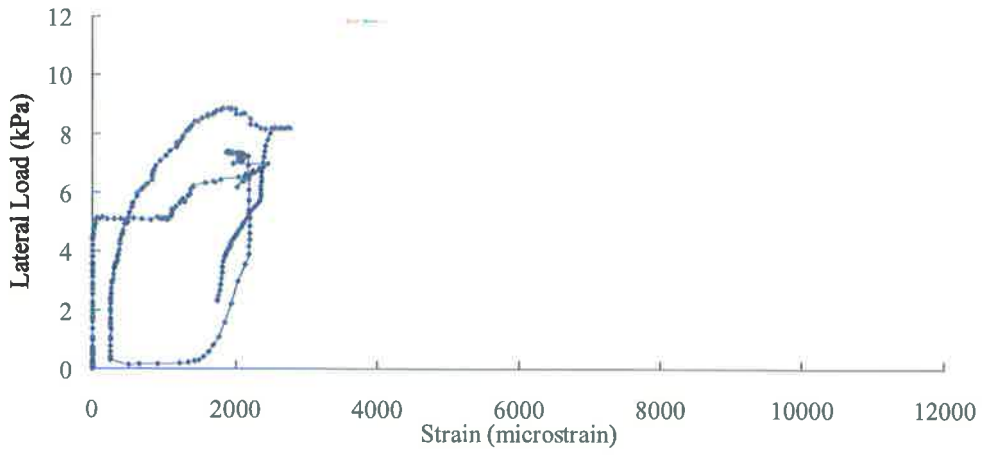
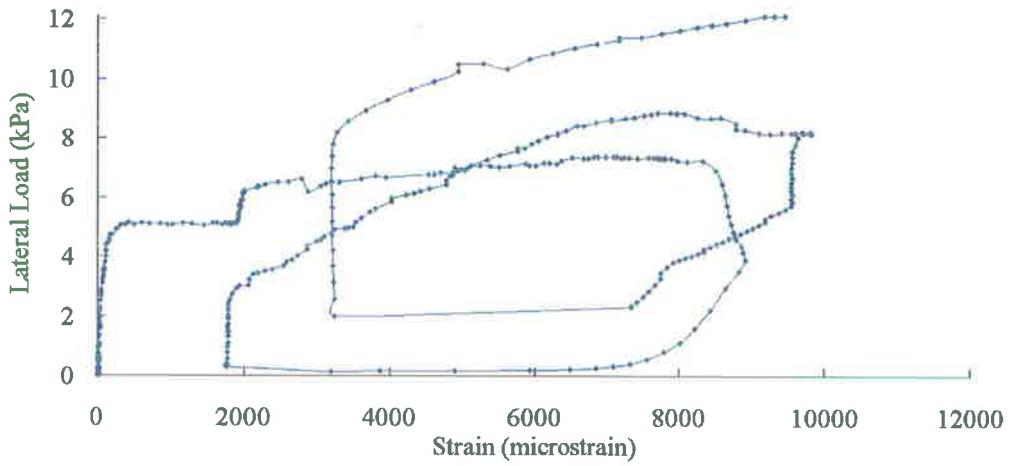


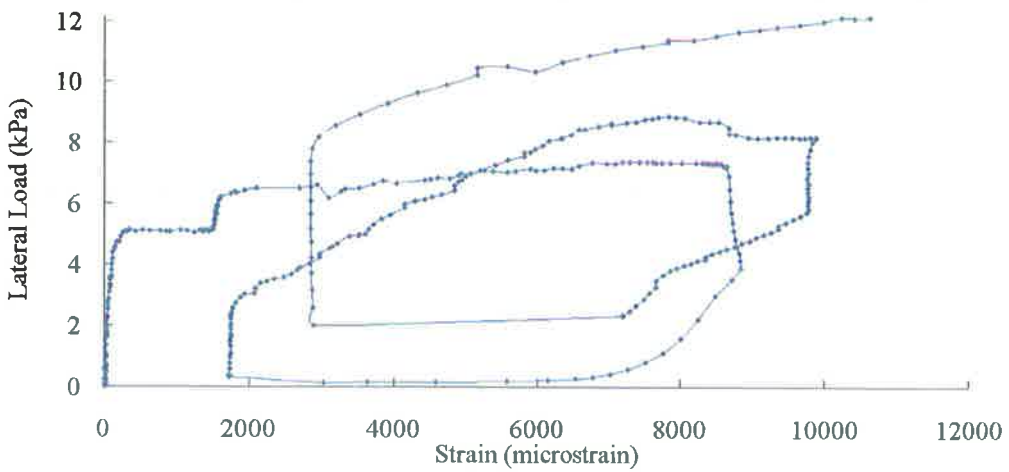
Figure E.3 (b) Lateral load-Displacement behaviour of Wall 3



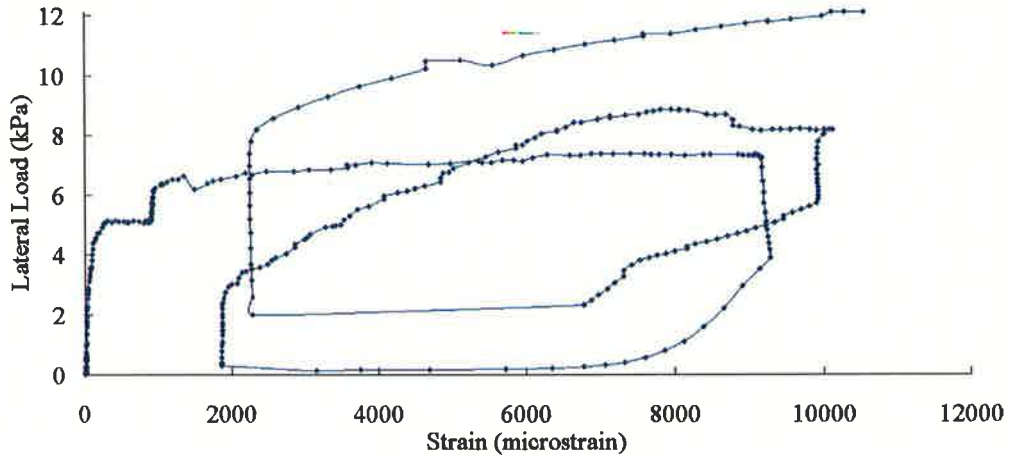
SG1 on Wall 3 FRP strip V1



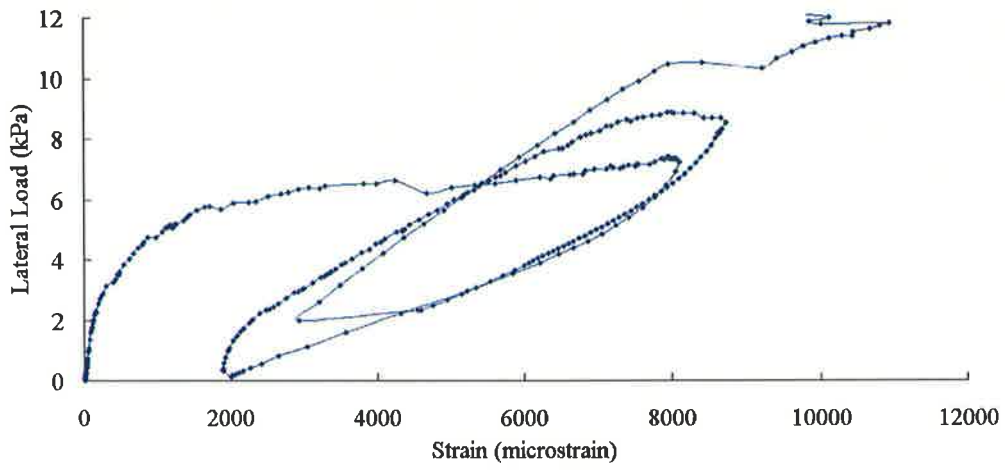
SG6 on Wall 3 FRP strip V2



SG13 on Wall 3 FRP strip V3



SG21 on Wall 3 FRP strip V4

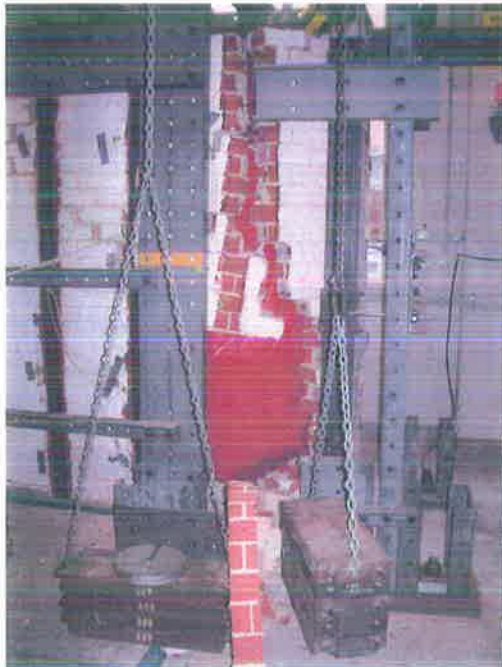


SG 29 on Wall 3 FRP strip V5

Figure E.3 (c) Load-strain response for maximum strains on each FRP strip



Overall cracking and failure pattern of Wall 3



Masonry collapse and FRP debonding



Masonry failure surface

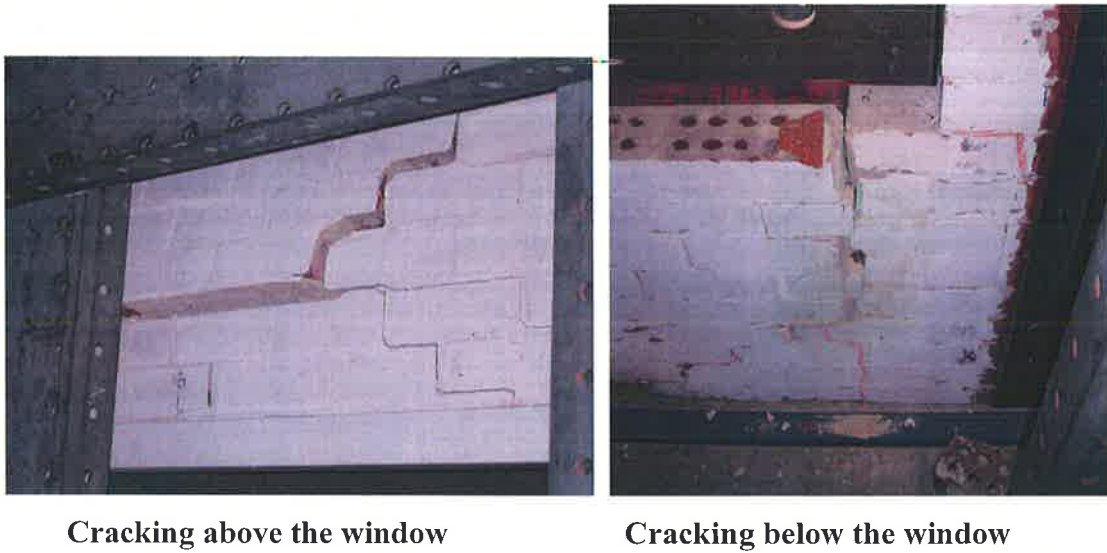


Figure E.3 (d) Cracking patterns and failure modes of Wall 3

E.4 WALL 4

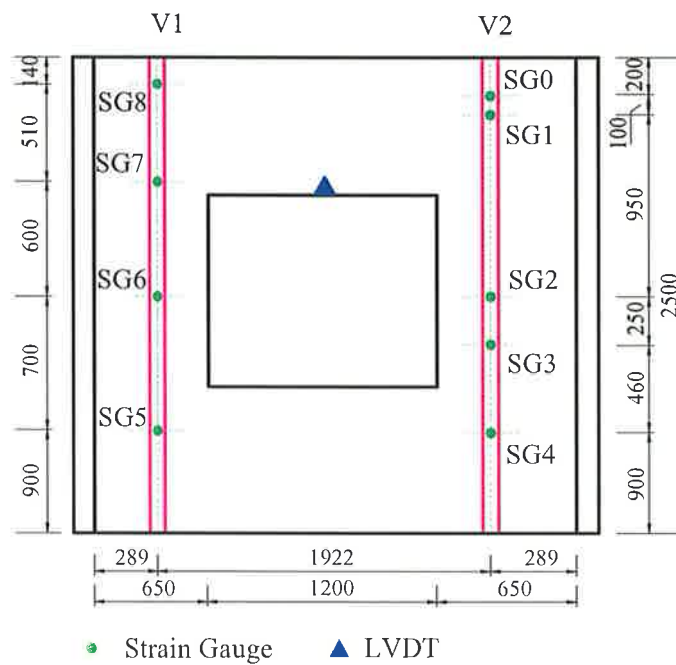


Figure E.4 (a) Test scheme and instrumentation layout of Wall 4

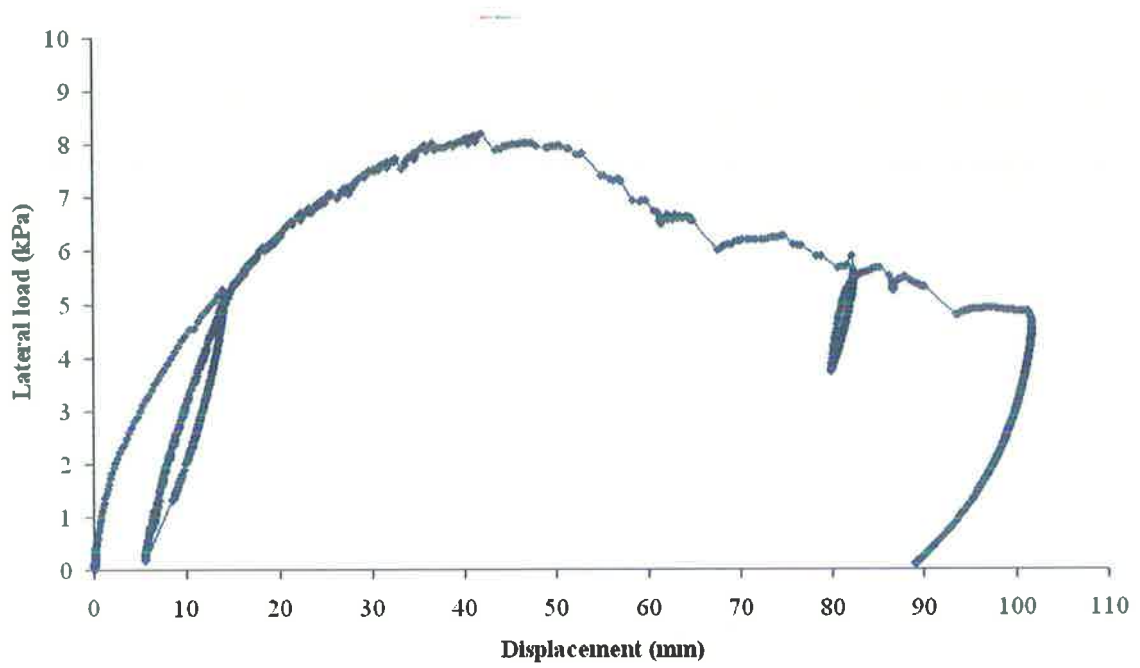
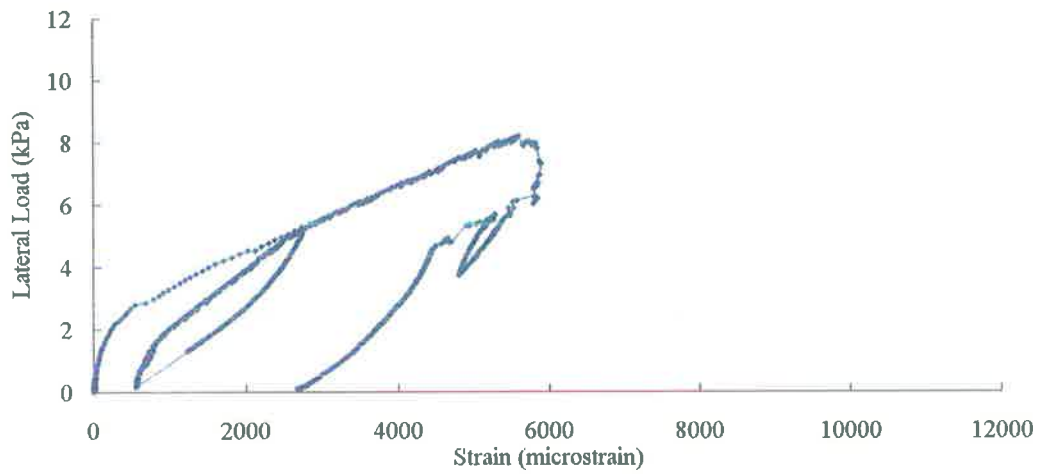
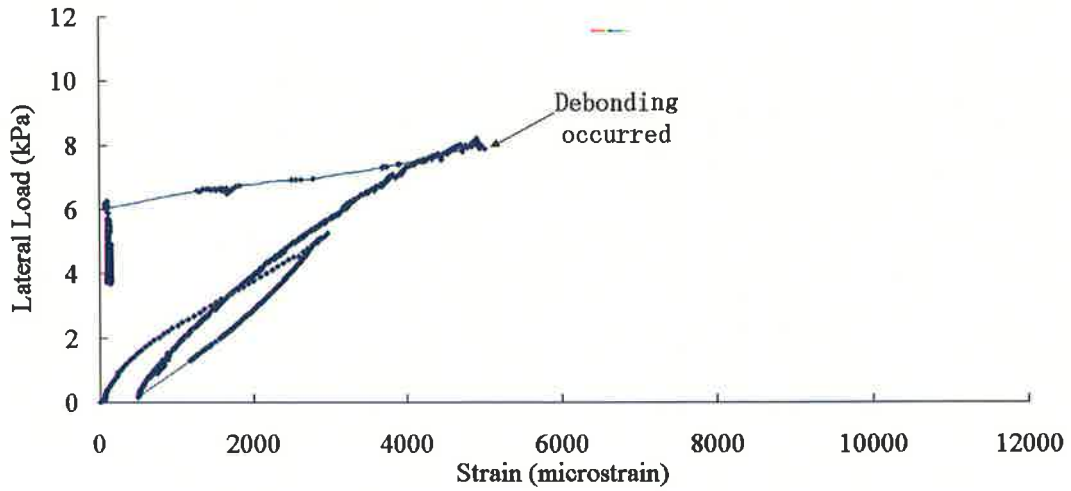


Figure E.4 (b) Lateral load-Displacement behaviour of Wall 4



SG5 on Wall 4 FRP strip V1

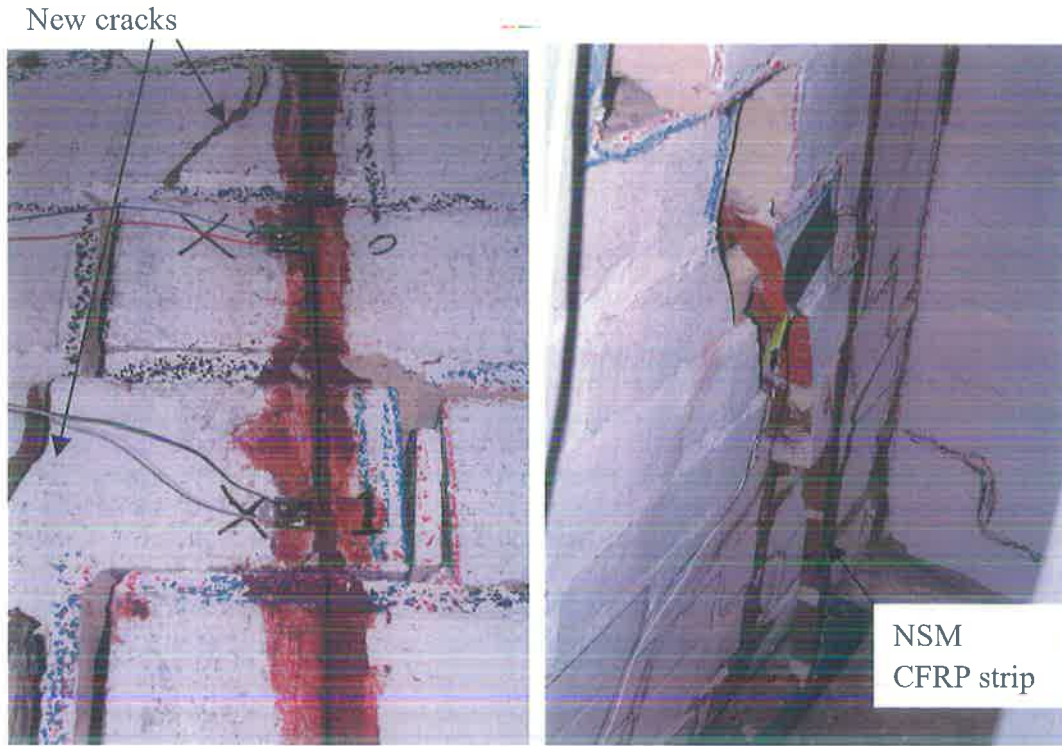


SG4 on Wall 4 FRP strip V2

Figure E.4 (c) Load-strain response for maximum strains on each FRP strip



Overall cracking and failure pattern of Wall 4



New cracking at top right part of Wall 4

CFRP debonding

Figure E.4 (d) Cracking patterns and failure modes of Wall 4